

Research in Optoelectronics (A)

Reprints published in 2013

by

Professor Larry A. Coldren

and Collaborators

Published as

Technical Report # ECE 14-01

of

The Department of Electrical & Computer Engineering

The University of California

Santa Barbara, CA 93106

Phone: (805) 893-4486

Fax: (805) 893-4500

E-mail: coldren@ece.ucsb.edu

<http://www.ece.ucsb.edu/Faculty/Coldren/>

Introduction:

Twenty journal and conference papers were published in 2013 from the research of, or collaborations with, Professor Coldren's group. Copies of these papers, and in one case presentation slides, are reprinted in this volume. The majority of these papers originated from proposals generated within Coldren's group, but a few are due to efforts that originated elsewhere and were supported by Coldren and his group members. As in recent years, the work had a focus on III-V compound semiconductor materials as well as the design and creation of photonic devices using these materials. The work spans efforts from basic materials and processing technology, through device physics, the design and formation of devices and photonic ICs, to the characterization of these devices and circuits within systems environments.

As in the past, the reprints have been grouped into a couple of areas: **I. Photonic Integrated Circuits**, and **II. Vertical-Cavity Surface-Emitting Lasers (VCSELs)**. Most of the work is in the first area, which has been further subdivided into *A. Review Articles*; *B. Novel Stable and Tunable Lasers*; *C. Results with Integrated Optical Phase-Locked Loops*; and *D. Coherent Beam Steering PICs*. Integrated coherent transmitters and receivers continues to be the leading application. MOCVD growth remains a support effort for this InP-based PIC work. On the other hand, our MBE growth effort is key to the second major activity on VCSELs (**II**). A book chapter on high-speed direct-modulation of VCSELs, a paper on the fabrication of a novel three-terminal gain-modulated structure, and two papers on our fast polarization modulation technique for VCSELs are given in this section. In nearly every project the work requires efforts in materials research, device physics, device design, process development, device fabrication, and device characterization. Most students are deeply involved in several, if not all, of these efforts, giving them an unusually broad education.

The work was performed with funding from several grants from industry and government, some gift funds from industry, and support from the Kavli Endowed Chair in Optoelectronics and Sensors. Two projects were funded by the MTO Office of DARPA, under the CIPhER and SWEEPER programs. One was supported by the UC-Discovery program in collaboration with Rockwell-Collins, and industry support included work with Ziva, JDS-Uniphase, Telcordia, Corning, Freedom-Photonics, and Rockwell-Collins.

The first group of reprints (*IA.*) includes two papers that summarize some of our work on Photonic ICs for coherent communication as well as one paper summarizing discussions about nanolasers at a "Rump" Session of the International Semiconductor Laser Conference.

The second group (*IB.*) includes four reprints, the first two of which describe new linewidth narrowing results possible with electronic feedback from detectors following an integrated optical filter. As illustrated in Fig. 1 and presented at CLEO'13, the linewidth of a widely-tunable Sampled-Grating Distributed-Bragg-Reflector (SGDBR) Laser can be narrowed by from 10 – 50 X by a short-delay, high-gain feedback loop. The filter can also act as a wavelength locker, if designed to have repeat modes at some desired interval.

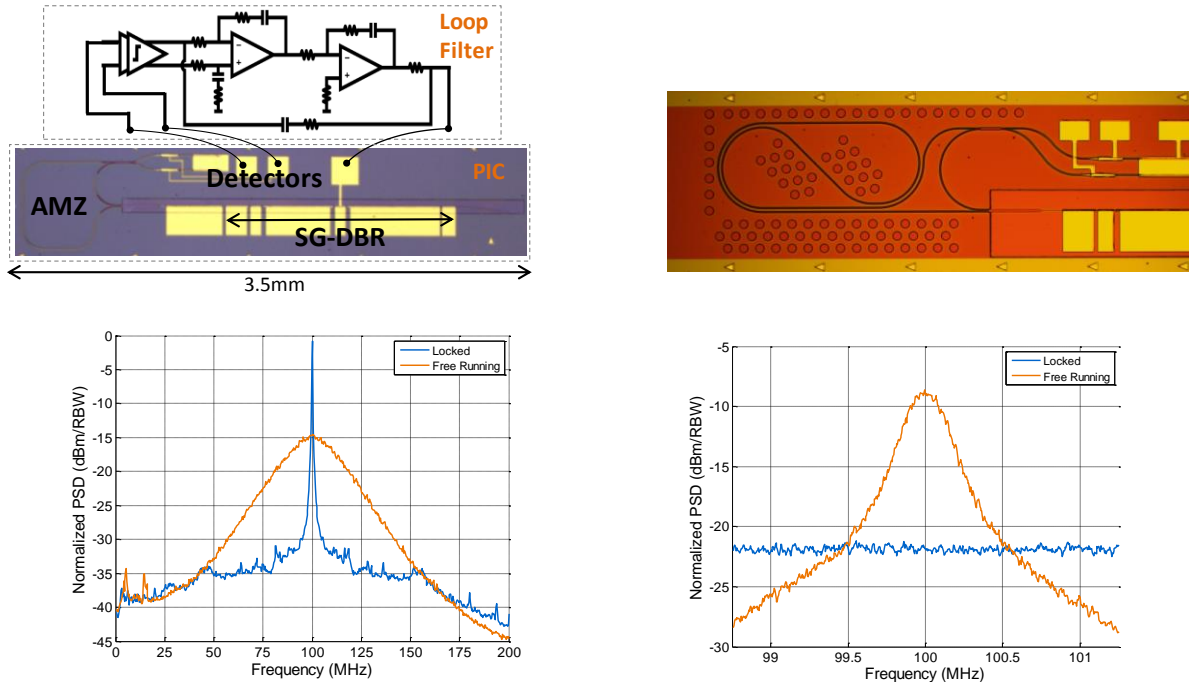


Fig. 1. (top-left) Photo of PIC with SGDBR and 60 GHz free-spectral-range (FSR) Asymmetric Mach-Zehnder (AMZ) filter and schematic of electronic feedback circuit (loop filter). (top-right) Photo of 10GHz FSR AMZ filter extending from PIC. (bottom-left) Wide spectral plot of locked and free-running linewidth from 10GHz FSR filter. (bottom-right) Narrow spectral plot of locked (150 kHz) and free-running linewidth—labels switched.

The third paper in *(IB)* gives details of the stability map of injection-locked lasers, while the fourth gives new results for integrated phase-locked, mode-locked lasers. A 430 GHz span comb is demonstrated with < 550 Hz linewidth on the locked comb line and < 1 kHz on adjacent tones.

Section *IC* gives results with integrated Optical Phase-Locked Loops (OPLLs). This work was done in close collaboration with Prof. Rodwell’s group. The first paper discusses the electronic IC design, the second gives slides from a review of the OPLL work at the conference on Optical Fiber Communications (OFC), the next three give details of heterodyne and homodyne OPLL circuits for wavelength synthesis and coherent receivers, and the last one discusses a new ‘super-channel’ WDM receiver technique with demultiplexing in the electrical domain.

Figure 2 gives some results from our OPLL homodyne BPSK receivers. The Photonic IC (PIC) included a widely-tunable SGDBR local oscillator, a 4-output $\pm I$ and $\pm Q$, 90° -hybrid, and 4 high-speed (~ 35 GHz), high-power UTC photodetectors with microstrip lines matched to the electronic-IC input lines. The use of directional couplers insured a 90° phase relationship. As illustrated in the circuit schematic, electronic feedback is applied to the tuning electrode of the SGDBR LO-laser to lock it to the carrier of the incoming optical signal. The feedback loop has sufficient bandwidth (1.1 GHz) to narrow the linewidth of the SGDBR to match that of the incoming optical carrier—in this case 100 kHz. The BER shows error-free operation without any FEC up to 35 Gb/s. The whole receiver occupies an

area of about 1 cm^2 , and uses about 3W due to the use of an InP electronic IC and discrete loop filter electronics. (Less than 1 W is predicted using Si-ICs.)

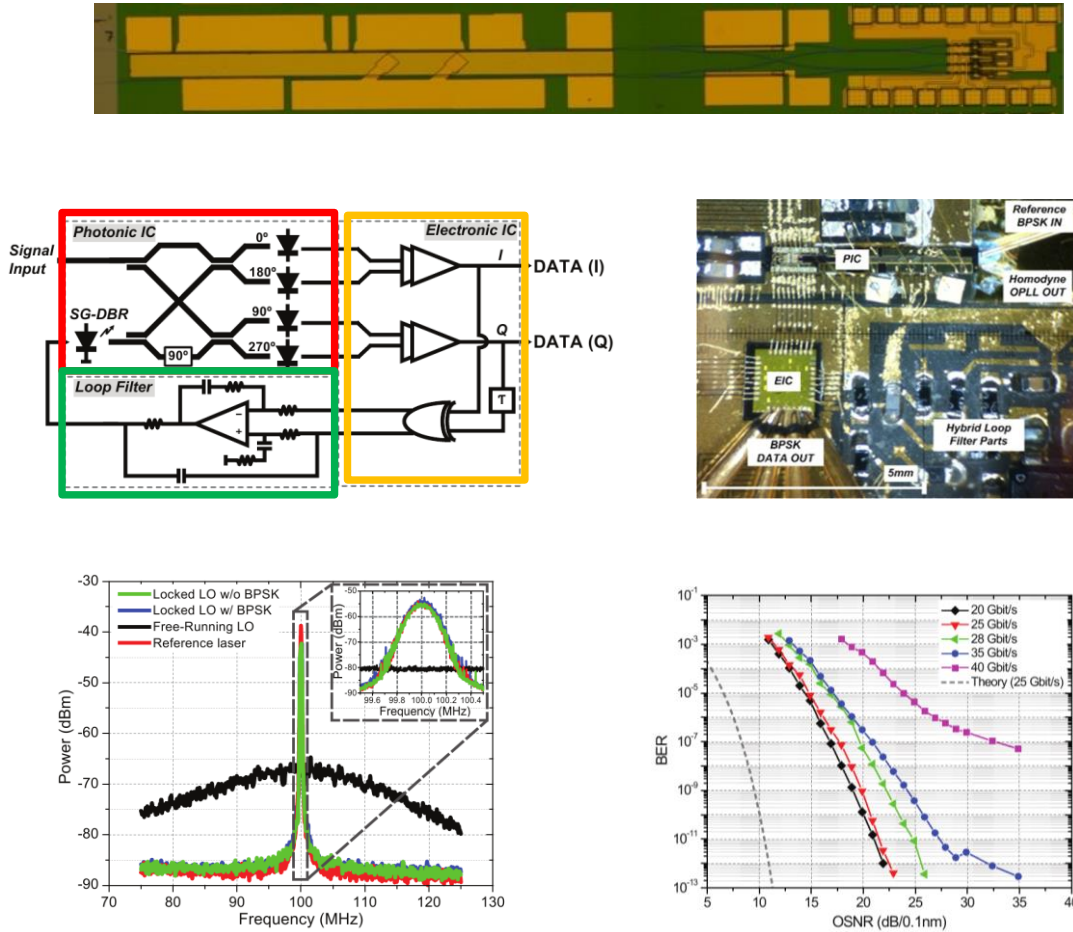


Fig. 2. BPSK-OPLL homodyne receiver results. (top) PIC; (middle-left) circuit schematic; (middle-right) photo of receiver; (bottom-left) linewidth of SGDBR-LO locked and free-running; (bottom-right) BER vs OSNR. [M. Lu, H. Park, E. Block, A. Sivanathan, J. Parker, Z. Griffith, L. Johansson, M. Rodwell, and L. Coldren, *JLT*, **31**, (13), 2244-2253 (July 1, 2013)].

Part (1D) in the PIC section gives papers describing a collaborative effort on coherent 2-D beam sweeping with Prof. Bowers' group and two outside companies: Packet Photonics and Rockwell-Collins. The first item was an invited paper from the Bowers' group overviewing results with a Si-photonics approach. With the InP-platform, we have been successful in fabricating and testing 32-waveguide array PICs. All 32 phase shifters and SOA-power amplifiers work after flip-chip bonding the 'PIC-on-carrier' to a connectorized circuit board. This 'intermediate board' is tested by plugging it into a larger computer-controlled control board. Figure 3 summarizes some results from this mounted 32 channel PIC. Complete characterization, including high-speed beam sweeping, still remains to be demonstrated.

As can be seen, beam widths of $< 1^\circ$ in the lateral and $< 0.5^\circ$ in the longitudinal directions are observed. Also, sweeping over far-field angles of $\sim 10^\circ$ in both directions has been demonstrated.

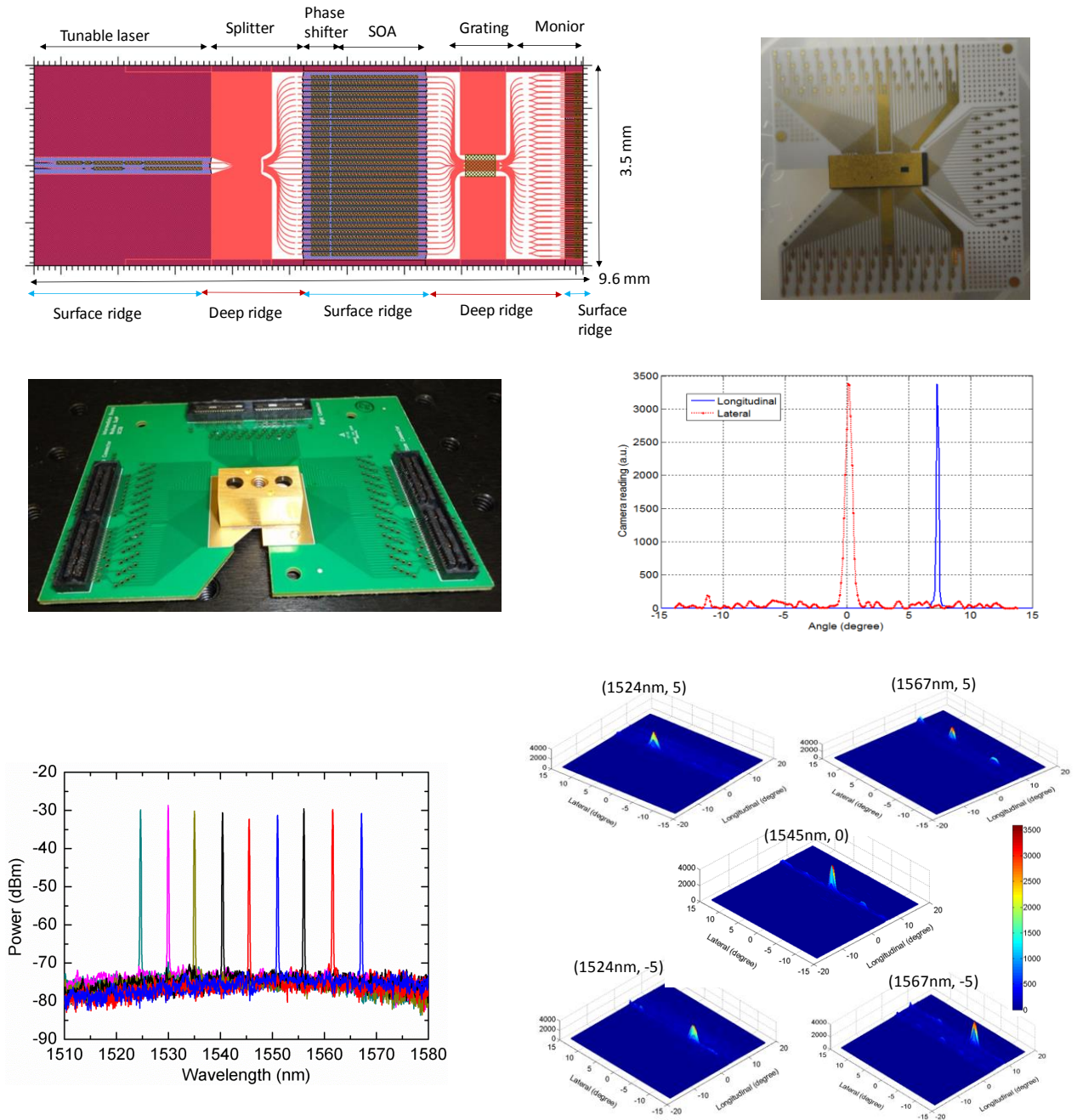


Fig. 3. 32-channel InP-SWEEPER PIC results. (top-left) PIC; (top-right) PIC-on-carrier; (middle-left) PIC/carrier flip-chipped on intermediate board with micro-channel cooler attached; (middle-right) lateral and longitudinal far-field beam profiles; (bottom-left) SGDBR tunable-laser superimposed outputs; (bottom-right) example 2-D far-fields for different wavelengths and phase-shifter currents.

The second major element of work in Prof. Coldren's group is on high-speed and polarization modulated VCSELs. This is broken out as Section II. The high-speed component of our work in 2013 resulted in a book chapter co-authored by Yu-Chia Chang

and Prof. Coldren. This work was actually performed about two years earlier, but the publishing process was slow. It was continued by Y. Zheng, who completed his work in 2012. The second paper discusses a high-yield contacting scheme, and the last two give new results for high-speed polarization modulation.

Figure 4 illustrates results for fast polarization modulation of a multimode, oxide-confined, elliptical diode VCSEL, a new regime of operation discovered this year. Prior work with purely electrically modulated VCSELs only showed kHz to MHz modulation rates. Dr. Barve in Coldren's group is the first to demonstrate that with dc + rf modulation, very high-speed switching can be obtained.

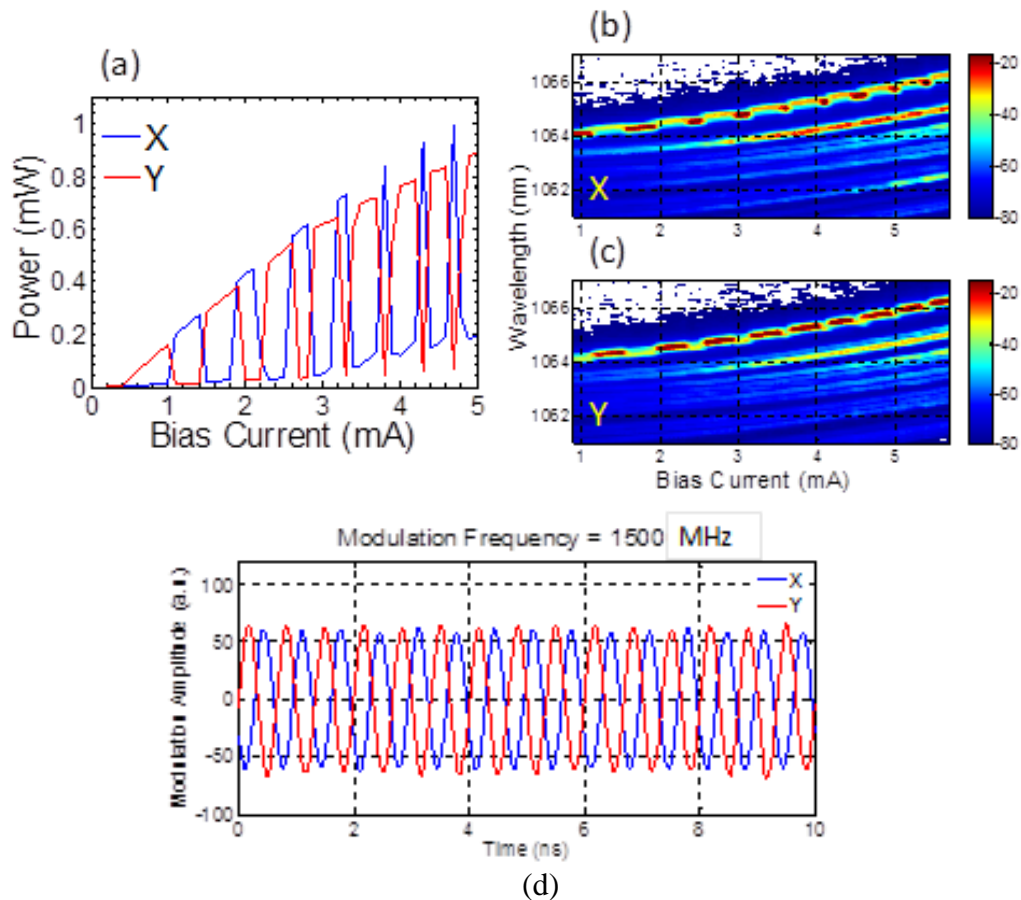
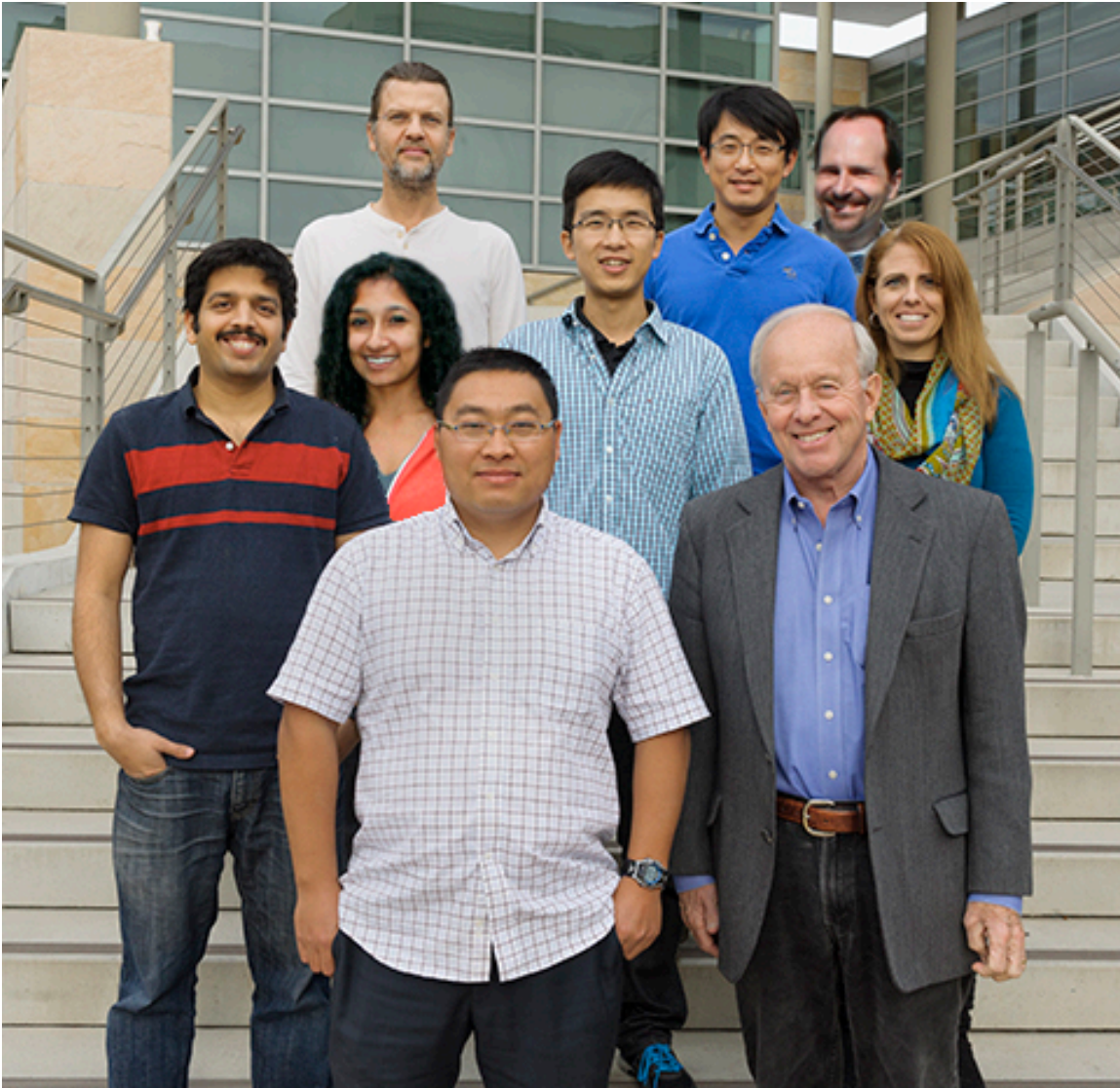


Fig. 4. (a) Measured L-I characteristics of an elliptical, oxide confined VCSEL showing high polarization contrast ratio even in multimode regime; (b)-(c) high resolution optical spectral measurements as a function of current, for X and Y polarization; (d) response for the VCSEL biased at 4.4 mA and subjected to a fixed RF frequency of 4.95 GHz with the RF power modulated at 1.5 GHz

Professor Coldren's Group



**Back Row: Leif Johansson, Hyun-chul Park, Milan Mashanovitch
Middle Row: Abi Siviathan, Mingzhi Lu, Tamara Berton
Front Row: Ajit Barve, Wiehua Guo, Professor Larry Coldren**

Professor Coldren's Group

I. Researchers

A. Barve	Postdoctoral Scholar, UCSB
P. Binetti	Postdoctoral Scholar, UCSB, now at JDS Uniphase
W. Guo	Project Scientist, UCSB
L. Johansson	Associate Research Engineer, UCSB
M. Lu	Postdoctoral Scholar, UCSB
M. Masanovic	Associate Project Scientist, UCSB

II. Students

J. Parker	Ph.D. Program, now at Freedom Photonics
A. Sivananthan	Ph.D. Program, now an Intern in the House of Representatives

III. Staff

D. Cohen	Principal Development Engineer, reports to Prof Nakamura
T. Berton	Center Assistant, OTC

Collaborators

I. Faculty

J. Bowers	UCSB
J. V. Crnjanski	Assistant Professor, University of Belgrade
D. M. Gvozdic	University of Belgrade
D. Ritter	Technion Israel - ITT
M. Rodwell	UCSB

II. Researchers

C. Althouse	Member of Staff, Packet Photonics (former Graduate Student)
H. Ambrosius	Director of Clean Room, Eindhoven University of Technology
J. Barton	CEO, Advanced Diagnostic Technologies

E. Bloch	Research Scientist, Technion Israel and UCSB (Rodwell)
Y. Chang	Member of Staff, Flir (former Graduate Student)
Z. Griffith	RF Design Engineer, Teledyne Scientific & Imaging
A. Husain	CEO, ZIVA Corporation
M.M. Krstic	Teaching and Research Assistant, University of Belgrade
C. Lin	Member of Staff, JDS Uniphase (former Graduate Student)
A. Mehta	Member of Staff, Ziva Corporation
E. Norberg	Member of Staff, Aurrion, Inc. (former Graduate Student)
J. Peters	Sr. Development Engineer, UCSB (Bowers)
B. Thibeault	Project Scientist, UCSB (Rodwell)
Y. Zheng	Member of Staff, Booz Allen Hamilton (former Graduate Student)

III. Collaborating Students

J. Bovington	UCSB, Bowers
M. Davenport	UCSB, Bowers
J. Doylend	UCSB, Bowers, now at Intel
M. Heck	UCSB, Bowers, now a Professor at Denmark Aarhus
H. Park	UCSB, Rodwell
M. Piels	UCSB, Bowers, now a Postdoctoral Scholar, Denmark Technical University, Copenhagen
T. Reed	UCSB, Rodwell

Table of Contents:

I. Photonic Integrated Circuits

IA. Tutorials, Review, and Books

M.L. Masanovic, L.A. Johansson, J.S. Barton, W. Guo, M. Lu, and L.A. Coldren, “High-performance InP/GaAs Based Photonic Integrated Circuits,” *Proc. CLEO Pacific Rim 2013*, paper no. TuN1-2, Kyoto, Japan (June 30 – July 4, 2013). INVITED. 1

L.A. Coldren, “What is a Diode Laser Oscillator?,” *IEEE J. Sel. Topics Quantum Electron., Special Issue on Semiconductor Lasers* **19** (4), pp. 1503503, (July/August 2013). 3

M.L. Masanovic, and L.A. Coldren, “Photonic Device Technology for Coherent Optical Communications,” *Telekomunikacije*, Professional and Scientific Journal of the Serbian State Agency for Communications, **10**, pp. 42-52. (December 2012). 6

IB. Laser Sources

A. Sivananthan, H. Park, M. Lu, J.S. Parker, E. Bloch, L.A. Johansson, M.J. Rodwell, and L.A. Coldren, “Monolithic Linewidth Narrowing of a Tunable SG-DBR Laser,” *Proc. Optical Fiber Communication Conference*, paper no. OTH3I.3, Anaheim, CA (March 17-21, 2013). 19

A. Sivananthan, H. Park, M. Lu, J.S. Parker, E. Bloch, L.A. Johansson, M.J. Rodwell, and L.A. Coldren, “Integrated Linewidth Reduction of a Tunable SG-DBR Laser,” *Proc. CLEO 2013*, paper no. CTu1L.2, San Jose, CA (June 9-14, 2013). 22

M.M. Krstic, J.V. Crnjanski, M.L.Masanovic, L.A. Johansson, L.A. Coldren, and D. Gvozdic, “Multi-Valued Stability Map of an Injection-Locked Semiconductor Laser,” *IEEE J. Sel. Topics Quantum Electron., Special Issue on Semiconductor Lasers*, **19** (4), pp. 1501408, (July/August 2013). 24

J. Parker, M. Lu, H. Park, A. Sivananthan, E. Bloch, Z. Griffith, L.A. Johansson, M.J. Rodwell, and L.A. Coldren, “Highly-stable Integrated InGaAsP/InP Mode-locked Laser and Optical Phase-locked Loop,” *Photonic Technology Letters*, **25** (18), pp. 1851-1854, (September 15, 2013). 32

IC. Integrated Optical Phase-Locked Loops

E. Bloch, H. Park, M. Lu, T. Reed, Z. Griffith, L.A. Johansson, L.A. Coldren, D. Ritter, and M.J. Rodwell, “A 1-20 GHz All-Digital InP HBT Optical Wavelength Synthesis IC,” *IEEE Transactions on Microwave Theory and Techniques*, **61** (1), pp. 570-580, (January 2013). 39

L.A. Coldren, M. Lu, H. Park, E. Bloch, J.S. Parker, L.A. Johansson, and M.J. Rodwell, “New Opportunities for Optical Phase-locked Loops in Coherent Photonics,” *Proc. Optical Fiber Communication Conference*, paper no., OTh3H.5, Anaheim, CA (March 17-21, 2013). INVITED. 50

M. Lu, H. Park, J.S. Parker, E. Bloch, A. Sivananthan, Z. Griffith, L.A. Johansson, M.J. Rodwell, and L.A. Coldren, “A Heterodyne Optical Phase-locked Loop for Multiple Applications,” *Proc. Optical Fiber Communication Conference*, paper no. OW3D.1, Anaheim, CA (March 17-21, 2013). 68

- M. Lu**, H. Park, A. Sivanathan, J.S. Parker, E. Bloch, L.A. Johansson, M.J. Rodwell, and L.A. Coldren, “Monolithic Integration of a High-speed Widely-tunable Optical Coherent Receiver,” *Photonic Technology Letters*, **25** (11), pp. 1077-1080, (June 1, 2013). 71
- M. Lu**, H. Park, E. Bloch, A. Sivanathan, J.S. Parker, Z. Griffith, L.A. Johansson, M.J. Rodwell, and L.A. Coldren, “An Integrated 40 Gbit/s Optical Costas Receiver,” *Journal of Lightwave Technology*, **31** (13), pp. 2244-2253, (July 1, 2013). 75
- H. Park**, M. Piels, E. Bloch, M. Lu, A. Sivanathan, Z. Griffith, L.A. Johansson, J. Bowers, L.A. Coldren, and M.J. Rodwell, “Integrated Circuits for Wavelength Division De-Multiplexing in the Electrical Domain,” *Proc. ECOC 2013*, paper no. Mo.4.C.3, London, England (September 22-26, 2013). 85

ID. Coherent Beam Steering PIC's

- J. K. Doyle**, M. J. R. Heck, J. T. Bovington, J. D. Peters, M. L. Davenport, L. A. Coldren, and J. Bowers, "Hybrid silicon free-space source with integrated beam steering," *Proc. SPIE 8629, Silicon Photonics VIII*, vol. 862911, (March 2013). 91
- W. H. Guo**, P.R.A. Binetti, C. Althouse, L.A. Johansson, and L.A. Coldren, “InP Photonic Integrated Circuit with On-chip Tunable Laser Source for 2D Optical Beam Steering,” *Proc. Optical Fiber Communication Conference*, paper no. OTH3I.7, Anaheim, CA (March 17-21, 2013). 100
- W.H. Guo**, P.R.A. Binetti, C. Althouse, M.L. Masanovic, H.P.M.M. Ambrosius, L.A. Johansson, and L.A. Coldren, “Two-Dimensional Optical Beam Steering with InP-based Photonic Integrated Circuits,” *IEEE J. Sel. Topics Quantum Electron., Special Issue on Semiconductor Lasers*, **19** (4), pp.6100212, (July/August 2013). INVITED. 103
- W.H. Guo**, P.R.A. Binetti, M.L. Masanovic, L.A. Johansson, and L.A. Coldren, “Large-scale InP Photonic Integrated Circuit Packaged with Ball Grid Array for 2D Optical Beam Steering,” *Proc. IEEE Photonics Conference*, paper no. ThE2.2, Bellevue, WA (September 8-12, 2013). 115

II. Vertical-Cavity Surface-Emitting Lasers (VCSELs)

- Y-C Chang** and L.A. Coldren, “Design and Performance of High-Speed VCSELs,” in *Springer Series in Optical Sciences*, Vol. 166, R. Michalzik, Ed. Berlin: Springer-Verlag, pp. 233-262, (2013). 119
- C.H. Lin**, B. J. Thibeault, Y. Zheng, M.J. Rodwell, L.A. Coldren, A. Mehta, and A. Husain, “Ultra-compact, High-Yield Intra-Cavity Contacts for GaAs/AlGaAs-based Vertical-Cavity Surface-Emitting Lasers,” *Journal of Vacuum Science & Technology B*, **31** (1), pp. 011205-01125-6, (January/February 2013). 149
- A.V. Barve**, Y. Zheng, L.A. Johansson, A. Mehta, A. Husain, and L.A. Coldren, “High Speed Polarization Modulation of Oxide Confined Asymmetric VCSELs in Multimode Regime,” *Proc. IEEE Photonics Conference*, paper no. TuE2.3, Bellevue, WA (September 8-12, 2013). 155
- A.V. Barve**, Y. Zheng, L. Johansson, A. Mehta, A. Husain, and L.A. Coldren, “Fast, Electrically Controlled Polarization Modulation of Multimode Vertical-Cavity Surface-Emitting Lasers by RF Frequency Modulation,” *Optics Express*, **21**, (25), pp. 31092-31097, (December 2013). 157

I. Photonic Integrated Circuits

A. Tutorials, Reviews, and Books

High-performance InP/GaAs Based Photonic Integrated Circuits

M. L. Mašanović^{1,2}, L.A.Johansson^{1,2}, J.S. Barton², W. Guo¹, M. Lu¹, and L. A. Coldren¹

¹ECE Department, University of California, Santa Barbara, CA 93106, USA

²Freedom Photonics, Santa Barbara, CA 93117, USA

Abstract

InP photonic integrated circuits continue to play important roles in realization of modern optical communication systems, optical sensing and free-space communication systems. In this paper, we report on our recent work on InP advanced modulation format tunable transmitters and receivers, as well as 2D optical beam steering InP PICs.

I. INTRODUCTION

InP photonic integrated circuits continue to play important roles in realization of modern optical communication systems, as well as to find new application areas, such as optical sensing and free-space communication. In this paper, we report on our work on advanced modulation format optical tunable transmitter and receiver components, as well as on 2D optical beam steering using PICs.

II. COHERENT OPTICAL RECEIVERS AND TRANSMITTERS

After more than three decades since conception, optical coherent systems are finally a reality. They are being deployed throughout transport optical networks in order to provide more optical bandwidth through existing optical fiber, as well as simplify dealing with the impairments of transmission, given that in most cases, both optical amplitude and phase are being recovered.

Arbitrary vector modulation can be generated using the combination of both amplitude and phase modulation. One popular way to accomplish this task is to use the nested Mach-Zehnder modulator structure shown in Figure 3c. Because this structure assigns the I axis to one MZM and the Q axis to a second MZM, it can modulate the resultant vector to any (I,Q) point in the plane of the I-Q diagram. For QPSK modulation, four equal amplitude (I-Q) points are accessed.

InP Photonic integration and photonic integrated circuits play a prominent role in realization of coherent optical systems. Example devices include modulators and receivers [1],[2], as well as fully integrated transmitter and receiver arrays [3].

Our fully integrated tunable coherent transmitter chip, reported in [4], consists of a widely-tunable sampled-grating DBR (SGDBR) laser monolithically integrated with a nested Mach-Zehnder modulator, as shown in Figure 1.

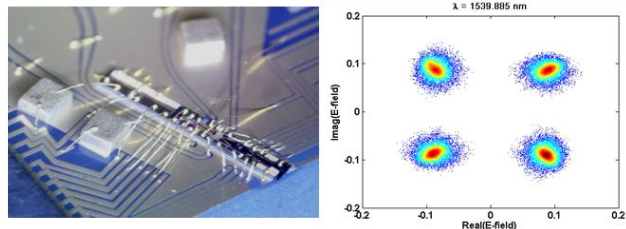


Figure 1 – (left) Photograph of the widely tunable optical transmitter integrated circuit mounted on an Aluminum-Nitride ceramic carrier. (right) A representative constellation diagram from coherent link demonstration using a 20 Gbps QPSK encoded optical signal with $2^{31}-1$ PRBS, after DSP post processing. Linear color coding corresponds to symbol density.

The chip was realized using monolithic integration in Indium Phosphide (InP) based on quantum well intermixing. The single-mode SGDBR laser provides 40 nm of tuning around 1550 nm. The signal from the laser is amplified with a semiconductor optical amplifier (SOA), and then split into 4 paths, using a 1x4 multimode interference (MMI) splitter. The light in each path is sent through a static phase adjustment electrode embedded in the S-bend waveguides, which is essential for setting the MZMs in the quadrature state. The high-speed MZMs are formed using 400 μm long quantum-well intermixed (QWI) regions, with a photoluminescence (PL) peak at 1.5 μm , utilizing the quantum-confined Stark effect (QCSE) for light absorption. After the light in each of the four arms is modulated, it is recombined in a 4x3MMI, which allows for monitoring of the MZM in the OFF state. Thus, the chip is capable of transmitting a single transverse-electric (TE) polarization QPSK data stream in a compact footprint. The key issue with tunable laser integration for coherent transmitter purposes is that of achieving sufficiently narrow linewidth and low phase noise, and this will remain the area of active research in the near future. Recent progress has been reported using a widely tunable laser with heater electrodes, which reduces the shot noise in the laser cavity [5], as well as through using frequency stabilization based on on-chip integrated monitoring [6].

As with coherent transmitters, integration of a widely tunable local oscillator would further benefit the level of integration in coherent receiver PICs. The first implementation of an integrated widely tunable coherent receiver, reported by Freedom Photonics, is shown in Figure 2 [7]. The chip was realized using photonic integration in Indium Phosphide. At the center of the chip is a widely tunable sampled grating distributed Bragg reflector (SGDBR) laser, used as the receiver LO,

providing 40 nm tunability and bandwidth coverage. The signal from the LO is split into two identical paths. In each of the two paths, the LO power is amplified with a semiconductor optical amplifier (SOA), before the signal is routed using 2 total internal reflection (TIR) mirrors with a perpendicular waveguide connecting them. The signal from the second TIR mirror is then guided into a 2x4 multimode interference (MMI) hybrid. The receiver chip has two signal input waveguides, which are used to independently couple each of the two demultiplexed polarization data streams from a polarization multiplexed network data stream. The four outputs of each of the hybrids are separated using S-bend waveguides, which terminate in 4 photodiodes. Thus, the chip is capable of simultaneously detecting two independent data streams from a polarization multiplexed QPSK data stream – however, polarization demultiplexing and rotation of the transverse-magnetic (TM) polarization into transverse-electric (TE) has to be performed external to the chip.

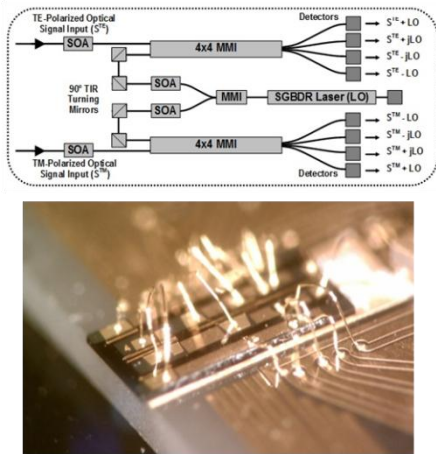


Figure 2 – (top) Schematic of Freedom Photonics' monolithically integrated dual-polarization tunable photonic integrated coherent receiver, including SOAs, MMIs and total internal reflection mirrors and a tunable local oscillator laser (bottom) Photograph of the widely tunable optical receiver integrated circuit mounted on a ceramic carrier [7].

Error-free, 20Gbps (10Gbaud) operation with this chip has been demonstrated. Our more recent work, using a similar device as part of an optical phase locked loop (OPLL) subsystem, for homodyne coherent detection, was reported as an alternative to high power consumption digital signal processing based detection methods. The OPLL was realized using Costa's loop, as shown in Fig.3.

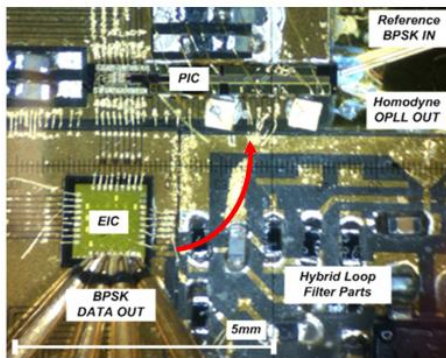


Figure 3 – Photograph of a homodyne optical receiver using an optical phase locked loop based on Costa's loop.

III. PICs FOR 2 DIMENSIONAL BEAM STEERING

Electronically controlled optical beam steering is potentially useful for a number of applications such as LIDAR (light detection and ranging), free space secure laser communication, printing, etc. Various methods have been demonstrated to achieve this goal. One typical method is the optical phased array (OPA) which is used for one-dimensional (1D) optical beam steering .

Recently, we have demonstrated 2D optical beam steering with an InP photonic integrated circuit (PIC) using the scheme of 1D OPA plus wavelength tuning with surface emitting gratings. The PIC used is shown in Figure 4. It consists of an on-chip widely tunable SGDBR laser, followed by a set of 1x2 splitters, forming 8 individual waveguides with an SOA array, and an emission array. On-chip power monitors are integrated as well.

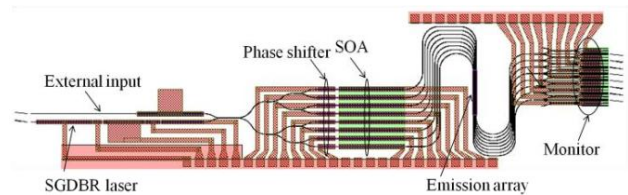


Figure 4 – Layout of the beam-steering photonic integrated circuit, consisting of an on-chip widely tunable SGDBR laser, followed by a set of 1x2 splitters, forming 8 individual waveguides with an SOA array, and an emission array.

Beam steering angle ranges of 5° in longitudinal and 10° in lateral direction have been achieved with this chip.

IV. REFERENCES

- [1] Doerr, C.R. et al., "Compact High-Speed InP DQPSK Modulator," *Photonics Technology Letters*, IEEE, vol.19, no.15, pp.1184-1186, Aug.1, 2007
- [2] Bottacchi S et al., "Advanced photoreceivers for high-speed optical fiber transmission systems. *IEEE Journal of Selected Topics in Quantum Electronics* 2010;16(5): 1099–1112.
- [3] Evans P, et al., "Multi-channel coherent PM-QPSK InP transmitter photonic integrated circuit (PIC) operating at 112 Gb/s per wavelength", *Optical Fiber Communication Conference, Post Deadline Paper PDP7*; 2011 March.
- [4] Estrella, S.B. et al., "First Monolithic Widely Tunable Coherent Transmitter in InP" *Photonics Technology Letters*, IEEE
- [5] M. Larson et al. "Narrow linewidth high power thermally tuned sampled grating distributed Bragg reflector laser", *OFC 2013*, paper OTh3I.4
- [6] A. Sivanathan et al., "Monolithic Linewidth Narrowing of a Tunable SG-DBR Laser", *OFC 2013*, paper OTh3I.3
- [7] Estrella, S.B. et al. , "Widely Tunable Compact Monolithically Integrated Photonic Coherent Receiver," *Photonics Technology Letters*, IEEE , vol.24, no.5, pp.365-367, March1, 2012
- [8] H. Park, "40Gbit/s Coherent Optical Receiver Using a Costas Loop," in *ECOC 2012*, paper Th.3.A.2.
- [9] P. F. McManamon et al., "Optical phased array technology," *Proc. IEEE* 84, 268-298 (1996) .
- [10] Guo, W. et al., "Two-Dimensional Optical Beam Steering with InP-Based Photonic Integrated Circuits," *Selected Topics in Quantum Electronics*, IEEE Journal of , vol.PP, no.99, 2013

What is a Diode Laser Oscillator?

Larry A. Coldren, *Life Fellow, IEEE*

(Invited Paper)

Abstract—This paper attempts to summarize some of the discussions that took place during the “Rump” Session at the 2012 International Semiconductor Laser Conference. The discussion mostly centered around the topic of how one can identify lasing in a given structure, and how one might differentiate between the different kinds of possible light emission.

Index Terms—Coherence, diode lasers, lasing.

I. INTRODUCTION

AS THE first speaker, I attempted to lay some familiar elementary groundwork for what one commonly encounters as the definition of lasing and the identification of the lasing threshold in diode lasers. To no ones surprise, I used a few equations and plots from our textbook on *Diode Lasers and Photonic Integrated Circuits* [1]. I also indicated my bias toward devices that had at least some future hope of having the desirable properties that we look for in diode lasers. That is, high-efficiency, high reliability, low cost, direct current pumping, a directed output beam, high direct-modulation speed, reasonable output power, and relatively good coherence in addition to small size. Integrability with other optics and perhaps electronic ICs has also become a key attribute as we consider future uses of small, efficient devices.

II. DYNAMIC CARRIER/PHOTON FLOW

Fig. 1 is [1, Fig. 5.1]. From the rates of flow R_j of charge carriers and photons across the various boundaries, this diagram not only allows for the derivation of rate equations from which the static and dynamic properties of diode lasers can be determined, but by including “shot noise” at all interfaces, it also provides the basis for the derivation of the relative intensity noise and linewidth of these devices [1]. It specifically illustrates the creation of charge carriers in a carrier reservoir (assumed equal holes and electrons) from a current pumping source. (For optical pumping the picture does not change; one just replaces I by the optical pump power, P_p , q to $h\nu$, and interprets η_i differently at the top of the diagram.) The carriers are lost both radiatively R_{sp} and nonradiatively R_{nr} and they interact with the photon reservoir via stimulated recombination R_{21} and generation R_{12} .

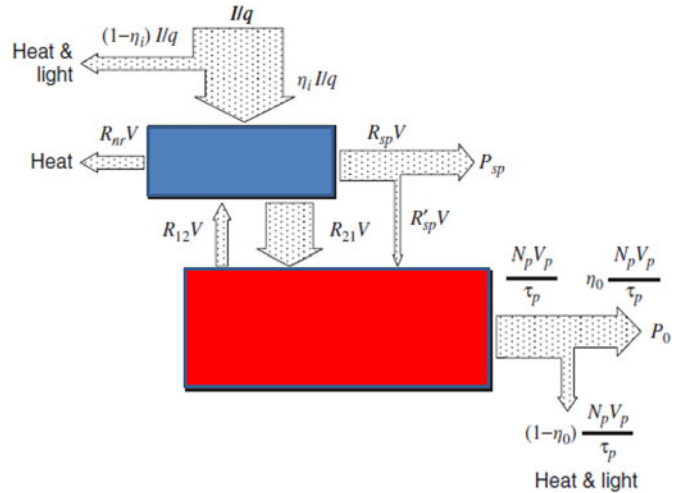


Fig. 1. Diode laser model illustrating the flow of input current I to create carriers in a carrier reservoir and the interaction of this reservoir with a single photon reservoir that provides an output power, P_0 . The carrier reservoir (active region) of volume V physically overlaps the photon reservoir of volume V_p to enable the spontaneous and stimulated generation of photons shown by the interconnecting flow arrows. For multimode lasers there are multiple photon reservoirs coupled to the single carrier reservoir. Reprinted from [1].

A small portion of the radiative recombination, $R'_{sp} = \beta R_{sp}$ is coupled into the single optical mode, which is implicitly assumed by the single photon reservoir. The number of photons in the mode, $N_p V_p$, decay with a time constant τ_p ; a fraction η_0 are coupled into a desired output pathway to provide the output power $P_0 = \eta_0 h\nu N_p V_p / \tau_p$.

III. OUTPUT CHARACTERISTICS

By inspection, we can write down a set of rate equations for the carrier (electrons = holes) and photon densities from Fig. 1. Then, to obtain an asymptote above the lasing threshold, we note that the steady-state modal gain cannot exceed the modal loss. In fact, it really never quite equals it because of the generally small amount of spontaneous emission, $R'_{sp} = \beta R_{sp}$, coupled into the mode as well. But, to get the asymptote, we neglect this spontaneous emission in the photon rate equation and solve for the power into the single lasing mode, P_0 . We can also solve for the total spontaneous emission P_{sp} above the lasing threshold from the carrier rate equation. Then, for $(I > I_{th})$ we have

$$P_0 = \eta_i \eta_0 \frac{h\nu}{q} (I - I_{th}) \quad \text{and} \quad P_{SP} = \eta_i \eta_r \frac{h\nu}{q} I_{th} \quad (1)$$

where η_r is the fraction of carrier recombination that is radiative. Note that because the gain clamps, the carrier density, and

Manuscript received April 9, 2013; revised ; accepted April 9, 2013.

The author is with the Departments of Electrical and Computer Engineering and Materials at the University of California, Santa Barbara, CA 93106 USA (e-mail: coldren@ece.ucsb.edu).

Color versions of one or more of the figures in this paper are available online at <http://ieeexplore.ieee.org>.

Digital Object Identifier 10.1109/JSTQE.2013.2258330

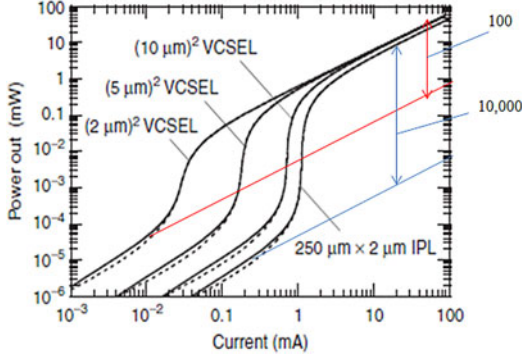


Fig. 2. Log-log output power versus current calculations for various lasers. Only one optical mode is included. Numbers in the right margin are ratios of slopes. Dashed curves assume a constant β , the solid curves use exact mode coupling approach.

P_{sp} should also clamp at threshold. However, if there is a large leakage current or poor injection efficiency, there can be additional spontaneous emission from this current outside of our single reservoir model.

Now, we can also calculate the below-threshold asymptote for the single lasing mode, by assuming only spontaneous emission into only this mode from the photon rate equation and neglecting stimulated emission

$$P_0(I < I_{th}) = \eta_i \eta_0 \eta_r \beta h\nu / q. \quad (2)$$

An approximate $P-I$ characteristic for diode lasers with a relatively small β , say $< 10^{-3}$, can be obtained by just plotting the asymptotes, (1) and (2), on a linear scale. This is generally true for most diode lasers unless quite small. For example, this holds for good VCSELs with diameters $> 6 \mu\text{m}$. However, for larger β , the juncture between the two equations becomes noticeably less abrupt.

One method of determining β and also identifying the threshold of nanolasers has been to plot the $P-I$ characteristic on a log-log scale, such as shown in Fig. 2. The ratio of the slope, dP/dI , above threshold to that below threshold from (1) and (2) can be seen to equal $1/\eta_r \beta$. In Fig. 2, η_r is assumed to be unity. Unfortunately, in practical situations, η_r tends to become small in the same situations as when β is made large—i.e., in nanocavity devices, where surfaces and other defects often are nearby. As shown, β for ideal $2 \mu\text{m}^2$ VCSELs is about 0.01, and it does not get larger than 0.1 until the cross section is considerably less than $1 \mu\text{m}^2$.

Another issue in measuring such curves experimentally is that it is difficult to only capture a single mode below threshold, and this makes the slope ratio appear smaller, and β appears larger.

Fig. 3 gives calculated gain and carrier density curves for the in-plane laser case. Also illustrated are some pitfalls that may occur if such material is used in nanocavities or some other structure where traps may exist. Although lasing does not actually occur until the region labeled #4, where the modal gain nearly equals the modal loss, the transition from region #1 to #2 can sometimes have a very distinct threshold, where the

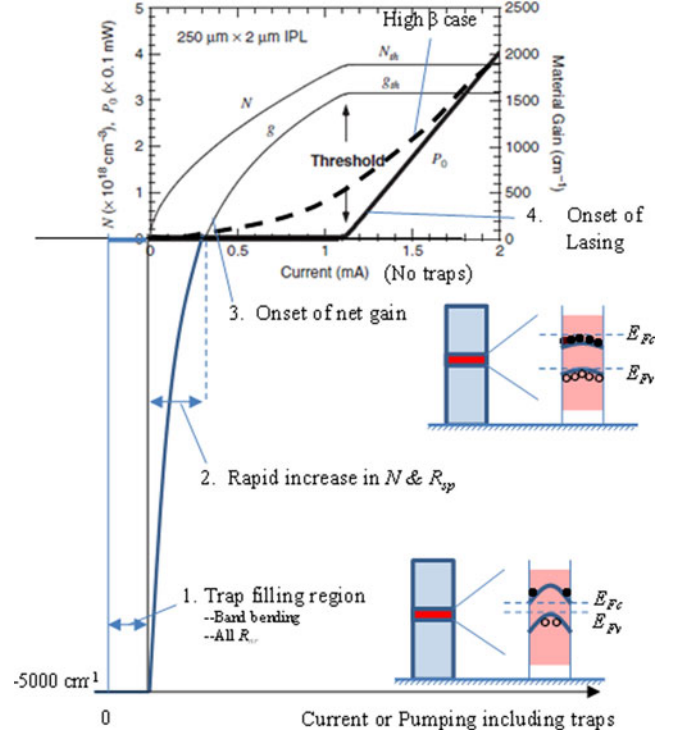


Fig. 3. Plots of carrier density and gain versus pumping. Regions of trap filling (1), reduced absorption (2), gain (3), and lasing (4) indicated. Dashed $P-I$ curve suggests the characteristic for a high β (~ 0.1) laser. Insets show schematics of nanolasers together with possible band structures for regions (1) and (3).

output light increases very sharply, and thereafter, its linewidth decreases substantially.

IV. SUMMARY

The classical characteristics for identifying lasing behavior are 1) a significant kink in the output light characteristic; 2) a narrowing of the output light spectrum; 3) perhaps some narrowing in the directivity of the emission; and 4) possibly some reduction in spontaneous emission in other directions. The first two are most widely used, and generally are used correctly. However, it is important to have a good idea of what the modal losses are in the laser, and if it is likely that the modal gain could possibly overcome these. Otherwise, one may not be observing lasing but perhaps a filling of traps or some other states, followed by spontaneous emission, maybe some filtering by the cavity, then possibly a reduction in loss and spectral narrowing with further pumping, etc., as discussed earlier.

It is also good to have some idea of what the laser linewidth should be for the power that is being generated. Although it is often difficult to measure the power accurately, it is important to get some estimate, so that it is possible to predict an order of magnitude linewidth that should be observed. The linewidth should be in the 10–40 MHz/mW, or 10–40 GHz/ μW range. A nanometer (415 GHz at 850 nm) is still a pretty wide linewidth for a laser. Of course, this can be confused by chirping if the pumping is with short pulses.

In retrospect, one of my conclusions from the Rump Session was that it is very difficult to do better than well-engineered VCSELs for small, low-threshold, and high-efficiency discrete devices. The main motivator to work on other structures appears to be to provide more efficient, compatible sources for planar photonic ICs.

REFERENCES

- [1] L. A. Coldren, S. W. Corzine, and M. L. Mašanović, *Diode Lasers and Photonic Integrated Circuits*, 2nd ed. New York, NY, USA: Wiley, 2012, ch. 5.



Larry A. Coldren (SM'67–M'72–SM'77–F'82–LF'12) received the Ph.D. degree in electrical engineering from Stanford University, Stanford, CA, USA.

He spent 13 years in research at Bell Laboratories. He is the Fred Kavli Professor of optoelectronics and sensors at the University of California at Santa Barbara (UCSB), Santa Barbara, CA, USA. He joined UC-Santa Barbara in 1984 where he now holds appointments in Materials and Electrical and Computer Engineering. In 1990, he cofounded optical concepts,

later acquired as Gore Photonics, to develop novel VCSEL technology; and in 1998 he cofounded Agility Communications, later acquired by JDSU, to develop widely tunable integrated transmitters. At Bell Labs he worked on surface-acoustic-wave filters and later on tunable coupled-cavity lasers using novel reactive-ion etching (RIE) technology that he developed for the then new InP-based materials. At UCSB, he continued work on multiple-section tunable lasers, in 1988 inventing the widely tunable multielement mirror concept, which is now used in numerous commercial products. Near this same time, he also made seminal contributions to efficient vertical-cavity surface-emitting laser (VCSEL) designs that continue to be implemented in practical devices. More recently, his group has developed high-performance InP-based photonic integrated circuits (PICs) as well as high-speed VCSELs, and they continue to advance the underlying materials growth and fabrication technologies. He has authored or coauthored more than a thousand journal and conference papers, a number of book chapters, a textbook, and has been issued 65 patents.

Prof. Coldren is a Fellow of the Optical Society of America, and the Institute of Electronics Engineers (U.K.). He received the 2004 John Tyndall and 2009 Aron Kressel Awards, and he is a member of the National Academy of Engineering.

Photonic Device Technology for Coherent Optical Communications

Milan L. Mašanovi , Freedom Photonics LLC and University of California, Santa Barbara

mashan@freedomphotonics.com

Larry A. Coldren, University of California, Santa Barbara

ABSTRACT

The bandwidth on the optical fiber network is now growing by two orders of magnitude per decade due to the tremendous increase in data transmission, and current WDM systems cannot meet the projected bandwidth demands. As a result, in recent years, first commercial deployments of coherent optical systems have occurred, in order to achieve more spectrally efficient data transmission through existing fiber infrastructure. Photonic integration will play a key role in reaching higher spectral efficiency in a cost efficient, high-performance manner. In this paper, we review the progress and examples of photonic integrated circuits for optical coherent communications. Coherent integrated transmitter and receiver photonic integrated circuits are now a reality, and an active area of research.

Keywords: *Photonic integrated circuits, coherent communications, coherent transmitter, coherent receiver, silicon photonics, Indium Phosphide*

1. INTRODUCTION

More than three decades since their conception, optical coherent systems are finally a reality. They are being deployed throughout transport optical networks in order to provide more optical bandwidth through existing optical fiber, as well as to simplify dealing with the impairments of transmission, given that in most cases, both optical amplitude and phase are being recovered.

Research on coherent optical technology started in the 1980s because of its promise of increased transmission distance due to improved receiver sensitivity. Er-doped fiber amplifiers (EDFAs) had not been developed at the time, and wavelength division multiplexing (WDM) was expensive due to the repeater cost and complexity (de-multiplexing, optical-electrical conversion, amplification, electrical demultiplexing to a lower data rate, regeneration, multiplexing back up, electrical-optical conversion, and multiplexing into optical fiber).

Coherent approaches have promised to double the repeater separation, and allow placing of the WDM channels closer together, because the channel filtering could be done by a fixed intermediate frequency filter in the RF-domain after heterodyne down-conversion by tuning the optical local oscillator (LO), similar to a radio. Bulk optical heterodyne receivers were quickly found to be very difficult to make due to stability issues. Thus, efforts were initiated early-on to explore the possibility of monolithic integration of Photonic Integrated Circuits (PICs) for coherent communications [1]. However, the invention of the erbium-doped fiber amplifiers and inexpensive, integrated arrayed-waveguide grating-based multiplexers and demultiplexers channeled the development toward modern WDM systems for much of the 1995–2010 timeframe.

WDM systems using amplitude modulation have so far been able to meet the growth of traffic in optical networks, but currently deployed systems and fibers are close to being at full capacity. The traffic on the optical fiber network is now growing by two orders of magnitude per decade due to the tremendous increase in data transmission. The aggregate optical network traffic, both historic and predicted, is shown in Figure 1.

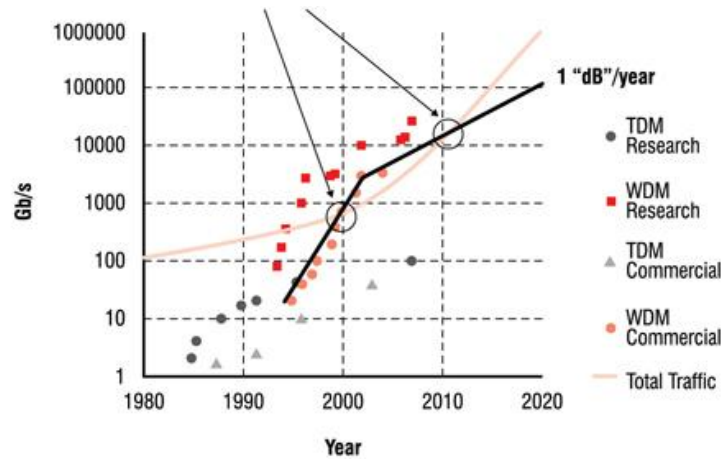


Figure 1. Historic and predicted optical network traffic growth as function of time

Therefore, it is a continuing challenge to meet the future demand for bandwidth. Figure 1 overlays some data for fiber capacity on this total demand curve for both research and commercial fiber links [1]. The straight lines indicate trends for commercial systems, which show that the tremendous growth in bandwidth, due to WDM adoption in the 1995-2002 timeframe, has now reached saturation due to the limitation in the number of practical WDM channels, as well as the data rate in each of them. In order to further increase the fiber capacity, we are either looking at the expensive proposition of laying more optical cables, or at improving the net data rate per Hz of bandwidth —spectral efficiency (SE), or, more simply, the channel rate/channel spacing ratio in existing fibers. This is being done using advanced (phase) optical modulation formats and coherent detection.

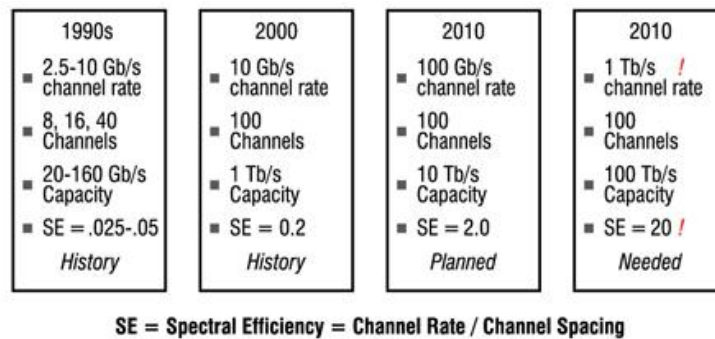


Figure 2. Optical system evolution in terms of bandwidth and spectral efficiency, past and future.

Figure 2 gives a set of tables that summarize the system evolution over the past few decades, as well as what a simple extrapolation might predict for the next decade [3].

As might be immediately obvious, an extrapolation of the current rapid growth in fiber capacity does not meet the network demand by 2020, even if doubled or tripled by using the fiber S and L bands in addition to the standard C-band which is plotted in Fig. 2. Even worse, calculations show that we will never be able to reach SE = 20 due to limitations in fiber dynamic range because of its limited power handling capacity [4]. A spectral efficiency of ~ 10 seems more realistic for transmission distances ~ 100 - 500 km, typical of WDM systems.

The need for improving the spectral efficiency of transmission in the future has led to renewed interest and intense research on optical coherent systems, as well as to the recent deployments of this technology. Coherent optical communications rely on digital modulation, a term used in radio, satellite, and terrestrial communications to refer to modulation in which digital states are represented by modification of carrier amplitude, frequency, and phase, simultaneously or separately. A common name for this arbitrary carrier phase and magnitude modulation is vector modulation. Different modulation states are represented by components of the electric field vector in the complex plane, using in-phase and quadrature (I-Q) constellation diagrams, illustrated in Figure 3. for three different modulation formats. In optical communication systems, the carrier frequency (laser wavelength) is usually fixed; thus we only need to consider the phase and magnitude changes. The unmodulated carrier is then the phase and frequency reference, aligned along the I axis, and the modulated signal is interpreted relative to the carrier. Q represents the quadrature (90 out of phase) vector component. A discrete point, modulation state on the I-Q diagram, can be represented by vector addition of a specific magnitude of the in-phase carrier with a specific magnitude of the quadrature carrier.

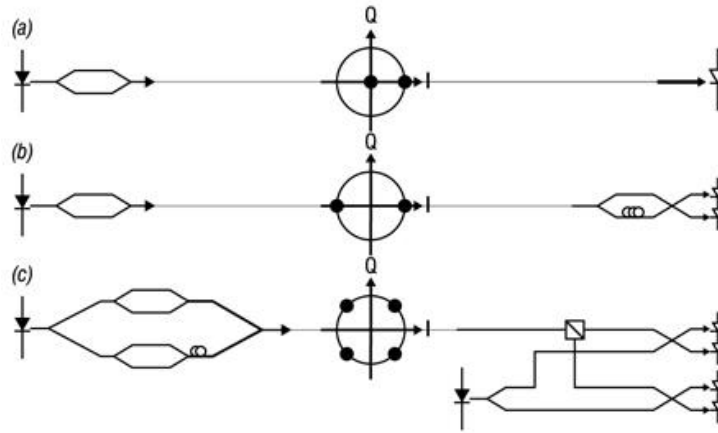


Figure 3. (a) Amplitude modulation (on-off keying) based noncoherent system with direct detection (b) Differential phase shift keying based coherent system with self-homodyne detection, without the need for a local oscillator (c) Quadrature phase shift keying coherent system with intradyne coherent detection, using a local oscillator matched in frequency and phase to the input signal.

Figure 3. illustrates some of the unique, commonly used vector modulation based links. The first link, part (a), utilizes simple binary amplitude modulation, the most widely exploited, noncoherent modulation format in optical communications to date. On the I-Q diagram, the field vector changes its amplitude from 0 to the maximum amplitude, along the I axis, as binary digital signals are translated into a stream of light pulses. The transmitter in this case is a simple amplitude modulator, and signal detection is achieved through direct detection, as shown in the link schematic.

Link (b) represents the next level of sophistication — a simple coherent system, in which the amplitude of the signal remains constant, but the phase of the carrier is differentially changed by π between bits, to reflect the change in adjacent bit value. To detect this type of signal, one approach is differential detection, where the signal is interfered with its own delayed version to produce an amplitude response at the receiver. No local oscillator is required in the receiver in this case. This system is limited to a particular bit rate, as it relies on exactly one bit delay for signal detection. Note that the receiver consists of two photodiodes that are connected in series, forming a balanced receiver, examined later in this section.

Figure 3. (c) illustrates a more complex and flexible system, where the carrier phase is modulated to one of four possible values — thus the name of this type of modulation is quadrature phase shift keying (QPSK). The advantage of this approach is in the fact that with the same bit rate as on-off keying, we can transmit twice the amount of information, since with each detected symbol (1 out of 4 possible phase values), we can recover two bits of information, a major benefit of vector modulation and coherent systems. The transmitter for this modulation format is relatively simple, consisting of two nested Mach-Zehnder phase modulators, which are delayed by 90° with respect to one another, allowing independent I and Q component modulation. The main complexity results from the receiver, where the incoming signal needs to be phase matched, locked and mixed with a local oscillator laser. In addition, the signals in the receiver need to be mixed and delayed properly, so that both the I and the Q signal components can be extracted independently, in the two sets of balanced receivers shown in the schematic. Any changes in phase of the incoming signal, caused by the laser phase noise, need to be tracked and neutralized in the receiver. A number of different techniques can be used to accomplish this. Optical phase-locked loops use optical feedback to control the phase of the local oscillator laser [5], showing promise for low power, simple implementation of true coherent receivers. Digital signal processing can be used to perform real time phase tracking and control as well, at the expense of electronic chip sophistication and power consumption [6].

Although these three examples show the progression from simple, noncoherent amplitude modulated system, through a differentially modulated coherent system to a true I-Q coherent system, it is important to emphasize that many other different vector modulation formats and links are possible and used: differential QPSK, where the phase changes to one of four states are recorded only when the adjacent bit changes; or quadrature amplitude modulation (QAM), where both the amplitude and the phase of the I and Q components are changed, resulting in a multitude of points on the constellation diagram, and further improvement of spectral efficiency, up to the fundamental limit imposed by the fiber dynamic range to around 10 bits/s per Hz of bandwidth. Finally, additional doubling in spectral efficiency for each of the coherent links can be accomplished by multiplexing two signals onto two degenerate orthogonal polarizations of an optical fiber, creating a polarization-multiplexed (PM) link.

2. COHERENT OPTICAL TRANSMITTERS COMPONENTS

As discussed in the previous section, arbitrary vector modulation can be generated using the combination of both amplitude and phase modulation. One popular way to accomplish this task is to use the nested Mach-Zehnder modulator structure shown in Figure 3. (c).

Because this structure assigns the I axis to one MZM and the Q axis to a second MZM, it can modulate the resultant vector to any (I,Q) point in the plane of the I-Q diagram. For QPSK modulation, four equal amplitude (I-Q) points are accessed.

An example of dual polarization, indium phosphide (InP) based QPSK modulator fabricated by NTT is shown in Figure 4. The InP dual, nested Mach-Zehnder modulator PIC has a single TE input and two individual output ports. The PIC is packaged on a carrier with a Silica based planar lightwave circuit (PLC) whose function is to couple the light from both PIC's outputs, to rotate the polarization from one of the PIC's outputs, and then to combine two polarizations in a single output waveguide. A special, high-speed interposer is used on top of the modulator to provide high-speed electrical connections for 112 Gbps operation [7].

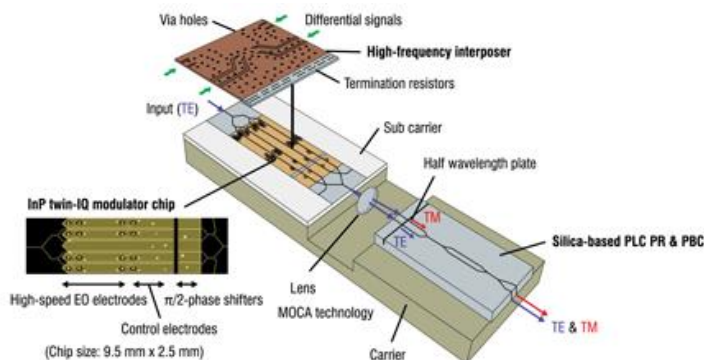


Figure 4. Configuration on an InP-based dual polarization QPSK modulator by NTT [7]. The solution consists of a dual modulator, dual output InP chip, microoptics, high-speed electrical interposer, and a PLC.

A 10-wavelength transmitter PIC by Infinera, utilizing a type of a nested I-Q Mach-Zehnder structure for QPSK modulation is shown in Figure 5[8]. Polarization multiplexing is implemented in this example to double the transmission rate, requiring a pair of identical nested I-Q MZ structures for each of the 10 DFB lasers on the chip. The constellation diagrams in the figure illustrate the four constellation points accessed by each of the 20 I-Q modulators. Each individual I and Q MZ modulator is running at 14.25 Gbps, but as discussed above with QPSK modulation, we double the amount of information transmitted (by effectively combining the I and Q signals in phase quadrature) resulting in 28.5 Gbps per IQ modulator. This chip utilizes DFB lasers for the light source, but one could imagine replacing them with the widely tunable variety.

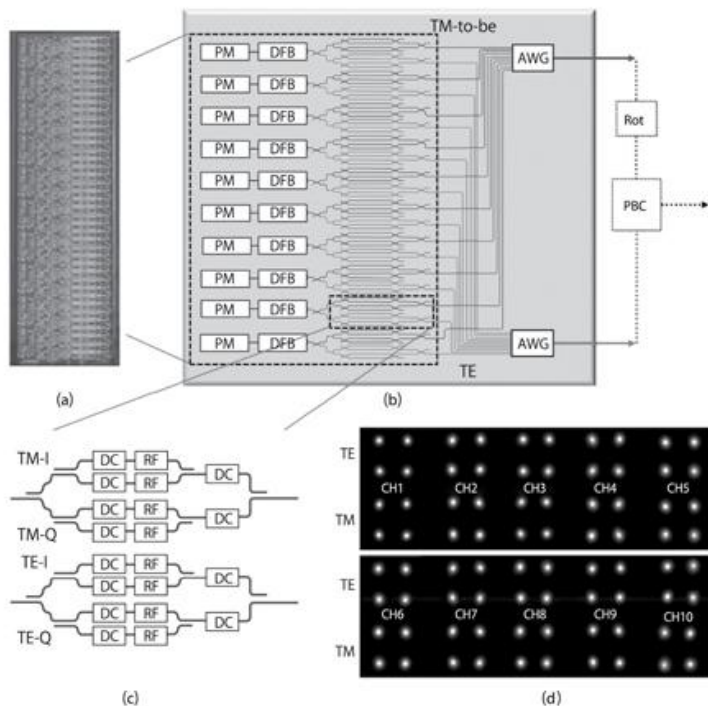


Figure 5. (a) Photograph of the active block of a 10-wavelength PM-QPSK transmitter IC, utilizing nested IQ Mach-Zehnder modulator, DFB-laser devices, (b) schematic layout of PIC illustrating the TE and TM-to-be duplicate sets of modulators, AWGs, and output waveguides, to support polarization-multiplexed operation through off-chip polarization beam combining, (c) schematic of

TE/TM nested IQ MZ modulator section of one wavelength showing RF and DC controls, and (d) IQ constellation diagrams for all 20 QPSK data streams, each IQ stream running at 28.5 Gbps for an aggregate 570 Gbps transmission capability across the 10 wavelengths [8].

The first such chip, reported in [9], consists of a widely-tunable sampled-grating DBR (SGDBR) laser monolithically integrated with a nested Mach-Zehnder modulator, as shown in Figure 6.

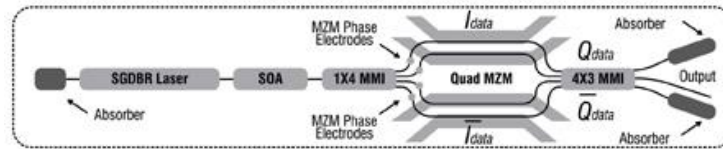


Figure 6. Schematic of a tunable monolithic photonic coherent transmitter, including SOAs, nested MZMs, and absorbers by Freedom Photonics [9].

The chip was realized using monolithic integration in Indium Phosphide (InP) based on quantum well intermixing. The single-mode SGDBR laser provides 40 nm of tuning around 1550 nm. The signal from the laser is amplified with a semiconductor optical amplifier (SOA), and then split into 4 paths, using a 1x4 multimode interference (MMI) splitter. The light in each path is sent through a static phase adjustment electrode embedded in the S-bend waveguides, which is essential for setting the MZMs in the quadrature state. The high-speed MZMs are formed using 400 μm long quantum-well intermixed (QWI) regions, with a photoluminescence (PL) peak at 1.5 μm , utilizing the quantum-confined Stark effect (QCSE) for light absorption. After the light in each of the four arms is modulated, it is recombined in a 4x3MMI, which allows for monitoring of the MZM in the OFF state. Thus, the chip is capable of transmitting a single transverse-electric (TE) polarization QPSK data stream in a compact footprint. The key issue with tunable laser integration for coherent transmitter purposes is that of achieving sufficiently narrow linewidth and low phase noise, and this will remain the area of active research in the near future.

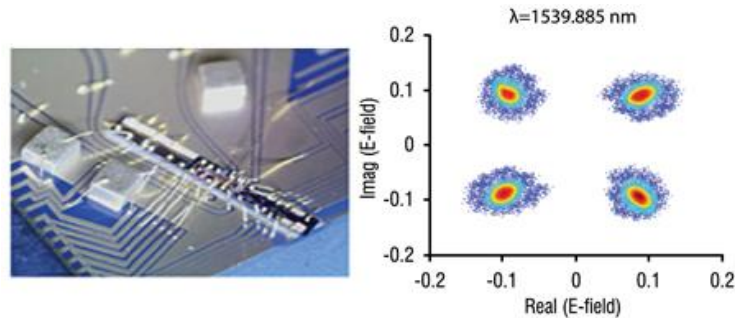


Figure 7. (left) Photograph of the widely tunable optical transmitter integrated circuit mounted on an Aluminum-Nitride ceramic carrier. (right) A representative constellation diagram from coherent link demonstration using a 20 Gbps QPSK encoded optical signal with $2^{31}-1$ PRBS, after DSP post processing. Linear color coding corresponds to symbol density.

Different integrated modulator configurations in addition to the nested MZMs can be used to generate QPSK and even more advanced modulation formats. Figure 8 shows a DQPSK modulator that uses two asymmetrical STAR couplers in a three-branch interferometer configuration. Two of the three branches contain electroabsorption modulators, which, when biased OFF, ON, and alternatively ON and OFF generate the 4- phase modulated constellation [10]. Also shown is the demodulated result at 20 Gb/s for one of the I or Q outputs.

3. COHERENT RECEIVER IMPLEMENTATIONS

The key idea behind coherent detection is to combine the input signal coherently with a locally generated continuous optical field (local oscillator) at the receiver and before the signal is detected. This action achieves two effects: it amplifies the detected signal through mixing with a high-power local oscillator signal, allowing improved receiver sensitivity, and it enables the demodulation of phase and amplitude/phase modulated signals, which is not possible through direct detection. This is a key enabler for achieving improved spectral efficiency in a coherent link.

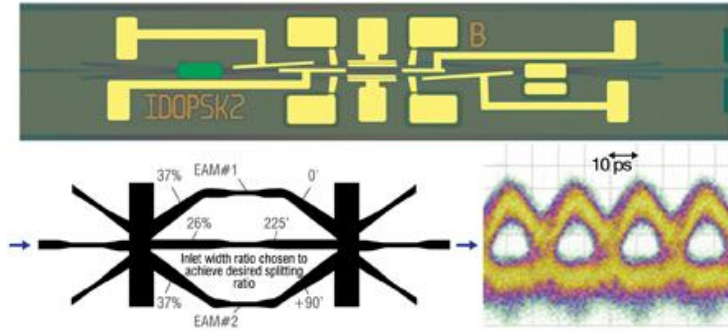


Figure 8. A DQPSK electroabsorption modulator photo, schematic, and received signal at 20 Gbps [10] by Bell Labs.

A couple of different coherent receiver architectures, for differential and regular detection were described in Figure 3. Since dual-polarization, dual-quadrature (DPDQ) coherent receiver requires many components, they should ideally be implemented as photonic integrated circuits (PIC). From the technological standpoint, this can be accomplished using a variety of integration platforms, starting from monolithic integration in Indium Phosphide, through hybrid integration using Silica or polymer waveguides, to Silicon photonics.

An example of a high-speed, integrated I-Q receiver in InP is shown in Figure 9. This device consists of two optical spot-size converters, input waveguides, a 90° hybrid implementation using a 2×4 multimode interference coupler, and two balanced photodiode pairs. The optical hybrid allows for mixing of the local oscillator L and the input signal S, and for balanced detection of both the in-phase I and the quadrature Q components of the input signal. This is accomplished through precise phase control in signal splitting, which results in the following signal combination at each of the photodiodes in Figure 9, from top down, assuming that the signal S is coupled to the top input waveguide: $L + S$, $L - S$, $L + jS$ and $L - jS$. The outputs from two balanced receiver pairs will be $2S$ and $2jS$, the in-phase and quadrature components of the input signal.

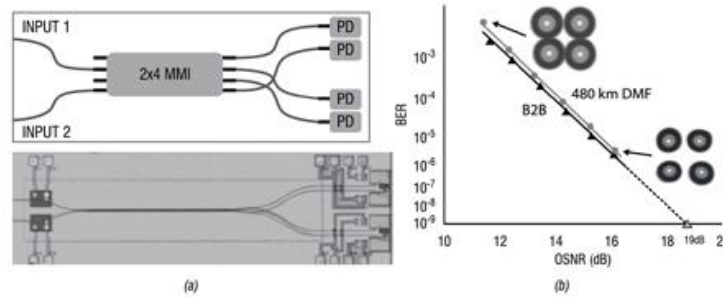


Figure 9. An integrated I-Q receiver in InP (a) Receiver architecture schematic, showing two inputs, a 90° hybrid implementation using a 4×4 MMI coupler, connected to two balanced photodiode pairs; a device photograph on the bottom. (b) Results of receiver operation at 50 Gbps, showing the bit error rate and constellation diagrams as function of optical signal to noise ratio [11].

This type of I-Q receiver chip can be used in a polarization diversity configuration, with additional micro-optics, to yield a full coherent receiver. A 100 Gbps polarization multiplexed BPSK and QPSK receiver architecture using the InP chip from Figure 9 and actual module are shown in Figure 10. Both the signal and the local oscillator (LO) are coupled through a collimator (C), and a first half waveplate (HWP) is inserted in the optical path in order to evenly split the LO signal between two polarizations. Both signals are split into two polarizations using a polarization beam splitter. To achieve highest symmetry in both channels, X and Y, a second HWP is integrated in the X channel to perform a TM-to-TE conversion. In return and to minimize the channel path length difference a skew compensator (SC) is integrated in the Y channel. The four beams are then coupled through a micro-lens array into the integrated optical spot size converters of the two InP I-Q receiver PICs. Four linear differential trans-impedance amplifiers (TIAs) are co-packed in the module.

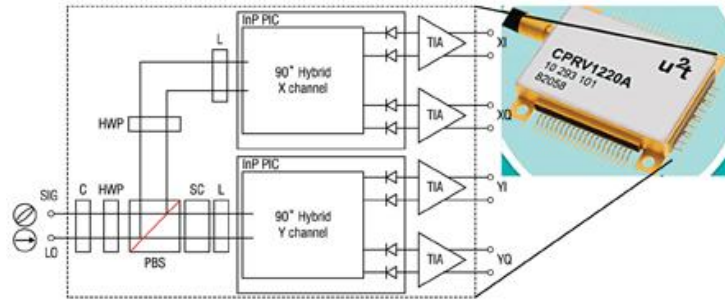


Figure 10. Architecture and module of a 100 Gbps coherent receiver [12] based on the InP PIC from Figure 9, and marketed by U2T.

Another integration platform concept for polarization-diversity receiver modules is polymer waveguide based, since it allows for low-loss, low-cost, simple processing implementation. One obvious challenge for this platform was the integration of photodiodes with minimal insertion loss. In the recent work reported in [13], this has been accomplished by integrating III-V active components via 45° turning mirrors, as shown in Figure 11. Also shown is the measured receiver performance in terms of the small signal bandwidth.

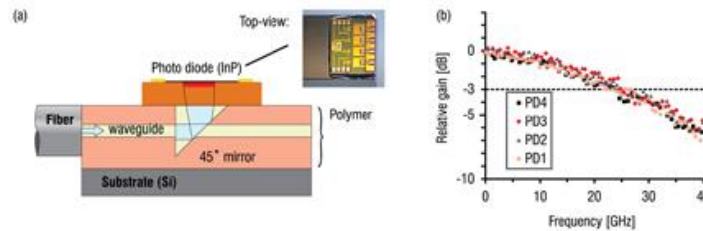


Figure 11. Detail of a Heinrich Hertz Institute's polymer based coherent receiver implementation, showing the photodiode coupled to the polymer waveguide via a 45 degree mirror [13].

Recent advances in silicon photonics have made realization of complex, high-performance PICs in silicon a reality. Silicon material system realization is beneficial because of the availability of 200-mm diameter or larger optical wafers allowing for low-cost chips. Silicon chips do not require a hermetic environment, allowing for low-cost packaging, and silicon can be oxidized allowing for high vertical index contrast and consequently high-performance polarization splitters and on-wafer testing.

An example of a Si DPDQ coherent receiver [14] is shown in Figure 12. The signal and local oscillator (LO) enter the PIC through 2-D grating couplers spaced by 127 μm . A key novel feature of this device is that grating couplers serve as spot-size converters, polarization splitters, and 50/50 splitters, they do not require anti-reflection coatings and allow for on-wafer testing. A scanning electron micrograph (SEM) of one of the fabricated grating couplers is shown the bottom of Figure 12. The fiber is oriented exactly vertically, i.e. no tilt angle, which results in the grating coupling equally to both directions in the waveguide and thus acting as a 50/50 coupler. After the grating couplers, portions of the LO and signal pass through a 90°, 11 μm wide waveguide crossing. The wide waveguide renders the crossing loss and crosstalk negligible.

The LO and signal portions pass by directional couplers which couple away any stray transverse-magnetic polarized light. The portions then interfere in four large 2x2 multimode interference (MMI) couplers (the large size improves fabrication tolerance). The MMI coupler outputs connect to eight photodiodes (PDs). The PDs are Ge-on-Si vertical PIN diodes.

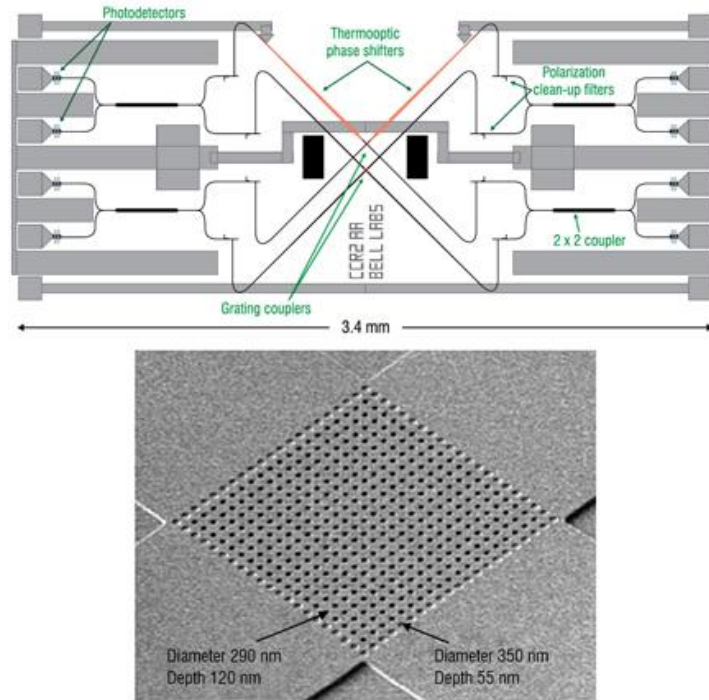


Figure 12. (top) Layout of a polarization multiplexed silicon photonics coherent receiver PIC, consisting of grating coupler inputs and two sets of I-Q balanced receivers. The waveguides are shown as black, the thermooptic phase shifters orange, and the top metal blue. (bottom) Input grating coupler close-up. This novel grating coupler serves as spot-size converter, polarization and 50/50 splitter [14]

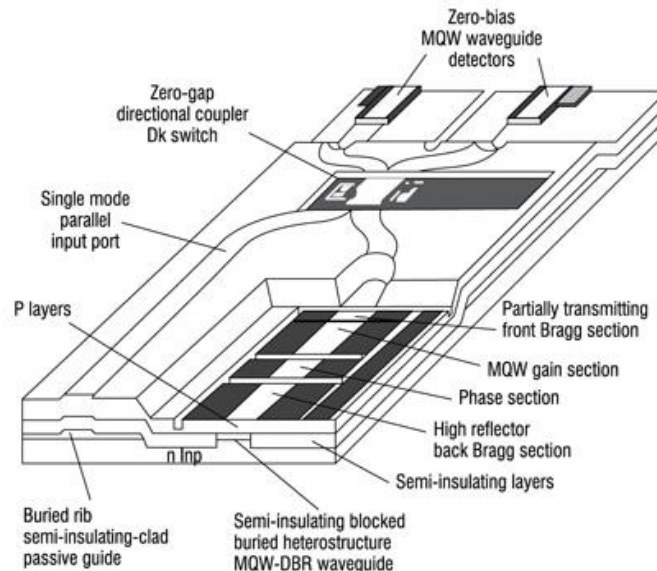


Figure 13. Schematic diagram of a Bell Labs MQW balanced heterodyne receiver photonic integrated circuit, containing a continuously tunable LO, a low-loss buried-rib parallel input port, an adjustable 3 dB coupler, and two zero-bias MQW waveguide detectors [1].

None of the implementations discussed so far include integration of the local oscillator with the receiver. A basic coherent receiver implementation with an integrated local oscillator [1], a historic example of one of the first complex PICs realized is shown in Figure 13. It consists of a DBR laser, light coupler, and a balanced receiver pair on the detection side. The local oscillator signal and the input signal are mixed inside a 2×2 coupler element, and detected by two individual photodiodes, connected in series. With this photodiode configuration and the phase differences introduced by the optical coupler, it is possible to easily obtain an output signal which will be given by the difference of the two photocurrents, thereby canceling out the current contributions and the intensity of noise from the local oscillator, and adding the photocurrents resulting from the signal modulation. This type of architecture therefore allows for complete rejection of the CW signal, and conversion of phase modulation into amplitude modulation.

As with coherent transmitters, integration of a widely tunable local oscillator would further benefit the level of integration in coherent receiver PICs. The first implementation of an integrated widely tunable coherent receiver, reported by Freedom Photonics, is shown in Figure 14[15]. The chip was realized using photonic integration in Indium Phosphide. At the center of the chip is a widely tunable sampled grating distributed Bragg reflector (SGDBR) laser, used as the receiver LO, providing 40nm tunability and bandwidth coverage. The signal from the LO is split into two identical paths. In each of the two paths, the LO power is amplified with a semiconductor optical amplifier (SOA), before the signal is routed using 2 total internal reflection (TIR) mirrors with a perpendicular waveguide connecting them. The signal from the second TIR mirror is then guided into a 2x4 multimode interference (MMI) hybrid. The receiver chip has two signal input waveguides, which are used to independently couple each of the two demultiplexed polarization data streams from a polarization multiplexed network data stream. The four outputs of each of the hybrids are separated using S-bend waveguides, which terminate in 4 photodiodes. Thus, the chip is capable of simultaneously detecting two independent data streams from a polarization multiplexed QPSK data stream – however, polarization demultiplexing and rotation of the transverse-magnetic (TM) polarization into transverse-electric (TE) has to be performed external to the chip.

Error-free, 20Gbps (10Gbaud) operation with this chip has been demonstrated. Recently, a similar device has been reported as part of an optical phase locked loop, for homodyne coherent detection, which was discussed as an alternative to high power consumption digital signal processing based detection methods [5].

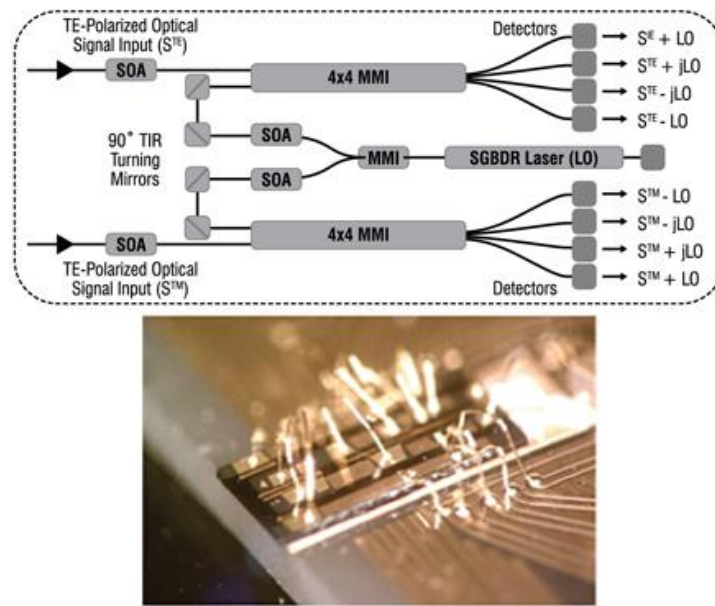


Figure 14. (top) Schematic of Freedom Photonics' monolithically integrated dual-polarization tunable photonic integrated coherent receiver, including SOAs, MMIs and total internal reflection mirrors and a tunable local oscillator laser. (bottom) Photograph of the widely tunable optical receiver integrated circuit mounted on a ceramic carrier [15].

4. CONCLUSIONS

The bandwidth on the optical fiber network is now growing by two orders of magnitude per decade due to the tremendous increase in data transmission, and current WDM systems cannot meet the projected bandwidth demands. As a result, in recent years, first commercial deployments of coherent optical systems have occurred, in order to achieve more spectrally efficient data transmission through existing fiber infrastructure. Photonic integration will play a key role in reaching higher spectral efficiency in a cost efficient, high-performance manner. In this paper, we have discussed the progress and examples of photonic integrated circuits for optical coherent communications. Both integrated transmitters and receiver PICs are now a reality, but this will remain an active research area for the foreseeable future. Some of the key challenges to be solved are with low phase noise tunable laser integrated technology, higher efficiency modulators, and reduced footprint receivers integrating polarization splitting on chip.

References

- [1] Koch TL, Koren U, Gnall RP, Chao FS, Hernandez-Gil F, Burrus CA, Young MG, Oron M, Miller BI., "GaInAs/GaInAsP multiple-quantum-well integrated heterodyne receiver", Electron Lett 1989;25: 1621.
- [2] L. A. Coldren, S. C. Nicholes, L. Johansson, S. Ristic, R. S. Guzzon, E. J. Norberg, U. Krishnamachari, "High Performance InP-based Photonic ICs—a Tutorial", IEEE Journal of Lightwave Technology, 2011

- [3] R. Tkach, "Optical Network Capacity: From Glut to Scarcity," OIDA Annual Meeting, Santa Clara, CA, Dec. 1-2, 2009.
- [4] R. Essiambre, et al, in talk by R. Alferness, "Optical communications—a view to the future," ECOC'08, Brussels, Sept. 2008. See also, R.-J. Essiambre, G. Kramer, P. J. Winzer, G. J. Foschini, and B. Goebel, "Capacity limits of optical fiber networks," *J. Lightwave Technol.*, vol. 28, pp. 662-701, 2010.
- [5] M. Lu, H. Park, E. Bloch, A. Sivanathan, J. Parker, Z. Griffith, L. A. Johansson, M. J. Rodwell, and L. A. Coldren, "A Photonic Integrated Circuit for a 40 Gbaud/s Homodyne Receiver Using an Optical Costas Loop", *IEEE Integrated Photonics Conference*, 2012.
- [6] O'Sullivan M. "Expanding network application with coherent detection" National Fiber Optic Engineers Conference; 2008.
- [7] Yamada, E.; Kanazawa, S.; Ohki, A.; Watanabe, K.; Nasu, Y.; Kikuchi, N.; Shibata, Y.; Iga, R.; Ishii, H.; , "112-Gb/s InP DP-QPSK modulator integrated with a silica-PLC polarization multiplexing circuit," *Optical Fiber Communication Conference and Exposition (OFC/NFOEC)*, 2012
- [8] Evans P, et al, "Multi-channel coherent PM-QPSK InP transmitter photonic integrated circuit (PIC) operating at 112 Gb/s per wavelength", *Optical Fiber Communication Conference, Post Deadline Paper PDPC7*; 2011 March.
- [9] Estrella, S.B.; Johansson, L.A.; Masanovic, M.L.; Thomas, J.A.; Barton, J.S.; , "First Monolithic Widely Tunable Coherent Transmitter in InP" *Photonics Technology Letters, IEEE*, submitted for publication
- [10] Doerr, C.R.; Zhang, L.; Winzer, P.J.; Sinsky, J.H.; Adamiecki, A.L.; Sauer, N.J.; Raybon, G.; , "Compact High-Speed InP DQPSK Modulator," *Photonics Technology Letters, IEEE*, vol.19, no.15, pp.1184-1186, Aug.1, 2007
- [11] Bottacchi S, Beling A, Matiss A, Nielsen ML, Steffan AG, Unterborsch G, Umback A. "Advanced photoreceivers for high-speed optical fiber transmission systems. *IEEE Journal of Selected Topics in Quantum Electronics* 2010;16(5): 1099–1112.
- [12] Matiss, A.; Nolle, M.; Fischer, J.K.; Leonhardt, C.C.; Ludwig, R.; Hilt, J.; Molle, L.; Schmidt-Langhorst, C.; Schubert, C.; , "Characterization of an integrated coherent receiver for 224 Gb/s polarization multiplexed 16-QAM transmission," *Optical Fiber Communication Conference and Exposition (OFC/NFOEC)*, 2011 and the National Fiber Optic Engineers Conference , vol., no., pp.1-3, 6-10 March 2011
- [13] Wang, J.; Kroh, M.; Richter, T.; Theurer, A.; Matiss, A.; Zawadzki, C.; Zhang, Z.; Schubert, C.; Steffan, A.; Grote, N.; Keil, N.; , "Hybrid-Integrated Polarization Diverse Coherent Receiver Based on Polymer PLC," *Photonics Technology Letters, IEEE* , vol.24, no.19, pp.1718-1721, Oct.1, 2012
- [14] Doerr, C.R.; Buhl, L.L.; Baeyens, Y.; Aroca, R.; Chandrasekhar, S.; Liu, X.; Chen, L.; Chen, Y.-K.; , "Packaged Monolithic Silicon 112-Gb/s Coherent Receiver," *Photonics Technology Letters, IEEE* , vol.23, no.12, pp.762-764, June15, 2011
- [15] Estrella, S.B.; Johansson, L.A.; Masanovic, M.L.; Thomas, J.A.; Barton, J.S.; , "Widely Tunable Compact Monolithically Integrated Photonic Coherent Receiver," *Photonics Technology Letters, IEEE* , vol.24, no.5, pp.365-367, March1, 2012

Authors

Dr. Milan L. Masanovic (S'98–M'04) received the Dipl. Ing. degree from the School of Electrical Engineering, University of Belgrade, Belgrade, Yugoslavia, in 1998 and the M.S. and Ph.D. degrees from the University of California Santa Barbara, in 2000 and 2004, respectively, all in electrical engineering. He is currently a General Manager at Freedom Photonics LLC, a Santa Barbara based photonic integration company, as well as a Research Scientist at the University of California Santa Barbara. He has co-authored of more than 85 journal and conference papers, and presented numerous invited talks at international conferences. His current research interests include InP photonic integrated circuits (diode lasers and tunable transmitters), component technologies for packet-switched optical networks, local area networks and harsh environments. Dr. Masanovic was the recipient of a number of merit based awards, including the 2004 IEEE Lasers and Electro-Optics Society Fellowship Award. He has taught graduate level course on semiconductor lasers and photonic integrated circuits at UCSB in 2009, 2010 and 2011, and has served as a reviewer for a number of journals, and on technical committees for Integrated Photonics Research conference, Indium Phosphide and Related Materials conference, Microwave Photonics conference, and Avionics, Fiber Optics and Photonics conference.

Dr. Larry A. Coldren (S'67–M'72–SM'77–F'82) received a Ph.D. degree in electrical engineering from Stanford University, Stanford, CA, in 1972.

He is the Fred Kavli Professor of Optoelectronics and Sensors at the University of California, Santa Barbara (UCSB). After 13 years

in the research area at Bell Laboratories, he joined UCSB in 1984, where he now holds appointments with the Department of Materials and the Department of Electrical and Computer Engineering. In 1990, he cofounded Optical Concepts, later acquired as Gore Photonics, to develop novel VCSEL technology, and, in 1998, he cofounded Agility Communications, later acquired by JDSU, to develop widely-tunable integrated transmitters.

At Bell Labs, he initially worked on waveguided surface-acoustic-wave signal processing devices and coupled-resonator filters. He later developed tunable coupled-cavity lasers using novel reactive-ion etching (RIE) technology that he created for the then new InP-based materials.

At UCSB, he continued work on multiple-section tunable lasers, in 1988 inventing the widely-tunable multi-element mirror concept, which is now used in some JDSU products. Near this same time period, he also made seminal contributions to efficient vertical-cavity surface-emitting laser (VCSEL) designs that continue to be implemented in practical devices to this day. More recently, his group has developed high-performance InP-based photonic integrated circuits (PICs) as well as high-speed VCSELs, and they continue to advance the underlying materials growth and fabrication technologies. He has authored or coauthored over a thousand journal and conference papers, seven book chapters and one textbook and has been issued 64 patents. He has presented dozens of invited and plenary talks at major conferences.

Prof. Coldren is a Fellow of the IEEE, OSA, IEE, and a member of the National Academy of Engineering. He was a recipient of the 2004 John Tyndall and 2009 Aron Kressel Awards.

OFFICE@TELEKOMUNIKACIJE.RS - COPYRIGHT:RATEL © 2008

I. Photonic Integrated Circuits

B. Laser Sources

Monolithic Linewidth Narrowing of a Tunable SG-DBR Laser

Abirami Sivananthan¹, Hyun-chul Park¹, Mingzhi Lu¹, John S. Parker¹, Eli Bloch², Leif A. Johansson¹, Mark J. Rodwell¹, Larry A. Coldren^{1,3}

¹Department of Electrical and Computer Engineering, University of California at Santa Barbara, Santa Barbara, CA 93106-9560

²Department of Electrical Engineering, Technion – Israel Institute of Technology, Haifa 32000, Israel

³Department of Materials, University of California, Santa Barbara, CA, 93106-9560, USA.

asivananthan@ece.ucsb.edu

Abstract: We demonstrate an InGaAsP/InP widely-tunable SG-DBR laser integrated with an asymmetric Mach-Zehnder interferometer (AMZI) for frequency stabilization. Negative feedback from the AMZI to the laser phase tuning section reduces the linewidth by a factor of 27.

OCIS codes: (250.5960) Semiconductor Lasers; (140.3425) Laser Stabilization; (250.5300) Photonic Integrated Circuits

1. Introduction

Tunable lasers have become increasingly important for a variety of applications, such as optical sensing and coherent detection. They can allow large cost savings by increasing flexibility and decreasing inventory demands in dense wavelength division multiplexing, compared to using many types of lasers with different wavelengths [1]. Many of these applications will be greatly aided by a low linewidth compact laser. As coherent detection moves to higher modulation formats, lower phase noise will be required of the local oscillator [2-4]. High resolution optical sensing, such as FMCW LIDAR, also requires a low phase noise laser for longer range detection.

Many different methods have been developed to reduce the linewidth of tunable lasers. Several extended cavity lasers with linewidths well below 100 kHz have been demonstrated [5,6]. Tunable DFB laser arrays have shown less than 160 kHz linewidth through optimization of the cavity [7]. The Pound-Drever-Hall technique can reduce linewidth to the sub 100 Hz level [8]. However, most optical methods of decreasing linewidth increase the laser size and are very sensitive to environmental fluctuations. Alternatively, tunable DFB arrays have high performance, but require many DFB lasers integrated on one chip to enable a large tuning range.

Much research has focused on negative electrical feedback using the error signal from a frequency discriminator to tune the laser and reduce the linewidth. This technique has the potential to be more stable and maintain a small cavity size. It has been successfully implemented using many different filters as the frequency discriminator, such as a Fabry-Pérot etalon, a fiber Mach-Zehnder and a fiber Bragg grating [9-12]. Advantages of this method include its simplicity and low cost. However, previous implementations have been bulky and increased the size of the laser package.

In this paper, we have demonstrated for the first time linewidth reduction through the use of an asymmetric Mach-Zehnder interferometer (AMZI) frequency discriminator that has been monolithically integrated in a photonic integrated circuit (PIC) with a 40nm tunable SG-DBR laser diode and waveguide detectors. When using an AMZI as a frequency discriminator, the quadrature point of the AMZI is used to convert the frequency error of the laser to amplitude error. This error is then fed back to the phase tuning section of the laser through a stabilizing loop filter, suppressing the frequency noise within the loop bandwidth of the negative feedback loop. The path length imbalance in the AMZI is 1.5 mm, leading to a free spectral range of 60 GHz. Integration has allowed us to keep the advantages of size, weight and power inherent in semiconductor lasers and simultaneously attain low linewidth. Due to the small chip size, the feedback loop delay is kept small, facilitating a loop bandwidth upwards of 250 MHz and linewidth reduction by a factor of 27.

2. Design and Fabrication

An SG-DBR laser, AMZI, semiconductor optical amplifiers (SOAs), compact 2x2 multimode interferometer couplers and waveguide detectors are integrated on an InGaAsP/InP centered quantum well platform consisting of 10/11 6.5 nm/8 nm InGaAsP QWs/barriers centered within a 105 nm upper and lower 1.3Q InGaAsP waveguide. Surface ridge (SR) waveguides are used for the SG-DBR laser for improved thermal characteristics and lower loss. Deep ridge (DR) waveguides have a higher confinement, thus smaller bending radius and are therefore used for the AMZI, so that a 1.5 mm path length difference can be achieved within a smaller device footprint. A waveguide transition element is used between the two waveguide topologies. A schematic of the epitaxial structure and SEMs of the device in various stages of fabrication are shown in Fig. 1.

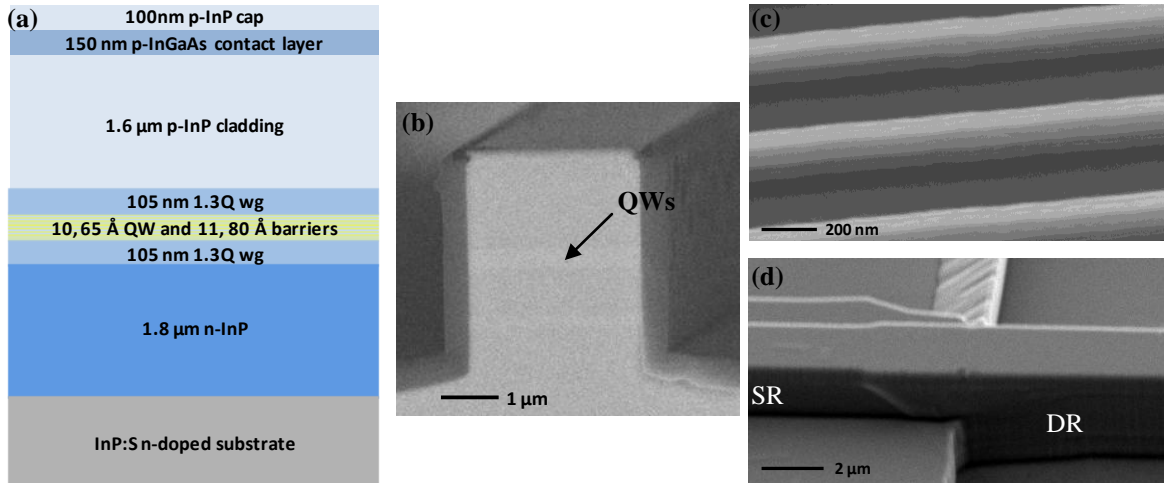


Fig. 1. a) Schematic of epitaxial structure after regrowth, and scanning electron micrograph (SEM) of b) cleaved deeply etched ridge facet, c) SG-DBR gratings pre-regrowth and d) surface ridge to deep ridge waveguide transition.

Quantum well intermixing is used to define the passive regions [13], and gratings are defined via electron beam lithography and dry etched using a $\text{CH}_4/\text{H}_2/\text{Ar}$ based RIE etch. Blanket regrowth of the p-InP cladding, p-InGaAs contact layer and p-InP protective cap layer is done using metalorganic chemical vapor deposition. The SR and DR waveguides are defined using a bilayer Cr and SiO_2 hardmask. The Cr is etched using a low power Cl_2/O_2 ICP RIE etch and the SiO_2 is etched using a SF_6/Ar ICP RIE etch. An initial shallow dry etch of both waveguides is performed using a $\text{Cl}_2/\text{H}_2/\text{Ar}$ 200°C 1.5 mT ICP RIE Etch [14], defining the waveguide everywhere. Then, the DR waveguide is protected and the SR waveguide is completed via a HCl based crystallo-graphic wet etch. Next, deposition and liftoff of SiO_2 is used to protect the SR regions and the DR waveguide is deeply etched using the $\text{Cl}_2/\text{H}_2/\text{Ar}$ etch mentioned above. An isolation layer of Si_3N_4 is then deposited, vias are opened using a semi-self alignment process for the top p-contacts, and Pt/Ti/Pt/Au p-contacts are evaporated via e-beam deposition. The sample is then thinned to 140 μm , Ti/Au backside metallization is deposited for the n-contacts, and output facets are formed via cleaving.

3. Linewidth Narrowing

The PIC, an electronic integrated circuit (EIC) and loop filter are mounted on AlN carriers and wirebonded together. The EIC consists of a differential limiting amplifier that allows use of both detectors on the PIC in a balanced detector configuration to decrease intensity variation, and provides a -2V bias to the detectors on the PIC. The loop filter is a second order frequency lock loop made of discrete resistors, capacitors and op-amplifiers that provides gain and the correct loop characteristics for stable frequency locking. A feed forward path is utilized to minimize loop delay at high frequencies and increase the loop bandwidth [15]. Schematics of the frequency response of the frequency discriminator and device set up are shown in Fig. 2.

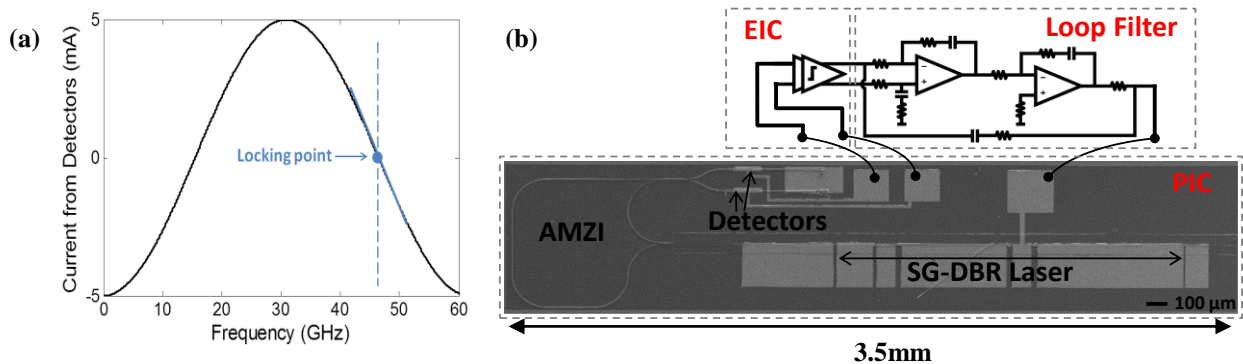


Fig. 2. a) Calculated detector current vs. operating frequency and b) SEM of the fabricated PIC along with a depiction of the connections to the EIC and loop filter.

Self-heterodyne was used to measure the 3-dB linewidth of the SG-DBR laser. The output of the SG-DBR was split using a 1x2 fiber coupler, one arm was delayed by 25 km, the other arm went through a 100 MHz acousto-optic modulator, and the arms were recombined. The signal was then detected by an external detector and monitored on an electrical spectrum analyzer (ESA).

The 3-dB linewidth of the SG-DBR laser prior to locking was 80 MHz, which was mainly dominated by large 1/f noise at low frequencies. After locking the linewidth was 3 MHz, showing a 27x improvement in linewidth. The linewidth spectrums have been overlaid and are shown in Fig. 3. The loop bandwidth was larger than 250 MHz.

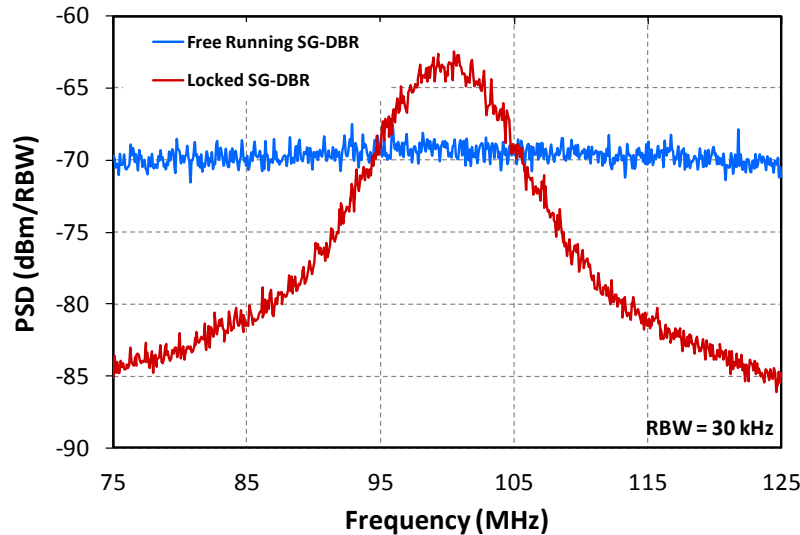


Fig. 3. Self-heterodyne linewidth spectrum of the free running SG-DBR laser and frequency locked SG-DBR laser taken from an ESA.

4. Conclusion

Self referencing was used to frequency lock an SG-DBR laser to an AMZI integrated within the same chip and a 27x linewidth improvement was demonstrated. Locking was extremely robust and was maintained over several hours with no environmental isolation. This technique shows promise for achieving a low-linewidth widely tunable laser with all the size, weight and power advantages of a photonic integrated circuit. Future optimization of the feedback loop gain and the test setup is anticipated to yield additional linewidth improvement.

5. References

- [1] J. Buus and E. J. Murphy, "Tunable lasers in optical networks," *J. Lightwave Technol.* 24, 5-11 (2006).
- [2] M. Seimetz, "Laser linewidth limitations for optical Systems with high-order modulation employing feed forward digital carrier phase estimation," in *Proc. OFC 2008*, Paper OTuM2.
- [3] T. N. Huynh et al, "Low linewidth lasers for enabling high capacity optical communication systems," in *Proc. ICTON 2012*, Paper Mo.C4.2
- [4] L. Kazovsky, G. Kalogerakis, and W. Shaw, "Homodyne phase-shift-keying systems: past challenges and future opportunities," *J. Lightwave Technol.* 24, 4876-4884 (2006).
- [5] D. Zhang et al, "Compact MEMS external cavity tunable laser with ultra-narrow linewidth for coherent detection," *Opt. Express* 20, 19670-19682 (2012).
- [6] N. Wang et al, "Narrow-linewidth tunable lasers with retro-reflective external cavity," *IEEE Phot. Technol. Lett.*, vol. 24, no.18, pp. 1591-1593, Sept. 2012.
- [7] H. Ishii, K. Kasaya, and H. Oohashi, "Narrow spectral linewidth operation (<<160 khz) in widely tunable distributed feedback laser array," *Electronics Letters* 46, no.10, pp.714-715, May 2010.
- [8] R. W. P. Drever et al, "Laser phase and frequency stabilization using an optical resonator," *Appl. Phys. B* 31, 97-105 (1983).
- [9] M. Ohtsu and S. Kotajima, "Linewidth reduction of a semiconductor laser by electrical feedback," *IEEE J. Quantum Electron.* QE-21, no. 12, 1905-1912 (1985).
- [10] V. Crozatier et al, "Phase locking of a frequency agile laser," *Appl. Phys. Lett.* 89, 261115 (2006).
- [11] W.K. Lee, C.Y. Park, J. Mun, and D.H. Yu, "Linewidth reduction of a distributed-feedback diode laser using an all-fiber interferometer with short path imbalance," *Rev. Sci. Instrum.* 82, 073105 (2011).
- [12] M. Poulin et al, "Ultra-narrowband fiber Bragg gratings for laser linewidth reduction and RF filtering," in *Proc. SPIE Photonics West 2010*, Vol. 7579.
- [13] E. J. Skogen, J. S. Barton, S. P. Denbaars, and L. A. Coldren, "A quantum-well-intermixing process for wavelength-agile photonic integrated circuits," *IEEE J. Sel. Topics Quantum Electron* 8, pp. 863-869 (2002).
- [14] J. S. Parker, E. J. Norberg, R. S. Guzzon, S. C. Nicholes, and L. A. Coldren, "High verticality InP/InGaAsP etching in Cl₂/H₂/Ar inductively coupled plasma for photonic integrated circuits," *J. Vac. Sci. Technol. B* 29, 011016-1-011020-5 (2011).
- [15] H. Park, M. Lu, E. Bloch, T. Reed, Z. Griffith, L. Johansson, L. Coldren, and M. Rodwell, "40Gbit/s coherent optical receiver using a Costas loop," *ECOC*, post-deadline (2012).

Integrated Linewidth Reduction of a Tunable SG-DBR Laser

Abirami Sivananthan,¹ Hyun-chul Park,¹ Mingzhi Lu,¹ John S. Parker,¹ Eli Bloch,² Leif A. Johansson,¹ Mark J. Rodwell,¹ Larry A. Coldren¹

¹Department of Electrical and Computer Engineering, University of California, Santa Barbara, CA 93106-9560

²Department of Electrical Engineering, Technion – Israel Institute of Technology, Haifa 32000, Israel

E-mail: asivananthan@ece.ucsb.edu

Abstract: We demonstrate frequency noise suppression of a widely tunable sampled-grating DBR laser using negative feedback from a Mach-Zehnder frequency discriminator integrated on the same InGaAsP/InP chip. The 3-dB laser linewidth is narrowed from 19 MHz to 570 kHz.

OCIS codes: (140.5960) Semiconductor lasers; (250.5300) Photonic integrated circuits; (250.0250) Optoelectronic

1. Introduction

Widely tunable semiconductor lasers have become increasingly attractive for transmitter and coherent detection purposes due to their compact size, low power usage, low cost and the potential for integration. However, tunable semiconductor lasers suffer from large linewidths that make meeting the stringent requirements of these applications difficult. As coherent detection moves to higher modulation formats even lower phase noise will be required, and for LIDAR systems, the phase noise is directly coupled to the system sensitivity [1-3]. Semiconductor lasers suffer from higher linewidths than their solid state laser counterparts in large part due to high $1/f$ noise at low frequencies. External cavities can be used to decrease the linewidth to the sub 100 kHz range, but with the loss of compact size.

In this paper, we demonstrate the use of negative feedback from an integrated frequency discriminator to reduce frequency noise within the loop bandwidth. This technique has been successfully implemented in the past using various discrete frequency discriminators, but always with a large increase in total size [4-6]. Our approach integrates detectors, an asymmetric Mach-Zehnder (AMZ) frequency discriminator and a sampled-grating DBR (SG-DBR) laser [7], tunable over 32 nm, on one chip. At the AMZ quadrature point the laser frequency fluctuations will be converted to amplitude fluctuations by the on-chip AMZ. This error signal is then detected on chip and fed back through a stabilizing loop filter to the phase tuning section of the SG-DBR laser, suppressing frequency noise within the loop bandwidth of the feedback circuit. We have previously presented self-heterodyne linewidth spectra showing linewidth reduction of the SG-DBR laser to 3 MHz [8]. In this demonstration, we have achieved a much lower locked linewidth of 570 kHz and the frequency noise power spectral density (PSD) before and after locking has been tested and is presented below. The frequency noise PSD was suppressed to approximately 2×10^5 Hz²/Hz within a loop bandwidth of 630 MHz.

2. Experiment and Discussion

The photonic integrated circuit (PIC) consists of an SG-DBR laser, a 60 GHz free spectral range (FSR) AMZ, a semiconductor optical amplifier, 2×2 multimode interferometer couplers and waveguide detectors integrated on a centered quantum well InGaAsP/InP platform. A microscope image of the PIC can be seen in Fig. 1(a). The active regions consist of 10(11) 6.5(8) nm InGaAsP quantum wells (barriers) centered within a 105 nm upper and lower 1.3Q InGaAsP waveguide. The SG-DBR front mirror (back mirror) has 4(12) grating bursts and a designed power reflectivity of 0.15(0.8). The grating pitch size is 236 nm. Quantum well intermixing is used to achieve active and passive regions on the same platform. More fabrication details can be found in Ref. [9].

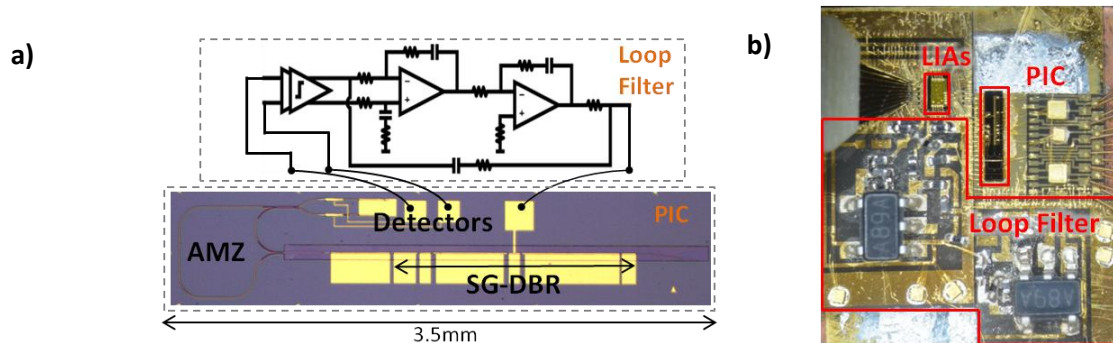


Fig. 1(a) Micrograph of the PIC with a schematic of the loop filter and (b) image of the entire chip.

The PIC, limiting differential amplifiers (LIAs), and a loop filter are mounted on separate AIN carriers and wirebonded together. The loop filter consists of discrete resistors, capacitors and op-amps and is a second order frequency lock loop with a feed forward path to minimize loop delay at high frequencies. The LIAs allow the use of the two on-PIC detectors in a balanced configuration, suppressing amplitude noise. Light from the front mirror of the SG-DBR laser is directed to the on-PIC AMZ and light from the back mirror is coupled off chip to test the laser characteristics. The signal travels from the detectors to the LIAs, then to the loop filter and back to the phase tuning pad of the SG-DBR laser. An image of the system is shown in Fig. 1(b). The size is mainly dominated by the loop filter and can easily be decreased by using an integrated circuit instead of discrete components.

The frequency noise before and after locking was measured using a frequency discriminator technique similar to Ref. [10]. The SG-DBR laser is coupled to an external 10 GHz FSR Mach-Zehnder interferometer (MZI), which converts frequency to amplitude fluctuations, which is then detected using discrete balanced detectors. The spectrum is read on an electrical spectrum analyzer and converted to frequency noise using the frequency to amplitude slope sensitivity of the MZI. The frequency noise PSD before and after locking is shown in Fig 2. The laser power measured on-PIC after the front mirror is 10 mW. The frequency noise PSD is suppressed to approximately 2×10^5 Hz²/Hz, and a resonance peak can be observed at the loop bandwidth of 630 MHz. The minimum level of frequency suppression possible with the feedback loop will be determined by noise from the loop and the discriminator, such as detector shot noise and incomplete relative intensity noise (RIN) rejection. Incomplete RIN suppression in the feedback loop can be seen in the low frequency peaks in the frequency noise spectrum of the locked laser. The 3-dB linewidth, measured using the self-heterodyne technique, shows a free running laser linewidth of 19 MHz and locked laser linewidth of 570 kHz.

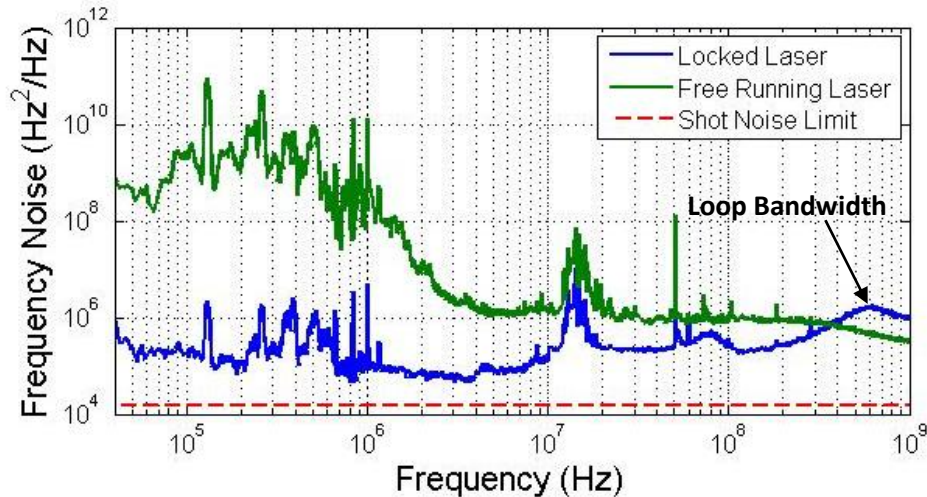


Fig. 2. Frequency noise of the SG-DBR laser before and after locking. The frequency noise suppression limit due to shot noise is also shown.

In conclusion, negative feedback from an AMZ integrated on the same InP/InGaAsP chip as an SG-DBR laser has been shown to suppress the laser linewidth by a factor of 33, from 19 MHz to 570 kHz. The PSD of the frequency noise was measured to be approximately 2×10^5 Hz²/Hz within the loop bandwidth.

References

- [1] J. Buus and E. J. Murphy, "Tunable lasers in optical networks," *J. Lightwave Technol.* 24, 5-11 (2006).
- [2] T. N. Huynh *et al.*, "Low linewidth lasers for enabling high capacity optical communication systems," in *Proc. ICTON 2012*, Paper Mo.C4.2.
- [3] L. Kazovsky, G. Kalogerakis, and W. Shaw, "Homodyne phase-shift-keying systems: past challenges and future opportunities," *J. Lightwave Technol.* 24, 4876-4884 (2006).
- [4] M. Ohtsu and S. Kotajima, "Linewidth reduction of a semiconductor laser by electrical feedback," *IEEE J. Quantum Electron.* QE-21, no. 12, 1905-1912 (1985).
- [5] W.K. Lee, C.Y. Park, J. Mun, and D.H. Yu, "Linewidth reduction of a distributed-feedback diode laser using an all-fiber interferometer with short path imbalance," *Rev. Sci. Instrum.* 82, 073105 (2011).
- [6] M. Poulin *et al.*, "Ultra-narrowband fiber Bragg gratings for laser linewidth reduction and RF filtering," in *Proc. SPIE Photonics West 2010*, Vol. 7579.
- [7] V. Jayaraman *et al.*, "Theory, design, and performance of extended tuning range in sampled grating DBR lasers," *IEEE J. Quantum Electron.*, vol. 29, pp. 1824-1834 (1993)
- [8] A. Sivanathan *et al.*, "Monolithic Linewidth Narrowing of a Tunable SG-DBR Laser," *Accepted*, OFC 2013 OTh31.3.
- [9] P. Binetti *et al.*, "Indium Phosphide Photonic Integrated Circuits for Coherent Optical Links," *IEEE J. Quantum Electron.* Vol.48, no.2, 279-291 (2012)
- [10] W. Sorin *et al.*, "Frequency Domain Analysis of an Optical FM Discriminator," *J. Lightwave Technol.* Vol.10, no.6, pp 787-793 (1992).

Multivalued Stability Map of an Injection-Locked Semiconductor Laser

Marko M. Krstić, Jasna V. Crnjanski, Milan L. Mašanović, *Member, IEEE*, Leif A. Johansson, *Member, IEEE*, Larry A. Coldren, *Fellow, IEEE*, and Dejan M. Gvozdić

Abstract—We present a novel and detailed analysis of the locking range and the stability map for side-mode injection-locked in-plane semiconductor multimode lasers. By including the usually neglected unlocked modes in our model, we predict a multivalued locking range and stability map for this type of lasers. We also explain and relate, the previously noticed slave laser bistability phenomenon with the multivalued character of the locking range and stability map, and experimentally validate our findings. Moreover, we find that the unstable operating region, commonly found in literature by stability analysis of the injection-locked mode alone, is actually much smaller.

Index Terms—Bistability, locking range, multimode semiconductor lasers, multivalued functions, stability map.

I. INTRODUCTION

INJECTION locking is a general phenomenon observed in many disciplines such as physics, engineering, biology, etc. For the first time, it was observed by C. Huygens, who noticed that the pendulums of two clocks on the wall move in unison if the clocks are hanged close to each other [1]. Later, other examples of this phenomenon were observed, such as human circadian rhythm locking to the length of day [1], or the locking of the Moon's to the Earth's rotation. Over time, injection locking has been used in a number of engineering applications comprising oscillators: electrical [2], microwave [3], or optical, i.e., lasers [4]. Semiconductor lasers are a type of electrically driven oscillators in which the number of supported oscillations or modes can be controlled by various feedback mechanisms, providing single- or multimode operation. For a multimode laser, a sophisticated method to control oscillations in this (slave) laser relies on synchronization with another (master) laser, i.e., on the technique of injection locking.

The stable locking regime of an injection-locked laser is usually characterized by a stability map, which is represented by a set of ordered pairs comprising angular frequency of detuning

$\Delta\omega$ between the master and the slave laser free-running frequencies, and the injection power ratio r (i.e., the ratio of the photon density S_{inj} injected into the slave laser and the photon density S_m of the injection-locked mode of the slave laser) for which the slave laser is stably locked to the master laser. Such map has previously been thought to be a single-valued function on $\Delta\omega$ and r [5]–[8]. However, in this paper, we show that the slave laser behavior is far more complex and that the stability map is a multivalued function. We arrive at this important conclusion, which revises the current understanding of the locking and the stability map, by studying, theoretically and experimentally, the effects of a side-mode injection into a Fabry–Perot in-plane quantum well laser.

In the prior work on the analysis of the stability maps [6], [7], the unlocked slave laser modes have not been taken into account, although it has been suggested that the unlocked modes should be included into the consideration in the case of their collateral excitation or gain suppression effects during the injection locking [5], [8]. Even in the case of unstable injection locking, followed by a variety of peculiar and chaotic effects, researchers were still focused only on the injection-locked mode [4], [9]. Here, we show that unlocked modes significantly impact the locking range, as well as the boundaries of the stable locking in the regions where the stability map is a single-valued function. As a consequence of the multivalued character of the stability map, we show that the bistability of the slave laser occurs within the region which was previously considered stable [5], [6]. Although the bistability was previously noticed [7], [8], it was never fully explored and explained. In this study, we also experimentally confirm and correlate this bistability with our modeling results.

In Section II, we present the model of the multimode rate equations (MREs) used in our work. In Section III, we show the locking map and theoretically explain its multivalued character. Section IV relates mapping of stationary points from $\Delta\omega - r$ space with phase plots and provides analysis of the stability plots. In Section V, we present the experiment and its results, which we compare with our theoretical findings. Finally, in Section VI, we provide the conclusion of this paper.

II. MODEL

The dynamics of the injection-locked slave laser is described by a system of MREs [10] with extra terms describing the locking phenomenon [4]–[10]. We consider a Fabry–Perot slave laser whose emission in the free-running regime is centered at the photon energy $\hbar\omega_0 = 0.8$ eV ($\lambda_0 = 1.55$ μm). The material gain spectrum used in the model $g(n, \omega)$ where n stands for

Manuscript received October 31, 2012; revised December 29, 2012; accepted January 9, 2013. This work was supported by the Serbian Ministry of Education and Science (project Photonics Components and Systems 171011).

M. M. Krstić, J. V. Crnjanski, and D. M. Gvozdić are with the School of Electrical Engineering, University of Belgrade, Belgrade 11000, Serbia (e-mail: marko.krstic@etf.rs; jafa@etf.bg.ac.rs; gvozdic@etf.bg.ac.rs).

M. M. Mašanović, L. A. Johansson, and L. A. Coldren are with Electrical and Computer Engineering Department, University of California, Santa Barbara, CA 93106 USA (e-mail: mashan@ece.ucsb.edu; leif@ece.ucsb.edu; coldren@ece.ucsb.edu).

Color versions of one or more of the figures in this paper are available online at <http://ieeexplore.ieee.org>.

Digital Object Identifier 10.1109/JSTQE.2013.2241026

the carrier density and ω for the angular photon frequency, is asymmetric. It reaches its maximum ($g_{\text{th}} = 1222 \text{ cm}^{-1}$) at the threshold carrier concentration $n = n_{\text{th}} = 2.85 \times 10^{18} \text{ cm}^{-3}$ and at the angular frequency $\omega = \omega_0$, corresponding to the central (dominant) mode. Due to the gain asymmetry with respect to ω , the number of side modes which can be supported by the laser cavity is $l_1 = 170$ for $\omega < \omega_0$ and $l_2 = 120$ for $\omega > \omega_0$.

The MREs describe the photon density for each mode in the mode ensemble. Since the phase and the photon density equations of the injection-locked side-mode are coupled with the photon density and the phase of injected light, it is necessary to add separate photon density and the phase equation of the injection-locked mode to the MRE system. Thus, the system comprises $l_1 + l_2 + 3$ nonlinear differential equations. One of the equations deals with the carrier concentration (n) dynamics, $l_1 + l_2 + 1$ equations describe the time dependence of the photon density of both the injection-locked m th mode (S_m) and other longitudinal modes (S_j), including the central mode ($j = 0$), while the last equation describes the time evolution of the phase difference θ_m between the free-running and the injection-locked state [10]:

$$\frac{dn}{dt} = \frac{I}{qV} - [A_{\text{SRH}}n + R_{\text{sp}}(n) + C_A n^3] - \sum_{j=-l_1}^{l_2} v_g g(n, \omega_j) S_j \quad (1)$$

$$\frac{dS_j}{dt} = \Gamma v_g g(n, \omega_j) S_j - \frac{S_j}{\tau_p} + \Gamma \beta_{\text{sp}} R_{\text{sp}}(n), \quad j \neq m \quad (2)$$

$$\frac{dS_m}{dt} = \Gamma v_g g(n, \omega_m + \Delta\omega) S_m - \frac{S_m}{\tau_p} + \Gamma \beta_{\text{sp}} R_{\text{sp}}(n) + 2k_c \sqrt{S_m S_{\text{inj}}} \cos \theta_m \quad (3)$$

$$\frac{d\theta_m}{dt} = \frac{\alpha}{2} \left[\Gamma v_g g(n, \omega_m + \Delta\omega) - \frac{1}{\tau_p} \right] - \Delta\omega - k_c \sqrt{\frac{S_{\text{inj}}}{S_m}} \sin \theta_m. \quad (4)$$

In (1), $I = 1.2I_{\text{th}}$ is the current of the slave laser ($I_{\text{th}} = 2.45 \text{ mA}$), $R_{\text{sp}}(n)$ is the total spontaneous optical emission rate, $A_{\text{SRH}} = 1.1 \times 10^8 \text{ s}^{-1}$ is the Shockley–Reed–Hall, and $C_A = 5.82 \times 10^{-29} \text{ cm}^6 \text{ s}^{-1}$ is the Auger recombination constant, while $V = 7.83 \times 10^{-12} \text{ cm}^3$ is the volume of the active area, corresponding to a laser width $w = 1.2 \text{ }\mu\text{m}$ and the laser cavity length $L = 250 \text{ }\mu\text{m}$. In the system of MREs $\tau_p = (\Gamma \cdot v_g \cdot g_{\text{th}})^{-1} = 2.04 \text{ ps}$ stands for the photon lifetime, $\Gamma = 0.056$ is the confinement factor, $v_g = c/n_g$ is the group velocity with $n_g = 4.2$, $k_c = 1.13 \times 10^{11} \text{ s}^{-1}$ is the external light coupling factor, $\alpha = 3$ is the linewidth enhancement factor, $\Delta\omega$ is the frequency detuning between the master and slave lasers, while $\beta_{\text{sp}} = 2.15 \times 10^{-4}$ is the spontaneous emission coupling factor, defined as the ratio of spontaneous emission coupling rate to the lasing mode and total spontaneous emission rate. Finally, S_{inj} is the injected photon density, which is proportional to the injected optical power P_{inj} and is given by relation $S_{\text{inj}} = \tau_p \cdot \Gamma \cdot P_{\text{inj}} / (\eta_0 \cdot \hbar\omega \cdot V)$, where $\eta_0 = 0.33$ is the optical efficiency. All numerical values for

these quantities in our model are taken from [10]. The angular frequencies of side longitudinal mode j and injection-locked mode m are denoted by ω_j and ω_m , respectively. We define ω_j as the longitudinal mode frequency, separated from the dominant mode ω_0 by integer multiple j of intermodal spacing, i.e., $\omega_j = \omega_0 + j(\pi c/n_g L)$, which for the injection-locked mode order $j = m$ yields $\omega_m = \omega_0 + m(\pi c/n_g L)$. As already defined, the frequency of the dominant mode ω_0 is the lasing frequency in the free-running regime, corresponding to the modal gain maximum, at $n = n_{\text{th}}$. Since our model does not account for the variation of the group refractive index n_g with frequency or carrier density, the frequencies of all of the modes are fixed with respect to the carrier density variation in the laser and the dominant mode ω_0 . An implicit frequency variation with carrier density change for the injection-locked mode is taken into account only by (7). However, the frequency detuning $\Delta\omega$ between the master and slave laser is defined with respect to the injection locked mode frequency ω_m , which is the closest to the frequency of injected signal from the master laser. In our computation, injected optical power P_{inj} and the photon density in any of the modes are at least two orders of magnitude smaller than those necessary to trigger the mechanism of nonlinear gain suppression which is therefore neglected in our computation.

The system of MREs (1)–(4), can be rewritten in a more compact form, in which instead of the injected photon density S_{inj} we introduce r , previously defined as the injection power/slave laser power ratio:

$$\frac{dn}{dt} = \frac{I}{qV} - Q(n) - \sum_{j=-l_1}^{l_2} v_g g(n, \omega_j + \delta_{jm} \Delta\omega) S_j \quad (5)$$

$$\frac{dS_j}{dt} = A_j(n) S_j + B(n) + \delta_{jm} 2k_c \sqrt{r} S_j \cos \theta_j \quad (6)$$

$$\frac{d\theta_m}{dt} = \frac{1}{2} \alpha A_m(n) - \Delta\omega - k_c \sqrt{r} \sin \theta_m. \quad (7)$$

In addition, we define $B(n) = \Gamma \beta_{\text{sp}} R_{\text{sp}}(n)$ as the effective spontaneous emission, $A_j(n) = \Gamma v_g g(n, \omega_j + \delta_{jm} \Delta\omega) - \tau_p^{-1}$ as the effective rate of stimulated photon generation for mode j , and Q as the total recombination rate, representing the sum of $R_{\text{sp}}(n)$ and nonradiative recombination rates. Equation (6) applies on all modes, injection-locked and unlocked, which is regulated by Kronecker delta δ_{jm} .

III. LOCKING RANGE ANALYSIS

Starting from the stationary (6) for $j = m$ and (7), assuming that $B(n)$ is negligible in comparison to the other terms, the stationary value for θ_m is

$$\theta_m = \text{Arcsin} \left[-\frac{\Delta\omega}{\sqrt{r k_c^2 (1 + \alpha^2)}} \right] - \arctan(\alpha). \quad (8)$$

The first term in the aforementioned equation is the generalized inverse sine, given by $\varphi(-1)^z + z\pi$, where $\varphi = \arcsin\{-\Delta\omega/[k_c(1 + \alpha^2)^{1/2} r^{1/2}]\}$ is its principal value, while

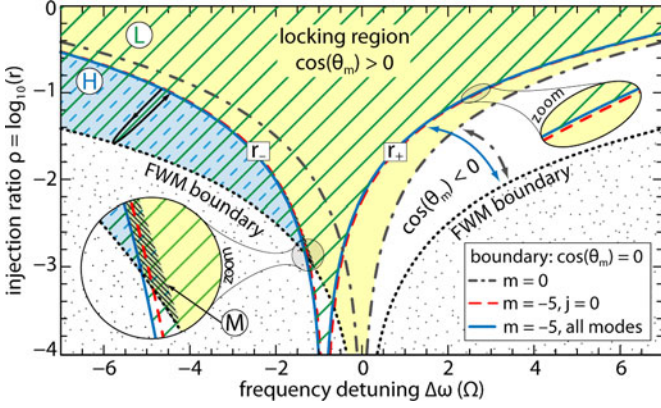


Fig. 1. Locking range for the injection into: the side mode $m = -5$ with all unlocked modes included (single and double hatched); the central mode $m = 0$, excluding unlocked modes (shaded). Boundary condition $\cos(\theta_m) = 0$ for injection into: $m = 0$ excluding unlocked modes (dash-dot line); $m = -5$ with the central mode ($j = 0$) included (dash line); $m = -5$ with all unlocked modes included (solid line). Distribution of the roots of (11): L (hatched), H (double-hatched), M (dense-hatched) for all modes included.

z is an integer, which has a physical meaning only for $z \in \{0, 1\}$. By introducing $\psi = \arctan(\alpha)$, (8) yields

$$r = \frac{\Delta\omega^2}{k_c^2(1 + \alpha^2)\sin^2(\theta_m + \psi)} \quad (9)$$

which for real θ_m , and extreme values for $\sin(\theta_m + \psi) = \pm 1$ defines the boundaries between the injection-locked and the four wave mixing (FWM) regions [6]. However, an additional condition comes from the fact that in the locked range $\cos(\theta_m) > 0$ [11]. The locking boundary can be derived from the condition $\cos(\theta_m) = 0$, which according to (8) can be converted to $\sin(\theta_m) = -1$ for $\Delta\omega > 0$ and to $\sin(\theta_m) = +1$ for $\Delta\omega < 0$. Insertion of $\sin(\theta_m) = \pm 1$ into the stationary form of (7) leads to $\alpha A_m(n)/2 = \Delta\omega - \text{sgn}(\Delta\omega)k_c r^{1/2}$. If the injection-locked mode is the central mode ($m = 0$) at $n = n_{th}$, then $A_m(n) = 0$. In this case, the locking boundary is given by $\Delta\omega = \pm k_c r^{1/2}$ or $r = (\Delta\omega/k_c)^2$ (dash-dot line in Fig. 1), where $\Delta\omega$ is given in units of Ω ($\Omega = 10^{10}$ rad/s). This can also be derived from (9), by taking into account that for $\theta_m = \pm\pi/2$, $\sin(\pm\pi/2 + \psi) = \pm(1 + \alpha^2)^{-1/2}$. If m is a side mode ($m \neq 0$), the stationary photon densities corresponding to $\cos(\theta_m) = 0$ are given by $S_j = -B(n)/A_j(n)$ for all modes. Thus, (5) can be written with respect to n as

$$\frac{I}{qV} - Q(n) + \sum_{-l_1 \leq j \leq l_2} v_g g(n, \omega_j + \delta_{jm} \Delta\omega) \frac{B(n)}{A_j(n)} = 0. \quad (10)$$

The solution to (10) in this case is $n_c < n_{th}$. It represents the stationary state of the laser, for which $A_m(n_c) < 0$. This last condition remains valid whether besides the central mode, we take into account all other side modes, a few side modes (including injection-locked mode) or only injection-locked mode $m \neq 0$. Therefore, the new locking boundaries (see Fig. 1) can be found from $\alpha A_m(n_c)/2 = \pm(|\Delta\omega| - k_c r^{1/2})$, leading to $r_{\pm} = \{[\pm|\Delta\omega| - \alpha A_m(n_c)/2]/k_c\}^2$ where (+) corresponds to positive and small negative $\Delta\omega$ (r_+ boundary), while (-) is used

for sufficiently large negative $\Delta\omega$ (r_- boundary). However, for the r_+ boundary, this condition imposes an additional, more rigid constraint, which due to the negative value of $A_m(n_c)$, additionally rises the boundary of r , leading to a shrinkage of the locking range (cf., Fig. 1). In this case, $\theta_m \in (-\pi/2, -\psi]$, since the other branch of φ in (4) i.e., $\pi - \varphi$ leads to $\cos(\theta_m) < 0$ and cannot be included in consideration. However, for the r_- boundary, it is possible to include both branches of φ (i.e., φ and $\pi - \varphi$), since for both of them $\cos(\theta_m)$ can be positive. In this case, $\theta_m \in \{[-\psi, 0] \cup (0, \pi/2)\}$ comprises $\theta_m = \pi/2 - \psi$, corresponding to the FWM boundary due to the fact that $\sin(\theta_m + \psi) = 1$. This means that for $\Delta\omega < 0$, FWM boundary divides θ_m range in two segments, $\theta_m \in [-\psi, \pi/2 - \psi]$ and $\theta_m \in [\pi/2 - \psi, \pi/2]$. Since FWM boundary corresponds to the smallest r for a given $\Delta\omega$, it can be concluded that the locking range in the $\Delta\omega - r$ space is folded down along the FWM boundary, leading to the overlap of the two locking regions in the r -range between the FWM boundary and r_- (dash and solid line hatched region in Fig. 1). For small negative detuning ($\Delta\omega \approx -1.13 \Omega$), the left FWM boundary crosses the locking range [$\cos(\theta_m) \geq 0$]. The intersection of the FWM and the $\cos(\theta_m) = 0$ boundary is possible, since at this point and its vicinity, there is more than one stationary solution, which can satisfy either one or the other condition imposed by these two boundaries. Within the locking range, the FWM boundary sets θ_m to $\pi/2 - \psi$, but it becomes irrelevant, since on its both sides, injection locking is possible. The folding down along FWM boundary and overlap of the locking regions between FWM and corresponding r boundaries is also valid for $m = 0$. Since we are more interested in the injection-locking into side modes, we do not show this case in Fig. 1.

The locking range shown in Fig. 1, which accounts for the unlocked modes, exhibits a nonzero detuning offset for small injection ratios r . The essential reason for this is in our definition of ω_m , and the uneven increase of the frequencies for the dominant mode and side longitudinal modes when the carrier density increases. The dominant frequency ω_0 is the lasing frequency corresponding to $n = n_{th}$, while ω_m is the frequency for the injection-locked side-mode, defined in the free-running regime by $\omega_m = \omega_0 + m(\pi c/n_g L)$. This definition for ω_m overestimates its value for $n \leq n_{th}$, since the gain change due to the carrier density change is smaller for the side mode m than for the dominant mode 0. Assuming a constant linewidth enhancement factor for both modes, a smaller gain change of the side mode leads to its smaller frequency change. Thus, the frequency maximum of a side mode m , which occurs at $n = n_{th}$, is smaller than the one predicted by $\omega_m = \omega_0 + m(\pi c/n_g L)$, which accounts for the dominant mode frequency increase. The correction term for the injection-locked mode frequency ω_m ; i.e., the frequency shift of the side-mode frequency ω_m , is proportional to its gain defect. For example, the gain defect is zero ($A_m = 0$) for the dominant mode $m = 0$ (ω_0), and it is negative ($A_m < 0$) for any side mode $m \neq 0$ (ω_m). Therefore, side modes should exhibit a negative frequency shift (red shift) with respect to the frequencies given by $\omega_m = \omega_0 + m(\pi c/n_g L)$. This shift is taken into account by the first term in (7), and for small or negligible injection ratio r ($r \approx 0$), in the stationary state ($d\theta_m/dt = 0$), it

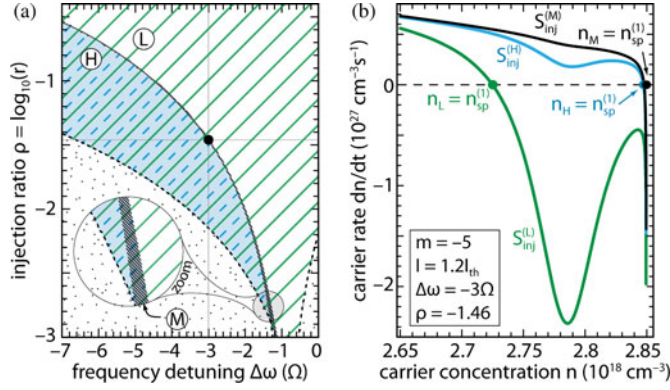


Fig. 2. (a) Distribution of roots of (11): L (hatched), H (shaded double-hatched), M (dark-dense-shaded) for all unlocked modes included. The dot corresponds to $\Delta\omega - r$ pair, for which all three roots occur simultaneously. (b) $dn/dt - n$ plots for all three roots and their corresponding stationary point $n_{sp}^{(1)}$ for $S_{inj}^{(L)} > S_{inj}^{(H)} > S_{inj}^{(M)}$.

can be compensated only by the negative detuning offset $\Delta\omega$, as noticed in Fig. 1.

IV. STABILITY MAP ANALYSIS

From the stationary (6) for $j = m$ and (7), one can eliminate $\cos(\theta_m)$ and $\sin(\theta_m)$ and derive an equation with respect to the carrier concentration n :

$$[\alpha A_m(n) - 2\Delta\omega]^2 + [A_m(n) + B(n)/S_m]^2 - 4k_c^2 r = 0. \quad (11)$$

S_m can be expressed as a function of n , using the stationary form of (5) as

$$S_m = \frac{\frac{I}{qV} - Q(n) + \sum_{-l_1 \leq j \leq l_2, j \neq m} v_j g(n, \omega_j) \frac{B(n)}{A_j(n)}}{v_j g(n, \omega_m + \Delta\omega)}. \quad (12)$$

Obviously, (11) is a nonlinear equation, solutions of which are stationary concentrations n_s dependent on $\Delta\omega$ and r . By solving (11) numerically, we find that for any $\Delta\omega - r$ pair in the locking range (hatched region in Fig. 1), there is at least one, basic solution, which we denote as n_L , while two additional solutions may appear for $\Delta\omega < -1.13 \Omega$ (crossing of FWM and r_- boundary). In Fig. 1, L denotes the region where there is only one solution (n_L), H is the region where each $\Delta\omega - r$ point represents two solutions (second-order root), the basic solution n_L and one more denoted as n_H , while M is the narrow third-order root region, which in addition to n_L and n_H comprises solution n_M . In further text, by n_s we denote any of the roots n_L, n_H , or n_M . The locking boundary r_- separates the H - and M -regions (cf., Fig. 1), and with the FWM boundary outlines the H -region. For the more negative detuning ($\Delta\omega < -2 \Omega$), the M -region is compressed into a line which can barely be seen.

Each n_s determines one pair of injected photon density $S_{inj}^{(s)}$ and injection-locked mode photon density $S_m^{(s)}$. For a given $S_{inj}^{(s)}$, phase plots $dn/dt - n$ may exhibit either one [see Fig. 2(b)] or three [see Fig. 3(b)–(d)] n -values, representing stationary points, which we denote in increasing order ($n_{sp}^{(1)} \leq n_{sp}^{(2)} \leq$

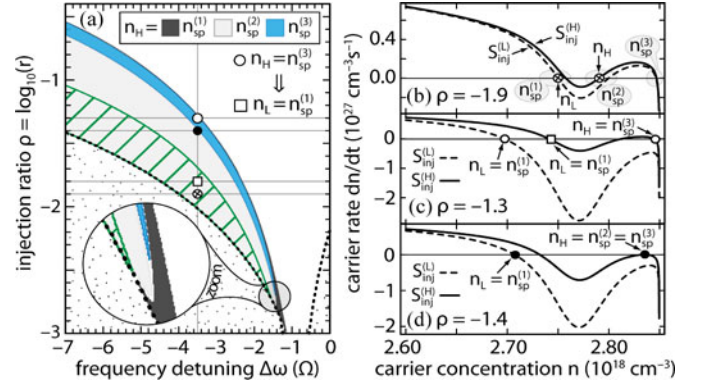


Fig. 3. (a) Partition of the H -region, with respect to the type of the stationary point n_H . The region $n_L = n_{sp}^{(1)}$ (hatched) coexisting with $n_H = n_{sp}^{(3)}$. (b) $dn/dt - n$ plot and mapping of n_L and n_H into stationary points for $\Delta\omega = -3.5 \Omega$ and $\rho = -1.9$. Same for (c) $\rho = -1.3$ and (d) $\rho = -1.4$. In (c) n_L for $\rho = -1.8$ (square dot) coexists with n_H for $\rho = -1.3$ (open dot), sharing the same injected power.

$n_{sp}^{(3)} \leq n_{th}$) as in [10]. Here, we analyze how the n_s roots map into these stationary points.

The root n_L from the region L corresponds to a pair $S_{inj}^{(L)}$ and $S_m^{(L)}$ for which there is only one stationary point in $dn/dt - n$ phase plot, denoted as $n_{sp}^{(1)}$. Similarly, a point from the M -region [cf., Fig. 2(a)], maps into stationary points $n_{sp}^{(1)}$ for each of three corresponding roots n_s [see Fig. 2(b)], all having different $n_{sp}^{(1)}$ values, since $S_{inj}^{(s)}$ is different for each of them.

The points from the H -region exhibit a more complex mapping. Each point from the H -region represents two roots, n_L and n_H , with two corresponding injection densities $S_{inj}^{(L)}$ and $S_{inj}^{(H)}$. However, the mapping into the stationary points of the phase plot $dn/dt - n$, shows that n_L always maps into $n_{sp}^{(1)}$, while n_H , may map either into $n_{sp}^{(2)}$ or $n_{sp}^{(3)}$ or even into $n_{sp}^{(1)}$ in the vicinity of the r_- boundary. Fig. 3(a) shows the full picture of the H -region partition with respect to the type of stationary point n_H . In order to provide a deeper analysis of the mapping we study character of the $dn/dt - n$ phase plots [see Fig. 3(b)–(d)] corresponding to the H -region for a fixed detuning $\Delta\omega = -3.5 \Omega$ and three different values of r (or ρ , where $\rho = \log_{10} r$), shown by circular dots in Fig. 3(a). Fig. 3(b) shows that for $\rho = -1.9$, n_L and n_H map into points $n_{sp}^{(1)}$ and $n_{sp}^{(2)}$. For $\rho = -1.3$ [see Fig. 3(c)] the situation is similar, with the exception that n_H maps into $n_{sp}^{(3)}$, while for the critical value $\rho = -1.4$, n_H maps into a point at which $n_{sp}^{(2)}$ and $n_{sp}^{(3)}$ merge in the single point [see Fig. 3(d)]. As it was already mentioned, one can see from all these examples that n_L always maps into $n_{sp}^{(1)}$.

This analysis shows that a point from the H -region maps into two points (n_L and n_H) each representing one stationary point in $dn/dt - n$ phase plot [e.g., Fig. 3(b)]. Each of these points corresponds to one injected photon density $S_{inj}^{(s)}$ and simultaneously exists with other stationary points, corresponding to the same injected photon densities, $S_{inj}^{(L)}$ or $S_{inj}^{(H)}$, but different r i.e., ρ . In these and similar cases [solid lines in Fig. 3(c) and (d)], coexistence of the stationary points may provide multistability.

Thus, we further study the range of r (ρ), for which multistability may occur. We again analyze $dn/dt - n$ plots for $\Delta\omega = -3.5 \Omega$ and find that for $S_{\text{inj}}^{(L)}$ and $\rho > -1.7$, there is only one stationary point i.e., $n_{\text{sp}}^{(1)}$ [dashed lines in Fig. 3(c) and (d)]. In other cases, multistability becomes feasible, since for a fixed $S_{\text{inj}}^{(s)}$ and consequently different r -values there are three coexisting stationary points, $n_L = n_{\text{sp}}^{(1)}$, $n_H = n_{\text{sp}}^{(2)}$, and $n_H = n_{\text{sp}}^{(3)}$. Fig. 3(a) shows that mapping of n_H from the H -region into $n_{\text{sp}}^{(2)}$ or $n_{\text{sp}}^{(3)}$, leads to the partition of the H -region into two disjunctive subsets. However, for a fixed $S_{\text{inj}}^{(s)}$ and detuning, each point from one subset has a corresponding point in the other [see Fig. 3(b)–(d)]. In other words, for a fixed $S_{\text{inj}}^{(s)}$, $n_{\text{sp}}^{(2)}$ and $n_{\text{sp}}^{(3)}$ always accompany each other. Therefore, both subsets of the H -region represent ranges of multistability for stationary points $n_{\text{sp}}^{(2)}$ and $n_{\text{sp}}^{(3)}$. It thus remains for us to find the multistability range corresponding to $n_L = n_{\text{sp}}^{(1)}$.

In order to do that, we search for the r -range for which $n_L = n_{\text{sp}}^{(1)}$ [e.g., square dot in Fig. 3(c)] coexists with points $n_{\text{sp}}^{(3)}$ [open dot in Fig. 3(c)] and $n_{\text{sp}}^{(2)}$ for a fixed $S_{\text{inj}}^{(s)}$. For any given $\Delta\omega$, we find this range by calculating the photon density of the injection-locked mode $S_m^{(L)}$ for injected density $S_{\text{inj}}^{(L)} = S_{\text{inj}}^{(H)}$, where $S_{\text{inj}}^{(H)}$ corresponds to $n_H = n_{\text{sp}}^{(3)}$ and $n_{\text{sp}}^{(2)}$. This finally yields $r = S_{\text{inj}}^{(H)}/S_m^{(L)}$. Fig. 3(a) depicts the hatched part of the H -region, in which $n_L = n_{\text{sp}}^{(1)}$ coexists with $n_H = n_{\text{sp}}^{(3)}$ and $n_{\text{sp}}^{(2)}$ for the same $S_{\text{inj}}^{(s)}$. Moreover, in the vicinity of the r_- boundary, there is a third narrow subset in which n_H maps into $n_{\text{sp}}^{(1)}$, which is irrelevant for multistability.

After identifying the areas in the $\Delta\omega - r$ space where $n_{\text{sp}}^{(1)}$, $n_{\text{sp}}^{(2)}$, and $n_{\text{sp}}^{(3)}$ coexist, we investigate their stability. This is done by calculating the eigenvalues of the linearized rate equations system (5)–(7), under the assumption of a small perturbation [10]. We simultaneously analyze how the number of modes included in the analysis affects the stability. For that, we investigate three cases, for which we take into account (i) the injected side-mode $m = -5$ only, (ii) the injected side-mode $m = -5$ and the central mode $j = 0$, and finally (iii) the injection-locked mode $m = -5$ and all unlocked modes. The stationary point is considered stable if all eigenvalues of the system lie in the left-half of the complex plain, which in the cases (i)–(iii) correspond to 3, 4, and $l_1 + l_2 + 3$ eigenvalues, respectively [6], [10]. For the case (i), $n_L = n_{\text{sp}}^{(1)}$ corresponding to the L - and the H -region in Fig. 4(a) [shaded area, shaded area beneath the single hatched region and cross-hatched area in Fig. 4(a)] reproduces the common stability plot as predicted by earlier works [5], [6]. The union of the unlocked (blank area) and unstable region (cross-hatched area) for $n_L = n_{\text{sp}}^{(1)}$ in Fig. 4(a) is usually classified as the region of nonlinear dynamics [6]. However, Fig. 4(a) also shows the root loci $n_H = n_{\text{sp}}^{(2)}$, outlining the H -region [single hatched region in Fig. 4(a)], which appear even in the single side-mode analysis. As has been explained previously, the stationary points $n_H = n_{\text{sp}}^{(2)}$ represent an additional layer on the top of $n_L = n_{\text{sp}}^{(1)}$ root loci in the H -region. A closer inspection shows that $n_H = n_{\text{sp}}^{(2)}$ root behave as the

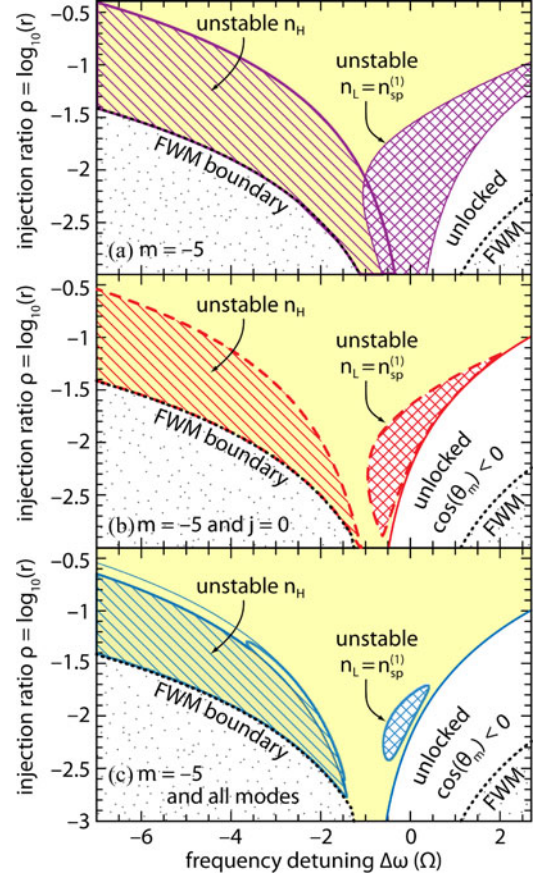


Fig. 4. (a) Stability plot for injection-locked mode $m = -5$ alone. Stable (shaded) and unstable (hatched) part of the locking range. The whole H -region is unstable. (b) Same, for two modes included i.e., injection-locked mode $m = -5$ and $j = 0$. The whole H -region is unstable. (c) Same, for all modes included. The whole subset $n_H = n_{\text{sp}}^{(2)}$ is unstable, while $n_H = n_{\text{sp}}^{(3)}$ is unstable only for small negative detuning. For all three cases, n_L is stable in the whole H -region (shaded under hatched).

repelling fixed point, not attracting one, as should be in case of a stable stationary point. The same is confirmed by the small signal analysis. Since the region for $n_H = n_{\text{sp}}^{(2)}$ is fully unstable and represents the layer which overlaps $n_L = n_{\text{sp}}^{(1)}$ layer in the H -region, one can conclude that the n_H region actually does not manifest its presence nor intersect the $n_L = n_{\text{sp}}^{(1)}$ layer. Therefore, this single hatched layer can be ignored in case (i), while the stability map remains as the one predicted in [5], [6]. Although the H -region in case (ii) besides $n_H = n_{\text{sp}}^{(2)}$, comprises $n_H = n_{\text{sp}}^{(3)}$, we find that similarly as in case (i), n_H is fully unstable for the whole H -region [cf., Fig. 4(a) and (b)]. However, it is found in case (iii) that $n_H = n_{\text{sp}}^{(2)}$ is always unstable, while $n_H = n_{\text{sp}}^{(3)}$ is unstable only for a small negative detuning [see Fig. 4(c)]. For all three cases, n_L corresponding to the H -region stays stable (shaded beneath the hatched region). It can be seen in Fig. 4(b) and (c) that the unstable region for $n_L = n_{\text{sp}}^{(1)}$ from Fig. 4(a), diminishes as the number of modes increases.

In addition to the repelling fixed point instability related to the stationary point $n_H = n_{\text{sp}}^{(2)}$, which can be also confirmed by

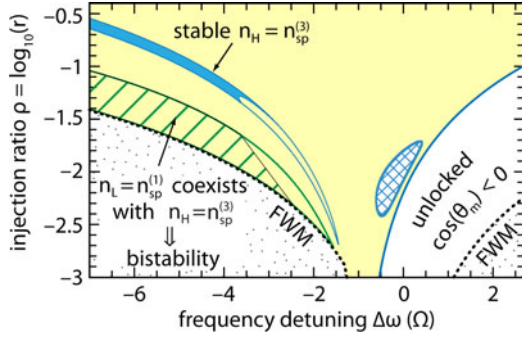


Fig. 5. Stable region for $n_H = n_{sp}^{(3)}$ (dark shaded) and the part of $n_L = n_{sp}^{(1)}$ (hatched) coexisting with it, for a fixed injection photon density S_{inj} , providing bistability. All modes are included.

the asymptotic Lyapunov stability check based on the small signal analysis, we find that a different type of instability is related to the other stationary points. In fact, instabilities which occur for positive detuning for $n_L = n_{sp}^{(1)}$ and negative detuning for $n_H = n_{sp}^{(3)}$ are related to the supercritical Hopf bifurcation, for which the laser operates on only one mode with the oscillatory output, while the suppressed modes follow the same oscillatory behavior. In the stable regions and for the fixed conditions, the slave laser remains in one of the stable points and in the injected mode over the entire range. However, the multivalued character of the locking range allows coexistence of the two stable, attractive fixed points for a sufficiently large negative detuning. As we show next, these stable points may provide shifting between modes as a result of injection power (or detuning) variation.

Since $n_H = n_{sp}^{(3)}$ is a stable state for a sufficiently large negative detuning (see Fig. 5), we conclude that this part of locking and stability plot diagram comprises two stable solutions n_L and $n_H = n_{sp}^{(3)}$ and represents multivalued function in $\Delta\omega - r$ space. In addition, for fixed injected densities $S_{inj}^{(s)}$, the state $n_H = n_{sp}^{(3)}$ coexists with $n_L = n_{sp}^{(1)}$ (hatched part in Fig. 5). Therefore, we conclude that the bistability becomes feasible as a result of the multivalued character of the locking and stability plot. This result confirms that inclusion of unlocked modes in the analysis of the stability map is crucial for multimode in-plane lasers. It is not clear, whether this effect is relevant for monomode in-plane lasers. However, it can be expected that in the case of the sufficient suppression of side modes, monomode lasers can be treated as before, i.e., regardless the influence of the unlocked modes. Recent investigation of nanostructure lasers based on quantum dashes [4], [12], suggests that our findings may help to understand some of bistability effects found there. Moreover, this complete model can be useful in the investigation of the bandwidth and the modulation response of injection-locked multimode lasers [13], [14] and their dynamics in general. In addition, it can be used to study the injection-locked lasers in all-optical flip-flop element applications, to investigate the switching time between the bistable states more precisely, previously analyzed only by a single-mode model [15]. Our model can also be of interest if the injection locking includes more than one master signal, as in the case of dual injection [16].

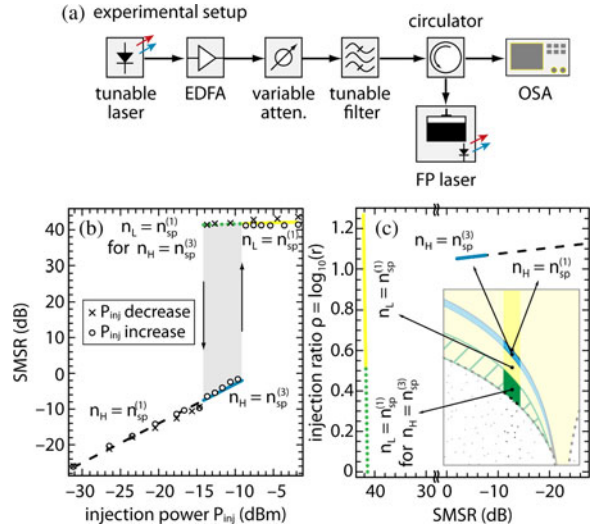


Fig. 6. (a) Experimental setup. (b) Measured SMSR for the mode $m = -5$ versus injection power P_{inj} . (c) Branches of the hysteresis from (b), mapped into r -SMSR space: (left) upper branch within (dots) and outside (solid) bistability range; (right) lower branch within (solid) and outside (dash) bistability range. (Inset) Schematic distribution of the hysteresis branches in the locking and the stability plot.

V. EXPERIMENT

In order to validate our findings regarding bistability, we conduct an experiment [see Fig. 6(a)], in which for a slave Fabry–Perot laser we measure the side-mode-suppression-ratio (SMSR) of the injection-locked mode $m = -5$ (with respect to the dominant mode) versus the injection power P_{inj} [see Fig. 6(b)]. We set $\Delta\omega = -5 \Omega$ and $I = 1.4I_{th}$. The decrease and then the increase of P_{inj} clearly show a hysteresis, which proves the existence of the bistability. By using the measured power corresponding to S_m for $m = -5$ and P_{inj} , we generate the r versus SMSR plot [see Fig. 6(c)]. Since the laser used in this experiment has a larger active region volume than the one used in our calculations, we qualitatively compare Fig. 6(c) with Fig. 5 for a fixed negative detuning. The upper branch of the hysteresis loop [see Fig. 6(b)] falls into a smaller r -range ($\rho < 0.5$) [see Fig. 6(c)]. This corresponds to the hatched region in Fig. 5 for which $n_L = n_{sp}^{(1)}$ coexists with $n_H = n_{sp}^{(3)}$, sharing the same P_{inj} . For $\rho > 0.5$, corresponding to the upper branch outside of the hysteresis loop, we find only one stable stationary point. This result is supported by Fig. 5, which shows a stable region between the hatched and shaded areas, corresponding to the part of the upper branch outside of the bistability range [cf., inset in Fig. 6(c)]. For a sufficiently large r ($\rho > 1.1$), there is an additional stable stationary point corresponding to lower branch of the hysteresis loop and $n_H = n_{sp}^{(3)}$ region in Fig. 5. The fact that for this range of r , we have two different values of SMSR, i.e., two different injected powers P_{inj} for one r , confirms the conclusion that the shaded region in Fig. 5 represents the multivalued function. The lower branch outside of the loop, corresponds to $n_H = n_{sp}^{(1)}$ [see Fig. 3(a)], which as we already mentioned, is not related to the bistability region. However, the experimental results suggest that the region corresponding to

$n_H = n_{sp}^{(1)}$ comprises a somewhat wider r -range than the one predicted by our theory, which proposes almost horizontal line for $n_H = n_{sp}^{(1)}$ part in Fig. 6(c). It is likely that small injected powers in this case may cause a measurement uncertainty and consequently the small noticed discrepancy between the theory and the experiment. It is also possible that the experimental results include not only the H -, but also the M -region, which supports multiplicity of $n_{sp}^{(1)}$ point. Therefore, the mapping shown in Fig. 6(c) completely resembles distribution of r -values in Fig. 5 and thin region $n_H = n_{sp}^{(1)}$ in Fig. 3(a).

VI. CONCLUSION

We show that the inclusion of the central and other unlocked modes in an injection-locked laser considerably modifies the commonly defined locking range map, ordinarily obtained by analysis of the injection-locked side-mode alone. For sufficient negative detuning, the locking range is degenerated and folded down between the FWM and the locking range boundary where $\cos(\theta_m) = 0$. Moreover, for a small r , this range is shifted toward the negative detuning. The folding down of the locking range leads to a multiplicity of the stationary points and consequently to the slave laser bistability. Qualitative agreement between our theory and our experiment has been found in this study. The stability analysis shows that when all of the modes are included in the numerical analysis, the potential bistability regions are generally stable, except for small negative detuning. However, if only the dominant and injection-locked modes are included in the stability analysis, the bistability cannot be observed since the folded part of the locking region becomes fully unstable.

Additionally, for a positive detuning, the inclusion of all unlocked modes predicts shrinkage of the unstable region on the stability map. All these results considerably modify the shape and features of the common single-valued locking and stability map [5].

REFERENCES

- [1] A. E. Siegman, *Lasers*. Mill Valley, CA, USA: University Science Books, 1986.
- [2] R. Adler, "A study of locking phenomena in oscillators," *Proc. IRE*, vol. 34, pp. 351–357, 1946.
- [3] M. J. Fice, A. Chiuchiarelli, E. Ciaramella, and A. J. Seeds, "Homodyne coherent optical receiver using an optical injection phase-lock loop," *J. Lightw. Technol.*, vol. 29, no. 8, pp. 1152–1164, 2011.
- [4] M. C. Pochet, N. A. Naderi, V. Kovanis, and L. F. Lester, "Modeling the dynamic response of an optically-injected nanostructure diode laser," *IEEE J. Quantum Electron.*, vol. 47, no. 6, pp. 827–833, Jun. 2011.
- [5] J. Ohtsubo, *Semiconductor Lasers: Stability, Instability, Chaos*. Berlin, Germany: Springer-Verlag, 2008.
- [6] A. Murakami, "Phase locking and chaos synchronization in injection-locked semiconductor lasers," *IEEE J. Quantum Electron.*, vol. 39, no. 3, pp. 438–447, Mar. 2003.
- [7] T. B. Simpson, J. M. Liu, K. F. Huang, and K. Tai, "Nonlinear dynamics induced by external optical injection in semiconductor lasers," *Quantum Semiclass. Opt.*, vol. 9, no. 5, pp. 765–784, 1997.
- [8] T. B. Simpson, "Mapping the nonlinear dynamics of a distributed feedback semiconductor laser subject to external optical injection," *Opt. Commun.*, vol. 215, pp. 135–151, 2003.
- [9] S. Wieczorek, B. Krauskopf, and D. Lenstra, "Multipulse excitability in a semiconductor laser with optical injection," *Phys. Rev. Lett.*, vol. 88, pp. 063901–063904, 2002.

- [10] M. M. Krstić, J. V. Crnjanski, and D. M. Gvozdić, "Injection power and detuning-dependent bistability in Fabry–Perot laser diodes," *IEEE J. Sel. Topics Quantum Electron.*, vol. 18, no. 2, pp. 826–833, Apr. 2012.
- [11] C. H. Henry, N. A. Olsson, and N. K. Dutta, "Locking range and stability of injection locked 1.54 μm InGaAsP semiconductor lasers," *IEEE J. Quantum Electron.*, vol. 21, no. 8, pp. 1152–1156, Aug. 1985.
- [12] A. Hurtado, M. Nami, I. D. Henning, M. J. Adams, and L. F. Lester, "Bistability patterns and nonlinear switching with very high contrast ratio in a 1550 nm quantum dash semiconductor laser," *Appl. Phys. Lett.*, vol. 101, pp. 161117–161121, 2012.
- [13] A. G. R. Zliti, M. M. Krstić, and D. M. Gvozdić, "Modulation response and bandwidth of injection-locked Fabry–Perot laser diodes," *Phys. Scr.*, vol. T149, pp. 014033–014037, 2012.
- [14] X. Jin and S. L. Chuang, "Bandwidth enhancement of Fabry–Perot quantum-well lasers by injection locking," *Solid State Electron.*, vol. 50, pp. 1141–1149, 2006.
- [15] D. M. Gvozdić, M. M. Krstić, and J. V. Crnjanski, "Switching time in optically bistable injection-locking semiconductor lasers," *Opt. Lett.*, vol. 36, pp. 4200–4202, 2011.
- [16] C. W. Chow, C. S. Wong, and H. K. Tsang, "All-optical NRZ to RZ format and wavelength converter by dual-wavelength injection locking," *Opt. Commun.*, vol. 209, pp. 329–334, 2002.

Marko M. Krstić received the Dipl. Inž. and M.S. degrees in electrical engineering from the University of Belgrade, Belgrade, Serbia, in 2007 and 2009, respectively. He is currently working toward the Ph.D. degree in electrical engineering at the University of Belgrade.

In 2009, he joined the academic staff at the School of Electrical Engineering, University of Belgrade, where he is a Teaching and Research Assistant. His research interests include modeling and simulation of semiconductor lasers and fiber optics.

Jasna V. Crnjanski received the Dipl. Inž. and M.S. degrees in electrical engineering from the University of Belgrade, Belgrade, Serbia, in 2002 and 2007, respectively, where she is currently working toward the Ph.D. degree.

In 2002, she joined the School of Electrical Engineering, University of Belgrade, where she is a Teaching and Research Assistant. Her research interests include modeling of optical properties of semiconductor nanostructures. She has coauthored more than ten publications.

Milan L. Mašanović (S'98–M'04) received the Dipl. Inž. degree from the School of Electrical Engineering, University of Belgrade, Belgrade, Serbia, and the M.S. and Ph.D. degrees from the University of California at Santa Barbara, Santa Barbara, USA in 1998, 2000, and 2004, respectively, all in electrical engineering.

He is currently an Associate Project Scientist at the University of California at Santa Barbara, and one of the principals at Freedom Photonics LLC, a photonic integration company he cofounded in Santa Barbara. His current research interests include semiconductor lasers and photonic integrated circuits. He has coauthored more than 85 research papers, has given numerous invited talks, and has coauthored one graduate-level text book.

Dr. Mašanović was the recipient of numerous awards and fellowships, including the 2004 IEEE Lasers and Electro-Optics Society Graduate Student Fellowship Award. He serves on technical program committees for a number of conferences in the area of integrated photonics.

Leif A. Johansson (M'04) received the Ph.D. degree in engineering from University College London, London, U.K., in 2002.

He is currently a Research Scientist with the University of California at Santa Barbara, Santa Barbara, USA, and a principal at Freedom Photonics LLC, a photonic integration company he cofounded in Santa Barbara. His current research interests include design and characterization of integrated photonic devices for analog and digital applications and analog photonic systems and subsystems. He has coauthored more than 100 papers, and presented at numerous conferences.

Larry A. Coldren (S'67–M'72–SM'77–F'82) received the Ph.D. degree in electrical engineering from Stanford University, Stanford, CA, USA, in 1972.

He is the Fred Kavli Professor of optoelectronics and sensors with the University of California (UCSB), Santa Barbara. After 13 years in the research area with Bell Laboratories, Holmdel, NJ, he joined UCSB in 1984, where he is currently with the Department of Materials and the Department of Electrical and Computer Engineering. In 1990, he cofounded optical concepts, later acquired as Gore Photonics, to develop novel vertical-cavity surface-emitting laser (VCSEL) technology, and in 1998, he cofounded Agility Communications, Inc., Goleta, CA, later acquired by JDS Uniphase Corporation (JDSU), Milpitas, CA, to develop widely tunable integrated transmitters. At Bell Laboratories, he was initially on waveguided surface-acoustic-wave signal processing devices and coupled-resonator filters. He later developed tunable coupled-cavity lasers using novel reactive-ion etching technology that he created for the new InP-based materials. At UCSB, he continued work on multiple-section tunable lasers, in 1988, inventing the widely tunable multielement mirror concept, which is currently used in some JDSU products. Near this time period, he also made seminal contributions to efficient VCSEL designs that continued to be implemented in practical devices till this day. More recently, his group has developed high-performance InP-based photonic integrated circuits as well as high-speed VCSELs, and they continue to advance the underlying materials growth and fabrication technologies. He has authored or co-authored over 1000 journals and conference papers, seven book chapters, and one textbook and has been issued 64 patents. He has presented dozens of invited and plenary talks at major conferences.

Prof. Coldren is a fellow of the Optical Society of America and a member of the National Academy of Engineering. He was a recipient of the John Tyndall and Aron Kressel Awards, in 2004 and 2009, respectively.

Dejan M. Gvozdić received the M.S. and Ph.D. degrees in electrical engineering from University of Belgrade, Belgrade, Serbia, in 1992 and 1995, respectively.

In 1989, he joined the School of Electrical Engineering, University of Belgrade, where he currently is a Professor of Physical Electronics, Quantum Electronics and Optical Communications. His general research interests are modeling and simulation of optoelectronic devices as nanostructure lasers, optical amplifiers, photodetectors and since recently spintronic effects. He has authored and co-authored over 30 peer-reviewed journal papers. He is a recipient of several scientific awards, and has been working as a referee for a number of IEEE publications and conferences.

Highly-stable Integrated InGaAsP/InP Mode-locked Laser and Optical Phase-locked Loop

John S. Parker, Mingzhi Lu, Hyunchul Park, Abirami Sivananthan, Eli Bloch, Zach Griffith, Leif A. Johansson, *member*, IEEE, Mark J. Rodwell, *Fellow*, IEEE, and Larry A. Coldren, *Fellow*, IEEE

Abstract—We demonstrate an integrated InGaAsP/InP mode-locked laser (MLL) stabilized with an optical phase-locked loop (OPLL). Using the OPLL, a single comb line is locked to a reference oscillator (a 200 Hz linewidth Brillouin laser). The comb linewidth is reduced from 100 MHz (unlocked) to <550 Hz (locked) using the OPLL. The RMS phase error between the comb and the reference laser is 20°. The linewidth of the adjacent comb lines is <1 kHz, and the comb spans 430 GHz.

Index Terms—Mode locked lasers, photonic integrated circuits, integrated optics, comb line generation, optical phase locked loop.

I. INTRODUCTION

Integrated mode-locked lasers (MLLs) are a common source for optical comb generation, whereas other comb sources include optical parametric oscillation (OPO) [1] and cavity-enhanced phase modulation [2]. InGaAsP/InP optical comb sources operating at 1.55 μm wavelength have applications in metrology [3], low-noise microwave and THz oscillators [4], sensing and imaging (e.g. frequency-resolved and frequency-modulated-continuous-wave (FMCW) LIDAR) [5], and wavelength-division-multiplexed (WDM) data communication [6]. Typically semiconductor combs have optical linewidth of >1 MHz and frequency drift in the MHz range arising from electrical, thermal, and mechanical fluctuations. Narrower optical linewidth and improved stability enables better resolution for sensing and imaging, as well as higher spectral efficiency, i.e., higher QAM, for telecommunications.

Stabilization of integrated comb sources can be achieved using optical injection locking and feedback circuits, such as phase-locked loops. Researchers have demonstrated injection-locked active, passive, and hybrid mode-locked lasers [7][8][9][10], with hold ranges for locking varying from ~200

to 800 MHz. As injection locking typically suppresses all modes but a few near the injected tone [10], these demonstrations used either large RF drive power with active mode locking (20.5 dBm) [8] to create multiple reference lines inside the cavity, or achieved this externally using a Mach-Zehnder modulator and injected multiple phase-locked tones with passive mode locking [9]. A trade-off quickly becomes apparent between phase-noise reduction and comb suppression. Higher injected powers reduce more of the phase noise. However, they also suppress the adjacent modes leading to single-mode lasing at high injected power.

The optical phase-locked loop (OPLL) is a promising device to achieve stabilized broadband comb sources with high levels of phase-noise suppression. An OPLL allows the phase noise to be cloned from a reference laser to a slave laser, i.e., a current controlled oscillator, within the loop bandwidth. Only recently have integrated OPLLs been demonstrated [11], and heterodyne locking at a frequency offset from -9 to 7.5 GHz has been shown [12]. Through optical integration, the loop is less affected by environmental noise and the loop bandwidth has been increased to over 1.1 GHz [13]. When integrated, the OPLL requires a semiconductor laser, an optical mixer, an optical detector, and a loop filter which can be as simple as resistors and capacitors or as complex as a custom HBT, CMOS, or BJT circuit with amplifiers and mixers. The entire system can fit in the palm of your hand, can be smaller than a quarter, and can run on batteries.

In this demonstration, a monolithic mode-locked laser with an optical mixer and photodetectors is integrated with transimpedance amplifiers (TIAs) and an electronic loop filter. The monolithic photonic integrated circuit (PIC) enables a short OPLL loop delay and provides stable and robust coupling between the optical components to reduce noise. The integrated OPLL comb source has a footprint <10x10 mm², where most of this area is due to the electronics and associated wire bonding. To our knowledge, this is the first demonstration of a monolithic semiconductor mode-locked laser stabilized with an OPLL. Short loop delay, realized through photonic integration, is crucial to achieving this stable locking.

II. MLL FABRICATION

A Fabry-Perot MLL, an optical coupler, an optical mixing element, and photodetectors are fabricated on an InGaAsP/InP offset quantum well (OQW) platform that consists of seven 0.9% compressively strained 6.5 nm QWs and eight -0.2%

Manuscript received March 21, 2013. This work was supported by the Defense Advanced Research Project Agency (DARPA) Photonic Integrated for Coherent Optics (PICO) program. A portion of this work was done in the UCSB nanofabrication facility, part of the National Science Foundation (NSF) funded NNIN network.

Eli Bloch is with the Dept. of Electrical Engineering, Technion – Israel Institute of Technology, Haifa 32000, Israel.

Zach Griffith is with Teledyne Scientific and Imaging Company, Thousand Oaks, 1049 Camino Dos Rios, CA, 91360, USA.

All other authors are with the Department of Electrical and Computer Engineering, University of California, Santa Barbara, CA 93106, USA (e-mail: JParker@ece.uscb.edu).

Copyright (c) 2012 IEEE. Personal use of this material is permitted. However, permission to use this material for any other purposes must be obtained from the IEEE by sending a request to pubs-permissions@ieee.org.

tensile strained 8 nm barriers that are epitaxially grown above a 300 nm thick 1.3Q InGaAsP layer as part of the base epi.

The PIC fabrication uses i-line photolithography for photoresist definition and standard cleanroom processing techniques on all steps. Passive areas are defined using a selective wet-etch and a single blanket regrowth is done to cover the device with a p+-doped InP cladding, a p++-doped InGaAs contact layer, and an InP capping layer to protect the InGaAs contact layer during device fabrication. The active material is used to define the semiconductor optical amplifiers (SOAs) and the saturable absorber (SA), whereas the passive material is used to define the low-loss waveguides, optical couplers, and current injection based phase shifters. A microscope image of the completed device is shown in Fig. 1.

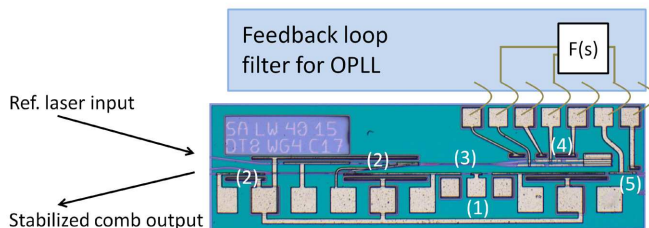


Fig. 1. Microscope image of the PIC and schematic of the loop filter with numbered components: (1) mode-locked laser, (2) optical coupler and SOA amplifiers for comb and reference laser, (3) optical mixer, (4) balanced photodetectors, and (5) current-injection based phase tuning pad.

III. OPTO-ELECTRONIC INTEGRATION

The fabricated laser bars are singulated into $500 \times 1700 \mu\text{m}^2$ PICs and mounted on gold coated AlN carriers with AuSn solder. The TIAs are InP based HBTs fabricated by Teledyne Scientific. The TIA chip also has limiting amplifiers with ~ 30 dB maximum gain for small signals. The loop filter for the OPLL is designed on a separate AlN carrier using a commercial Op-Amp with 0603 resistors and capacitors optimized for the correct transfer function, and simulated using Advanced Design Systems software by Agilent. The three OPLL systems (PIC, TIA, and loop) are soldered onto a thin gold coated AlN mount in close proximity to minimize loop delay and GSG signal pads are connected with short wire bonds. An image of the finished system is shown in Fig. 2(a), and in Fig. 2(b) under test.

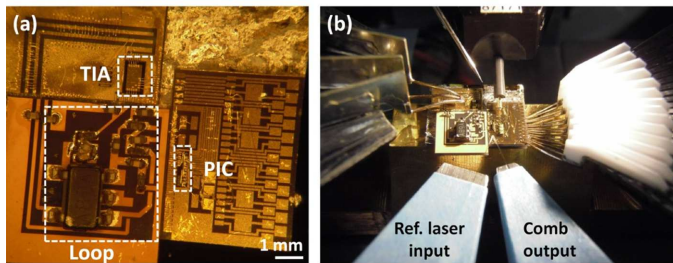


Fig. 2. Images of (a) the integrated PIC, TIA, and loop filter on AlN carriers, and (b) the OPLL system under testing. The input fiber for the reference laser is shown on the left side, the output fiber for the comb is shown on the right side. High-speed probes (left and back) and DC probes (right) are shown.

Nearly balanced photodetectors (BPDs) (with 20% power

imbalance) are used on the PIC with current subtraction done with the Op-Amp. The BPDs reduce the influence of RIN since this noise is common to both detectors.

IV. OPTICAL LOCKING RESULTS

The OPLL system is first locked using a 1 MHz optical linewidth DFB laser as an optical reference. The OPLL comb is passively mode locked and 3 mW optical power is coupled into a lensed optical fiber at the left laser facet. The reference laser is optically mixed on-chip with the output of the MLL and measured on the integrated photodetectors. This error signal is fed through the TIAs, the loop filter, and finally back into a current-controlled phase pad on the MLL. The MLL with the phase pad operates as a current controlled oscillator (CCO) to clone the phase error of the reference within the loop bandwidth.

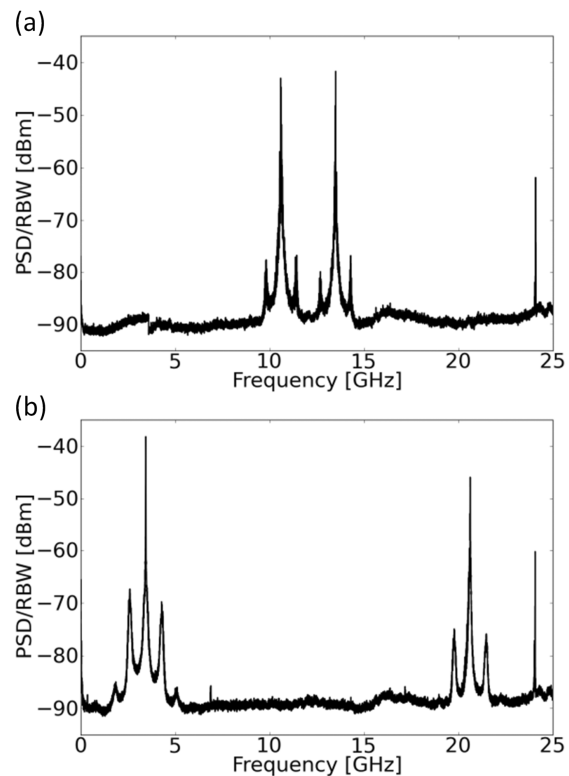


Fig. 3. Heterodyne beat spectrum of a DFB laser and the locked comb lines under passive mode locking (RBW 200 kHz). (a) Comb lines on the low-wavelength side of the comb are arbitrarily measured at 3 and 21 GHz. (b) Comb lines on the high-wavelength side of the comb are arbitrarily measured at 11 and 13 GHz. In both plots f_{rep} is shown at 24 GHz. Locking is achieved using a second DFB laser. The optical linewidths measured are 2-4 MHz.

Once locked, the optical comb lines are measured using a heterodyne technique with a second DFB laser arbitrarily placed near the comb lines of interest. The spectrum of the low- and high-wavelength side of the comb is shown in Fig. 3(a) and Fig. 3(b), respectively; two comb lines and f_{rep} are visible. The RF beat tone linewidth at f_{rep} is 2 MHz under passive mode locking, where f_{rep} is the cavity repetition frequency of 24 GHz. The loop bandwidth is ~ 790 MHz, and

resonance peaks at ± 790 MHz are visible on both sides of all comb lines. The optical linewidth of the locked comb line is 1 MHz. The measured linewidths of the adjacent comb lines are 2-4 MHz within a 10 dB bandwidth of the locked tone, thus nearly matching the RF beat tone linewidth. Without the OPLL locking to the reference laser, the comb linewidths are ~ 100 MHz. This demonstrates that the phase errors between adjacent comb lines are partially correlated, within the f_{rep} linewidth, and therefore reducing the phase noise of a single comb line reduces the phase noise of all comb lines.

To improve the stabilized comb, the NP “The Rock” 200 Hz linewidth laser is used as the optical reference, and is positioned at 1550 nm. The MLL is also hybrid mode-locked using an RF power of +15 dBm, which increases the precision of the frequency spacing between the comb lines. The beat tone linewidth at f_{rep} is < 10 Hz (limited by the ESA resolution), see Fig. 7(a). The laser drive current is 120 mA and the SA is biased at 0 V. The optical spectrum of the locked tone is shown in Fig. 4(a).

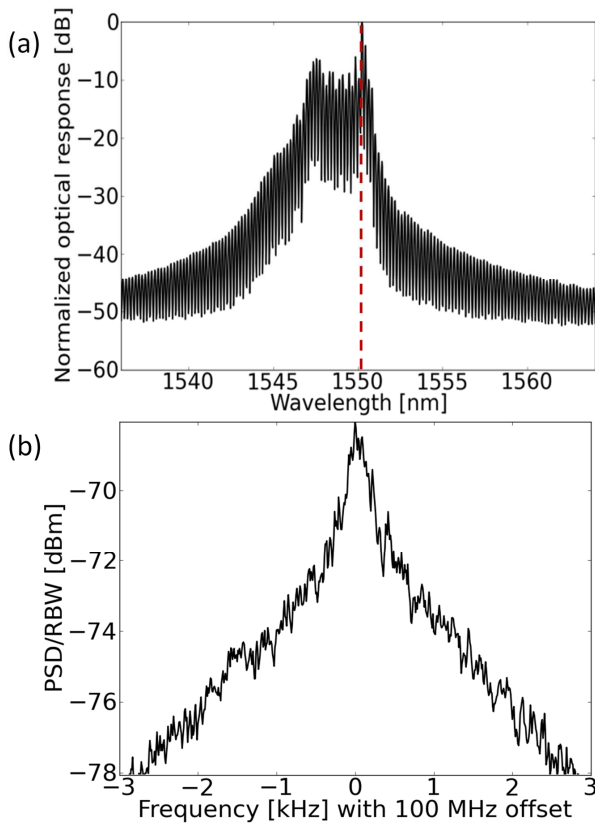


Fig. 4. (a) The optical comb spectrum measured on the OSA with the wavelength of the reference laser shown in the dashed vertical line (res. 60 pm), and (b) heterodyne beat-tone measurement on the ESA used to calculate optical linewidth (RBW 200 Hz). The beat-tone width is 550 Hz at -3 dB from the peak.

The linewidth of the locked comb line is measured using a delayed heterodyne technique, as shown in Fig. 5. The reference laser is put through 150 km of fiber and a 100 MHz acousto-optic modulator (AOM), and then mixed in a 2x2 fiber coupler with the output of the mode-locked laser. The output of the optical mixer is measured on an electrical spectrum

analyzer (ESA) at 100 MHz.

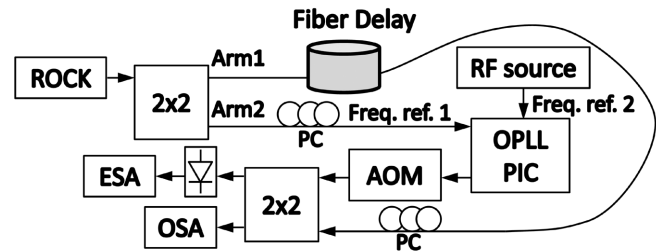


Fig. 5. Optical phase-locked loop measurement set-up using the 200 Hz linewidth Rock laser. The fiber delay in Arm1 is set to 150 km for linewidth measurement, and matched path length with Arm2 for residual phase-noise measurement. AOM: Acousto-optic modulator. PC: Polarization controller. ESA: Electrical spectrum analyzer. OSA: Optical spectrum analyzer.

The measured frequency width at -3 dB is 550 Hz, as shown in Fig. 4(b), which means the actual optical linewidth of the comb line is below this due to the self-heterodyne technique. The measured linewidth is the combined phase noises of the two lasers. However, 150 km of fiber provides only 734 μs of delay, which is shorter than the coherence time of the Rock laser (1.59 ms). The self-heterodyne measurement is hence operating near the limit $t_{\text{delay}} = t_{\text{coherence}}$ [14], which means that an upper bound of 550 Hz can be set on the linewidth, but the exact linewidth cannot be determined without additional fiber such that $t_{\text{delay}} \gg t_{\text{coherence}}$. The optical linewidth of the comb lines without the OPLL is 100 ± 30 MHz, as shown in Fig. 6, more than 10^5 times larger than the locked linewidth.

Stable locking is achieved for the duration of testing, > 3 hrs without any adjustment. The duration of locking is limited by the fiber coupling from the reference laser into the PIC, which drifts over time. To verify the OPLL locking, the loop filter is turned off and the measured 100 MHz AOM tone is no longer observed. The unwanted reference laser power that reflects from integrated PIC components and reaches the laser cavity is measured to be < -30 dBm, and no injection locking is observed.

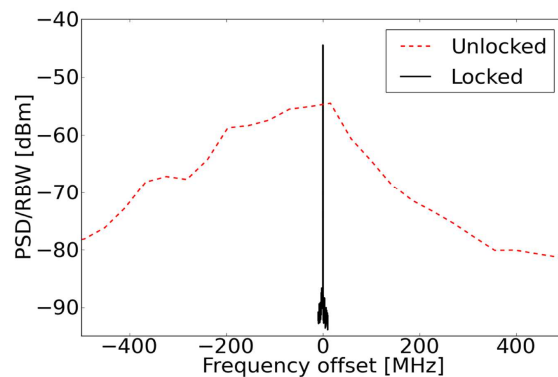


Fig. 6. Optical linewidth measurement with (solid black, RBW 200 Hz) and without (dashed red, RBW 2 MHz) the optical phase-locked loop. The optical linewidth is reduced from 100 MHz to < 550 Hz.

The optical linewidths of the adjacent comb lines are measured at $f_{\text{rep}} \pm f_{\text{AOM}}$ on the ESA, as shown in Fig. 7. These linewidths are < 1 kHz measured with a 75 km fiber delay,

which are greater than the locked tone linewidth due to added phase noise induced by amplitude noise in the MLL OPLL system.

The measured residual phase noise of the locked comb line compared to the reference laser is shown in Fig. 8. This is measured by matching the paths lengths of Arm1 and Arm2 by adjusting the fiber delay shown in Fig. 5. The phase noise has a pedestal from 1 kHz to 10 MHz, which arises due to the laser RIN. The phase-noise below 1 kHz is dominated by the acousto-optic modulator and the RF source operating at 100 MHz used in the set-up. Thus, the measured phase noise is most accurate above 1 kHz. The phase-noise variance is 0.12 rad^2 from 1 kHz to 10 GHz, corresponding to 20° standard deviation from the locking point.

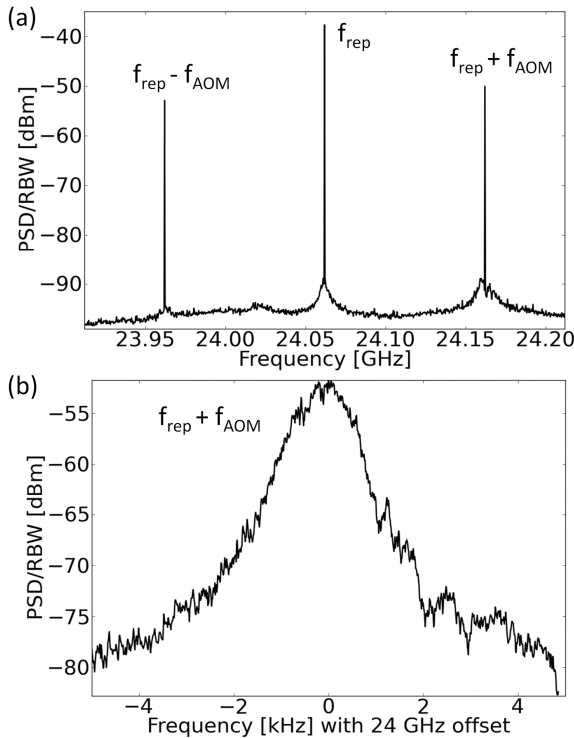


Fig. 7. (a) Linewidth of the adjacent comb lines measured at $f_{\text{rep}} \pm f_{\text{AOM}}$ on the ESA after 75 km of delay (RBW 10 kHz), and (b) zoomed in at $f_{\text{rep}} + f_{\text{AOM}}$ (RBW 100 Hz).

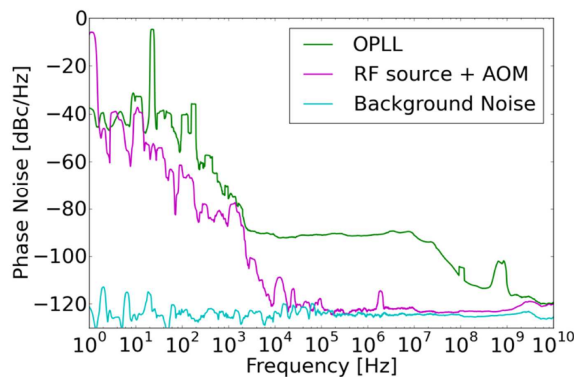


Fig. 8. Residual phase noise of the locked comb line measured on the ESA (green). The low frequency phase noise is dominated by the acousto-optic modulator (AOM) and the RF driver used in this measurement (purple).

V. CONCLUSIONS

Close integration of OPLLs and PICs enables low phase-noise, stable, and highly compact optical frequency comb generators. A 430 GHz span comb is demonstrated with <550 Hz optical linewidth at the locked tone and <1 kHz on adjacent tones. The OPLL achieves a 20° standard deviation from the locking point. Using a suitable CMOS TIA, amplifier, and loop filter could reduce the dimensions to $<2 \times 2 \text{ mm}^2$, and further reduction to noise can be achieved through the use of well-balanced detectors.

REFERENCES

- [1] T. J. Kippenberg, R. Holzwarth, and S. A. Diddams, "Microresonator-based optical frequency combs," *Science (New York, N.Y.)*, vol. 332, no. 6029, pp. 555–9, Apr. 2011.
- [2] D. Kuizenga and A. Siegman, "FM and AM mode locking of the homogeneous laser - Part I: Theory," *IEEE Journal of Quantum Electronics*, vol. 6, no. 11, pp. 694–708, Nov. 1970.
- [3] T. Yasui, S. Yokoyama, H. Inaba, K. Minoshima, T. Nagatsuma, and T. Araki, "Terahertz Frequency Metrology Based on Frequency Comb," *IEEE Journal of Selected Topics in Quantum Electronics*, vol. 17, no. 1, pp. 191–201, Jan. 2011.
- [4] S. A. Diddams, A. Bartels, T. M. Ramond, C. W. Oates, S. Bize, E. A. Curtis, J. C. Bergquist, and L. Hollberg, "Design and control of femtosecond lasers for optical clocks and the synthesis of low-noise optical and microwave signals," *IEEE Journal of Selected Topics in Quantum Electronics*, vol. 9, no. 4, pp. 1072–1080, Jul. 2003.
- [5] M.-C. Amann, T. Bosch, M. Lescure, R. Myllylä, and M. Rioux, "Laser ranging: a critical review of usual techniques for distance measurement," *Optical Engineering*, vol. 40, no. 1, p. 10, Jan. 2001.
- [6] Y. Ben M'Sallem, Q. Q. T. Le, Y. Ben M'Sallem, L. Bramerie, Q.-T. Nguyen, E. Borgne, P. Besnard, A. Shen, F. Lelarge, S. LaRochelle, L. A. Rusch, and J.-C. Simon, "Quantum-dash mode-locked laser as a source for 56-Gb/s DQPSK modulation in WDM multicast applications," *IEEE Photonics Technology Letters*, vol. 23, no. 7, pp. 453–455, 2011.
- [7] T. Jung, D. T. K. Tong, S. Murthy, M. C. Wu, T. Tanbun-Ek, R. Lodenkamper, R. Davis, L. J. Lembo, and J. C. Brock, "CW injection locking of a mode-locked semiconductor laser as a local oscillator comb for channelizing broad-band RF signals," *IEEE Transactions on Microwave Theory and Techniques*, vol. 47, no. 7, pp. 1225–1233, Jul. 1999.
- [8] M. Teshima, K. Sato, and M. Koga, "Experimental investigation of injection locking of fundamental and subharmonic frequency-modulated active mode-locked laser diodes," *IEEE Journal of Quantum Electronics*, vol. 34, no. 9, pp. 1588–1596, 1998.
- [9] Z. Ahmed, H. F. Liu, D. Novak, Y. Ogawa, M. D. Pelusi, and D. Y. Kim, "Locking characteristics of a passively mode-locked monolithic DBR laser stabilized by optical injection," *IEEE Photonics Technology Letters*, vol. 8, no. 1, pp. 37–39, Jan. 1996.
- [10] B. R. Koch, A. W. Fang, E. Lively, R. Jones, O. Cohen, D. J. Blumenthal, and J. E. Bowers, "Mode locked and distributed feedback silicon evanescent lasers," *Laser & Photonics Review*, vol. 3, no. 4, pp. 355–369, Jul. 2009.
- [11] S. Ristic, A. Bhardwaj, M. J. Rodwell, L. A. Coldren, and L. A. Johansson, "An Optical Phase-Locked Loop Photonic Integrated Circuit," *Journal of Lightwave Technology*, vol. 28, no. 4, pp. 526–538, Feb. 2010.
- [12] M. Lu, H. Park, E. Bloch, A. Sivanathan, A. Bhardwaj, Z. Griffith, L. A. Johansson, M. J. Rodwell, and L. A. Coldren, "Highly integrated optical heterodyne phase-locked loop with phase/frequency detection," *Optics Express*, vol. 20, no. 9, p. 9736, Apr. 2012.
- [13] H. Park, M. Lu, E. Bloch, T. Reed, Z. Griffith, L. Johansson, L. Coldren, and M. Rodwell, "40Gbit/s coherent optical receiver using a Costas loop," *Optics Express*, vol. 20, no. 26, p. B197, Nov. 2012.
- [14] A. Yariv and P. Yeh, *Photonics*, 6th ed. Oxford University Press, Inc., 2006.

I. Photonic Integrated Circuits

C. Integrated Optical Phase-Locked Loops

A 1–20-GHz All-Digital InP HBT Optical Wavelength Synthesis IC

Eli Bloch, Hyunchul Park, Mingzhi Lu, Thomas Reed, Zach Griffith, Leif A. Johansson, *Member, IEEE*, Larry A. Coldren, *Life Fellow, IEEE*, Dan Ritter, and Mark J. Rodwell, *Fellow, IEEE*

Abstract—An integrated circuit (IC) for heterodyne optical phase locking in a 1–20-GHz offset range is hereby reported. The IC, implemented in a 500-nm InP HBT process, contains an emitter coupled logic digital single-sideband mixer to provide phase locking at a ± 20 -GHz offset frequency, and a wideband phase-frequency detector designed to provide loop acquisition up to ± 40 -GHz initial frequency offset. The all-digital IC design has phase-frequency detection gain independent of IC process parameters or optical signal levels, and provides a wide offset locking range. A 100-ps delay decreases the overall loop delay, making wideband loop filter design possible. In addition, a medium-scale high-frequency logic design methodology is presented and fully discussed.

Index Terms—Bipolar integrated circuits (ICs), high-speed ICs, microwave circuits, mixers, optoelectronic devices, phase-locked loops (PLLs), wavelength division multiplexing.

I. INTRODUCTION

THE ever-growing data volume transmitted through the optical fiber communication systems requires increasingly efficient transmission and receiving techniques. Coherent communication methods have been of a great interest due to their superior noise performance comparing to the direct-detection ones. However, coherent communication is mainly based on a free-running optical local oscillator (LO) and digital processing after detection for data and clock recovery. Wavelength-division-multiplexed (WDM) optical communications systems use optical resonators coupled to diode lasers to produce optical channel spacing, typically ~ 50 GHz. The WDM receiver, in

turn, is implemented by optical filters to separate the channels. In marked contrast, in microwave systems, frequencies are precisely determined by phase-locked loop (PLL)/synthesis techniques, allowing close frequency spacing of communications channels and efficient use of the spectrum. Using optical PLLs [1], [2], pairs of lasers can be locked in both optical phase and frequency. By introducing frequency offsets within the optical PLL, the frequency difference between a pair of lasers can be set to this injected frequency, allowing wavelength spacing within WDM, LIDAR, and other optical systems to be set precisely and under digital control. This is optical wavelength synthesis.

Due to the large optical frequency (e.g., 193 THz for a 1550-nm laser), frequency-division techniques cannot be used for frequency synthesis. Due to the large ratio of optical oscillator frequency to the typical loop bandwidth in optical PLLs (~ 200 MHz–1 GHz), it is also much more difficult to force the loop to lock. The large initial frequency offset between lasers forces development of frequency difference detectors operating over a 100-GHz bandwidth. To get a large loop bandwidth, yet preserving stability, the loop delay must be minimized [3]. One factor determining loop delays is the speed-of-light propagation delay on both optical waveguides and electrical interconnects. To minimize this delay, the loop must be physically small. This goal is best achieved by monolithic integration. Previously reported optical PLLs [1], [2], [4]–[6] have used an optical interferometer, which measures the sign of the phase offset between the two lasers. This is insufficient to extract the sign of the laser frequency offset, information required for either frequency offset detection or for frequency offset locking with an unambiguous sign to the frequency offset. By measuring both the sine and cosine of the laser phase offset in a quadrature-phase (I/Q) interferometer, both in-phase and quadrature-phase components of the offset signal are measured. This allows both measurement of frequency offset and use of a single-sideband (SSB) mixer to perform offset locking with controlled frequency offset magnitude and sign. Fan *et al.* [7] reported heterodyne phase locking of lasers using an external cavity. This work permits rapidly tunable phase-locked systems and does not require the addition of external optics.

Table I. summaries important milestones in optical offset phase locking.

An optical PLL contains a photonic integrated circuit (PIC) comprising a widely tunable sample grating distributed Bragg feedback (SG-DBR) laser, an I/Q detector including a star-coupler [8] and photodiodes, a microwave electrical integrated circuit (EIC) containing frequency offset control and phase-frequency detectors—reported in this study and recently reported

Manuscript received June 08, 2012; revised October 02, 2012; accepted October 15, 2012. Date of publication December 04, 2012; date of current version January 17, 2013. This work was supported by the Defense Advanced Research Projects Agency (DARPA) under the PICO program. This paper is an expanded paper from the IEEE MTT-S International Microwave Symposium, Montreal, QC, Canada, June 17–22, 2012.

E. Bloch and D. Ritter are with the Microelectronics Research Center, Department of Electrical Engineering, Technion—Israel Institute of Technology (IIT), Haifa 32000, Israel (e-mail: bleli@tx.technion.ac.il; ritter@ee.technion.ac.il).

H. Park, M. Lu, T. Reed, L. A. Johansson, L. A. Coldren, and M. J. Rodwell are with the Department of Electrical and Computer Engineering, University of California at Santa Barbara, Santa Barbara, CA 93106 USA (e-mail: hcpark@ece.ucsb.edu; mlu@ece.ucsb.edu; treed@ece.ucsb.edu; leif@ece.ucsb.edu; coldren@ece.ucsb.edu; rodwell@ece.ucsb.edu).

Z. Griffith is with Teledyne Scientific and Imaging, Thousand Oaks, CA 91360 USA (e-mail: zgriffith@teledyne-si.com).

Color versions of one or more of the figures in this paper are available online at <http://ieeexplore.ieee.org>.

Digital Object Identifier 10.1109/TMTT.2012.2226599

TABLE I
 HETERODYNE OPTICAL PHASE LOCKING—PARALLEL STUDIES

Work (year)	Loop Delay	Frequency detection	Single side-band locking	Comments
[1] R.J. Steed (2011)	1 ns	No	No	Hybrid XOR gate
[5] L.N. Langley (1999)	380 ps	No	No	Hybrid mixer and PD
[4] U. Gliese (1992)	400 ps	No	No	
[11] M. Lu (2012) using the reported IC	200 ps	Yes	Yes	Fully integrated SSB Mixer and PFD

in [9], and a high-frequency (500 MHz), low-delay feed-forward-compensated op-amp loop-filter [10]. PIC design and optical wavelength synthesis results are reported in [11]. Here, we report the design methodology and performance of an InP HBT optical wavelength synthesis IC comprised of a 1–20-GHz *digital* SSB mixer and a ± 40 -GHz phase-frequency difference detector (PFD). The digital design eliminates the dependence of loop bandwidth on optical signal levels (i.e., input photocurrent magnitudes) and enables a wide frequency locking range. In this paper, optical heterodyne locking methods and considerations are examined, a novel digital mixing technique is in-depth analyzed, and design methodologies of complex high-frequency digital ICs are discussed.

II. OPTICAL SYNTHESIZER DESIGN

Optical and electrical PLLs differ fundamentally in that the ratio of carrier frequency to loop bandwidth is a ratio of $\sim 10^4 : 1$ larger in optical than in electrical PLLs. This vast ratio of oscillator frequency to loop bandwidth has a profound impact upon the range of wavelengths over which an optical PLL will acquire lock, and greatly impairs the rate both at which the optical PLL can scan its frequency and its absolute frequency tuning range.

The wide (~ 200 GHz) frequency tuning range of semiconductor lasers, of great value in tunable sources, imposes the demand for very wide bandwidth electronics. The initial frequency offset between reference and controlled lasers may exceed 200 GHz, approaching the range of operation of electronic amplifiers and far beyond the control bandwidth of feedback loops. To acquire a homodyne lock, the beat note between lasers must fall within the PLL loop bandwidth f_{PLL} . In fact, PLLs have a maximum locking range of $\Delta f_{lock} \sim 3f_{PLL}$, as noted by Razavi [12]. Attempts to increase the locking range by dividing the beat note frequency using a frequency divider have two main drawbacks: an increase in a loop delay due to an introduction of a divider into a loop, and a disability of the divider to operate in an absence of a beat note, when the loop is locked.

A simplified offset locked optical PLL block diagram is presented in Fig. 1. The loop is comprised of an optical interferometer acting as a phase detector, a microwave mixer to apply frequency offset (Δf_{ext}), and a loop-filter to control the loop bandwidth and dynamics. For a reference laser frequency f_R

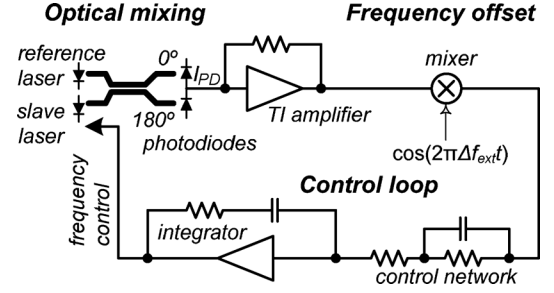


Fig. 1. Simplified optical PLL block diagram.

and a slave laser frequency f_L , the photodiodes output current, given by (1), is proportional to $\cos(\Delta\theta(t))$. Here, E_R , θ_R , and f_R are the electric field amplitude, phase, and frequency of the reference laser, while E_L , θ_L , and f_L are those of the locked laser, and $\Delta\theta(t) = 2\pi\Delta f t + \Delta\theta_0$, where $\Delta f = f_R - f_L$ and $\Delta\theta_0 = \theta_R - \theta_L$

$$I_{PD} \propto \left| E_R e^{j(2\pi f_R t + \theta_R)} + E_L e^{j(2\pi f_L t + \theta_L)} \right|^2 = |E_R|^2 + |E_L|^2 + 2|E_R||E_L| \cos(\Delta\theta(t)) \quad (1)$$

$$K_{PD} = I_{PD} = 2|E_R||E_L| \cos(\Delta\theta(t)) \stackrel{\Delta\theta(t) \ll 1}{\approx} 2|E_R||E_L|. \quad (2)$$

Since $\cos(\Delta\theta(t)) = \cos(-\Delta\theta(t))$, the frequency offset sign cannot be extracted unambiguously; hence, measurement or control of the sign of the frequency offset is not possible. In addition, such loop topology imposes phase detection gain, K_{PD} , directly proportional to the product of reference and LO laser field intensities (2). This makes the PLL open loop gain, and hence, bandwidth dependent upon optical intensity, potentially subjecting the loop to instability for varying component parameters or operating conditions.

The microwave mixer downconverts the beat note to $\cos(2\pi(\Delta f - \Delta f_{ext})t + \Delta\theta_0)$. Since the downconverted signal frequency falls within the loop bandwidth range, the loop lock the lasers with Δf_{ext} offset.

In a type II PLL, which has a zero steady-state error in response to a ramp input, the loop filter includes an integrator with a compensating zero, with a loop filter current gain transfer function of $(1 + \tau_1 s)/\tau_2 s$, where τ_1 and τ_2 are integration and zero time constants. Given this filter transfer function, the overall PLL loop transmission is as in (3). A laser operates as a current-controlled oscillator (CCO) whose tuning coefficient is defined as $K_{CCO} = df_L/dI$. As with a voltage-controlled oscillator (VCO), the CCO provides additional integration in the loop transmission.

The loop bandwidth, f_{PLL} , is the frequency for which $\|T(2\pi j f_{PLL})\| = 1$ approximated by (4) and determined by the loop-filter time constants, phase-detection gain, and the laser's current-to-frequency conversion gain

$$T(s) = K_{PD} \frac{K_{CCO}}{s} \frac{1 + \tau_1 s}{\tau_2 s} \quad (3)$$

$$f_{PLL} \approx \frac{\tau_1}{2\pi\tau_2} K_{PD} K_{CCO}. \quad (4)$$

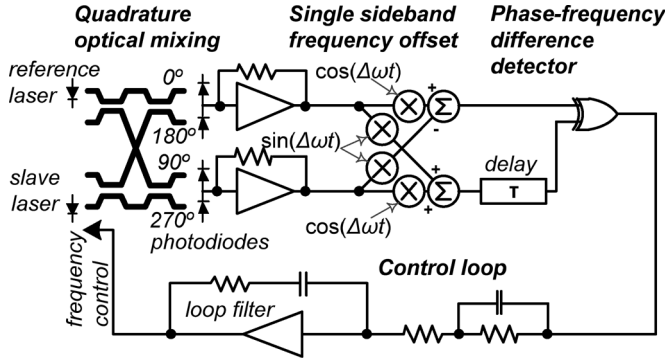


Fig. 2. General diagram of an optical PLL consisting of reference and locked lasers, four-phase optical mixing, offset frequency injection with an SSB mixer, PFD, and loop filter.

To measure the sign of the frequency offset, both the in-phase (I) and quadrature-phase (Q) [(5) and (6)] components of lasers offset beat-note are required. Since a simple optical interferometer provides only the in-phase component, I_{PD} , a 90° optical hybrid [8] should be used

$$I \propto \left| E_R e^{j(2\pi f_R t + \theta_R)} + E_L e^{j(2\pi f_L t + \theta_L)} \right|^2 = |E_R|^2 + |E_L|^2 + 2|E_R||E_L| \cos(\Delta\theta(t)) \quad (5)$$

$$Q \sim \left| E_R e^{j(2\pi f_R t + \theta_R)} + E_L e^{j(2\pi f_L t + \theta_L + \frac{\pi}{2})} \right|^2 = |E_R|^2 + |E_L|^2 + 2|E_R||E_L| \sin(\Delta\theta(t)). \quad (6)$$

A PLL will not by itself acquire lock if the initial reference-slave lasers offset frequency exceeds the required final offset frequency by ~ 2 – 3 times the PLL loop bandwidth f_{PLL} [12]. At $\lambda = 1550$ nm, $\pm 0.02\%$ wavelength detuning corresponds to a ± 39 -GHz offset frequency, much larger than the ~ 1 -GHz f_{PLL} , feasible given typical laser tuning characteristic [11] and minimum delays, achievable by a discrete loop. Hence, in order to obtain initial lock, the lasers should be manually brought into the locking range, and if the lock is lost, it will not be automatically obtained again.

The I/Q signals provided for the offset sign control allow designing a loop with an ability to measure the initial loop frequency detuning using a PFD [13]; the initial lasers detuning can then be as large as that of the available photodetectors and integrated circuit (IC) bandwidths, about ± 100 GHz. The time to acquire frequency lock is set by the loop bandwidth operating in frequency-control mode and its damping factor.

Fig. 2 suggests a block diagram of an analog optical PLL loop with a SSB mixer for offset sign control, and a phase-frequency detection mechanism to extend the frequency locking acquisition range. In this optical PLL, the reference and slave laser are mixed at (0° , 90° , 180° , 270°) phase offsets and detected by photodiodes, producing photocurrents proportional to the cosine (I) and sine (Q) [(5) and (6)] of the optical phase difference. The coupler and photodiodes thus form an I/Q mixer.

To control optical frequency offset spacing, the slave laser must be locked to a controlled positive or negative frequency offset from that of the reference laser. The offset is introduced by shifting the I/Q photodetector signal frequencies using a two-

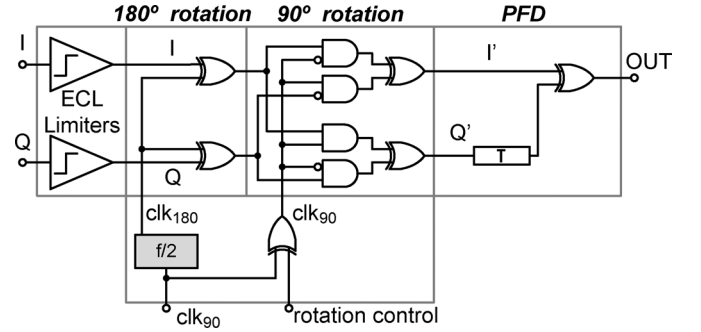


Fig. 3. Digital block diagram of the electrical PLL IC, consisting of input limiter amplifiers, a digital SSB mixer implemented with 180° and 90° rotation blocks, and a PFD.

stage (Weaver) SSB mixer implemented using quadrature optical and microwave mixers. The microwave offset reference LO, provided by a microwave synthesizer, thus controls the optical frequency spacing.

A Quadraticorrelator PFD [14] provides an error signal proportional to the offset frequency [see (7)]. The first term of (7) is responsible for the phase detection, when $\Delta f = 0$, and provides a 180° period characteristic. In case of $\Delta f \neq 0$, the second term of the equation provides a frequency detection indication with detection range set by the τ delay

$$\begin{aligned} I'(t)Q'(t-\tau) &= \cos(2\pi\Delta f t + \Delta\theta_0) \sin(2\pi\Delta f(t-\tau) + \Delta\theta_0) \\ &= 0.5 \sin(4\pi\Delta f t - 2\pi\Delta f\tau + 2\Delta\theta_0) \\ &\quad + 0.5 \sin(2\pi\Delta f\tau). \end{aligned} \quad (7)$$

The analog optical PLL loop will only operate well for I/Q signals within the linear range of the mixers and any amplifiers between them and the photodetectors. Given variable photocurrents, this will require automatic gain control (AGC). Even with such AGC, the phase detection gain, K_{PFD} , will still depend upon the reference and slave lasers optical intensity. It is also difficult to design a wideband SSB mixer using standard analog topologies since these require cosine and sine components of the RF signals [15], and hence, 90° phase shifters. Such phase shifters are generally narrowband. To obtain a wide offset locking frequency range, a digital frequency translation technique was developed.

III. THEORY AND DESIGN

A. Operation Principles

To enable tuning of a frequency offset over a wide ± 1 to ± 20 -GHz bandwidth, and to reduce the dependency on the photocurrents from the PIC, an all-digital SSB mixer is proposed (Fig. 3). The I/Q photocurrents generated by the PIC detectors are converted to digital levels using a chain of limiting amplifiers. Since the mixer and phase/frequency detector are entirely digital, the phase-detector and frequency-detector gains are independent of IC process parameters (transistor and passive element parameter values). In marked contrast, had a linear analog mixer and phase detector been designed, the loop bandwidth would have varied with variations of optical component parameters (hence, photocurrent amplitudes), and mixer and pream-

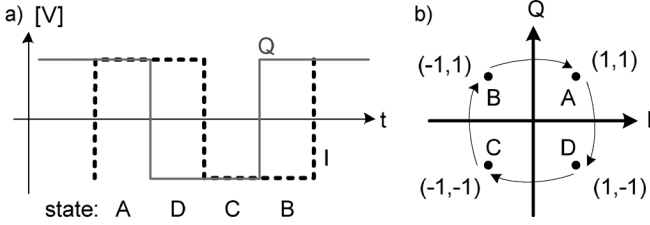


Fig. 4. Digitally limited I/Q signals for optical frequency offset. (a) Time-domain square wave. (b) Rotating constellation in the (I,Q) plane.

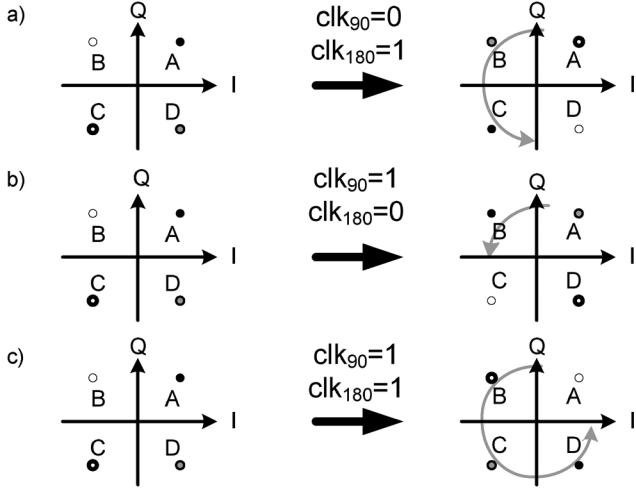


Fig. 5. Digital state rotation. (a) 180° rotation. (b) 90° rotation. (c) 270° rotation.

plier gains. In this circumstance, precise control of the PLL bandwidth would have been difficult to obtain.

Subsequent to digital limiting, frequency shifts are introduced with a digital SSB mixer (Fig. 3). Given a positive laser frequency offset Δf , the I/Q photocurrents rotate counterclockwise through the points (1,1), (−1,1), (−1,−1), (1,−1) in the (I,Q) plane (Fig. 4). For a negative frequency offset, $-\Delta f$, this rotation reverses. For zero frequency offset, the constellation remains static at one of the four points as determined by the relative laser phases.

The digital SSB mixer provides a frequency offset by rotating this constellation in the opposing direction, producing a static output pair (I' , Q'). The mixer is formed of cascaded 180° and 90° rotation blocks. The 180° block rotates the (I,Q) state by 180° (i.e., $A \rightarrow C, B \rightarrow D$, etc.) when its input clock is 1, but provides no rotation when its input clock is 0. The 90° block rotates the (I,Q) state by 90° (i.e., $A \rightarrow B, B \rightarrow C$, etc.) when its input clock is 1, but provides no rotation when its input clock is 0. Applying high clock signals to both blocks rotates the state by 270° (Fig. 5). Applying periodically clock signals f_{clk90} , f_{clk180} at a 2:1 frequency ratio to the 180° and 90° rotation blocks rotates the I'/Q' constellation and provides frequency shifts Δf ; these signals are derived from a static frequency divider [16], (Fig. 3). Inverting the sign of f_{clk90} , by changing the rotation control signal, inverts the rotation direction, and therefore, the sign of the frequency offset.

The PFD is an emitter-coupled logic (ECL) XOR gate with a delay line of 10 ps in the Q arm. This frequency detector

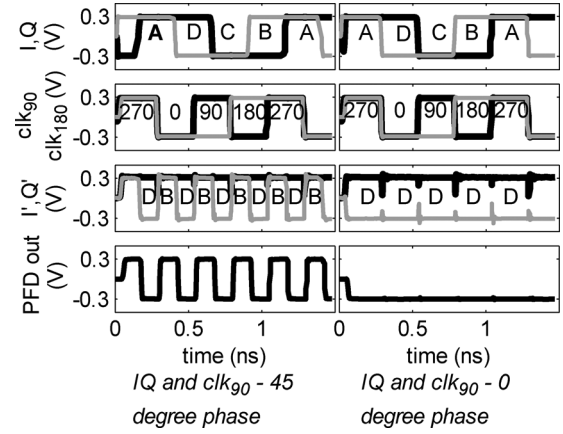


Fig. 6. SSB mixer at phase detection mode. Signal propagation as a function of various I/Q phases relative to clk_{90} . For 45° phase, a 50% duty cycle output signal with zero average dc.

permits automatic loop acquisition for offset frequencies below ± 50 GHz. To force equal transistor delays on both inputs, the gate uses two parallel multipliers with crossed inputs and shunt outputs. The small-signal analysis of the PFD is developed in (7).

In the phase-locked mode, i.e., when the laser offset, Δf , matches the clk_{90} frequency (i.e., $f_{clk90} = 2\Delta f$) under a suitable rotation control sign, the relative phase between the lasers will change the I/Q signals phase relative to clk_{90} and clk_{180} . This will eventually result in the (I' , Q') state oscillating at a frequency $2f_{clk90}$ between two adjacent states (A and B, B and C, etc.) with a duty cycle determined by the phase offset (Fig. 6). In this operation mode, either I' or Q' is constant, while the other signal oscillates between 1 and 0 at a frequency of f_{clk90} with a duty cycle varying linearly with the phase offset. In this mode, the output of the XOR gate is a similar oscillating digital signal. For a 45° (I,Q) phase relative to clk_{90} , the oscillation has 50% duty cycle; hence, the PFD provides zero dc (average) output. This brings the system into lock. Since the PFD output is digital with only its pulse duty cycle varying as a function of loop phase offset, there is no dependence on the photocurrent magnitudes of the circuit's parameters.

In PLL frequency acquisition mode, which occurs when the frequency offset between the reference and the offset laser Δf does not match the clk_{90} frequency (i.e., $f_{clk90} \neq 2\Delta f$), the I' and Q' outputs are quadrature square waves whose frequency is error frequency (Fig. 7). Since the PFD output is formed by forming the XOR product of these signals after introducing a relative delay τ , the PFD output has a dc component varying as $\sin(2\pi\Delta f\tau)$ (7). This dc signal forces the RF and LO lasers into frequency synchronization at the offset frequency f_{clk90} , i.e., forces the loop into lock. The digital frequency-detector gain is independent of all optical or electronic IC parameters, except that of the delay line τ , and hence, is well controlled in the presence of normal optical and IC process parameter variations.

B. High-Frequency Digital Design

The circuit is a complex digital IC operating with digital signals over a dc–40-GHz range. Circuit design and layout required

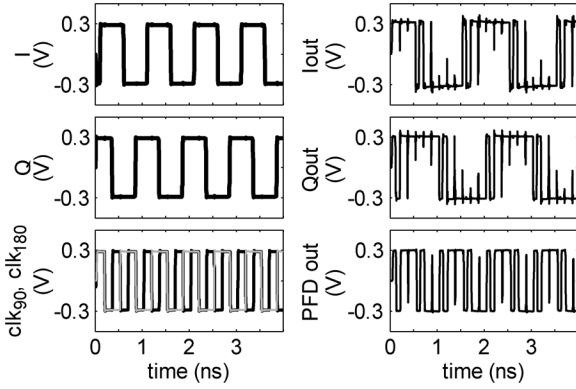


Fig. 7. SSB mixer at frequency locking mode. $\Delta_f = 1$ GHz and $f_{clk90} = 3$ GHz. Since frequency lock occurs only for $\Delta_f = 1.5$ GHz, the (I', Q') state will rotate at the error frequency of 0.5 GHz.

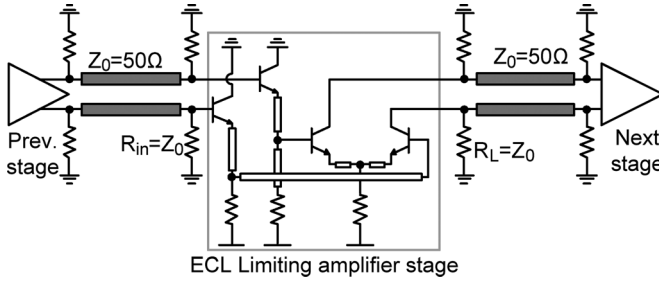


Fig. 8. ECL two-level logic with double terminated line interconnects.

a combination of digital and controlled-impedance millimeter-wave techniques. The limiting amplifiers and buffers were implemented using differential ECL (Fig. 8). To avoid reduced circuit bandwidth from interconnect capacitance, all digital interconnects between the gate were implemented as double-terminated transmission lines (Fig. 8) [17]. This introduces a resistive 25- Ω load to the driving stage. By working in such a 50- Ω environment, the degradation increase in gate delay caused by driving a long line is simply $\tau = l/v$, where l is the length and v is the propagation velocity. In contrast, if the gate were instead loaded with resistance $R_L \gg Z_0$, the additional delay would be $R_L C_{wire} = (l/v)(R_L/Z_0)$ [18].

The ECL emitter followers are placed at gate inputs rather than gate outputs. If emitter followers are instead placed at gate outputs, their inductive output impedance can interact with any load capacitance to cause ringing or instability.

To fully switch a bipolar differential pair with large noise margin, a logic voltage swing of $\Delta V \approx 6 kT/q + 3I_0 R_{ex}$ is selected, where R_{ex} is the emitter access resistance and I_0 is the differential tail current. Based on an equivalent collector load resistor of 25 Ω , the differential pair tail current is $I_0 = 12$ mA. Transistors are sized to operate at current densities approaching the Kirk-effect limit [19].

Boolean logic, such as the 180° and 90° rotation blocks, XOR gate, and frequency divider are implemented in two-level differential ECL logic. To maintain a 50- Ω interconnect environment, these cells were placed along a 50- Ω double-terminated bus (Fig. 9). Interconnects from the gate to the bus present wiring

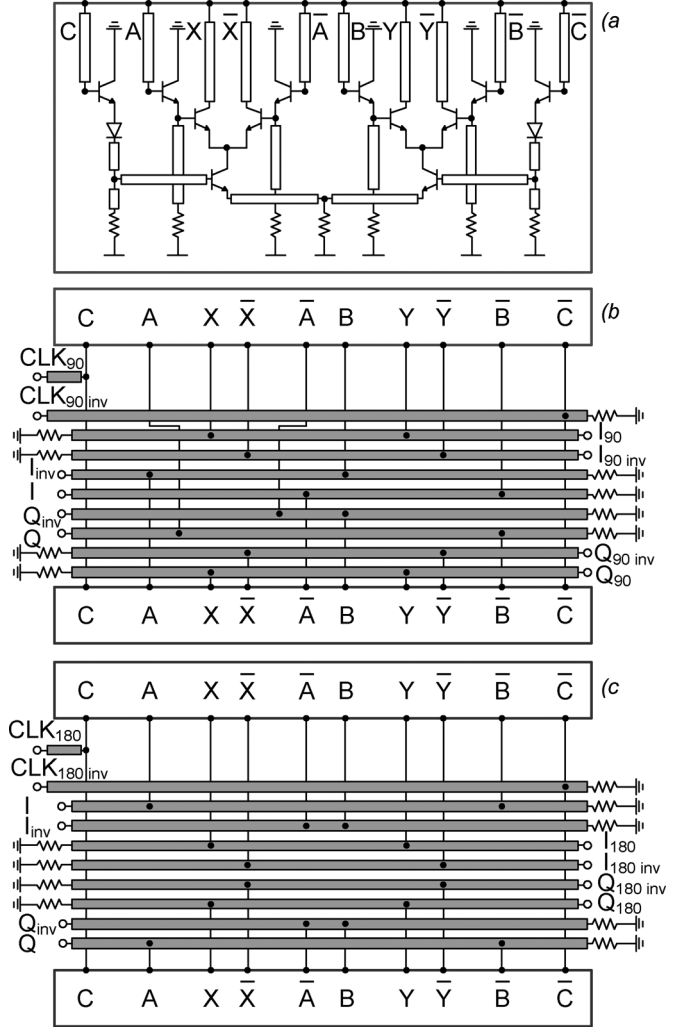


Fig. 9. (a) Gilbert cell as a building block for Boolean logic. (b) 90° rotation. (c) 180° rotation blocks schematics.

parasitics and are kept short. The typical length of such vertical stubs is 30 μm , much shorter than a typical wavelength of 2.5 mm at 40 GHz.

The two-level ECL cells [see Fig. 9(a)] have three inputs: two on the upper level (A,B) and one on the lower level (C). The lower level inputs have longer delay so when balanced delays are required, two parallel gates are used, with interchanged inputs and parallel outputs. Such realization was used with the PFD XOR gate.

High-frequency digital signal distribution (fan-out) was implemented by three techniques (Fig. 10). In the first method [see Fig. 10(a)], the fan-out is implemented by simply splitting the 50- Ω line into two high-impedance 100- Ω lines. The long line is correctly terminated in 50 Ω , while the driving buffer sees a total load of 25 Ω . The RC charging time is $\tau = 2C_L \cdot 25 \Omega$. The second technique [see Fig. 10(b)] uses a pair of 50- Ω lines, driven from a second gate. Each line, in the absence of the next stage capacitive loading, C_L (Fig. 10), is correctly terminated. The RC charging time is $\tau = 2C_L \cdot 25 \Omega$. Since the sending end of the transmission line is not correctly terminated, topologies shown in Fig. 10(a) and (c) suffer from round-trip pulse reflections if the CL is significant. This is eliminated in the

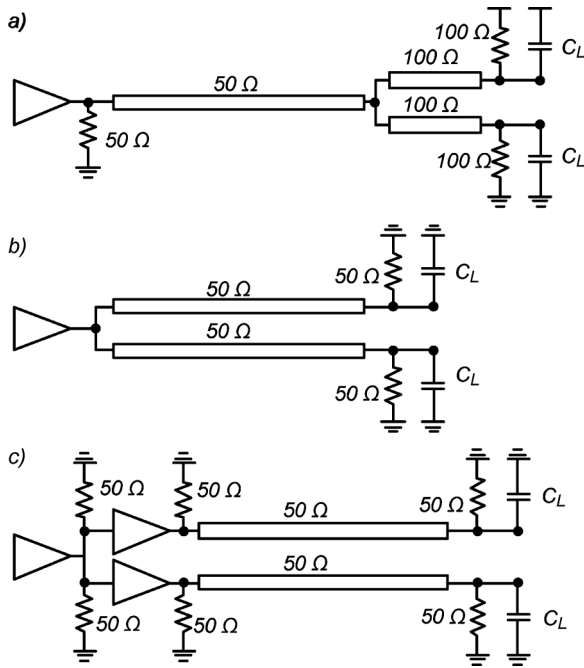


Fig. 10. Digital fan-out techniques. (a) Single-line fan-out. (b) Double-line fan-out. (c) Isolated double-line fan-out.

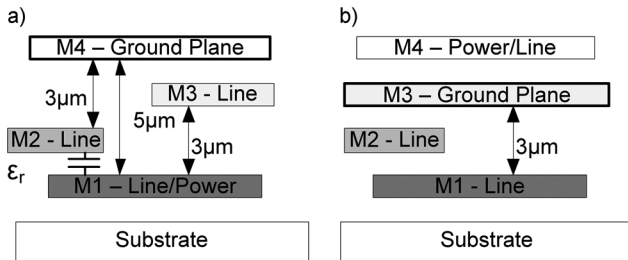


Fig. 11. Metal stack cross section. (a) M4 as a ground plane. (b) M3 as a ground plane.

final topology [see Fig. 10(c)] signals are split 2:1 locally and buffered with gates before distribution on 50-Ω doubly terminated interconnects. In this technique, the reflections are well controlled and the RC charging time is $\tau = C_L \cdot 25 \Omega$. The technique shown in Fig. 10(c) introduces additional power consumption and layout complexity.

The design of a 40-GHz digital logic with a synchronized clock network requires precise electromagnetic (EM) modeling and verification, obtained by the Agilent Momentum computer-aided design (CAD) tool. The top metal (M4) was assigned as a ground plane, while the majority of interconnects were implemented on M1 and M2 in a form of inverted thin-film microstrip lines [see Fig. 11(a)]. M3 was primarily used for local routing solutions and local interconnects within gates. The use of inverted microstrip allows narrow line spacing (approximately two times the line-to-ground distance: 8–10 μm), and continuous ground plane without breaks, maintaining ground integrity and avoiding ground bounce. The use of a bottom ground plane within a complex IC environment would eventually lead to a highly fragmented ground (Fig. 12), unable to provide parasitics free current return paths. Due to the thin dielectric, the top ground plane makes the ground via inductance negligible and

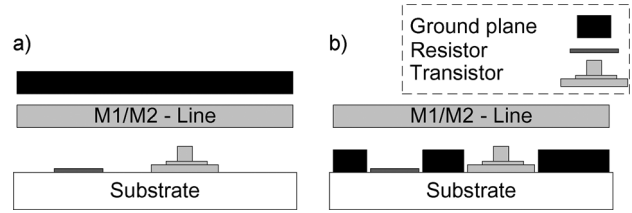


Fig. 12. (a) Top ground-plane versus (b) bottom ground-plane layout.

allows dense ground vias spacing, as requires in a complex IC. The drawbacks, however, of the thin dielectrics is the reduced line inductance, demanding thinner lines for high characteristics impedances. Thin lines also demonstrate increased skin loss and limit the maximum possible dc current [20].

Compared to M1, the dielectric thickness between M2 and the ground plane is smaller, creating difficulty in implementing high-impedance lines and leading to increased resistive losses. The power grid was routed on M1, crossing M1 lines with M3 bridges, and M2 from beneath. The crossovers of M1–M2 lines and M2—power lines introduce additional capacitance of $C_{cross} \approx 2$ fF for typical $5 \times 8 \mu\text{m}^2$ overlaps [see Fig. 11(a)]. This capacitance creates signal crosstalk.

The other possible wiring strategy is to assign M3 as a ground plane [see Fig. 11(b)] and to use M4 mainly as a power grid or for sensitive lines requiring complete crosstalk isolation. This approach completely eliminates the parasitic capacitance formed between the power and signal lines and greatly simplifies the design by separating the routing of power grids from signal lines. However, this methodology also has limitations. Due to a thinner dielectric, M2 lines are made narrower (3-μm wide for 50-Ω impedance), presenting even higher losses and unsuitable for long connections. Even with M1, the implementation of high-impedance lines becomes impossible. To provide a power path to active devices, M3 needs to be perforated to allow vias to pass through, consequently violating the unity of the ground plane. However, the impact of these openings on M3 can be neglected if they are local and small in size. Eventually, both of the M3 and M4 ground-plane approaches allow a full EM simulation to be performed on the entire interconnects, rather than separately modeling individual segments.

All of the in-cell and external transmission lines were individually EM modeled. Fig. 9(a) shows the in-cell lines, which are not terminated due to their lumped behavior ($\sim 30 \mu\text{m}$). However, both of them introduce capacitive and inductive parasitic loading with a delay and these effects must be taken into account for a precise simulation of the entire system.

The clock distribution network (Fig. 13) is the most critical part in terms of speed and timing precision. After the microwave offset reference has been split into 180° and 90° clocks, it must arrive in a synchronized fashion to both of the 180° and 90° rotation blocks. Each clock signal and its corresponding complementary must arrive simultaneously to all of the four ports at each rotation block (Fig. 13). In addition, clk_{90} must be delayed behind clk_{180} exactly the amount of time takes for the I/Q signal to pass the 180° rotation block and reach the 90° rotation block. This ensures synchronized operation of both of the rotation blocks on the same I/Q state. The delay was tuned

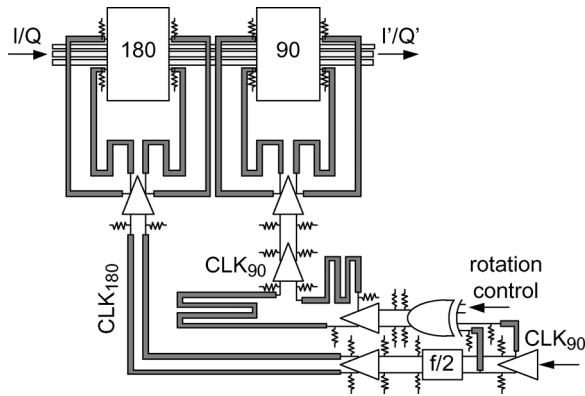


Fig. 13. Clock distribution diagram.

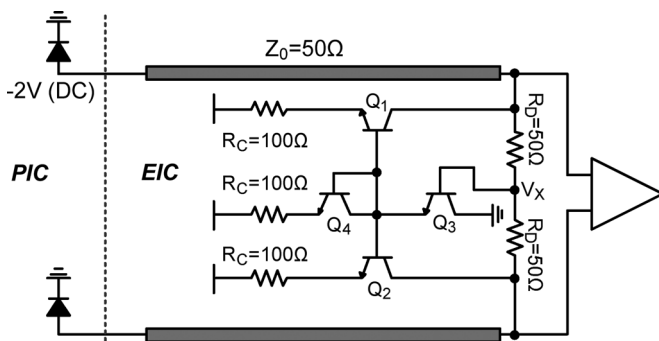


Fig. 14. Input biasing circuit.

by adjusting the line lengths as well as using buffer stacking. The clock network was implemented on M2, while the signal lines are mainly on M1. To maintain a symmetrical wiring structure and minimize the crossovers, the methodology shown in Fig. 10(b) was used for the final clock splitting. The IC demonstrates a total delay of 100 ps, reducing the limitation on wide-band loops design. Delays achieved by hybrid mixers and phase detectors are typically longer [1].

The input differential limiting amplifiers are designed to operate with unbalanced photodiodes PIC [11]; hence, a new biasing topology was proposed (Fig. 14). The dc current provided by the photodiodes is drawn by Q_1 and Q_2 , biasing the photodiodes at $V_X \approx -V_{EE} + 2V_{BE} \approx -2$ V, a dc voltage, enabling direct PIC–EIC connection without the use of dc blocks. In the differential operation mode, the node V_X becomes a virtual ground, providing a differential input impedance of $R_D = 50 \Omega$. A common mode signal will alter the V_X voltage, activating the $Q_3 - Q_{1,2}$ negative feedback loop, which results in the common mode current drawn by $Q_{1,2}$. Small-signal analysis shows a common mode input impedance of $R_C/2$. This way the common and the differential input impedances can be controlled separately.

IV. INDIUM–PHOSPHIDE (InP) HBT TECHNOLOGY

The IC presented in this study was implemented using InP HBT 0.5- μm emitter width technology [21], [22] with cutoff frequencies $f_t = 300$ GHz and $f_{\text{max}} = 300$ GHz.

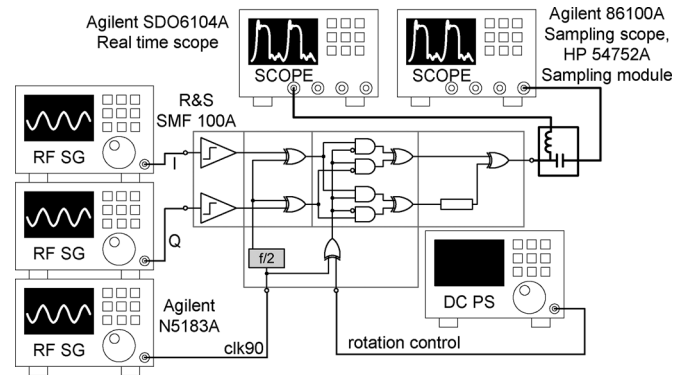


Fig. 15. SSB mixer measurement setup.

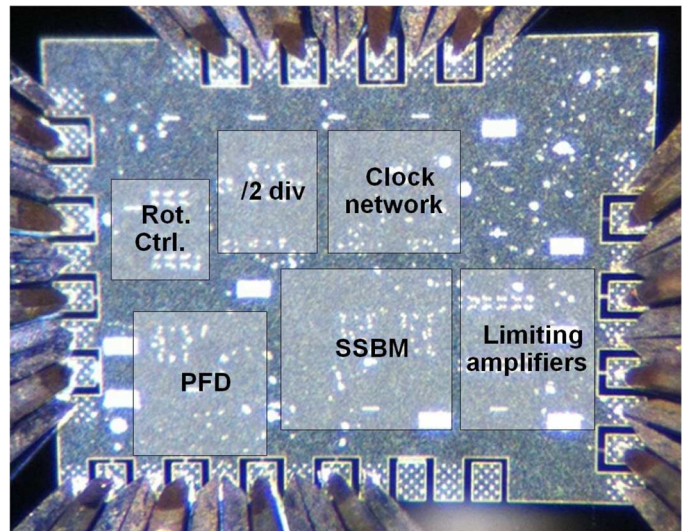


Fig. 16. IC chip image.

A four-metal interconnect stack was used with metal–insulator–metal (MIM) capacitors of $0.3 \text{ fF}/\mu\text{m}^2$ implemented between the first and the second metal layers. Signal lines were implemented using metal 1 and metal 2 as inversed microstrips with metal 4 serving as a ground plane. The resistors were implemented by a $50\text{-}\Omega/\text{sq}$ thin-film deposition.

V. MEASUREMENT AND CHARACTERIZATION

The integrated SSB mixer chip was measured for phase and frequency detection. To separate the output's average component from the time-varying component, a bias-tee was used (Fig. 15). The average component was inspected using an Agilent SDO6104A real-time oscilloscope with a sampling rate of 4 GSa/s, while the time-varying component was inspected using an Agilent 86100A sampling oscilloscope with a 50-GHz HP 54752A sampling module. The optical I/Q signals were emulated by two R&S SMF 100A synchronized microwave synthesizers and the clk_{90} signal was supplied by a third, an Agilent N5183A synthesizer. The input power was set to -4 dBm for both the I/Q input and clk_{90} . Signals were delivered on-wafer using microwave wafer probes. The IC was biased by a negative power supply of -3.8 V and the overall dc power was 5.3 W. The IC photograph is shown in Fig. 16 and the total area is 1.8 mm^2 .

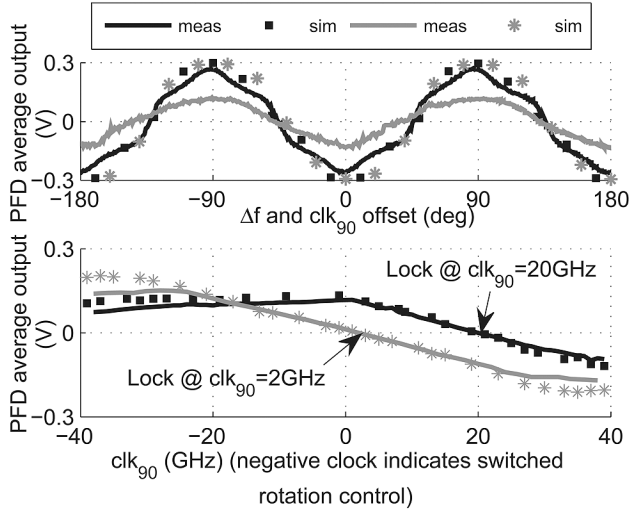


Fig. 17. PFD phase, frequency detection measurements. (*top*) Phase detection characteristic, measurement versus simulation for $\Delta f = 20$ GHz, $f_{\text{clk}90} = 40$ GHz (grey) and for $\Delta f = 15$ GHz, $f_{\text{clk}90} = 30$ GHz (black). (*bottom*) Frequency detection characteristic, measurement versus simulation for $\Delta f = 10$ GHz (black) and $\Delta f = 1$ GHz (grey).

The experimental and simulation results are shown in Fig. 17. In Fig. 17 (*top*), the PFD output is plotted as a function of phase difference with the emulated I/Q photocurrent signals set at 15 (20) GHz and with $f_{\text{clk}90}$ set at 30 (40) GHz, i.e., with the system operating in phase-detection mode. The phase error signal varies ± 300 mV at 15-GHz offset and ± 120 mV at 20-GHz offset as the phase is varied through 360° . This indicates proper operation of the phase detector for frequency offsets as large as ± 20 GHz. The phase detection characteristic demonstrates periodicity of 180° , forming two stable points for the loop to lock; a property enables the system to lock on a binary phase-shift keying (BPSK) modulated signal, thus potentially turning the system into a WDM selectable channel receiver. A phase-detection characteristic forms a triangle wave with K_{PD} independent on inputs photocurrents. Such phase-detection behavior results from a phase error measure between the I/Q signal and the offset signal rather than the actual phase between the two lasers; a phase error changing the SSB mixer output duty cycle only.

In Fig. 17 (*bottom*), the PFD output is measured at laser offset frequencies of $\Delta f = 1$ and 10 GHz, by adjusting the SSB mixer LO frequency $f_{\text{clk}90}$. This measured the PFD characteristic in the frequency detection mode. The frequency detection characteristic shows frequency error detection over a ± 40 -GHz range, with zero frequency detector output when, as designed, the laser offset frequency is equal to $f_{\text{clk}90}/2$.

The PFD output time waveforms in phase detection mode, as a function of phase offset, for $\Delta f = 2$ GHz and $f_{\text{clk}90} = 4$ GHz are presented in Fig. 18. The output waveform duty cycle varies in a linear fashion as a function of phase offset, forming a triangle characteristic shown in Fig. 17. The ± 20 -GHz offset limit for phase detection operation might be explained by the quadrupled frequency beat note, produced at the output of the PFD at a phase detection mode (Fig. 18), pushing the gates to their speed limit (i.e., 80 GHz).

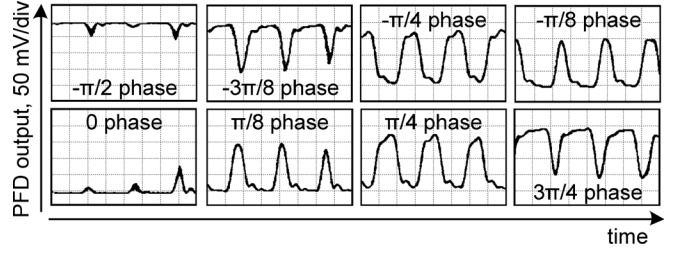


Fig. 18. PFD OUT measured waveforms in phase detection mode for $\Delta f = 2$ GHz and $f_{\text{clk}90} = 4$ GHz.

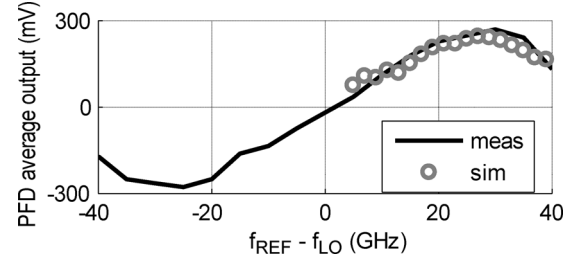


Fig. 19. PFD standalone frequency detection response, measurements versus simulation.

Standalone PFD measurements in frequency detection mode were also performed for ± 40 -GHz offset I/Q inputs. Fig. 19 demonstrates the measured triangular wave behavior with a ± 50 -GHz period when extrapolated. The ± 50 -GHz period is achieved by the 10-ps delay line $\sin(2\pi\Delta f\tau)$ [see (7)]. Modifying the delay line length will result in a tradeoff between the K_{FD} magnitude in the linear mode and the frequency acquisition range. The K_{FD} value and the triangular wave behavior are similar to Fig. 17 (*bottom*), only that the zero crossing point is shifted to the origin as expected for a PFD standalone.

The next 250-nm InP HBT technology node allows design of frequency dividers up to 204 GHz [16] and faster digital logic [18], [23], [24]. In complex ICs, however, the maximum clock rate might also be limited by fan-in, fan-out, gates delay or complex interconnects. By implementing the SSB mixer using the suggested technology it is possible to achieve clock rates of around 80–100 GHz for 40–50-GHz offset locking to meet the modern WDM standards.

A combined phase-frequency characteristic was also numerically generated using a behavioral model with $f_{\text{clk}90} = -10$ GHz (the negative sign denotes a rotation control bit “zero” value) (Fig. 20). The linear frequency detection characteristic crosses zero at $\Delta f = -5$ GHz, where the frequency locking occurs. At this point, the loop switches to a phase detection mode characterized by a triangle function. Yet the plot suggests another phase detection mode for $\Delta f = +5$ GHz as well. This parasitic phenomenon occurs due to the digital (versus linear) nature of the mixer; however, since the frequency detection curve does not cross zero at this offset frequency, a lock cannot occur, as was also shown experimentally [11].

As in the phase-lock state, the IC output produces an output beat note with $f_{\text{clk}90}$ frequency (Fig. 6), any attempts to perform lock on frequency offsets lower than the loop bandwidth

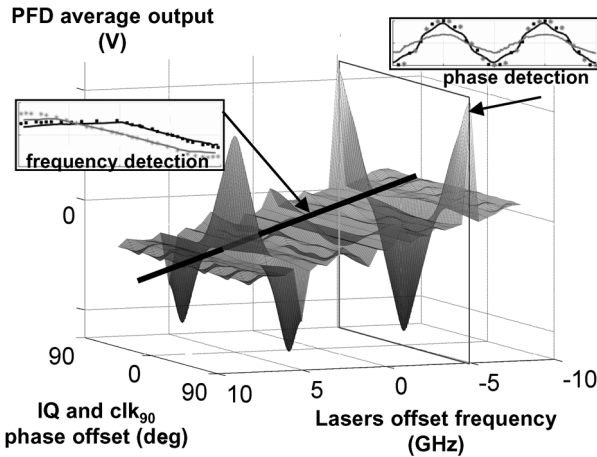


Fig. 20. Numerical PFD simulation for simultaneous phase–frequency detection modes. The offset clock, f_{clk90} , was set to -10 GHz while the laser offset was swept over various phases and frequencies.

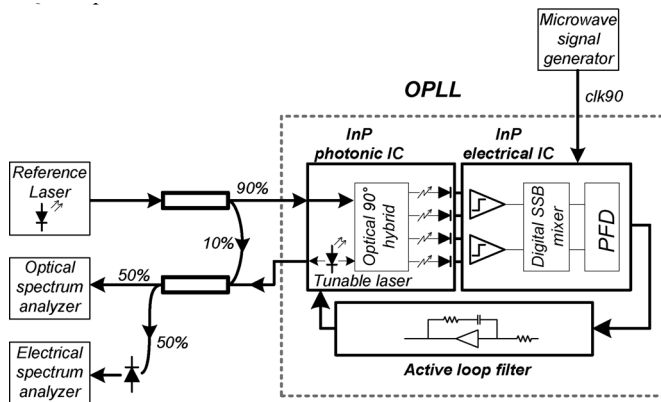


Fig. 21. Simplified offset locking experiment setup (Lu *et al.* [11]).

(f_{PLL}) will bring the loop to track the output beat note, driving the system into a direct laser modulation rather than locking. This behavior imposes a limitation on the lower limit of the frequency offsets range to be $\sim 2f_{PLL}$.

VI. SYSTEM EXPERIMENT

A system experiment comprising the reported SSB mixer IC was carried out by Lu *et al.* and was reported in [11].

The optical PLL was integrated on a 10×10 mm AlN carrier substrate. The system (Fig. 21) includes an InP photonic IC [8], the SSB mixer/phase–frequency detector IC described in this paper and an external 500-MHz loop bandwidth, feed-forward-compensated op-amp loop filter [10]. The photonic IC contains a tunable SG-DBR laser, an optical 90° hybrid, and four photodiodes for delivering a differential I/Q components of the lasers beat note.

The reference laser was provided to the photonic IC by an Agilent 8164B Lightwave Measurement System featuring a 100-kHz linewidth, while the offset frequency, clk_{90} , was set by an Agilent E8257D microwave signal generator. The local SG-DBR laser was coupled out and externally mixed with the reference laser for monitoring purposes. The linewidth of

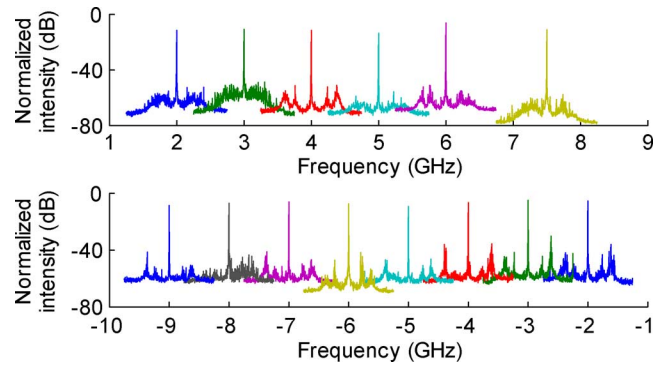


Fig. 22. Electrical spectrum analyzer image of the two lasers beat note when phase locked with various frequency offsets (Lu *et al.* [11]).

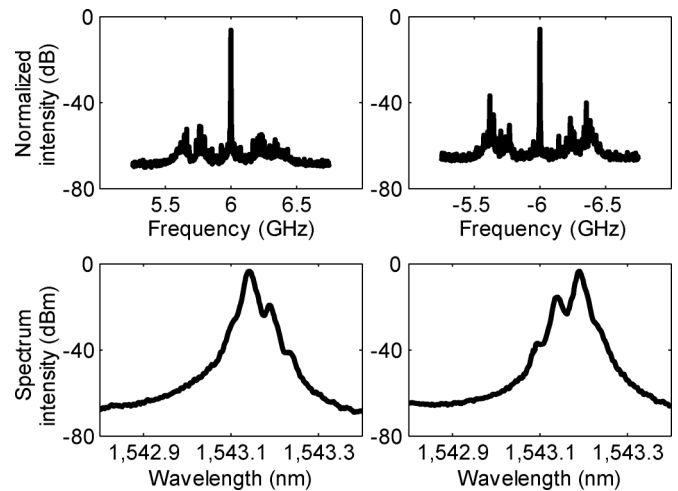


Fig. 23. (left) Beat note spectrum of two lasers (top) and optical spectrum (bottom) when phase locked with $+6$ -GHz offset. (right) Beat note spectrum of two lasers (top) and optical spectrum (bottom) when phase locked with -6 -GHz offset. The reference laser has the higher power. Measured with 5-kHz resolution bandwidth (Lu *et al.* [11]).

an unlocked SG-DBR laser was above 100 MHz. The overall optical spectrum was inspected by an HP 70004A optical spectrum analyzer to verify a SSB locking nature, while the locked laser linewidth was measured by inspecting the mixed beat note using the R&S FSU spectrum analyzer.

The integrated SG-DBR laser was successfully phase locked to the reference with offsets ranging from -9 to $+7.5$ GHz (Fig. 22). The offset locking sign was set by applying proper rotation control signal and the system kept locked while the RF offset frequency (clk_{90}) was gradually swept both in the negative and positive ranges. To confirm the SSB fashion of locking, the optical spectrum was measured to compare the reference and the local laser wavelengths (Fig. 23). It was impossible to lock with frequency offsets as low as the loop bandwidth since the low-frequency beat note provided by the PFD cannot be integrated.

The phase noise of the optical PLL includes contributions from the RF source, the EIC, and the optical system (laser open loop noise divided by the loop transmission). Additional study on a full system characterization and phase-noise performance is currently carried out.

VII. CONCLUSION

We have demonstrated a novel broadband ± 20 -GHz optical frequency synthesis IC in $0.5\text{-}\mu\text{m}$ InP HBT technology. The all-digital mixer topology eliminates the dependency on input photocurrent, increases the offset locking range, and improves the design robustness by shifting to a digital domain. The IC is comprised of a SSB mixer and a Quadratorrelator PFD with frequency acquisition range up to ± 40 GHz. A full integration of the mixer with the PFD drastically reduces the limitation on loop delay, making larger loop bandwidths possible.

ACKNOWLEDGMENT

The authors would like to thank Teledyne Scientific and Imaging, Thousand Oaks, CA, for MMIC fabrication.

REFERENCES

- [1] R. J. Steed, L. Ponnampalam, M. J. Fice, C. C. Renaud, D. C. Rogers, D. G. Moodie, G. D. Maxwell, I. F. Lealman, M. J. Robertson, L. Pavlovic, L. Naglic, M. Vidmar, and A. J. Seeds, "Hybrid integrated optical phase-lock loops for photonic terahertz sources," *IEEE J. Sel. Top. Quantum Electron.*, vol. 17, no. 1, pp. 210–217, Jan.–Feb. 2011.
- [2] R. J. Steed, F. Pozzi, M. J. Fice, C. C. Renaud, D. C. Rogers, I. F. Lealman, D. G. Moodie, P. J. Cannard, C. Lynch, L. Johnston, M. J. Robertson, R. Cronin, L. Pavlovic, L. Naglic, M. Vidmar, and A. J. Seeds, "Monolithically integrated heterodyne optical phase-lock loop with RF XOR phase detector," *Opt. Exp.*, vol. 19, Sep. 2011, Art. ID 20048.
- [3] M. Grant, W. Michie, and M. Fletcher, "The performance of optical phase-locked loops in the presence of nonnegligible loop propagation delay," *J. Lightw. Technol.*, vol. JLT-5, no. 4, pp. 592–597, Apr. 1987.
- [4] U. Gliese, T. N. Nielsen, M. Bruun, E. Lintz Christensen, K. E. Stubkjaer, S. Lindgren, and B. Broberg, "A wideband heterodyne optical phase-locked loop for generation of 3–18 GHz microwave carriers," *IEEE Photon. Technol. Lett.*, vol. 4, no. 8, pp. 936–938, Aug. 1992.
- [5] L. N. Langley, M. D. Elkin, C. Edge, M. J. Wale, U. Gliese, X. Huang, and A. J. Seeds, "Packaged semiconductor laser optical phase-locked loop (OPLL) for photonic generation, processing and transmission of microwave signals," *IEEE Trans. Microw. Theory Techn.*, vol. 47, no. 7, pp. 1257–1264, Jul. 1999.
- [6] S. Ristic, A. Bhardwaj, M. J. Rodwell, L. A. Coldren, and L. A. Johansson, "An optical phase-locked loop photonic integrated circuit," *J. Lightw. Technol.*, vol. 28, no. 4, pp. 526–538, Feb. 2010.
- [7] Z. F. Fan, P. J. S. Heim, and M. Dagenais, "Highly coherent RF signal generation by heterodyne optical phase locking of external cavity semiconductor lasers," *IEEE Photon. Technol. Lett.*, vol. 10, no. 5, pp. 719–721, May 1998.
- [8] M. Lu, A. Bhardwaj, A. Sivananthan, L. A. Johansson, H. Park, E. Bloch, M. J. Rodwell, and L. A. Coldren, "A widely-tunable integrated coherent optical receiver using a phase-locked loop," in *IEEE Photon. Conf.*, 2011, pp. 769–770.
- [9] E. Bloch, H. Park, M. Lu, T. Reed, Z. Griffith, L. A. Johansson, L. A. Coldren, D. Ritter, and M. J. Rodwell, "A 1–20 GHz InP HBT phase-lock-loop IC for optical wavelength synthesis," in *IEEE MTT-S Int. Microw. Symp. Dig.*, 2012, pp. 1–3.
- [10] H. Park, M. Lu, E. Bloch, T. Reed, Z. Griffith, L. Johansson, L. Coldren, and M. Rodwell, "40 Gbit/s coherent optical receiver using a costas loop," in *Eur. Opt. Commun. Conf.*, Amsterdam, The Netherlands, 2012, Paper Th.3.A.2.
- [11] M. Lu, H. Park, E. Bloch, A. Sivananthan, A. Bhardwaj, Z. Griffith, L. A. Johansson, M. J. Rodwell, and L. A. Coldren, "Highly integrated optical heterodyne phase-locked loop with phase/frequency detection," *Opt. Exp.*, vol. 20, pp. 9736–9741, Apr. 2012.
- [12] B. Razavi, *Monolithic Phase-Locked Loops and Clock Recovery Circuits: Theory and Design*. Piscataway, NJ: IEEE Press, 1996.
- [13] F. M. Gardner, *Phaselock Techniques*. New York: Wiley, 1979.
- [14] F. Gardner, "Properties of frequency difference detectors," *IEEE Trans. Commun.*, vol. COM-33, no. 2, pp. 131–138, Feb. 1985.
- [15] D. K. Weaver, "A third method of generation and detection of single-sideband signals," *Proc. IRE*, vol. 44, no. 12, pp. 1703–1705, Dec. 1956.
- [16] Z. Griffith, M. Urteaga, R. Pierson, P. Rowell, M. Rodwell, and B. Brar, "A 204.8 GHz static divide-by-8 frequency divider in 250 nm InP HBT," in *IEEE Compound Semicond. Integr. Circuit Symp.*, 2010, pp. 1–4.
- [17] Y. Betser, S. Jaganathan, T. Mathew, Q. Lee, J. Guthrie, D. Mensa, and M. J. W. Rodwell, "Low voltage swing techniques for 100 GHz logic," in *Int. Infrared Millim. Waves Conf.*, Monterey, CA, 1999.
- [18] Z. Griffith, Y. Dong, D. Scott, Y. Wei, N. Parthasarathy, M. Dahlstrom, C. Kadow, V. Paidi, M. J. W. Rodwell, M. Urteaga, R. Pierson, P. Rowell, B. Brar, S. Lee, N. X. Nguyen, and C. Nguyen, "Transistor and circuit design for 100–200-GHz ICs," *IEEE J. Solid-State Circuits*, vol. 40, no. 10, pp. 2061–2069, Oct. 2005.
- [19] M. Urteaga, S. Krishnan, D. Scott, Y. Wei, M. Dahlstrom, S. Lee, and M. J. W. Rodwell, "Submicron InP-based HBTs for ultrahigh frequency amplifiers," *Int. J. High Speed Electron. Syst.*, vol. 13, pp. 457–495, 2003.
- [20] M. J. W. Rodwell, S. Krishnan, M. Urteaga, Z. Griffith, M. Dahlstrom, Y. Wei, D. Scott, N. Parthasarathy, Y. Kim, and S. Lee, "Interconnects in 50–100 GHz integrated circuits," in *Int. Union Radio Sci.*, Maastricht, The Netherlands, 2002.
- [21] M. Urteaga, R. Pierson, P. Rowell, M. Choe, D. Mensa, and B. Brar, "Advanced InP DHB T process for high speed LSI circuits," in *20th Int. Indium Phosphide and Rel. Mater. Conf.*, 2008, pp. 1–5.
- [22] M. Rodwell, E. Lind, Z. Griffith, A. M. Crook, S. R. Bank, U. Singiseti, M. Wistey, G. Burek, and A. C. Gossard, "On the feasibility of few-THz bipolar transistors," in *IEEE Bipolar/BiCMOS Circuits Technol. Meeting*, 2007, pp. 17–21.
- [23] Z. Griffith, M. Dahlstrom, M. J. W. Rodwell, X.-F. Fang, D. Lubyshchev, Y. Wu, J. M. Fastenau, and W. K. Liu, "InGaAs-InP DHB Ts for increased digital IC bandwidth having a 391-GHz $f\tau$ and 505-GHz f_{max} ," *IEEE Electron Device Lett.*, vol. 26, no. 1, pp. 11–13, Jan. 2005.
- [24] M. Rodwell, Z. Griffith, V. Paidi, N. Parthasarathy, C. Sheldon, U. Singiseti, M. Urteaga, R. Pierson, P. Rowell, and B. Brar, "InP HBT digital ICs and MMICs in the 140–220 GHz band," in *Joint 30th Int. Infrared Millim. Waves Conf. and 13th Int. Terahertz Electron. Conf.*, 2005, vol. 2, pp. 620–621.



Eli Bloch received the B.Sc. and M.Sc. degrees in electrical engineering from the Technion–Israel Institute of Technology (IIT), Haifa, Israel, in 2006 and 2010, respectively, and is currently working toward the Ph.D degree in electrical engineering at the Technion–IIT.

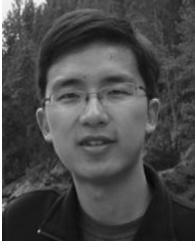
From 2005 to 2007 he was with the Research and Development Laboratories, IBM, Haifa, Israel, where he was involved with analog and mixed-signal circuit design. His current research focuses on millimeter-wave and mixed-signal ICs,

based on InP/GaInAs HBTs, for optical coherent communication and optical phase locking.



Hyunchul Park received the B.S. and the M.S. degrees in electrical and computer engineering from Sungkyunkwan University, Suwon, Korea, in 2006 and 2008, respectively, and is currently working toward the Ph.D. degree in electrical and computer engineering at the University of California at Santa Barbara.

His past research interests include high-efficiency and power-amplifier designs. He is currently focused on high-speed IC designs for optical links and microwave/millimeter-wave communication systems.



Mingzhi Lu received the B.S. degree in electrical engineering from Southeast University, Nanjing, China, in 2008, and is currently working toward the Ph.D. degree in electrical engineering at the University of California at Santa Barbara.

His past research experience includes microwave and terahertz frequency-selective surfaces (FSSs) and metamaterials. He is currently focused on InGaAsP/InP-based photonic integrated coherent receivers and the optical PLL.



Thomas Reed (M'08) received the B.S. degree in electrical engineering from Brigham Young University, Provo, UT, in 2008, the M.S. degree in electrical engineering degree from the University of California at Santa Barbara (UCSB), in 2009, and is currently working toward the Ph.D. degree in electrical engineering at UCSB.

Since 2008, he has been a member of the High Frequency Electronics Group, UCSB. His research focuses on solid-state power amplifier and RF IC design using nanoscale HBT technologies at millimeter-wave and sub-millimeter-wave frequencies.



Zach Griffith received the Ph.D. degree in electrical engineering from the University of California at Santa Barbara, in 2005. His doctoral research concerned the development of record bandwidth InP HBTs.

Since joining Teledyne Scientific and Imaging, Thousand Oaks, CA, in 2008, his efforts are focused on designing millimeter-wave op-amps for highly linear (>55 dBm OIP3), low-gigahertz amplification with low Pdc, as well as high millimeter-wave, sub-millimeter-wave power amplifiers. He has authored or coauthored over 75 publications across these fields.



Leif A. Johansson (M'04) received the Ph.D. degree in engineering from University College London, London, U.K., in 2002.

He is currently a Research Scientist with the University of California at Santa Barbara. His current research interests include design and characterization of integrated photonic devices for analog and digital applications and analog photonic systems and sub-systems.



Larry A. Coldren (S'67–M'72–SM'77–F'82–LF'12) received the Ph.D. degree in electrical engineering from Stanford University, Stanford, CA.

He is currently the Fred Kavli Professor of Optoelectronics and Sensors with the University of California at Santa Barbara (UCSB). He spent 13 years in research with Bell Laboratories prior to joining UCSB, in 1984, where he holds appointments in electrical and computer engineering and materials. He cofounded Optical Concepts (acquired as Gore Photonics), to develop novel vertical-cavity surface-emitting laser (VCSEL) technology, and later Agility Communications (acquired by JDSU), to develop widely tunable integrated transmitters. With Bell Laboratories, he was involved with surface acoustic wave (SAW) filters and tunable coupled-cavity lasers using novel reactive ion etching (RIE) technology. With UCSB, he has continued his involvement on multiple-section lasers, in 1988 inventing the widely tunable multielement mirror concept that is now used in numerous commercial products. He has also made seminal contributions to efficient VCSEL designs. His group continues efforts on high-performance InP-based PICs and high-speed VCSELs. He has authored or coauthored over 1000 journal and conference papers, a number of book chapters, and a textbook. He holds 64 patents.

Dr. coldren is a Fellow of Optical Society of America (OSA) and the Institution of Electrical Engineers (IEE). He is a member of the National Academy of Engineering. He was a recipient of the 2004 John Tyndall Award and 2009 Aron Kressel Award.



Dan Ritter received the B.Sc., M.Sc., and Ph.D. degrees in electrical engineering from the Technion–Israel Institute of Technology (IIT), Haifa, Israel, in 1979, 1982, and 1988, respectively.

From 1988 to 1992, he performed postdoctoral research with AT&T Bell Laboratories, Murray Hill, NJ. In 1992, he joined the Department of Electrical Engineering, Technion–IIT, where he is currently a Professor. His fields of research are semiconductor epitaxial crystal growth, compound semiconductor devices, and high-speed circuits.



Mark Rodwell (M'89–SM'99–F'03) received the Ph.D. degree from Stanford University, Stanford, CA, in 1988.

He holds the Doluca Family Endowed Chair in Electrical and Computer Engineering with the University of California at Santa Barbara (UCSB). He directs the UCSB node of the National Science Foundation (NSF) Nanofabrication Infrastructure Network (NNIN), and the SRC Nonclassical CMOS Research Center. His research group works to extend the operation of ICs to the highest feasible

frequencies.

Prof. Rodwell was the recipient of the 2010 IEEE Sarnoff Award and the 2009 IEEE IPRM Conference Award for the development of InP-based bipolar IC technology, at both device and circuit design level, for millimeter-wave and sub-millimeter-wave applications. His group's work on GaAs Schottky-diode ICs for subpicosecond/millimeter-wave instrumentation was awarded the 1997 IEEE Microwave Prize and the 1998 European Microwave Conference Microwave Prize.

New Opportunities for Optical Phase-locked Loops in Coherent Photonics

Larry A. Coldren^{1,3}, Mingzhi Lu¹, Hyun-chul Park¹, Eli Bloch², John Parker¹, Leif A. Johansson¹, and Mark J. Rodwell¹

¹Department of Electrical and Computer Engineering, University of California, Santa Barbara, CA, 93106, USA.

²Department of Electrical Engineering, Technion – Israel Institute of Technology, Haifa 32000, Israel.

³Department of Materials, University of California, Santa Barbara, CA, 93106, USA.
coldren@ece.ucsb.edu

Abstract: New efforts demonstrate that integrated optical phase-locked loops can provide stable and robust phase locking. Coherent receivers now use DSP processing for long haul communications. However, given a low-cost, low-power coherent receiver, uses in shorter links become viable, and other approaches for removing impairments can be explored.

OCIS codes: (250.5300) Photonic integrated circuits; (060.1660) Coherent communications; (060.2840) Heterodyne; Optical phase-locked loop.

1. Introduction

As fiber optic communication developed through the 1970s and into the early 1980s, link distances increased to tens of kilometers and single-channel bandwidths toward the Gb/s range, as single-mode fiber and 1300 nm wavelength InGaAsP/InP-based materials became the norm for such ‘long-distance, ‘high-capacity’ communication. To increase capacity, a few wavelengths could be multiplexed onto a single fiber, although this was not very common. Every 30 km or so, these directly-modulated channels had to be (demuxed if WDM), received by a photodetector-preamp, 3-R regenerated in the electrical domain, and remodulated back onto a lightwave, (and muxed if WDM) for further optical transmission. The switch to 1550 nm aided the loss budget by almost a factor of two, but dispersion was added and now had to be dealt with by using well-engineered external modulation.

To improve the reach between such repeaters, coherent receivers, which could vastly improve the sensitivity, and thus the repeater spacing, were intensively explored throughout the 1980s [1-8]. With the highest sensitivity, homodyne phase-shift-keying (PSK) receivers were well studied, and several prototypes were demonstrated with very high sensitivity [1,3-5,7,8]. However, theoretical studies showed that because of the shot noise limit and the limited optical phase-locked loop (OPLL) bandwidth, these homodyne PSK receivers had a high requirement on the LO laser linewidth [3,6,9]. Moreover, the limited loop bandwidth also placed a stringent requirement on system stability [5]. Any small temperature change of the LO laser or other environment fluctuations may cause the OPLL to lose lock. Therefore, there were no commercial products based on OPLLs, as they were seen as being very difficult to use, and perhaps costly and unreliable.

The interest in coherent receivers and PSK modulation dropped greatly after the invention of the erbium-doped fiber amplifier (EDFA), and also as wavelength division multiplexing (WDM) technology became more mature in the 1990s. With this, many optical channels of different wavelengths could be multiplexed onto a single fiber, and they could be amplified all together within the fiber after some nominal distance without any need for the conversion into the electrical domain for regeneration. This was much more cost effective for long-haul, high-capacity networks. Dense WDM/EDFA capacity has grown exponentially, first very rapidly in the 1990s, and more slowly since about 2002 [10], the slow-down being initially associated with the burst of the ‘tech bubble.’

However, more recently, since about 2008, coherent detection has returned, not so much because of enhanced sensitivity, but because of the *spectral efficiency* that it can provide when the full vector optical field is detected. It turns out that we really were about to run out of fiber bandwidth, as many claimed around 1998, it just didn’t happen until a decade later! Of course, coherent detection is complementary to WDM/EDFA transmission systems, but it enables a higher data rate without using a higher fundamental baud rate. Thus, issues like fiber dispersion and other impairments can be lessened, even as the link capacity is enhanced.

Optical phase-locked loops (OPLLs) are still not widely used in communication, although they continue to be used in some sensor applications, for the reasons mentioned above. Intradynic techniques, which use high-speed ADCs and sophisticated digital-signal-processors (DSPs) dominate the long-distance communications field [1,10]. By applying complicated algorithms, most of the linear and nonlinear effects introduced by the long-distance propagation can be eliminated, and multiple-phase as well as multiple-level two-dimensional modulation formats

can be achieved, such as QPSK, 16QAM, and 256 QAM [9-12]. Unfortunately, such intradyne systems tend to be very costly to design, fabricate and operate, given the market quantities involved, and they consume a lot of power. They do not appear to be very competitive for the emerging higher-volume, shorter-link markets in data centers, high-performance computing, and high-capacity metro-links where spectral efficiency, and oftentimes fiber cable volume, are becoming key issues [13].

In this paper we will briefly review some of the past work, and then discuss some more recent efforts to make much more stable OPLLs that are also small in size, low in required power, have virtually no latency, and should be low in cost to produce, even in modest volumes. Although research on OPLLs has continued [14-17], the loop bandwidth problem had not been fundamentally solved until the work of the authors [18-22]. Also, relatively simple, but elegant, custom electronic ICs have been designed to solve many of the other stability issues [20,22]. Unlike the homodyne PSK receivers of the 1980s, advanced integration technologies were used for these OPLLs to make the system very compact and much more stable. 40 Gbit/s data rate has been achieved [20]. Compared to intradyne, this OPLL system has a much simpler architecture, and consumes much less power. Although it may suffer from fiber impairment issues for long haul communications, this is probably not its primary target market. Compared to OOK systems, this OPLL-based receiver retains the inherent highest available sensitivity as a homodyne PSK receiver, which provides for the maximum link reach [23]. The frequency/phase locking function in this OPLL also prevents channel wavelength drift due to temperature or aging, and this can enable many new system capabilities such as a dense (25 GHz spacing) WDM PON system [24] for example.

2. Homodyne receiver with an OPLL

The homodyne receivers that have been proposed by the authors is based on the classic Costas loop structure [20], which includes an optical I/Q receiver including an LO laser, a phase/frequency detector (PFD), and a loop filter. The architecture of this OPLL is shown in Fig. 1.

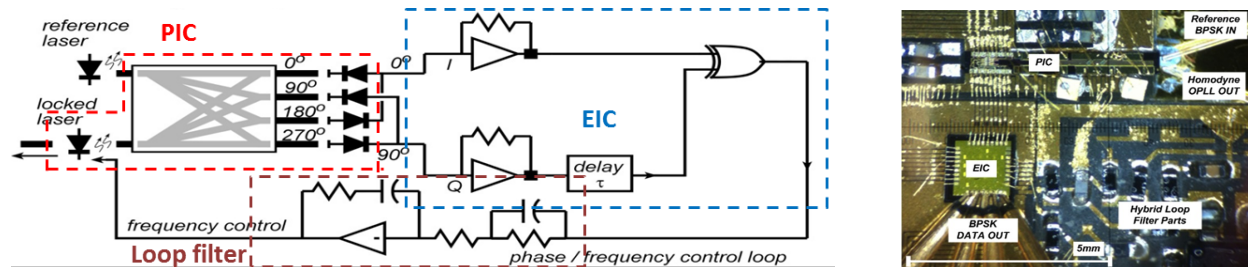


Fig. 1. (a) The architecture of the homodyne receiver. (b) A microscope picture of the receiver (mostly dominated by the discrete loop filter).

As shown, it is composed of a photonic integrated circuit (PIC) [20], an electronic integrated circuit (EIC), and a loop filter (LF). The PIC is a commonly used coherent circuit, including a widely-tunable SG-DBR laser as the LO laser, a 90 degree hybrid, and four high-speed uni-travelling-carrier (UTC) photodetectors (PDs). The detected I/Q signals are fed back to the LO laser phase-tuning section by current injection. Fast feedback tuning can be achieved. The EIC includes limiting amplifiers as the front-end, and a quadri-correlator as the PFD. The discrete LF is used to introduce more gain and stabilize the loop. The EIC and LF potentially can be integrated on a single CMOS ASIC with relatively low cost.

The system is built within a $10 \times 10 \text{ mm}^2$ carrier, and the phase locking is achieved with 1.1 GHz closed loop bandwidth. The system testing setup is shown in Fig. 2(a), and the BER vs OSNR results are shown in Fig. 2(b) as well as the eye diagram.

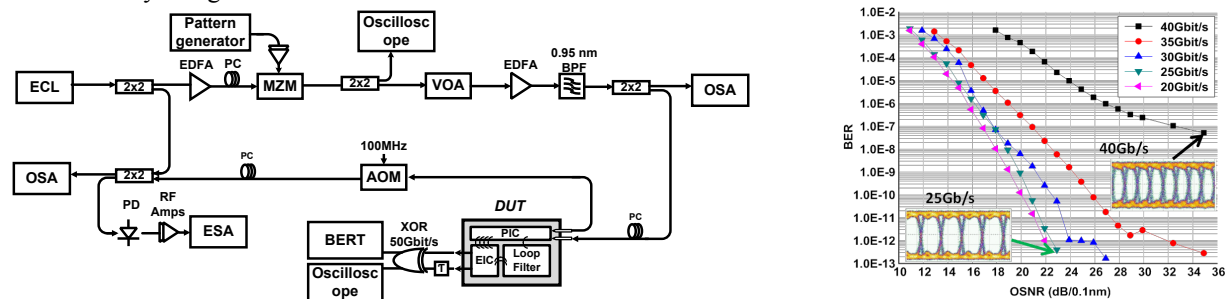


Fig. 2. (a) The test setup for the homodyne receiver testing. (b) BER vs OSNR from 25 Gbit/s to 40 Gbit/s. The eye diagrams are also shown.

Compared to previous efforts on homodyne receivers, this integrated OPLL receiver shows very high data rate and low BER at the same time. The integration ensures wider loop bandwidth, which leads to superior system stability and more flexibility with the LO linewidth. (The free-running widely-tunable LO linewidth is more than 10 MHz in this experiment, but it duplicates that of the signal carrier once locked—here $\sim 100\text{kHz}$.)

3. Heterodyne transmitter with an OPLL

By using a similar architecture and integration platform, a heterodyne OPLL has also been demonstrated [17]. Compared to the homodyne OPLL shown in Section 2, the heterodyne OPLL includes a single-sideband mixer (SSBM) in the EIC, which introduces the desired single-sideband frequency shift. Offset locking can be achieved with an offset frequency ranging over about 40 GHz. Since PFD is integrated, continuous phase-locked frequency sweeping can be achieved by *only* tuning the RF synthesizer frequency. The system is also very stable, and the phase error variance has been measured to be $< 0.03 \text{ rad}^2$, integrating from 100 Hz to 10 GHz.

4. Conclusions

The reasons why the OPLL-based homodyne receivers are not currently used are mainly because i) the homodyne receiver has the most stringent requirement on linewidth [4,9], and ii) the limited bandwidth also makes the loop hard to be stable. However, as we have shown, photonic and electronic integration changes the situation. Since loop bandwidth is increased by orders of magnitude compared to early homodyne, the OPLL works and the data rate also goes up by orders of magnitude; thus, the homodyne receiver becomes viable for real communication systems. The advantages of higher receiver sensitivity remain. Although the removal of long-haul impairments still remain at issue, integrated OPLL-based receivers would appear to offer many advantages for shorter distance links where such impairments are not a big issue. The power dissipation is low, the footprint is low, and the cost should also be low.

Acknowledgement

This work is supported by the DARPA-CIPHER (PICO) project. A portion of this work is done in the UCSB nanofabrication facility, part of NSF funded NNIN network. The EIC fabrication is done at Teledyne Scientific.

5. References

- [1] K. Kikuchi, *High Spectral Density Optical Communication Technology*, (Springer, 2010), Chap. 2.
- [2] Y. Yamamoto and T. Kimura, *IEEE J. Quantum Electron.*, **17** (6) 919-925 (Jun. 1981).
- [3] M. Grant, W. Michie, and M. Fletcher, *J. Lightwave Technol.*, **4**, 592-597 (1987).
- [4] T. Hodgkinson, *Electron. Lett.*, **22**, 394-396 (1986).
- [5] L. Kazovsky, *J. Lightwave Technol.*, **4**, 182-195 (1986).
- [6] T. L. Koch, U. Koren, R. P. Gnall, F. S. Choa, F. Hernandez-Gil, C. A. Burrus, M. G. Young, M. Oron, and B. I. Miller, *Electron. Lett.*, **25** (24) 1621-1623 (Nov. 1989).
- [7] S. Norimatsu and K. Iwashita, *J. Lightwave Technol.*, **10**, 1367-1375, Oct. (1991).
- [8] U. Gliese, T. N. Nielsen, M. Bruun, E. L. Christensen, K. E. Stubkjr, S. Lindgren, and B. Broberg, *Photon. Tech. Lett.*, **4**, 936-938 (1992).
- [9] Leonid G. Kazovsky, Georgios Kalogerakis, and Wei-Tao Shaw, *J. Lightwave Technol.*, **24**, 12 (2006).
- [10] P. J. Winzer, *IEEE Comm. Mag.*, (June 2010).
- [11] P. J. Winzer, A. H. Gnauck, C. R. Doerr, M. Magarini, and L. L. Buhl, *J. Lightwave Technol.*, **28**, 4 (2010).
- [12] Akihide Sano, Hiroji Masuda, Takayuki Kobayashi, Masamichi Fujiwara, Kengo Horikoshi, Eiji Yoshida, Yutaka Miyamoto, Munehiro Matsui, Masato Mizoguchi, Hiroshi Yamazaki, Yohei Sakamaki, and Hiroyuki Ishii, *J. Lightwave Technol.*, **29**, 4, 578-586 (2011).
- [13] C. R. Cole, *Optical Fiber Technology*, **17** (5) 472-479 (October, 2011).
- [14] Tatsunori Omiya, Kazushi Toyoda, Masato Yoshida, and Masataka Nakazawa, *OFC, OM2A* (2012).
- [15] S. Ristic, A. Bhardwaj, M. Rodwell, L. Coldren, and L. Johansson, *J. Lightwave Technol.*, **28**(4), 526-538 (2010).
- [16] R. Steed, F. Pozzi, M. Fice, C. Renaud, D. Rogers, I. Lealman, D. Moodie, P. Cannard, C. Lynch, L. Johnston, M. Robertson, R. Cronin, L. Pavlovic, L. Naglic, M. Vidmar, and A. Seeds, *Opt. Express* **19**, 20048-20053 (2011).
- [17] T. Sakamoto, A. Chiba, A. Kanno, I. Morohashi, and T. Kawanishi, *ECOC'2010 conference*, P3.12 (2010).
- [18] M. Lu, H. Park, E. Bloch, A. Sivananthan, A. Bhardwaj, Z. Griffith, L. Johansson, M. Rodwell and L. Coldren, *Opt.Express* **20**, 9736-9741 (2012).
- [19] Mingzhi Lu, Hyun-chul Park, Eli Bloch, Abirami Sivananthan, Zach Griffith, Leif A. Johansson, Mark J. Rodwell, and Larry A. Coldren, *IEEE Photon. Conf.*, ThR 2 (2012).
- [20] Hyun-chul Park, Mingzhi Lu, Eli Bloch, T. Reed, Z. Griffith, L. Johansson, L. Coldren, and M. Rodwell, *ECOC, PD-2*, (Sept, 2012).
- [21] Mingzhi Lu, Hyun-chul Park, Eli Bloch, Abirami Sivananthan, John Parker, Zach Griffith, Leif A. Johansson, Mark J. Rodwell and Larry A. Coldren, *IEEE Photon. Conf.*, PD-4 (Sept., 2012).
- [22] E. Bloch, H. Park, M. Lu, T. Reed, Z. Griffith, L. Johansson, L. Coldren, D. Ritter and M. Rodwell, submitted to *Trans. Microwave Theory and Tech.*
- [23] G. P. Agrawal, *Fiber-optic communication systems*, Wiley-Interscience (2002).
- [24] Gee-Kung Chang; Chowdhury, A.; Zhensheng Jia; Hung-Chang Chien; Ming-Fang Huang; Jianjun Yu; Ellinas, G.; , *J. Optical Communications and Networking* , vol.1, no.4, pp.C35-C50, September 2009.

**New Opportunities for Optical
Phase-locked Loops in
Coherent Photonics**

Larry A. Coldren

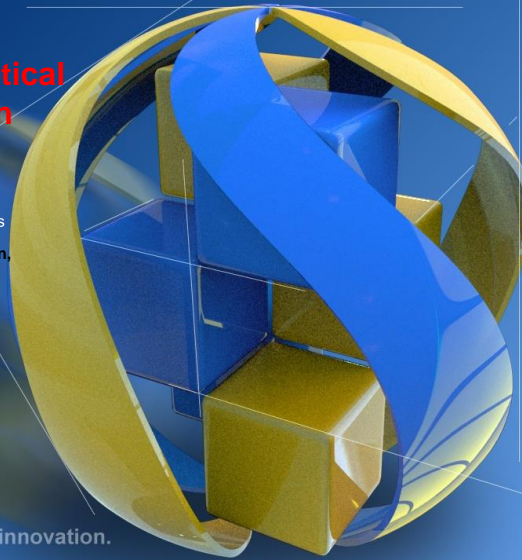
Fred Kavli Professor of Optoelectronics and Sensors

**M. Lu, H. Park, E. Bloch, J. Parker, L. Johansson,
and M. Rodwell**
ECE and Materials Departments,
College of Engineering
UCSB

Acknowledgements

Funding from: DARPA, Rockwell-Collins.

The convergence of research and innovation.



Introduction and Overview

- Why optical phase-locked loops (OPLLs)?
- Early development of OPLLs
- The role of photonic integration in OPLLs
- Recent achievements from UCSB
 - Coherent communication receivers
 - Optical wavelength synthesis and sensing
- Future directions

Why OPLL

UC SANTA BARBARA
engineering


The convergence of research and innovation.

Motivation for phase locking

Most electrical communication / sensing systems have PLL.

Give full control of transmitted phase
Detect the received phase info

- LO phase noise suppression
- Clock synchronization
- RF synthesizer
- Enable homodyne/heterodyne detection
- et. al.

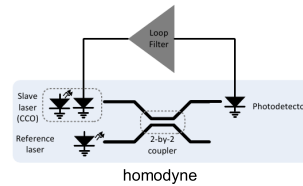


→ Why not in photonics → carrier 6 orders higher; loops longer?

The convergence of research and innovation.

What if we had optical PLL as in the electrical world?

- Laser linewidth will not be a big problem (if OPLL BW $\sim \omega_R$)
 - No stringent requirement on LO
 - Only residual phase noise matters
 - No extra wavelength stabilization circuit is needed
- Sub-Hz-level accuracy wavelength synthesis becomes possible
 - Ultra-narrow-linewidth widely tunable lasers
 - Ultra-accurate wavelength with little temperature control
- Homodyne coherent receiver
 - Low power consumption, small footprint
 - Low cost
- Advanced sensing and imaging system
 - LIDAR
 - Holography
 - Fiber sensing
 - OCT
- All-optical phase and amplitude amplification--PSAs (e.g., U of Southampton)



Revolutionary Systems Improvements and Simplifications

Early development of OPLLs

Prior Work

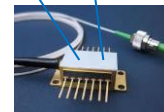
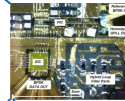
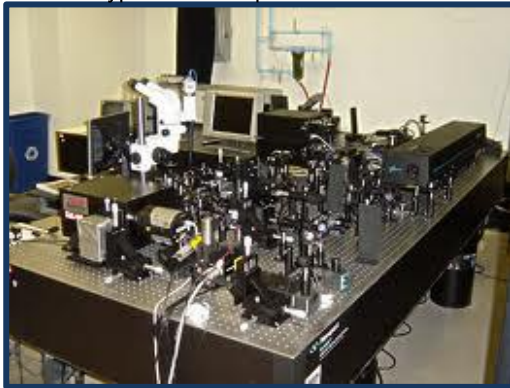
The convergence of research and innovation.

- 1965— 1st OPLL; Enloe and Rodda; locked two He-Ne lasers using piezoelectric mirrors
- 1989— 1st integrated chip (OPLL); Koch and Koren; coherent receiver— L.O./coupler/detectors
- 1990— Optical Costas loop; Norimatsu, et al; frequency & phase lock ECLs; 10Gb/s @ 1550 nm, BPSK
- 1990— QPSK @ 280 Mb/s; Derr, et al; narrow linewidth, He-Ne lasers
- 1992— Microwave offset-locked (Heterodyne); Gliese, et al; 3-T DFBs @ 1550 nm 3-18GHz using micro-optics
- 1999— Micro-optics co-packaging; Langley, et al; 70 MHz loop BW; 0.05 rad² phase error variance; 7-14 GHz heterodyne offset locking

Need Integration

The convergence of research and innovation.

Typical OPLLs prior to 2000



Basic control theory tells us: short loop physical delay → stable OPLL:

$$\text{OPLL loop bandwidth} * \text{loop delay} < 0.736$$

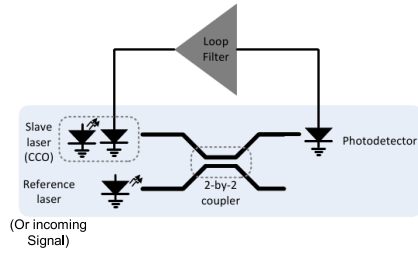
[M. Grant, JLT, 1987]

e.g. 1 GHz loop bandwidth → < 120 ps loop delay

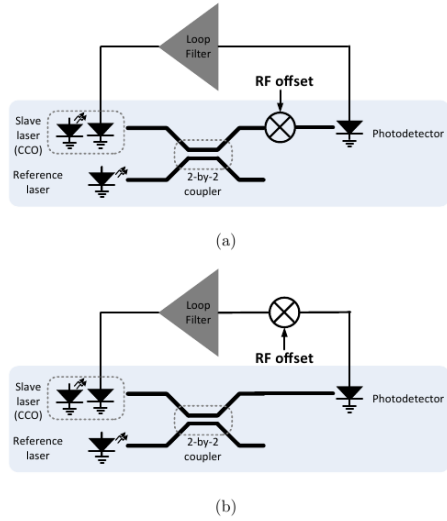
Two Kinds of OPLLs

The convergence of research and innovation.

Homodyne: Receivers



Heterodyne: Wavelength synthesis



The role of photonic integration
in OPLLs

UC SANTA BARBARA
engineering

First Demonstrated Integrated OPLL

The convergence of research and innovation.

- Offset locking (heterodyne) of two SGDBRs → viable using close integration of PICs with electronics in a OPLL → Hz-level relative frequency control, potentially over 5 THz

Quasi-continuous phase-locked digital tuning up to 5 THz offsets possible

Ristic, et al: JLT v.28 no.4, pp526-8, Feb., 2010

UC SANTA BARBARA
engineering


Need Detailed Characterization

The convergence of research and innovation.

- Simple OPLLs still not stable due to environmental perturbations, even with relatively wide BW loops (and cannot select desired sideband)
- Incorporate Costas Loop design and side-band selection
 - Combines frequency and phase locking
 - Enables very stable operation with large capture range, rapid phase locking, frequency sweeping, and data demodulation

Recent achievement from UCSB – Homodyne BPSK Receivers

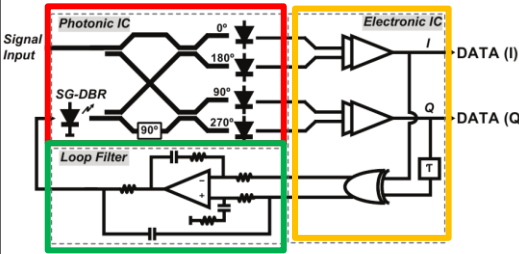
(Coldren and Rodwell groups)



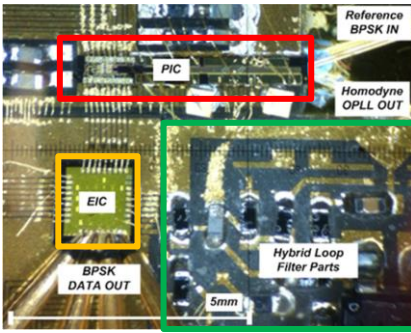
The convergence of research and innovation.

Receiver Incorporating Costas Loop

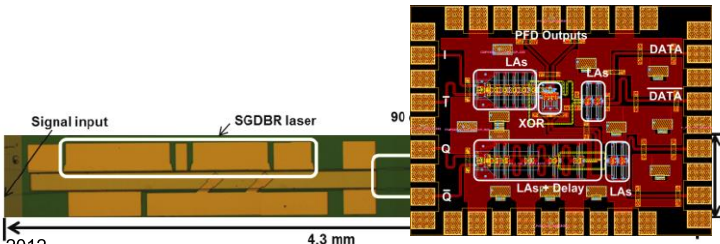
Costas Loop



UCSB Homodyne OPLL - Architecture



- Com
- Tota



InP HBT IC
300 GHz
unity gain
bandwidth
0.54mm

Lu, Park, et al., 2012

UC SANTA BARBARA engineering The convergence of research and innovation.

Phase/Freq. Locked Receiver: Int. components

UCSB Homodyne OPLL

- Photonic IC (PIC)
 - Widely-tunable LO laser (SG-DBR laser, 40 nm tuning range)
 - 90-degree 2 x 4 hybrid (0-phase error)
 - High-speed UTC detectors
 - RF transmission lines
- Electronic IC

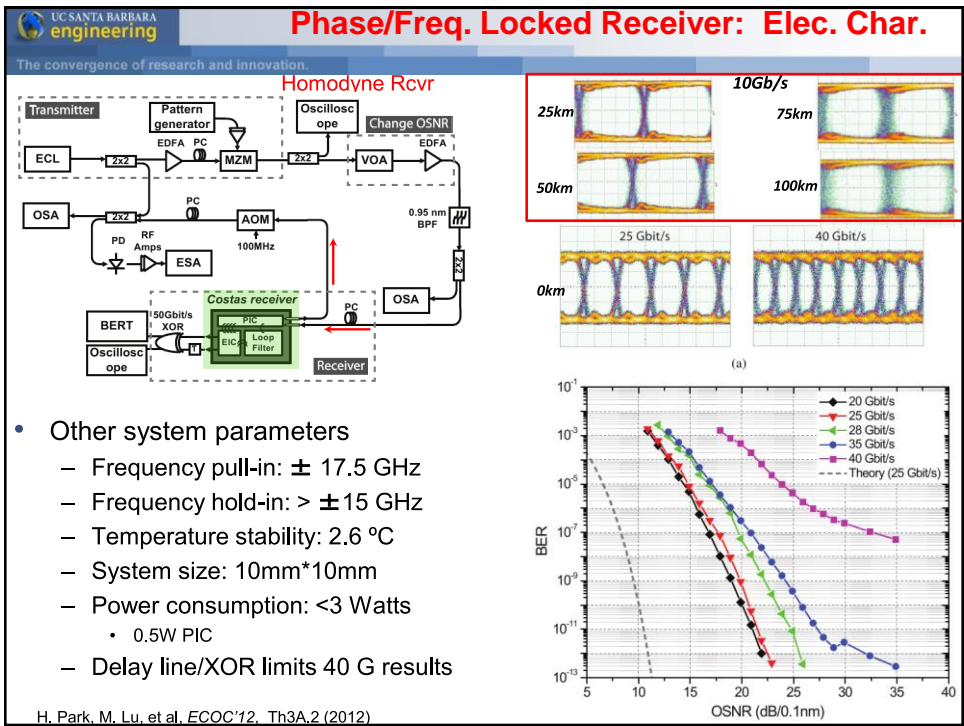
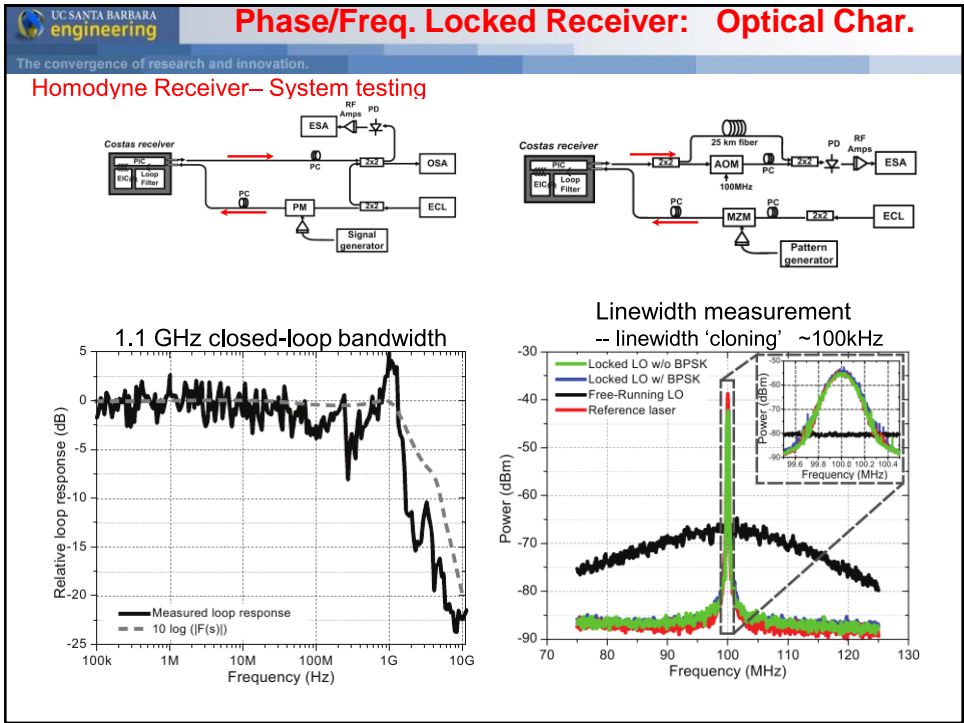
Lu, Park, et al, 2012

UC SANTA BARBARA engineering The convergence of research and innovation.

Phase/Freq. Locked Receiver: PIC

InP	1.1Q - N contact	SiNx
P-metal	N-metal	BCB
P-InGaAs	1.3Q - WG layer	QW layers
Intermixed QWs		

Lu, Park, et al, 2012



UC SANTA BARBARA
engineering

Phase/Freq. Locked Receiver: Locking time


The convergence of research and innovation.

Homodyne Rcvr

Ref laser: 800 kHz ON-OFF, 50% duty cycle
 Locking conditions: EIC output – DC,
 External PD output – 100MHz

Frequency pull-in time ~600ns
 Phase lock time <10ns
 (Not best condition)

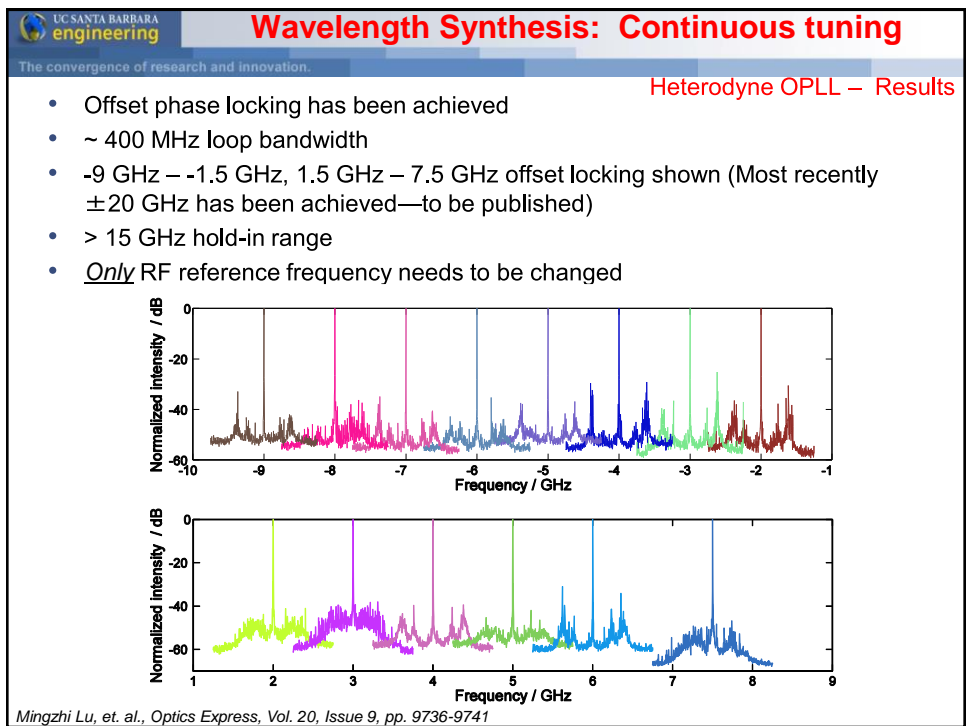
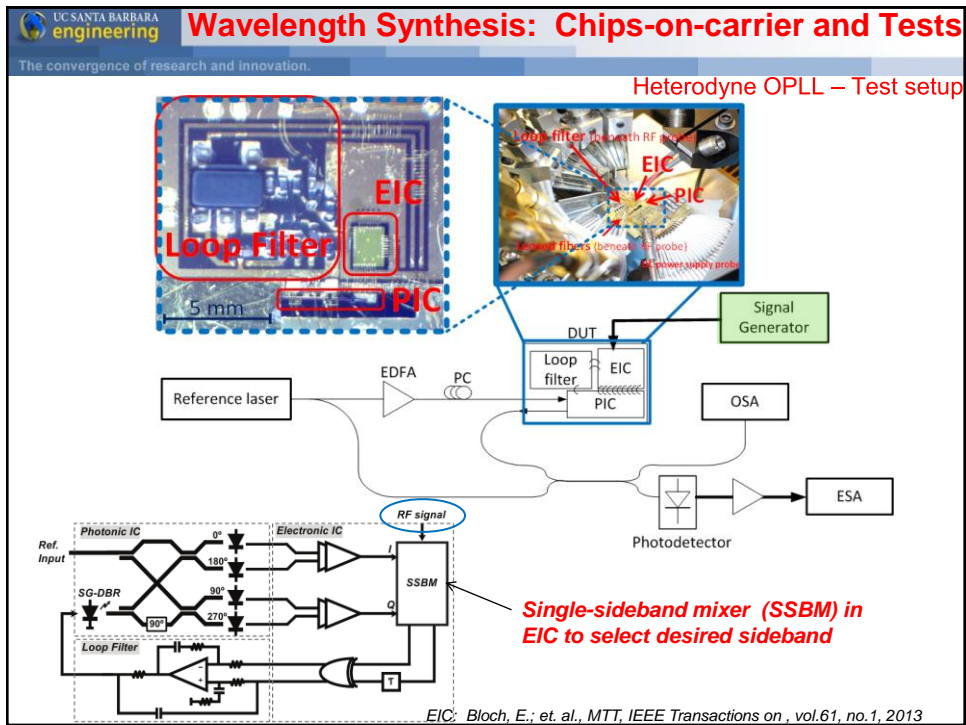
Free-running offset: 3-4 GHz



H. Park, M. Lu, et al, ECOC'12, Th3A.2 (2012)

**Recent achievement from UCSB –
 Heterodyne Wavelength Synthesis
 (Presented in OW3D.1)**

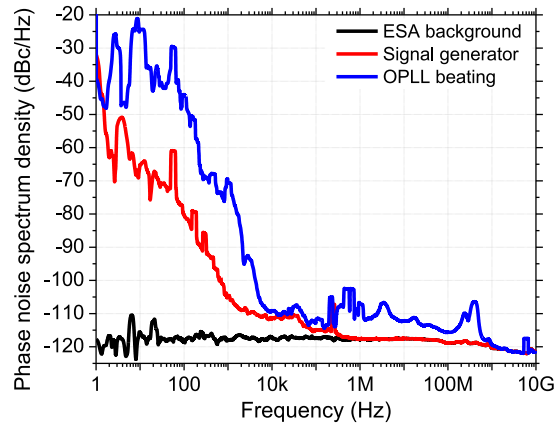
(Coldren and Rodwell groups)



The convergence of research and innovation.

Heterodyne OPLL – Results

- Phase noise is comparable to commercial RF synthesizer
 - < -100 dBc/Hz phase noise above 5 kHz
 - 0.03 rad^2 phase error variance (Integration from 100Hz)



Conclusion and future outlook

Comparison with recent work

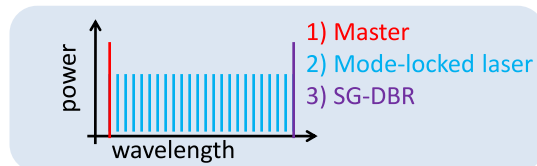
The convergence of research and innovation.

Work (Year)	Heterodyne /homodyne	Loop delay	Loop BW	Frequen cy pull-in	Hold-in range	SSBM
R.J. Steed (2011)	0.6-6.1 GHz	1.8 ns	~ 200 MHz	No	-	No
R.J. Steed (2011)	2-7 GHz	1 ns	-	No	-	No
S. Ristic (2010, UCSB)	Homodyne and 5 GHz	-	300 MHz	No	-	No
L. N. Langley (1999)	7-14 GHz	380 ps	70 MHz	No	-	No
U. Gliese (1992)	3-18 GHz	400 ps	180 MHz	No	-	No
UCSB OPLL #1	Homodyne Rcvr	120 ps	1.1 GHz	17.5GHz	>15 GHz	No.
UCSB OPLL #2	-20 – +20 GHz Heterodyne Source	200 ps	400 MHz	> 10 GHz	> 15 GHz	Yes.

- *More stable and robust*
 - *Smaller size*
 - *Larger pull-in range*
 - *Fast frequency pull-in and sweeping*
 - *Wider offset locking range*
 - *Lower phase noise*
- *Real applications*
 - *Coherent receiver*
 - *Wavelength synthesizer*
 - *Optical Sensing*
 - *OCT, etc.*

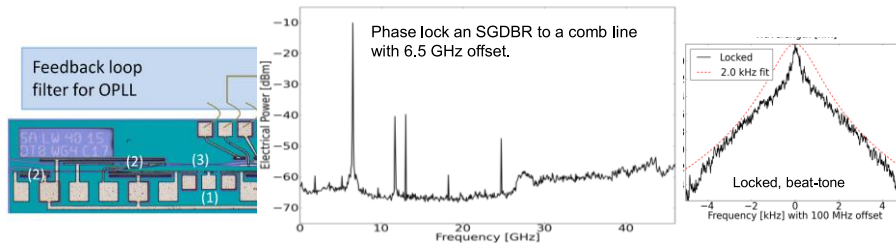
Wideband optical synthesizer (to ~ 5 THz)

The convergence of research and innovation.

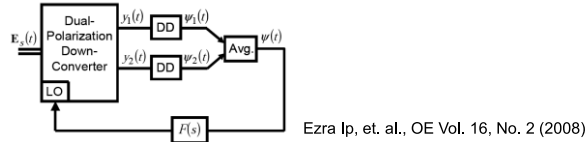


J. Parker, M. Lu, et al, IPC, 2012
J. Parker, M. Lu, et al, PTL, 2013

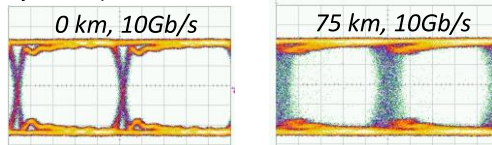
- Phase lock a mode-locked laser to a master laser ✓
- Actively mode-lock to stabilize comb ✓
- Phase lock a widely-tunable laser to one comb line ✓
- Integrate all into a single system **Doable**



- Higher order modulation
 - QPSK has been demonstrated using discrete components (F. DERR (1990))
 - 16 QAM is possible (LO: SG-DBR laser with 3 MHz linewidth)
- Polarization mode dispersion (PMD) problem
 - Phase lock to the average phase



- Build a slow loop to de-embed the polarization
 - Can base on BER, since it is a phase lock system
- Chromatic dispersion (CD) problem (carrier can be recovered somewhat beyond dispersion limit for data)



Can be compensated by DSF or linear compensator.

- Carrier recovery in DSP
 - Feed-forward
 - Feedback -- Digital delay-locked loop
 - Loop delay relies on clock freq and # of clocks
- Advantage of OPLL
 - Better phase noise suppression, less stringent requirement on laser linewidth
 - Less temperature stability necessary
 - Simplicity (→ low cost, small size, low power)
 - Error-free (BER < 1e-12)
 - Ideal for short-haul applications where impairments are small
- Advantage of DSP
 - Flexibility
 - Deal with complicated situation (PMD, CD, etc.)
 - Good for long-haul where many impairments arise, and cost & power are not such large issues
- Common problem – phase ambiguity

Summary

- **Combined photonic and electronic integration supports a new era for OPLL research → High stability, low power & cost, and small components**
- **Integration enables large loop bandwidth, greatly suppressing laser phase noise.**
- **Good laser phase noise suppression leads to applications in efficient, stable, error-free, low latency coherent receivers.**
- **Good laser noise suppression also enables optical wavelength synthesizers with only a few degrees of average phase error.**
- **Advanced optical sensing engines are possible in addition to communication sources and receivers.**
- **More effort is needed for system development and commercialization.**

A Heterodyne Optical Phase-locked Loop for Multiple Applications

Mingzhi Lu¹, Hyun-Chul Park¹, John S. Parker¹, Eli Bloch², Abirami Sivananthan¹, Zach Griffith³, Leif A. Johansson¹, Mark J. Rodwell¹, and Larry A. Coldren^{1,4}

¹Department of Electrical and Computer Engineering, University of California, Santa Barbara, CA, 93106, USA.

²Department of Electrical Engineering, Technion – Israel Institute of Technology, Haifa 32000, Israel.

³Teledyne Scientific and Imaging Company, Thousand Oaks, 1049 Camino Dos Rios, CA, 91360, USA

⁴Department of Materials, University of California, Santa Barbara, CA, 93106, USA.

mlu@ece.ucsb.edu

Abstract: A novel heterodyne optical phase-locked loop (OPLL) has been achieved and testing results are demonstrated with a 0.03 rad^2 phase error variance. Based on the superior performance of this OPLL, a system prototype is shown for multiple applications, including free-space LIDAR systems, widely-and-fast-tunable ultra-narrow-linewidth lasers, and ultra-accurate optical spectrum analyzers.

OCIS codes: (250.5300) Photonic integrated circuits; (060.2840) Heterodyne; Optical phase-locked loop; (010.3640) LIDAR.

1. Introduction to the highly-integrated heterodyne OPLL

Since the first optical phase-locked loop (OPLL) was demonstrated in 1965, considerable effort has been devoted to the research of OPLLs. However, the biggest roadblock is the short loop delay requirements for stable operation. By using traditional free space optics, most OPLLs show a loop delay of more than tens of nanoseconds, which makes the loop bandwidth smaller than 10 MHz, according to the fundamental control theory of feedback systems. Narrow loop bandwidth not only gives rise to a high requirement on the laser linewidth and stability, but also makes the system more sensitive to environmental fluctuations. Micro-optics can possibly improve this number to close to 200 MHz, but it still suffers the same stability issue. Limited bandwidth is one of the major reasons why the OPLL is not as widely used today as that of its counterpart, the PLL in electronic communication systems [1,2].

In order to decrease the loop delay and therefore increase the loop bandwidth, photonics integration becomes necessary. Recent research shows that an integrated OPLL can have a closed-loop bandwidth of several hundreds of MHz [3-5], or even more than 1 GHz [6]. Based on advanced photonic and electronic integration technology, a heterodyne OPLL is made and a part of the testing results can be found in [5]. This OPLL is integrated with an I/Q receiver, a phase/frequency detector (PFD) and a single-sideband mixer for the first time [5,6]. The whole OPLL system has been realized within a size of $10 \times 10 \text{ mm}^2$. The architecture is shown in Fig. 1. The system includes a photonic integrated circuit (PIC), an electronic integrated circuit (EIC) and a hybrid loop filter built on an AIN carrier. An on-PIC sampled-grating DBR (SG-DBR) laser is used as a widely-tunable slave laser, and it covers a 40 nm bandwidth. By integrating the I/Q receiver and the PFD in the system, frequency pull-in has been achieved, which means that even if the free running slave laser is several GHz away from the targeted locking frequency, it will be pulled-in and become phase-locked automatically. The SSBM enables the system to achieve offset locking, and the offset frequency between two lasers can be either positive or negative [7]. The sign is set by the control pad on the EIC and there is no frequency ambiguity. Based on the frequency pull-in function and the SSBM, a phase-locked frequency sweep has been achieved from -9 GHz to -1.5 GHz, and from +1.5 GHz to +7.5GHz. The electrical beating spectra are shown in Fig. 2. Injection locking is observed below 1.5 GHz frequency offset because of internal reflections on the PIC.

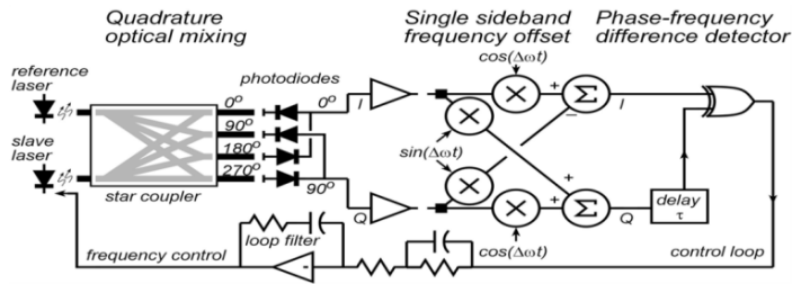


Fig. 1. The architecture of the OPLL.

Moreover, this heterodyne OPLL also shows > 15 GHz hold-in range. The phase locking is very stable. Within a submount temperature change of 2.3 °C, the OPLL can keep phase-lock. The phase noise measurement also shows that the beating tone of the master laser and the slaver laser has a phase noise <-100 dBc/Hz above 5 kHz, and the phase error variance is 0.03 rad², integrating from 100 Hz to 10 GHz.

The details about this heterodyne OPLL can be found in [5]. The preliminary testing result of this OPLL is summarized in Table 1. Compared to all the OPLLs that have been proposed in the past, this heterodyne OPLL has superior performance in almost all the specifications listed in Table 1. The hold-in range, stability, pull-in range have improved by orders of magnitude.

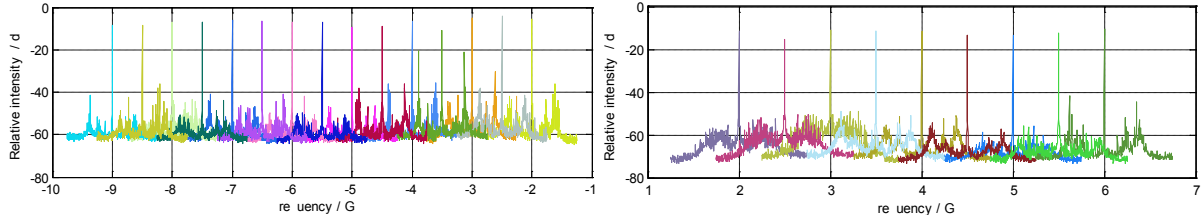


Fig. 2. Shows the beating tones of the two lasers when they are phase locked at various frequency offsets.

Loop delay	~ 200 ps	Hold-in range	> 15 GHz
Closed-loop bandwidth	~ 400 MHz	Temperature range	2.3 °C
Pull-in range	Close to 10 GHz	System size	10 × 10 mm ²
Offset frequency range	-9- + 7.5 GHz	Phase error variance	0.03 rad ²

Table 1. Performance summary of the heterodyne OPLL system.

By replacing the PIC with a new PIC with wider photodetector bandwidth, which has already been demonstrated in [8], the continuous frequency sweeping range can be as wide as the laser cavity mode spacing (~40 GHz for the SG-DBR laser). Furthermore, no injection locking has been observed on this new PIC, because of a fundamental design change of the waveguide structure. Therefore, continuous sweeping across the zero frequency offset is achievable.

2. System prototypes

Using the heterodyne OPLL discussed in Section 1 as a key building block, many communication or sensing systems can be created with superior performance. Full engineering control over the optical phase of the laser becomes feasible. The system stability ensures that it is possible to build some commercial systems based on this heterodyne OPLL.

i) Frequency-Modulated Continuous-Wave (FMCW) Light Detection and Ranging (LIDAR) systems

FMCW radar has been using in the field for decades and a lot of research based on this principle has been carried out [9]. Compared to FMCW radar, FMCW LIDAR has much higher resolution. The resolution of the LIDAR is inversely proportional to the frequency sweeping range, which is mainly limited by the laser tuning range. By applying this heterodyne OPLL to a LIDAR system, 40 nm quasi-continuous tuning is achievable, which potentially leads to a 30 μm resolution.

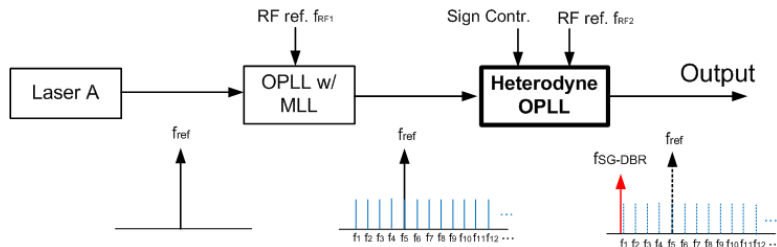


Fig. 3. A system built on the heterodyne OPLL.

The proposed system architecture is shown in Fig. 3. The continuous-wave laser A is a single-fixed-wavelength narrow-linewidth laser, which is used as a reference laser in this system. By using an OPLL with an integrated mode-locked laser (MLL), one of the comb lines of the MLL can be phase-locked to laser A, and at the same time, the MLL is actively mode-locked. By both phase locking and active mode locking, timing jitter is eliminated and the linewidth of each line is the same as the CW laser A. The RF source frequency f_{RF1} is the same as the mode-locking frequency. Hence, stable and narrow-linewidth comb lines can be generated.

The comb lines are then used as the reference for the heterodyne OPLL. RF frequency f_{RF2} is applied on the EIC of the OPLL to introduce a frequency offset, which is $f_{RF2}/2$ [7]. By tuning the SG-DBR mirror currents, phase

section current and f_{RF2} , SG-DBR laser can phase-lock to the frequency of $f_i \pm f_{RF2}/2$, where $i=1,2,3,4\dots$. As long as the heterodyne OPLL offset frequency range is larger than half of the comb line spacing, quasi-continuous frequency sweeping can be achieved. Moreover, the SG-DBR linewidth can be the same as CW laser A, because of the linewidth ‘cloning’ of OPLL. Since the linewidth is directly related to the detection range, by using a better reference, the system range can be greatly increased. In addition, the sweeping speed can be quite fast. It will not be limited by the interaction between red-shifting thermal effects and blue-shifting carrier density effects.

Our preliminary results have already shown that an InGaAsP/InP integrated MLL can achieve 2.06 THz spectrum width with 29 GHz line spacing under active mode-locking [10]. A MLL has also been used as a reference laser, and the heterodyne OPLL has successfully phase locked to one of the comb lines [11].

Furthermore, since both the MLL and the PIC in the heterodyne OPLL system are integrated on InGaAsP/InP platform and the fabrication processes are very similar, integrating them on the same PIC monolithically is feasible. If the LIDAR system doesn’t have strict requirement on linewidth, it is possible to get rid of the CW laser A, and the system size will decrease down to the tens of millimeter scale, which means that a 30 μm -resolution handheld FMCW LIDAR can be achieved, and it becomes possible to integrate in a watch or a cell phone.

ii) Widely-and-fast-tunable ultra-narrow-linewidth lasers

Commercial state-of-the-art fixed-wavelength lasers can achieve <1 kHz linewidth, whereas the linewidth of most widely-tunable lasers is still at the 100’s of kHz range. $1/f$ noise on the tuning sections is a fundamental noise source that limits the linewidth of rapidly tunable lasers to be higher than fixed-linewidth laser.

By utilizing the topology in Fig. 3, and using a narrow-linewidth fixed-wavelength laser as CW laser A, the narrow linewidth can be ‘cloned’ to comb lines and therefore to the SG-DBR laser in the heterodyne OPLL system. The low phase error of the system ensures the linewidth does not get broadened when it gets ‘cloned’.

iii) Ultra-accurate optical spectrum analyzers

Optical spectrum analyzers (OSAs) normally have limited resolution bandwidth at the GHz range. By using the frequency sweeping system in Fig. 3 as a local oscillator (LO), and beating the measuring signal with the LO on a photodetector, the resolution of the OSA is only limited by the linewidth of the LO, which can be as small as 1 kHz across the whole C band. The resolution of this new prototype of OSA can be so high that it is possible to measure the linewidth of a DFB laser accurately without any extra test setup.

3. Conclusions

In this work, preliminary results of a heterodyne OPLL have been demonstrated. Based on this novel OPLL, a new system prototype has been shown for the first time, and several potential applications have been illustrated. The applications of this OPLL include, but are not limited to: FMCW LIDAR, narrow-linewidth widely-tunable lasers, and ultra-accurate optical spectrum analyzers. The applications can also extend to the area of fiber optic sensing and coherent communications. More system testing results will be shown at the conference.

4. References

- [1] U. Gliese, T. N. Nielsen, M. Bruun, E. L. Christensen, K. E. Stubkjr, S. Lindgren, and B. Broberg, “A wideband heterodyne optical phase-locked loop for generation of 3-18 GHz microwave carriers,” IEEE Photon. Technol. Lett. 4, 936-938 (1992).
- [2] L. G. Kazovsky, “Decision-driven phase-locked loop for optical homodyne receivers: Performance analysis and laser linewidth requirements,” Journal of Lightwave Technology, vol. LT-3, No. 6 (1985).
- [3] S. Ristic, A. Bhardwaj, M. Rodwell, L. Coldren, and L. Johansson, “An optical phase-locked loop photonic integrated circuit,” J. Lightwave Technol. 28, 526-538 (2010).
- [4] R. Steed, F. Pozzi, M. Fice, C. Renaud, D. Rogers, I. Lealman, D. Moodie, P. Cannard, C. Lynch, L. Johnston, M. Robertson, R. Cronin, L. Pavlovic, L. Naglic, M. Vidmar, and A. Seeds, “Monolithically integrated heterodyne optical phase-lock loop with RF XOR phase detector,” Opt. Express 19, 20048-20053 (2011).
- [5] M. Lu, H. Park, E. Bloch, A. Sivanathan, A. Bhardwaj, Z. Griffith, L. A. Johansson, M.J. Rodwell, and L.A. Coldren, “Highly integrated optical heterodyne phase-locked loop with phase/frequency detection,” Opt. Express 20, 9736-9741 (2012).
- [6] H. Park, M. Lu, E. Bloch, T. Reed, Z. Griffith, L. Johansson, L. Coldren, and M. Rodwell, “40Gbit/s coherent optical receiver using a Costas loop,” ECOC, post-deadline (2012).
- [7] E. Bloch, H. Park, M. Lu, T. Reed, Z. Griffith, L. Johansson, L. Coldren, D. Ritter, and M. Rodwell, “A 1-20 GHz InP HBT phase-lock-loop IC for optical wavelength synthesis,” IEEE Int. Micro. Symposium (2012).
- [8] M. Lu, H. Park, E. Bloch, A. Sivanathan, J. Parker, Z. Griffith, L. A. Johansson, M. J. Rodwell and Larry A. Coldren, “A photonic integrated circuit for a 40 Gbaud/s homodyne receiver using an optical Costas loop,” IEEE Photon. Conf., post-deadline (2012).
- [9] A. Vasilyev, N. Satyan, G. Rakuljic, and A. Yariv, “Terahertz chirp generation using frequency stitched VCSELs for increased LIDAR resolution,” CLEO, CF3C.1(2012).
- [10] J. Parker, A. Sivanathan, M. Lu, L. Johansson, and L. Coldren, “Integrated phase-locked multi-THz comb for broadband offset locking,” Opti.I Fiber Comm.Conf., OM3E.5 (2012).
- [11] J. Parker, M. Lu, H. Park, E. Bloch, A. Sivanathan, Z. Griffith, L. A. Johansson, M. J. Rodwell, and L. A. Coldren, “Offset locking of an SG-DBR to an InGaAsP/InP mode-locked laser,” IEEE Photon. Conf., ThR 3 (2012).

Monolithic Integration of a High-Speed Widely Tunable Optical Coherent Receiver

Mingzhi Lu, Hyun-Chul Park, Abirami Sivananthan, John S. Parker, Eli Bloch, Leif A. Johansson, *Member, IEEE*, Mark J. W. Rodwell, *Fellow, IEEE*, and Larry A. Coldren, *Fellow, IEEE*

Abstract—In this letter, a monolithically integrated widely tunable optical receiver is demonstrated. A sampled-grating DBR (SG-DBR) laser, an optical 90-degree hybrid, four high-speed uni-travelling-carrier photodetectors and microstrip transmission lines are integrated on a single InGaAsP/InP chip. A 42-nm tuning range and a 35-GHz detector bandwidth are achieved. Experiments show real-time reception of 40 Gb/s BPSK data.

Index Terms—Coherent receiver, photonic integrated devices, optical communications.

I. INTRODUCTION

WITH the fast growth of internet data streaming, a lot of recent efforts have been devoted to the research of coherent communications, which allows higher transmission capacity and higher sensitivity. As a key component of coherent communications, the demand for an integrated dual-quadrature coherent receiver with an integrated local oscillator (LO) is increasing dramatically.

Previous work has shown many coherent receiver designs [1]–[5] and some of them are already commercialized [4], [5]. However, in most of these coherent receiver designs the LO laser is usually not integrated monolithically [1], [4] mainly because of the limitation of the integration platforms. The work in [2], [3] demonstrated dual-quadrature coherent receivers with a LO laser integrated. However, the photodetector bandwidths are limited by the quantum-well PIN detector epitaxial structure.

In this letter, we will demonstrate a coherent receiver with a widely-tunable LO laser and high-speed uni-travelling-carrier (UTC) photodetectors integrated monolithically. Although this is a single-polarization coherent receiver, by combining two

Manuscript received January 24, 2013; revised February 27, 2013 and April 3, 2013; accepted April 14, 2013. Date of publication April 23, 2013; date of current version May 15, 2013. This work was supported in part by DARPA CIPHER (PICO) program. A great portion of this work was done in the UCSB nanofabrication facility, part of NSF funded NNIN network.

M. Lu, H.-C. Park, A. Sivananthan, J. S. Parker, L. A. Johansson, and M. J. W. Rodwell are with the Department of Electrical and Computer Engineering, University of California, Santa Barbara, CA 93106 USA (e-mail: mlu@ece.ucsb.edu; hcpark@ece.ucsb.edu; asivananthan@ece.ucsb.edu; JParker@ece.ucsb.edu; leif@ece.ucsb.edu; rodwell@ece.ucsb.edu).

E. Bloch is with the Department of Electrical Engineering, Technion Israel Institute of Technology, Haifa 32000, Israel (e-mail: bleli@tx.technion.ac.il).

L. A. Coldren is with the Departments of Electrical and Computer Engineering and Materials, University of California, Santa Barbara, CA 93106 USA (e-mail: coldren@ece.ucsb.edu).

Color versions of one or more of the figures in this letter are available online at <http://ieeexplore.ieee.org>.

Digital Object Identifier 10.1109/LPT.2013.2259474

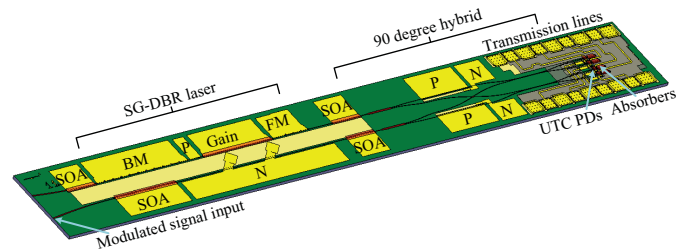


Fig. 1. To-scale picture of the PIC. The components are labeled (P: phase shifter. BM: back mirror. FM: front mirror. N: N contact and N pads).

such devices with an off-chip polarization splitter and rotator, a dual-polarization receiver can be achieved [3].

II. PIC DESIGN

As mentioned above, a widely-tunable sampled-grating DBR (SG-DBR) laser [6], an optical 90-degree hybrid, four UTC photodetectors (PDs), and electrical transmission lines are monolithically integrated on an InGaAsP/InP photonic integrated circuit (PIC). The structure of the PIC is shown in Fig. 1. It has the same relative dimensions as the real device. The device size is 4.3 mm by 0.54 mm.

The grating sections of the SG-DBR laser are periodically blanked to generate comb-like reflection peaks. By careful design of the front and back mirrors, the reflective peak spacings are slightly different, which enables a sensitive frequency tuning of the lasing peak. The SG-DBR laser can sweep quasi-continuously across the whole optical C band (40 nm) [6].

The 90-degree hybrid design is shown in Fig. 1. It uses two 1-by-2 multi-mode interference (MMI) couplers as the first stage, which split the LO and the incoming signal into two paths, respectively. The symmetry of 1-by-2 MMI coupler ensures equal splitting. Directional couplers are used as the second stage couplers in the 90-degree hybrid, because they have minimum reflection and perfect 180 phase relation between the two outputs, regardless of splitting ratio. In a design aspect, a decrease of waveguide width will increase the coupling coefficient, while, on the other hand, the increase of the gap width will decrease the coupling coefficient. In real cases, the gap will increase when the waveguide width shrinks, and vice versa. The spacing between the waveguides is accurate, independent from fabrication errors. Thus by choosing the right waveguide spacing, these two effects can be canceled out

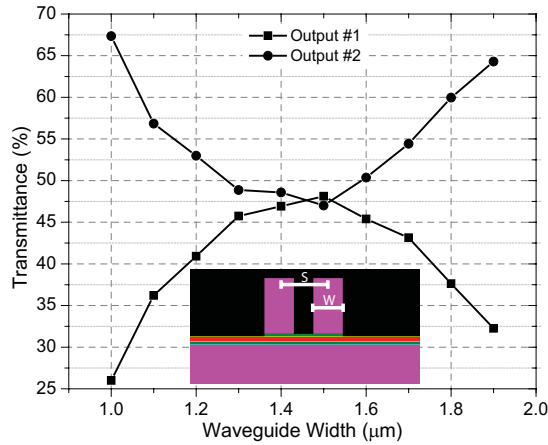


Fig. 2. Simulated transmittance of the directional coupler. Outputs #1 and #2 represent the output power ratios from the two output waveguides, respectively, compared to the launched power. The x axis is the waveguide width (W), and the spacing between two waveguides (S) is $2.5 \mu\text{m}$.

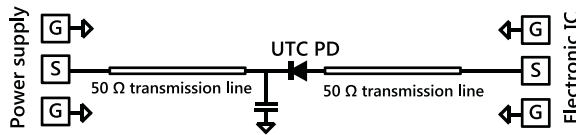


Fig. 3. Circuit schematic diagram of the PD bias circuit on PIC.

first order, and the directional coupler dimensions can be very tolerant to waveguide width variation caused by fabrication. The waveguide etching depth is also a key factor for directional coupler fabrication. A surface ridge waveguide structure has been chosen, and a selective wet etch is used to finish the waveguide etching, as will be discussed in Section III. The etching depth is defined by metal-organic vapour phase epitaxy (MOCVD) growth, the accuracy of which is within 2% for each epitaxial layer.

The directional coupler design is shown in Fig. 2. By varying the waveguide width and fixing the waveguide spacing, the coupling ratio is shown. With a $0.3 \mu\text{m}$ fabrication error (from 1.3 to $1.6 \mu\text{m}$), a decent splitting ratio (better than 47% : 53%) can be achieved according to the beam-propagation method simulation, as shown in Fig. 2. The radiation loss is around 5% from the waveguide bends and tapers on two sides of the directional coupler, which have also been taken into account in the simulation. The designed directional coupler has the following parameters: length = $145 \mu\text{m}$, waveguide width (W) = $1.5 \mu\text{m}$, waveguide spacing (S) = $2.5 \mu\text{m}$.

Four UTC PDs are also integrated on this PIC as well as microstrip transmission lines. For our design, the UTC PDs have voltage supplies to both N and P-contacts [7]. The circuit model is shown in Fig. 3. P and N contacts are led to ground-signal-ground (GSG) pads on the edges of the PIC by transmission lines, and capacitors are also integrated to provide a high frequency ground on the PIC. The capacitance is around 1 pF, which is more than 50 times that of the UTC PD junction capacitance. The thickness of the absorber layer is designed to be 150 nm so that the effective index matches the fundamental mode in the waveguide, which enables the light

to couple into the absorber layer and therefore get absorbed quickly. The doping level of the absorber is also graded from 5×10^{17} to $2 \times 10^{18} \text{ cm}^{-3}$ to facilitate the electron transport in the absorber. The collector thickness is optimized to be 250 nm to get faster coupling and lower junction capacitance. With a size of $20 \mu\text{m}$ long and $3 \mu\text{m}$ wide, the designed quantum efficiency is above 95%, and with a 50Ω load the 3-dB bandwidth can be above 50 GHz, depending on the contact resistance.

As shown in Fig. 3, two transmission lines need to be integrated for each UTC PD, and therefore there are totally 8 transmission lines on the PIC. Bisbenzocyclobutene (BCB) is used as the dielectric layer. An Au ground plane is needed beneath the BCB as the RF ground. In order to partially compensate the inductance introduced by wirebonds, the GSG pads are designed to be slightly capacitive. The GSG pad schematic can be found in Fig. 5. The pitch size is $100 \mu\text{m}$, and signal pad size is 75-by-75 μm . The electromagnetic simulation results can be found in [7].

III. PIC FABRICATION

The PIC is designed and fabricated based on a semi-insulating (SI) InGaAsP/InP substrate and centered-quantum-well (CQW) waveguide structure [8]. The fabrication starts with the base epitaxial wafer, which contains a 1.1 Q (InGaAsP quaternary material with photoluminescence peak at $1.1 \mu\text{m}$) N-contact layer, N-cladding layer, waveguide layers, CQWs, and 450 nm thick InP as the buffer layer for the quantum well intermixing process [9]. After an alignment marks etch, a patterned phosphorus ion-implant is carried out to define the active/passive areas on the wafer. The sample is then annealed at 675°C , and in consequence the photoluminescence (PL) peak of the implanted areas have a blue shift of around 130 nm, while the un-implanted areas stay almost the same. Therefore, the active (PL peak: 1550 nm) and passive (PL peak: ~ 1420 nm) areas are defined. After removing the implant buffer layer and the stop etching layer, a blanket MOCVD UTC-PD regrowth is carried out. Using Si_3N_4 as a hard mask, UTC layers are then removed from most of the wafer by wet etch, left in only the places where UTC PDs will be defined in the later steps. Gratings for the SG-DBR laser are then defined using electron-beam lithography, and a Methane-Hydrogen-Argon (M/H/A) reactive-ion-etch (RIE) is used to etch the gratings. The grating pitch size is 238 nm, and the etching depth is 80 nm into the top waveguide layer. A scanning electron microscope (SEM) picture of the finished gratings is shown in Fig. 4(a). Following the grating step, a second blanket MOCVD regrowth is fulfilled. The P-cladding layer, P-InGaAs contact layer, and top InP sacrificial layer are grown. The full epitaxial structure is shown in Table I. The rows with a shaded background show the UTC layers, and the normal waveguide structure contains all the layers except the UTC layers.

Following the second regrowth is the waveguide definition, which consist of multiple dry etches and wet etches. M/H/A RIE is used for the waveguide dry etching, and it etches through the top InP sacrificial layer and the contact layer.

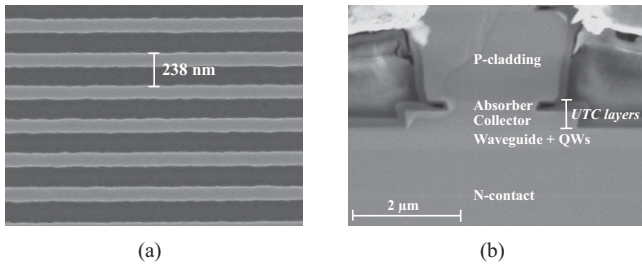


Fig. 4. (a) An SEM picture of the gratings with a pitch size of 238 nm. (b) An SEM picture of the cross section of a fully-fabricated UTC photodetector.

TABLE I
FULL EPITAXIAL STRUCTURE

No.	Material	Thick (nm)	Doping (cm^{-3})	Function
1	InGaAs:Zn	150	2E19	P-contact
2	InP:Zn	1800	5E17-1E18	P-cladding
3	InP:Zn	200	5E17-1E18	P-cladding
4	InGaAs:Zn	50	2E18	Absorber
5	InGaAs:Zn	50	1E18	Absorber
6	InGaAs:Zn	50	5E17	Absorber
7	InGaAs	8	UID	Band smooth
8	1.24Q	16	UID	Band smooth
9	InP	6	UID	Band smooth
10	InP:Si	7	1E18	Band smooth
11	InP	250	UID	Collector
12	InP:Si	30	1E18	Subcollector
13	1.33Q:Si	20	1E17	Etch stop layer
14	InP:Si	5	8E16	Regrowth layer
15	InP:Si	30	5E16-8E16	Regrowth layer
16	1.3Q:Si	105	5E16	Waveguide
17	10 QWs	153	UID	Quantum Wells
18	1.3Q:Si	105	1E17	Waveguide
19	InP:Si	850	1E18	N-cladding
20	1.1Q:Si	100	1E18	N-contact
21	InP:Si	1000	1E18	N-cladding
22	InP:Fe			SI Substrate

An HCl-based wet etch is applied to finish the waveguide definition, and the etch stops accurately at the top waveguide layer. At this point, the gap of the directional coupler needs to be protected. A 10-nm atomic layer deposition (ALD) Al_2O_3 film and a 100-nm plasma-enhanced chemical vapor deposition (PECVD) Si_3N_4 film are deposited. The ALD Al_2O_3 film is used as a stop etch for the Si_3N_4 dry etch. After protective Si_3N_4 definition, the Al_2O_3 film in open areas is removed by a strong base, AZ400K developer. After that, several M/H/A RIE and wet etches are carried out alternatively to remove the UTC layers beside the UTC PDs. The to-be-etched UTC layers, from top to bottom, are layer 4 - 15 shown in Table I. Several wet etches and dry etches are carried out alternatively, and the processing steps are shown in Table II, in which $\text{H}_2\text{SO}_4:\text{H}_2\text{O}_2:\text{H}_2\text{O}$ (1:1:10) is used for InGaAs wet etch, and $\text{HCl}:\text{H}_3\text{PO}_4$ (1:3) is used for InP wet etch. During these etches, the normal waveguide is also etched around 80 nm into the waveguide layer (No. 16 in Table I) except the protected directional coupler gaps. The cross section of a UTC detector is shown in Fig. 4(b). The undercut of the InGaAs absorber is because of the wet etch. It is also noticed that the collector is wider than the P-cladding layer, which is mainly caused by the

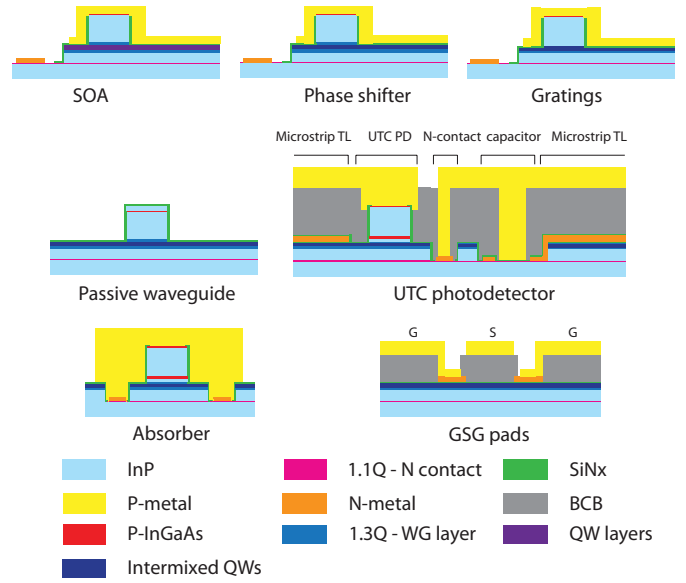


Fig. 5. Cross sections of the fabricated PIC.

TABLE II
UTC LAYER ETCHING PROCESS

Etch Steps	Removed UTC Layer	Removed Waveguide Layer
InGaAs wet etch	InGaAs absorber	~25 nm 1.3 Q layer
M/H/A dry etch	1.24 Q layer	~25 nm 1.3 Q layer
InP wet etch	InP collector layer	Negligible
M/H/A dry etch	1.33 Q layer	~30 nm 1.3 Q layer
InP wet etch	InP regrowth layer	Negligible
Summary	All UTC layers	~80 nm waveguide layer

masking of the top of the waveguide during the dry etch process.

Finally, the wafer is thinned down, and backside metalization is carried out. After cleaving and facet anti-reflective coating, the samples are ready for testing. The whole process includes 2 MOCVD regrowths, > 20 lithographies, and 2 ion implantations. The schematics of the cross sections of the fully fabricated PIC are shown in Fig. 5, and an SEM picture of the PIC can be found in Fig. 6.

IV. TESTING RESULTS

The PIC has been fully characterized. The SG-DBR laser covers from 1541 nm to 1583 nm without temperature tuning. The optical spectra of the super-modes are shown in Fig. 7(a). The side-mode suppression can be further improved if the output power is higher. The preliminary result shows a self-heterodyne linewidth of around 10 MHz [7], [10], and the low-frequency linewidth drift is within 100 MHz. The output power can be as high as 20 mW without the boosting amplifier. The ac response of the phase diode of the SG-DBR has also been

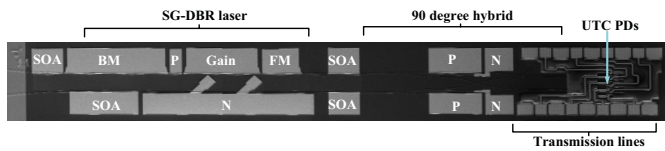


Fig. 6. An SEM picture of the fabricated PIC. The components are labeled (P: phase shifter, BM: back mirror, FM: front mirror, N: N contact and N pads).

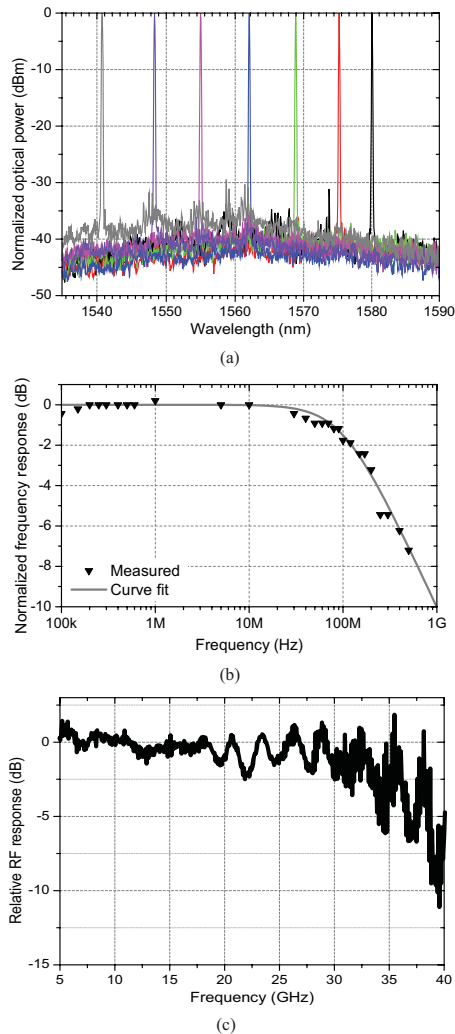


Fig. 7. (a) Optical spectra of the SG-DBR laser lasing at different mirror super-modes. The resolution bandwidth is 0.1 nm. (b) Relative frequency response of the phase section diode in the SG-DBR laser. (c) Shows optical-electrical response of the UTC PD. The 3-dB bandwidth is 35 GHz [12].

characterized by measuring the modulation side peaks after applying a small RF signal on the phase diode. The relative E-O response is plotted in Fig. 7(b). The pole at 100 MHz is introduced by the minority carrier lifetime (~ 1.6 ns). The low-frequency tuning sensitivity is around 5 – 10 GHz/mA, depending on how the lasing cavity mode is aligned to the mirror reflectivity. The relative fast RF response of the phase section diode is favorable for opto-electrical feedback systems [7], [10], [11].

The UTC photodetector is measured by a lightwave component analyzer, and it shows a 35 GHz 3-dB bandwidth

with -2 Volts bias as shown in Fig. 7(c). It is measured with the device wirebonded. By direct probing on chip, similar results have been observed. The main limit of the RF bandwidth is from the high contact resistance, which can be solved by increasing the doping level of P-InGaAs or by improving the surface preparation before P-contact metal deposition.

Since the phase relation of the 90-degree hybrid is adjustable by injecting current into the on-PIC phase shifter, the output phase is exact. The power imbalance is within 5%.

A system measurement is also carried out. By using this integrated coherent receiver PIC, an optical Costas receiver is built, and 40 Gbit/s BPSK demodulation is achieved. The bit error rates from 20 Gbit/s up to 40 Gbit/s are measured [7], [10].

V. CONCLUSION

In summary, a highly-integrated widely-tunable optical dual-quadrature coherent receiver has been demonstrated. An SG-DBR laser, a 90-degree hybrid, four UTC photodetectors and microstrip transmission lines are integrated monolithically. Device characterization and system measurements are shown.

REFERENCES

- [1] C. Doerr, *et al.*, "Monolithic polarization and phase diversity coherent receiver in silicon," *J. Lightw. Technol.*, vol. 28, no. 4, pp. 520–525, Feb. 15, 2010.
- [2] K. Nguyen, J. Garcia, E. Lively, H. Poulsen, D. Baney, and D. Blumenthal, "Monolithically integrated dual-quadrature coherent receiver on InP with 30 nm tunable SG-DBR local oscillator," in *Proc. 37th Eur. Conf. Exhibit. Opt. Commun.*, Sep. 2011, pp. 1–3.
- [3] S. Estrella, L. Johansson, M. Masanovic, J. Thomas, and J. Barton, "Widely tunable compact monolithically integrated photonic coherent receiver," *IEEE Photon. Technol. Lett.*, vol. 24, no. 5, pp. 365–367, Mar. 1, 2012.
- [4] A. Matiss, *et al.*, "Novel integrated coherent receiver module for 100G serial transmission," in *Proc. Opt. Fiber Commun. Conf.*, 2010, pp. 1–3, paper PDPB3.
- [5] R. Nagarajan, *et al.*, "Terabit/s class InP photonic integrated circuits," *Semicond. Sci. Technol.*, vol. 27, no. 9, p. 094003, 2012.
- [6] B. Mason, G. Fish, S. DenBaars, and L. Coldren, "Widely tunable sampled grating DBR laser with integrated electroabsorption modulator," *IEEE Photon. Technol. Lett.*, vol. 11, no. 6, pp. 638–640, Jun. 1999.
- [7] M. Lu, *et al.*, "An integrated 40 Gbit/s optical Costas receiver," *J. Lightw. Technol.*, 2013, to be published.
- [8] J. Raring, *et al.*, "Advanced integration schemes for high-functionality/high-performance photonic integrated circuits," *Proc. SPIE*, vol. 6126, pp. 61260H-1–61260H-20, Jan. 2006.
- [9] E. Skogen, J. Barton, S. Denbaars, and L. Coldren, "A quantum-well-intermixing process for wavelength-agile photonic integrated circuits," *IEEE J. Sel. Topics Quantum Electron.*, vol. 8, no. 4, pp. 863–869, Jul./Aug. 2002.
- [10] H. Park, *et al.*, "40 Gbit/s coherent optical receiver using a Costas loop," *Opt. Express*, vol. 20, no. 26, pp. B197–B203, Dec. 2012.
- [11] M. Lu, *et al.*, "Highly integrated optical heterodyne phase-locked loop with phase/frequency detection," *Opt. Express*, vol. 20, no. 9, pp. 9736–9741, 2012.
- [12] M. Lu, *et al.*, "A photonic integrated circuit for a 40 Gbaud/s homodyne receiver using an optical Costas loop," in *Proc. IEEE Photon. Conf.*, Sep. 2012, p. PD-4.

An Integrated 40 Gbit/s Optical Costas Receiver

Mingzhi Lu, Hyun-chul Park, Eli Bloch, Abirami Sivananthan, John S. Parker, Zach Griffith, Leif A. Johansson, *Member, IEEE*, Mark J. W. Rodwell, *Fellow, IEEE*, and Larry A. Coldren, *Fellow, IEEE*

Abstract—In this paper, a highly-integrated widely-tunable optical homodyne receiver is reported with 40 Gbaud/s data rate. By using photonic and electronic integration, the receiver is realized within a size of $10 \times 10 \text{ mm}^2$, and the system is very robust and resistive to environmental changes. An integrated photonic coherent receiver circuit is demonstrated with 35 GHz photodetector bandwidth, and the integrated local oscillator (LO) laser covers a 40 nm range. The electronic IC (EIC) has a working frequency up to 50 GHz. The feedback loop is carefully analyzed and designed, and the experimental results show $> 1.1 \text{ GHz}$ loop bandwidth, which matches the design. The hold-in range is measured to be $> 15 \text{ GHz}$. The phase noise of the transmitting laser has been cloned to the LO laser quite well, and both the linewidth measurement and phase noise measurement show no observable cross talk between binary phase shift keying (BPSK) data and the optical phase-locked loop (OPLL). Error free (bit error rate $< 10^{-12}$) is achieved up to 35 Gbit/s. The system consumes 3 Watts of power.

Index Terms—Coherent receiver, Costas loop, homodyne detection, optical phase-locked loops, optical receivers.

I. INTRODUCTION

RECENTLY, a resurgence of effort is being devoted to the research of coherent optic fiber communications, because of the advantages of higher sensitivity, better noise tolerance, and, more importantly, its compatibility with complex modulation format, such as QPSK, 16 QAM, which leads to higher spectrum efficiency [1]–[5].

In order to demodulate phase shift keying (PSK) signals, coherent detection is needed. There are generally two ways to achieve coherent detection for the optical phase shift keying (PSK) signals – homodyne detection and intradyne detection [4], [5]. The homodyne detection relies on the fixed phase relation between the transmitting laser and the local oscillator (LO) laser, which can be achieved by injection locking [6] or optical

phase-locked loops (OPLLs) [7]–[12]. On the other hand, intradyne detection is depended on digital signal processor (DSP) to correct the frequency and phase difference between the transmitting laser and the LO [5].

Research on the coherent receiver started in the early 1980s, and most of the early efforts focused on homodyne technologies. Homodyne receivers have been well studied both theoretically and experimentally [7]–[9], [12]–[15]. The main driving force of the homodyne receiver research was its highest sensitivity – 10^{-9} bit error rate (BER) can be achieved with only 9 photons per bit. However, one of the biggest problems that researchers were facing was the insufficient phase locking bandwidth relative to the LO laser linewidth. In other words, a very narrow linewidth laser was required to achieve a stable phase locking with respect to the limited loop bandwidth at that time. The limited speed of photodetectors and electronics components also limited the data rate, which gave rise to an even higher requirement on LO laser linewidth [9]. Therefore, external cavity lasers were normally used, which made the system bulky and expensive. As for an OPLL with absolute stability, the loop natural frequency ω_n and the loop delay τ should satisfy a relation of $\omega_n \cdot \tau < 0.736$ [16], which means that in order to achieve $> 100 \text{ MHz}$ loop bandwidth, $< 1.2 \text{ ns}$ loop delay is required. By using external cavity laser, bulk optics and discrete component electronics, this was very difficult at that time [17]. In order to increase the loop bandwidth and therefore make the loop more stable, photonic and electronic integration becomes necessary.

Later on, in the 1990s, with the invention of the Erbium-doped fiber amplifier (EDFA) and the wide application of wavelength division multiplexing (WDM), the interest in homodyne coherent receivers and PSK modulation dropped greatly. Many optical channels could be multiplexed into one fiber and get amplified together. Long-haul communication, and high-capacity network became more cost effective. At around year 2008, the focus on coherent communication returned, with most of the efforts focused on the intradyne receiver. The architecture of an intradyne coherent receiver normally consists of an LO laser, an optical I/Q receiver, high speed analogue-to-digital converters (ADC), and a digital signal processor (DSP). The I/Q receiver is normally built with a 90-degree hybrid and four balanced photodetectors. Complicated DSP algorithms are used to recover the data. For under-sea and long haul communications, the DSP algorithms normally include, but may not limit to, chromatic dispersion (CD) compensation, clock recovery and timing adjusting, polarization de-multiplexing and polarization mode dispersion (PMD) compensation, frequency offset estimation, phase recovery, soft forward error correction (FEC), and decision [5].

The DSP-based intradyne receiver is powerful, but the high-speed sophisticated DSP not only increases the cost of coherent

Manuscript received January 15, 2013; revised May 10, 2013; accepted May 21, 2013. Date of publication May 29, 2013; date of current version June 14, 2013. This work is supported by DARPA CIPHER (PICO) program. A portion of this work was completed in the UCSB nanofabrication facility, part of NSF funded NNIN network. The EIC fabrication was done at Teledyne Scientific.

M. Lu, H.-C. Park, A. Sivananthan, J. S. Parker, L. A. Johansson, and M. J. W. Rodwell, are with the Department of Electrical and Computer Engineering, University of California, Santa Barbara, CA 93106 USA (e-mail: mlu@ece.ucsb.edu; hcpark@ece.ucsb.edu; asivananthan@ece.ucsb.edu; JParker@ece.ucsb.edu; leif@ece.ucsb.edu; rodwell@ece.ucsb.edu).

E. Bloch is with Department of Electrical Engineering, Technion—Israel Institute of Technology, Haifa 32000, Israel (e-mail: bledi@tx.technion.ac.il).

Z. Griffith is with Teledyne Scientific and Imaging Company, Thousand Oaks, 1049 Camino Dos Rios, CA, 91360 USA (e-mail: zgriffith@teledyne-si.com).

L. A. Coldren is with the Department of Electrical and Computer Engineering and the Department of Materials, University of California, Santa Barbara, CA 93106 USA (e-mail: coldren@ece.ucsb.edu).

Color versions of one or more of the figures in this paper are available online at <http://ieeexplore.ieee.org>.

Digital Object Identifier 10.1109/JLT.2013.2265075

receiver tremendously, but also suffers from high power consumption. For shorter distance, where dispersion effects are not severe, the application of DSP may be overkill, even though only part of the algorithm steps are necessary for short distance.

In order to solve the high-cost and high power consumption problems that intradyne receivers have, OPLL-based homodyne receivers become an alternative. Regarding the technical problems that researchers had in the 1980s, most of them can be solved by advanced integration technologies. Integration makes the system smaller and more stable. The smaller size also leads to a shorter loop delay for the OPLL, and therefore a much wider loop bandwidth [16]–[21]. Wide loop bandwidth contributes to the better system reliability, and better laser phase noise suppression. Since there is no high-speed DSP involved, the OPLL-based receiver can be much cheaper, and has significantly lower power consumption, compared to DSP-based intradyne receivers.

The first highly integrated homodyne BPSK optical coherent receiver was proposed, and a part of the measurement results were demonstrated in our recent publications [11], [22]–[25]. In this paper, more detailed and comprehensive system design, analysis, implementation, device fabrication, and measurement results are described systematically. By photonic and electronic integration, the whole receiver system is realized within a size of $10 \times 10 \text{ mm}^2$. The loop bandwidth is measured to be $> 1.1 \text{ GHz}$, which is the highest to the best of our knowledge. 40 Gbit/s real-time BPSK data demodulation has been achieved. The system also shows very good stability and reliability in terms of temperature fluctuation. The power consumption is below 3 Watts, 0.5 Watts from the PIC and < 2.5 Watts from the EIC, negligible (~ 0.07 Watts) from the loop filter. The thermoelectric controller power consumption is not included.

II. COSTAS LOOP AND SYSTEM ANALYSIS

A. Optical Costas Loop and its Components

Among all homodyne coherent receiver architectures, Costas loop is one of the most robust and commonly used. The electrical Costas loop has been applied to many applications, such as GPS receivers and orthogonal frequency-division multiplexing (OFDM). Sharing a similar architecture, optical Costas loops have also been well studied, such as decision-driven Costas loop [7]. The general architecture of the Costas loops are shown in Fig. 1(a). By phase shifting one branch of the LO by 90° , and beating with the incoming signal, in-phase (I) and quadrature (Q) signals are generated and mixed at a mixer. The mixer output feeds back to the LO, which can either be a voltage-controlled oscillator (VCO) or a current-controlled oscillator (CCO). A loop filter is built in the loop to realize the desired loop characteristics, such as loop order, bandwidth, phase margin and gain margin.

The optical Costas loop shares the same architecture [8]. A more detailed schematic of this optical Costas-loop-based coherent receiver is shown in Fig. 1(b). A widely-tunable sampled-grating DBR (SG-DBR) laser acts as the CCO, and the quadrature signals are generated in an optical 90° -degree hybrid, where the 90° phase shift is introduced by an optical phase shifter, based on current injection. The I/Q signals are detected by four high speed photodetectors, which not only convert the

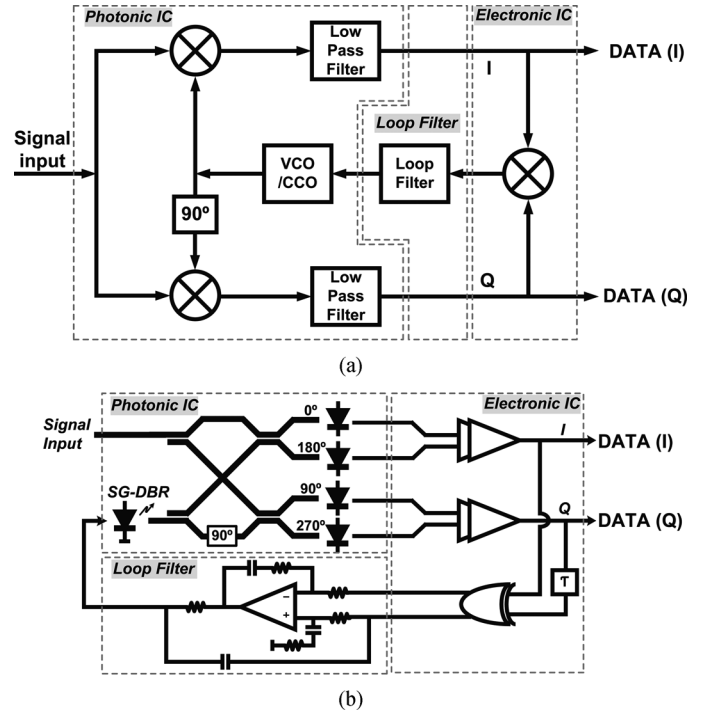


Fig. 1. (a) The classic model of a Costas loop. (b) shows the detailed architecture of the Costas loop based OPLL. The PIC, EIC and loop filter are labeled in both (a) and (b).

optical signal to electrical signal, they also act as low pass filters. The mixer is realized by a delay line and an XOR gate, which act together as a quadri-correlator phase/frequency detector (PFD) [26]. The error signal from the PFD feeds back to the laser tuning section through the loop filter.

By photonic and electronic integration, the system has been realized within a size of $10 \times 10 \text{ mm}^2$, and the total loop delay is as small as approximately 120 ps, where 40 ps is from the photonic IC (PIC), 50 ps is from the electronic IC and 30 ps is from the loop filter. On the photonic integrated circuit (PIC), a widely-tunable SG-DBR, an optical 90° -degree hybrid, four photodetectors and RF transmission lines are integrated monolithically [22]. The Electronic IC (EIC) integrates four limiting amplifier (LIA) chains, a 10 ps delay line and an XOR gate. The input signals from the photodetectors on PIC are hard limited by the LIAs and therefore small optical power fluctuations will not influence the system performance. The delay lines and the XOR gate together act as a phase and frequency detector, which can also be understood as a quadri-correlator [25], [26]. The frequency error response is linear, and the frequency detection sensitivity is $0.3 \text{ V}/25 \text{ GHz}$, which is determined by the delay time and EIC output maximum voltage. The XOR gate itself also acts as a nonlinear phase detector, which can be analyzed by the equivalent linear gain for simplicity [11].

The third part of this Costas loop is an active loop filter (LF), where a novel two-path loop structure has been applied [11], including an active slow path and a passive feed-forward fast path. The feed-forward path includes no active components and provides the shortest delay possible for high frequency signals, while the active path is composed of an operational amplifier (Op-amp) based active filter, which gives more gain at lower frequency, and also makes sure the loop type (type II) does not

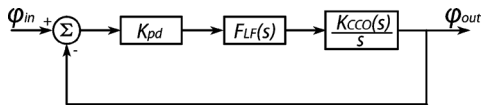


Fig. 2. Basic PLL model.

get jeopardized [27]. The structure of this loop filter is also shown in Fig. 1(b).

B. Loop Analysis

As for the loop analysis, both analytical and numerical methods are used to characterize this Costas OPLL, as well as the frequency-locked loop. Based on the loop model as shown in Fig. 2, the open loop transfer function of this OPLL is

$$G(s) = K_{PD} \cdot \frac{K_{CCO}(s)}{s} \cdot F_{LF}(s) \cdot e^{-s\tau}, \quad (1)$$

where K_{PD} is the phase detector sensitivity [V/rad], $F_{LF}(s)$ is the loop filter response [A/V], $K_{CCO}(s)$ is the CCO (LO laser) sensitivity [rad/Hz/A], and $e^{-s\tau}$ represents the loop delay effect. As mentioned before, the phase detector sensitivity K_{PD} is defined by the EIC gain and its output peak-to-peak voltage. Since the signal is digitized in the LIAs, the phase detector becomes a bang-bang type. To simplify the analysis, linear equivalent sensitivity is estimated and used in the loop analysis [11]. $K_{PD} = 0.2 - 0.4$ V/rad.

The CCO sensitivity $K_{CCO}(s)$ is a function of frequency, and can be expanded as

$$\frac{K_{CCO}(s)}{s} = \Re_{CCO} \cdot \frac{1}{1 + s\tau_{laser}} \cdot \frac{1}{s}, \quad (2)$$

where \Re_{CCO} is the laser phase section tuning responsivity in unit of [Hz/A], τ_{laser} is time constant from the minority carrier lifetime, and the pole at zero frequency shows the frequency to phase conversion integral.

In order to obtain wider loop bandwidth, enough phase margin and gain margin for loop stability, the loop filter response $F_{LF}(s)$ need to be carefully designed. It is a two-path loop filter design, and the expression of $F_{LF}(s)$ can be written as

$$F_{LF}(s) = A \cdot \frac{1 + s\tau_2}{s(1 + s\tau_1)} \cdot \frac{1}{R_1 + R_{ph}} \cdot e^{-s\tau_{OP}} + \frac{1}{2} \cdot sC_{FF}. \quad (3)$$

The first term on the right hand side of this equation represents the Op-amp path, and the second term is the feed-forward path. τ_1 is the parasitic parameter from the commercial Op-amp, and τ_2 is a RC time constant introduced to avoid 180° phase difference when the responses of the two paths cross each other in frequency domain. A is the gain constant of the first path of the loop filter. R_{ph} represents the laser phase section diode I-V curve slope at the biased current (normally ~ 2 mA for this Costas receiver). τ_{OP} is the extra delay introduced by Op-amp, which can be around or even larger than several ns.

The total closed-loop response is

$$H(s) = \frac{G(s)}{1 + G(s)}. \quad (4)$$

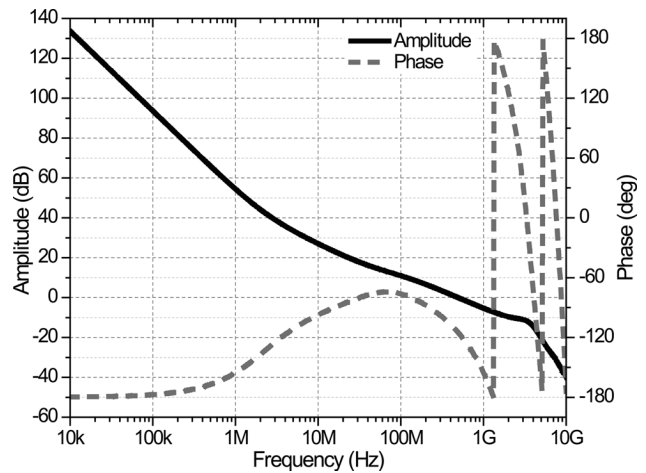
Fig. 3. Bode plot of the open loop response $G(s)$.

TABLE I
DESIGNED LOOP PARAMETERS

Parameters	Values	Descriptions
K_{PD}	0.2 - 0.4 V/rad	Phase detector sensitivity
τ	120 ps	Loop delay with feed-forward path
\Re_{CCO}	8 GHz/mA	CCO laser tuning responsivity
τ_{laser}	1.6×10^{-9} sec	Time constant for laser tuning
A	1×10^6 sec ⁻¹	LF constant
τ_1	8.0×10^{-10} sec	Parasitic time constant from Op-amp
τ_2	7.2×10^{-8} sec	RC Time constant of LF
R_1	500 Ω	Series resistor value at LF output
R_{ph}	100 Ω	Phase tuning section AC resistance
C_{FF}	1.0 pF	Feed-forward capacitor value

The loop parameters are listed in Table I. The simulated loop response is plotted in Fig. 3. As we can see, a 550 MHz open-loop bandwidth has been achieved with 65 degree phase margin, and 7.4 dB gain margin at 1.35 GHz, where the phase response is π .

III. LOOP COMPONENTS – PIC, EIC AND LOOP FILTER

In order to design a robust synchronized homodyne coherent receiver, one of the most important considerations is the loop delay, and photonic and electronic integration becomes a perfect solution. Integration not only decreases the size of the device, which leads to shorter loop delay, but also makes the coherent system more stable and more resistive to environment changes [28]. In this section, the design details about the PIC, the EIC and the loop filter will be explained respectively.

A. PIC Design and Fabrication

As mentioned in the previous sections, the PIC includes an SG-DBR laser as the LO laser, an optical 90-degree hybrid to mix the signal and the LO, four high-speed uni-traveling-carrier (UTC) photodetectors, and microstrip transmission lines. The PIC is designed and fabricated based on semi-insulating (SI) InGaAsP/InP material. The architecture of the PIC is shown in Fig. 4 as well as a microscope picture.

The SG-DBR laser has a super-mode spacing of 7 nm, and is designed to cover 40 nm range. The phase tuning pad of the SG-DBR laser is used for the current feedback. Compared to other tuning mechanisms, such as temperature tuning or quantum stark effect, the current injection to a phase diode with a wider bandgap can change the laser frequency fast

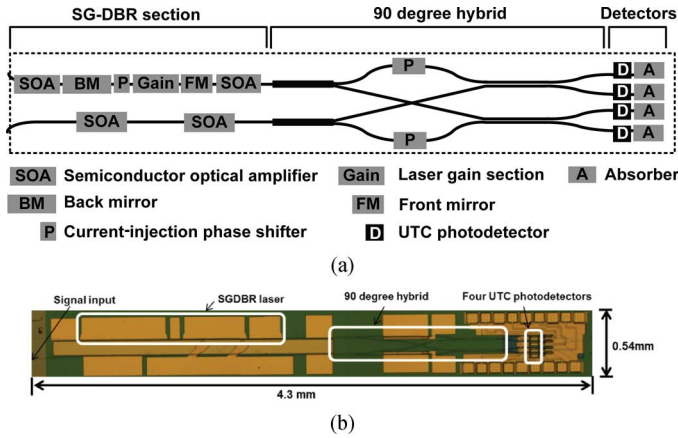


Fig. 4. (a) shows the schematic of the PIC, including three sections: an SG-DBR laser, a 90-degree hybrid and four uni-travelling carrier (UTC) photodetectors. (b) shows a microscope picture of the PIC. The different integrated components are labeled in both (a) and (b).

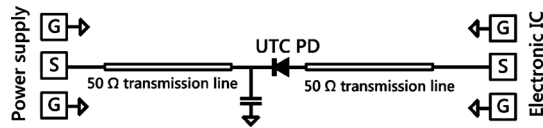


Fig. 5. Circuit schematic of the photodetector bias circuit on PIC.

and efficient, which leads to wider loop bandwidth and larger pull-in range. It also does not have the 180° phase transition at low frequency (normally < 1 MHz) as single-electrode lasers have [29].

The 90-degree coupler design is also shown in Fig. 1(b). It uses a 1-by-2 multi-mode interference (MMI) couplers as the first stage, which split the LO and the incoming signal into two paths, respectively. The symmetry of 1-by-2 MMI coupler ensures equal splitting. Directional couplers are used as the second stage couplers in the 90-degree hybrid, because a) directional couplers have the minimum reflection among all couplers, which is very important to avoid injection locking since there is no isolator on PIC; b) it acts as a perfect 180 degree hybrid and the phase relationship is always correct, regardless of splitting ratio.

Four UTC photodetectors are also integrated on this PIC as well as transmission lines. Because the EIC can only provide a voltage between -1.5 and -2 V, it is designed so that the UTC photodetectors can have positive voltage supplies to the N-contact in order to deplete the collector. The circuit model is shown in Fig. 5. Both P and N contacts are led to the GSG pads on the edges of the PIC by transmission lines, and a capacitor is also integrated to provide a high frequency ground on the PIC. The photodetector has a size of $3 \times 20 \mu\text{m}$. The designed quantum efficiency is above 95%, and with a 50Ω load the 3-dB bandwidth can be above 50 GHz depending on the contact resistance. [23]

B. Electronic IC and Loop Filter

The electronics part of this Costas receiver includes an EIC and a loop filter. The BPSK receiver EIC is designed to work with the PIC having a 4-phase (I/Q) optical interferometer. With measurement of the I and Q signals, a signal proportional to optical frequency difference is formed by amplifying the I and

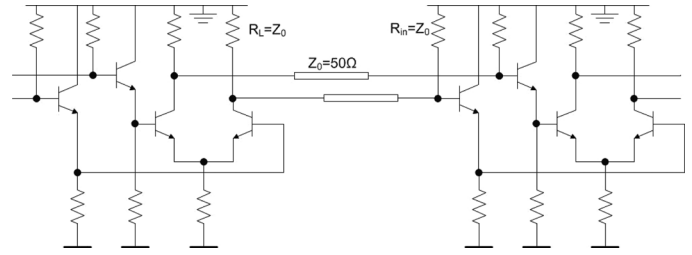


Fig. 6. Schematics of the limiting ECL gates merged in a 50Ω transmission lines environment.

Q signals, providing a relative delay, and mixing. Under zero offset frequency, the IC output is proportional to the optical phase difference; in the presence of an optical frequency difference, the IC output is proportional to this frequency difference. The phase/frequency difference function is provided to enable PLL locking even with initial frequency offsets as large as $+/- 50$ GHz, although in real case the LO laser cavity mode spacing sets a limit to the largest possible initial offset frequency range.

Fig. 1(b) shows a block diagram of the full BPSK receiver. The BPSK phase-frequency detector, denoted by the grey frame, receives its input from the optical interferometer. Assuming the LO laser electrical field is $E_{LO} = A_{LO} \cos(\omega t + \Delta\theta)$ and the carrier laser electrical field is $E_c = A_c \cos(\omega t + \Delta\theta)$, the optical interferometer provides the in-phase beat note $I = B \cos(\Delta\omega t + \Delta\theta)$ and the quadrature-phase beat note $Q = B \sin(\Delta\omega t + \Delta\theta)$, thus carrying an information on both phase and frequency offset magnitude and sign. The core of the phase-frequency detector (PFD) [25] consists of a delay line in the Q arm and a XOR gate, which is based on a Gilbert multiplier topology. To reduce the dependency on the LO and reference lasers photocurrent, The PFD is preceded by a high gain emitter coupled logic (ECL) limiting amplifier chain in order to convert the signals into a rail to rail square wave – Fig. 6. All the ECL gates are biased by a tail current of 12 mA, hence providing a differential signal of 600 mV at a full swing mode, large enough to provide a full limiting ($\gg kT/q$) as more is explained in [25].

In case of frequency detection, the Q signal is delayed by τ and then mixed with I. A linear, small signal analysis of the PFD, (5), suggests that the output signal consists of two components: a high frequency component with a double frequency but zero average and a DC component with magnitude proportional to the offset frequency Δf . Since the PFD output is integrated by a low frequency hybrid loop filter, the low frequency component is the one to consider.

$$\begin{aligned} I'(t) \oplus Q'(t - \tau) &= \cos(\Delta\omega t + \Delta\theta) \cdot \sin(\Delta\omega(t - \tau) + \Delta\theta) \\ &= 0.5 \sin(2\Delta\omega t - \Delta\omega\tau + 2\Delta\theta) + 0.5 \sin(\Delta\omega\tau) \end{aligned} \quad (5)$$

By setting $\tau = 10$ ps, the DC term of (5), provides an unambiguous frequency detection characteristics of $\Delta f = \pm 50$ GHz.

Due to the limiting amplifiers, the I/Q signals result in a hard limited square waves. In this case, the PFD output will provide a double frequency square wave with varying duty-cycle that depends on the frequency offset, resulting in the same frequency detection characteristics. Measurement data of the PFD in frequency detection mode is presented in then next section.

At phase detection mode, when $\Delta f = 0$, the PFD output is $\sin(2\Delta\theta)$. The periodic phase detection characteristic, with a factor of 2 in the sin argument makes the loop stable for both 0 and 180 degrees offset. This particular property allows the loop to lock on a BPSK modulated carrier.

This EIC is fabricated using Teledyne's 500 nm HBT process, and each transistor has 300 GHz f_t and f_{max} .

The output of the EIC goes into a loop filter. It contains a short passive path and an active path with longer delay [11]. A commercial Op-amp is used as the active component, and it provides 200 MHz unity-gain bandwidth. The loop filter is built on an AlN carrier with chip resistors and capacitors with a size of 0201.

C. PIC to EIC Interconnections

Since the output of the UTC photodetectors are directly connected to the EIC input and the signal frequencies can be as high as 40–50 GHz, signal integrity may be a serious issue if the interconnection is not well designed. Both RF pads on PIC and EIC have a pitch size of 100 μm . In order to partially compensate the inductance introduced by wirebonds, the ground-signal-ground (GSG) pads on PIC are carefully designed to be a little capacitive. The finite-element full-wave simulation shows that as long as the wirebonding is shorter than 200 μm ($\sim 60 \mu\text{m}$ between the edges of the two GSG pads), 100 GHz interconnection between can be achieved between PIC and EIC with less than 1 dB loss. The simulated S-parameters are shown in Fig. 7(a) as well as a picture of the simulation model. Another situation is also simulated, where the PIC and EIC are wirebonded to the AlN carrier separately, and they are connected through the co-planar waveguide on the carrier. The distance between the two chips is 0.85 mm, and wire length is 380 μm from PIC to carrier, and 500 μm from EIC to carrier. The simulation shows that the 3-dB bandwidth is more than 40 GHz (Fig. 7(b)). The latter case is used for this Costas receiver packaging.

The two pictures in Fig. 7(a) and (b) are plotted in different scales, and the real device sizes are the same. As mentioned above, the GSG pads have a 100 μm pitch size, the signal pad on the PIC is 75-by-75 μm , and the signal pad on EIC is 75 μm wide and 100 μm long. The InP substrate thicknesses of both PIC and EIC are 6 mil.

IV. DEVICE CHARACTERIZATION AND SYSTEM MEASUREMENT

A. Device Characterization

The PIC and EIC are characterized separately before they are used to build the Costas receiver.

The on-PIC SG-DBR laser shows a tuning range from 1541 to 1583 nm. For the L-I-V measurement, only the gain section of the laser is biased, and the boosting semiconductor optical amplifier (SOA) next to the front mirror is reversed biased as an absorber to measure the output optical power. The threshold current of the SG-DBR laser is 25 mA, and with 180 mA bias, output power can almost reach 20 mW without the boosting SOA [23]. Since the whole circuit is built on surface ridge waveguide structure, which provides small on-chip reflection, there is no injection locking has been observed.

The phase tuning section of the SG-DBR laser shows around $\Re_{CCO} = 5 - 10 \text{ GHz/mA}$ tuning sensitivity. Because the

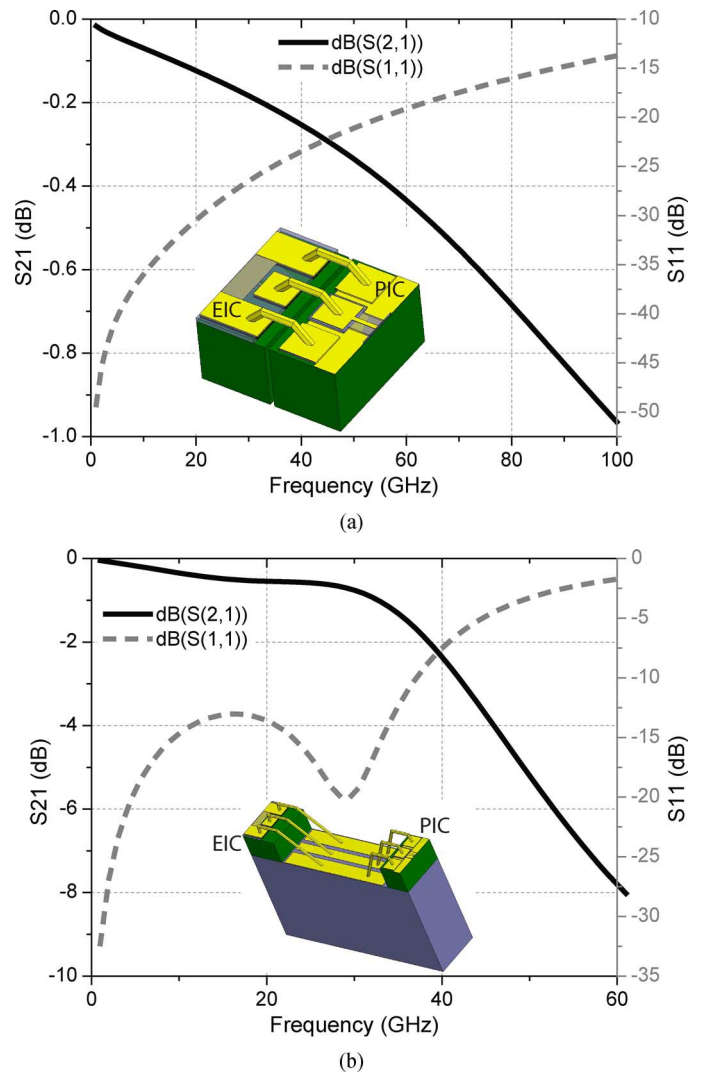


Fig. 7. Full-wave simulation results of the GSG pads for interconnections. The golden color represents gold, green color represents InP, and gray box represents AlN. (a) The wirebond is directly from one chip to the other. (b) The PIC and EIC are wirebonded to the carrier separately, and they are connected through the co-planar waveguide on the carrier.

mirror reflectivity of the SG-DBR is not necessarily flat, the lasing wavelength change leads to the change of mirror reflectivity, which therefore changes the threshold current and the carrier density in the gain section. If the reflectivity slope is negative versus wavelength, the carrier density change in the laser gain section will increase with the current injection into the phase tuning section, which favors the frequency tuning sensitivity. Otherwise, if the reflectivity slope is positive, the tuning sensitivity is lower. The measurement shows that \Re_{CCO} can vary roughly by a factor of 2, depending on how the lasing peak is aligned to the mirror reflection peak.

The RF response of the phase section is also measured. By injecting AC current into the phase diode, the laser is modulated. The injected AC current generates two modulation side lobes, which indicates the frequency response of the laser phase section. The measurement result is shown in Fig. 8. Curve fitting confirms a pole at 100 MHz, which means the time constant τ_{laser} equals 1.59 ns. This also presents the carrier life time in

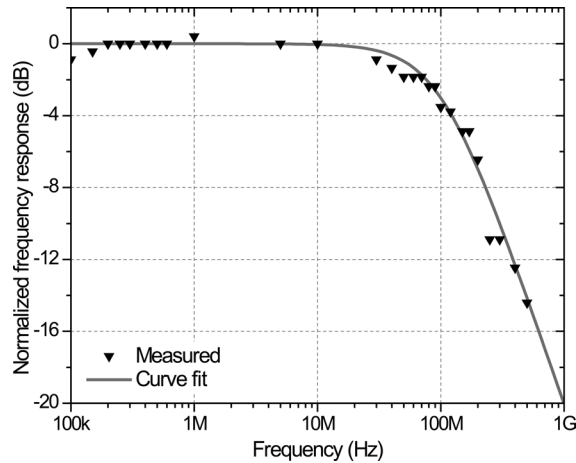


Fig. 8. Relative frequency response of the phase section diode in the SG-DBR laser.

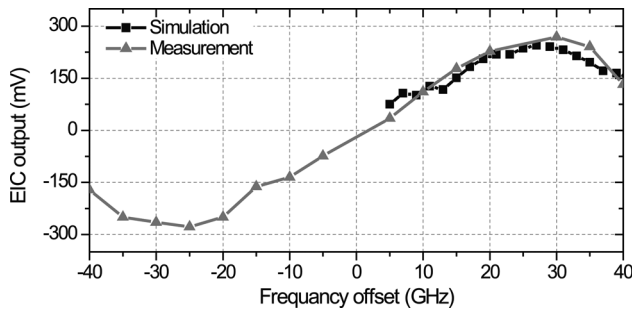


Fig. 9. PFD standalone frequency detection response, measurements versus simulation [25].

the waveguide passive section of this integration form. The mismatch between experimental result and fitted curve at low frequency is due to the cut-off frequency of the bias-Tee used in the measurement.

The 90-degree hybrid is also characterized. The power imbalance in the four photodetectors are within 5%, and the phase can be exact, since there is a tunable phase shifter in the hybrid, and the directional coupler always acts as an 180 degree hybrid, regardless of coupling ratio.

The UTC photodetector characterization is carried out by using a lightwave component analyzer (LCA). The UTC photodetector is wirebonded to the AlN carrier before testing, since in the following system testing they have to be wirebonded. Amplitude modulated laser signal is coupled into the waveguide and detected by the UTC photodetector, and the RF response is then measured by the LCA. All the cable and probe losses are de-embedded. The measurement is based on the 50 Ω load. The 3-dB bandwidth is measured to be around 35 GHz with -2 V bias [22], [23]. The major limit of the bandwidth is from the contact resistance. The measured contact resistance of this PIC is around $7000 \Omega \cdot \mu\text{m}^2$, which leads to around 100Ω contact resistance for each UTC photodetector. The saturation current is 18 mA with -5 V bias.

As for the EIC, the electrical testing shows it fully functional. By adjusting the input frequency, the output voltage of the EIC is measured. As shown in Fig. 9, the measured result matches with simulation quite well.

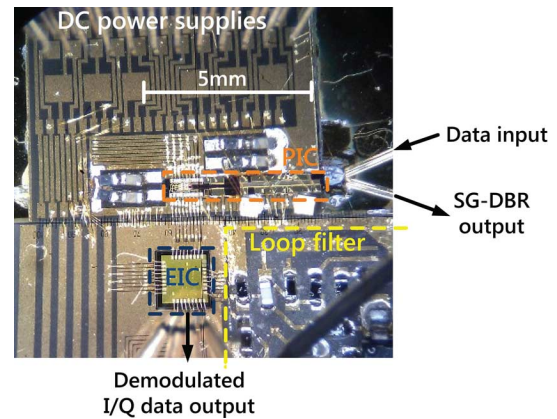


Fig. 10. Microscope picture of the Costas receiver on the test stage. The DC probe card provide DC supplies to the device from the top side of the image. The optical input and output are from the right hand side of the picture, and a four-signal-line RF probe is used to measure the demodulated I/Q output.

The more detailed testing results of this EIC is discussed in [25], and the design, fabrication and measurement result of the PIC can also be found in [22], [23].

B. OPLL Testing

The PIC, EIC and loop filter are then mounted on AlN carriers and wirebonded together. The size of the system is around $10 \times 10 \text{ mm}^2$. The incoming signal is coupled into the PIC through a lensed fiber, and the SG-DBR power is coupled out to another lensed fiber through the back mirror for monitoring purpose. All the DC power supplies are connected through a DC probe card. The demodulated signal is obtained from the EIC output ports. A microscope picture of the Costas receiver is shown in Fig. 10, and PIC, EIC and loop filter are also labeled in the picture.

The Costas receiver is first tested as an OPLL. A tunable external cavity laser (ECL) is used as a reference laser with a linewidth of 80 kHz. The power of the reference laser is first coupled into the Costas receiver directly without any modulation, and the optical power of the SG-DBR laser is coupled out from the PIC and beat with the reference on an external high speed photodetector. An acousto-optic modulator (AOM) is applied to introduce a 100 MHz frequency offset. The beating spectrum between the reference laser and phase-locked SG-DBR laser is observed on an electrical spectrum analyzer (ESA). The test setup is shown in Fig. 11(a), and the beating spectrum on ESA is shown in Fig. 11(b) [18]. In Fig. 11(b), the 100 MHz peak is the beating between the SG-DBR laser and the reference ECL when they are phase locked. The 1.2 GHz peak is because of the damping of the OPLL, which indicates the loop bandwidth, and the 1 GHz peak is the ‘folded’ peak from the lower sideband. Therefore, the frequency difference between the main peak and the sidelobes is 1.1 GHz. Since the sidelobes are caused by the damping of the loop, the actually loop bandwidth is wider than the damping peaks [27]. The sidelobes set a lower limit for the actual closed-loop bandwidth, and the actual loop bandwidth is larger than 1.1 GHz. To the best of our knowledge, it is the widest OPLL bandwidth that has ever been reported.

Loop bandwidth measurement is also done by introducing a phase error signal in the loop. A LiNbO_3 phase modulator has

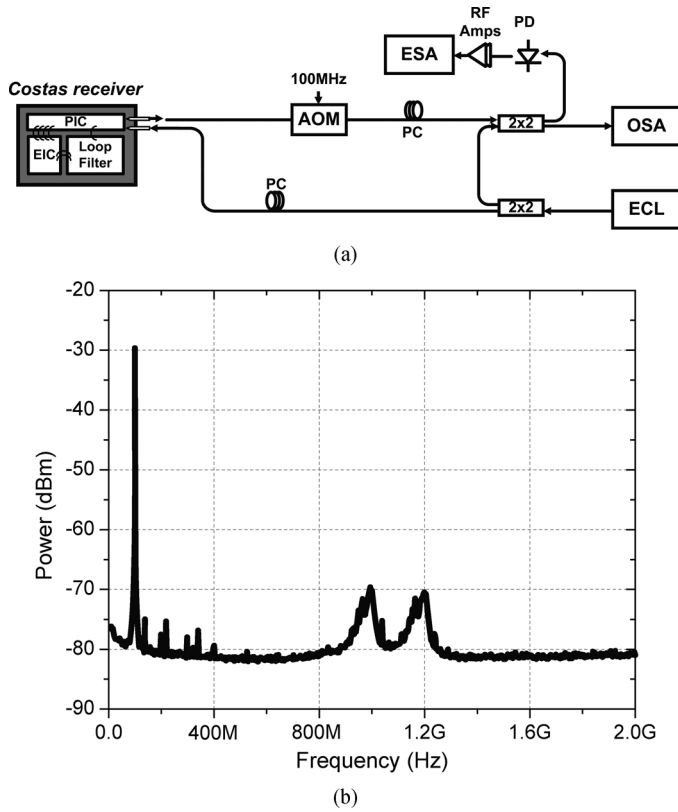


Fig. 11. (a) The test setup for the OPLL. (b) The beating spectrum of the two lasers when they are phase locked. The resolution bandwidth is 100 kHz.

been included in the loop and relative loop response is measured on the ESA [27]. The test setup is shown in Fig. 12(a). The phase error $\Delta\varphi_{e,in}(s)$ is generated at the phase modulator, and the SG-DBR laser phase response to this phase error can be written as

$$\Delta\varphi_{e,out}(s) = \Delta\varphi_{e,in}(s) \cdot H(s) \quad (6)$$

according to (4). Since the ESA measures the residual phase noise spectrum between the SG-DBR laser and the unmodulated reference, the spectrum peak power, introduced by the modulated reference, is proportional to the square of the closed-loop transfer function.

$$P_{ESA}^{peak}(f_s) \propto \left| \frac{\varphi_{e,out}(j2\pi f_s)}{\varphi_{e,in}(j2\pi f)} \right|^2 = |H(j2\pi f_s)|^2, \quad (7)$$

where $P_{ESA}^{peak}(f_s)$ is the measured peak intensity on ESA, f_s is the signal generator frequency and also the peak frequency on ESA, and $j2\pi f \equiv s$. The normalized measurement result is shown in Fig. 12(b) as well as the simulated closed-loop function. The peaking at 1 GHz is probably because of the parasitic inductance in PIC and loop filter interconnection.

Furthermore, frequency pull-in and phase-locking is observed. By simply tuning on the loop, the two lasers are phase locked automatically. Even under the condition that the original frequency offset between two lasers is as large as 17.5 GHz, success frequency pull-in and phase locking has been observed after tuning on the loop. The pull-in range is dependent on the working conditions of the OPLL, especially on the LO laser.

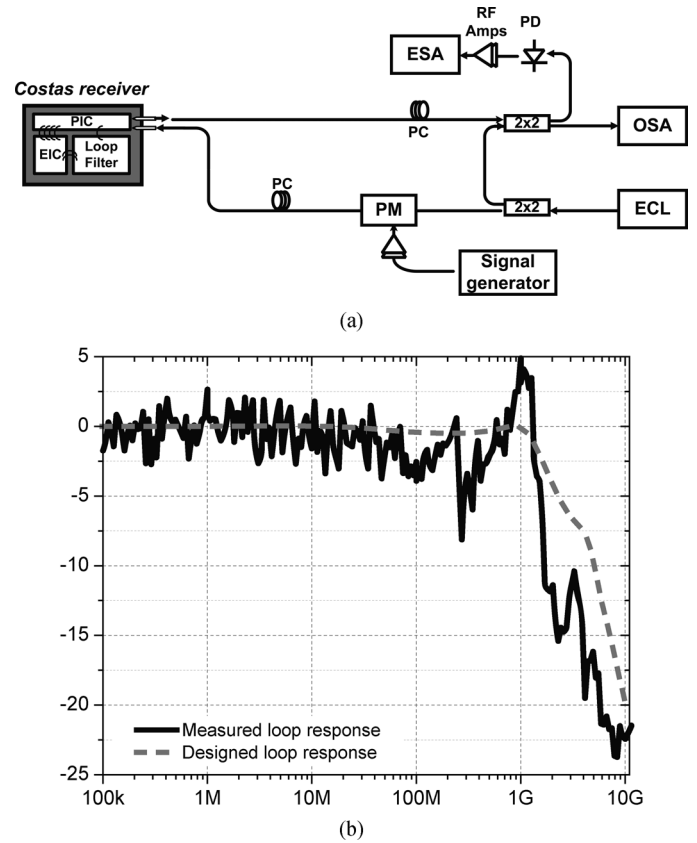


Fig. 12. (a) The test setup for loop bandwidth measurement. (b) shows the measured loop bandwidth (solid line) and the simulation result (dash line) as a comparison.

Frequency pull-in can only happen within one laser cavity mode.

By turning on the feedback loop, the SG-DBR laser frequency will be automatically pulled towards the reference laser frequency, and the phase lock loop starts to function when the frequency difference is within around 1 GHz. It is worth mentioning that it is the frequency locked-loop (FLL) that decides the pull-in range rather than the phase-locked loop, and FLL pull-in range is decided by the delay line in the EIC and the laser cavity mode spacing. In other words, it is not limited by the OPLL bandwidth any more. The whole pull-in and locking process takes hundreds of nanoseconds. The relatively slow frequency pull in is because of the bandwidth of the FLL bandwidth. As a first order loop, the FLL only has a designed bandwidth of 178 kHz. The frequency/phase pull-in curve is shown in Fig. 13. It is measured by applying an on-off keying modulation on the incoming signal. The OPLL will have frequency/phase pull in and lock when the incoming signal is *ON*, and lose lock when it is *OFF*. The in-phase output of the EIC is monitored on a real-time oscilloscope. As we can see, the SG-DBR laser is locked and unlocked periodically. The frequency pull-in speed is still relatively slow in the range of hundreds of nano-second. However, by redesign the loop characteristics, the pull-in speed can be possibly decreased by roughly two orders.

In addition, more than 30 GHz (> 15 GHz single-sideband) hold-in range has been observed. Within a 2.6°C temperature fluctuation, the OPLL stays locked.

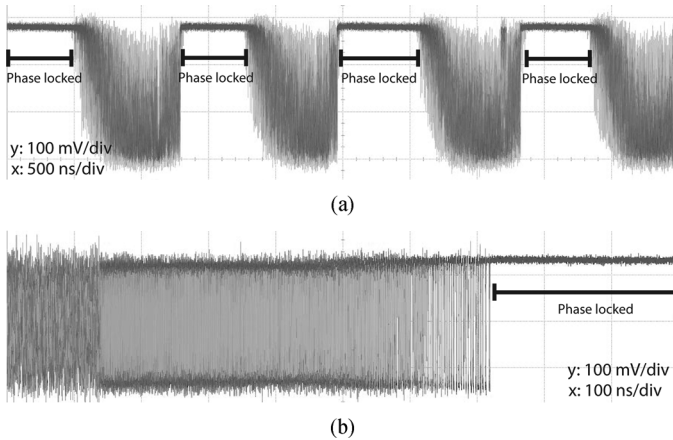


Fig. 13. The real-time oscilloscope result of the OPLL frequency pull-in and phase locking. Four periods are shown in (a), and (b) shows another set of time domain data with a smaller span.

C. Linewidth and Phase Noise Measurement

As for the linewidth measurement, self-heterodyne method is used. The laser under testing is split into two branches, a 25-km fiber delay is in one branch to get rid of the coherence and an acousto-optic modulator (AOM) is in the other branch to introduce the 100-MHz offset frequency. The linewidth of the reference laser is first measured, and 80 kHz full width at half maximum (FWHM) linewidth is obtained. The free-running SG-DBR (LO) laser linewidth has also been measured using the same method, and the FWHM linewidth is roughly 10 MHz.

The SG-DBR laser is then phase locked to the reference laser, and the linewidth of the phase-locked SG-DBR laser is measured. After applying the BPSK-modulated signal on the reference laser, the linewidth of the SG-DBR laser has been measured again. The test setup is shown in Fig. 14(a), and the results can be found in Fig. 14(b). As we can see, the locked SG-DBR laser has the same linewidth as the reference, even when the reference is modulated by a BPSK signal. The data rate is 25 Gbit/s, and $2^{31} - 1$ pseudo-random binary sequence (PRBS) data is used.

The phase noise of this OPLL system is also measured on the ESA, and the test setup is shown in Fig. 15(a). In order to cancel out the reference laser noise, the fiber length is well matched with a length error smaller than 1 meter. As indicated in Fig. 15(b), the phase noise curves with and without data modulation match very well, which confirms that there is no observable data-OPLL cross talk in this Costas receiver, and also verifies the good matching in the linewidth measurement. The phase noise of the RF source that is used to drive the AOM is also measured for comparison. For all four sets of measurement, the signal power is always kept at -30 dBm, and the background noise is taken based on the assumption of the same signal power.

Comparing the OPLL phase noise with the signal generator phase noise, both of them reach the ESA noise floor at the frequency above 50 kHz, and the 1.1 GHz peak indicates the closed-loop bandwidth. However, at frequencies below 50 kHz, the OPLL present more noise compared to the RF source. This low frequency noise component is believed to be introduced by the test setup rather than OPLL itself. The fiber vibration can be one of the possible justifications. It causes phase fluctuation

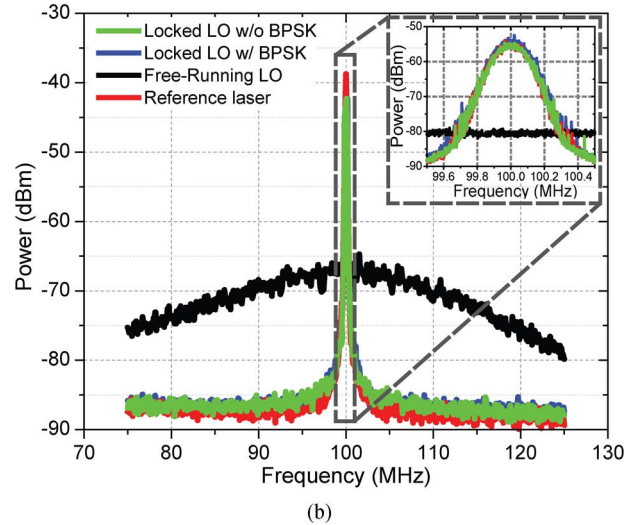
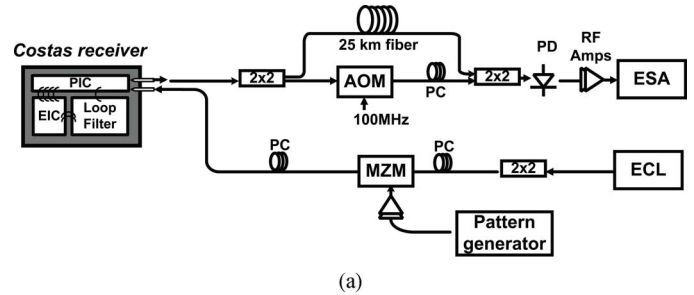


Fig. 14. (a) The test setup for linewidth measurement. (b) shows the measured linewidth of the reference laser (red), the free running SG-DBR (LO) laser (black), the phase-locked SG-DBR laser without modulated signal input (green), and the phase-locked SG-DBR with BPSK modulated signal input (blue). A zoomed-in plot is shown in the upper right corner. The resolution bandwidths are 50 kHz and 3 kHz, respectively.

in the Mach-Zehnder Interferometer formed by two 2-by-2 fiber couplers, which may lead to higher low-frequency residual phase noise. Another possible cause is the fiber mismatch. If the fiber path length matching is not perfect, the laser phase noise will not be totally canceled out, and consequently shown on the OPLL phase noise.

D. Bit Error Rate Measurement

As for data reception of a Costas loop, the same as DSP-based intradyne systems, phase ambiguity needs to be taken into consideration. The incoming signal phase will be doubled in the quadri-correlator PFD, by which the 0 and π signal phase will be erased. However, the carrier phase will also be doubled at the same time, which means that the carrier phase of π and 2π become identical and indistinguishable to the OPLL. One way to solve this phase ambiguity problem is using differential encoding and decoding.

In the experiment, since PRBS data is used (the differential sequence of a PRBS is itself), no encoder is needed at the transmitter side. On the receiver output, the output data sequence needs to be decoded. One bit delay is introduced to the \bar{I} output, and an XOR operation is carried out on the I and delayed \bar{I} signals, and resulting output of the XOR gate is the inverse of the original PRBS sequence. The output of the XOR gate is connected to a bit error rate tester (BERT), and BER is then obtained. The eye diagram is measured at the EIC output directly

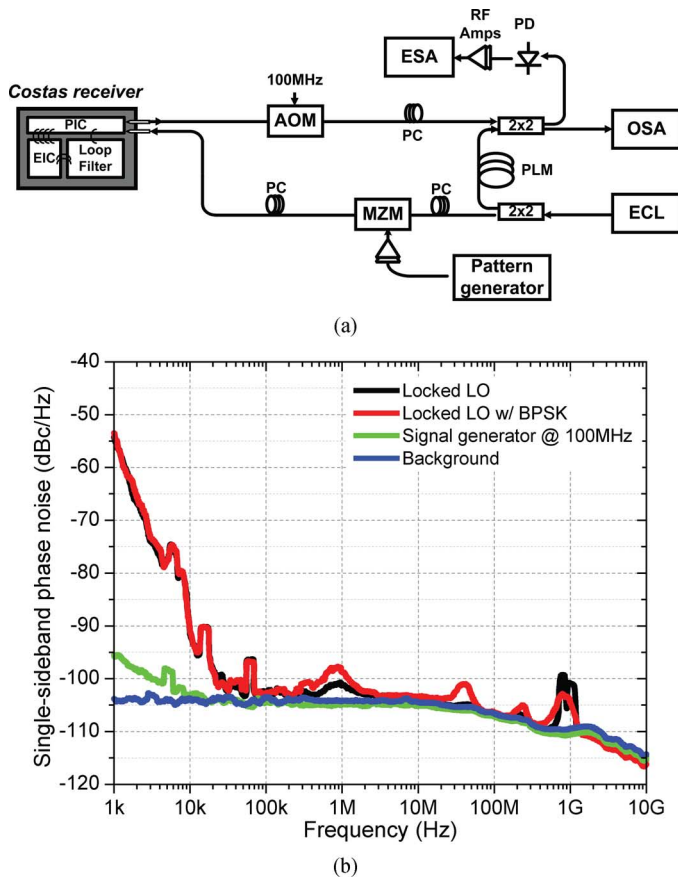


Fig. 15. (a) The test setup for phase noise measurement. (PLM: path length matching.) (b) shows the measured phase noise of the beating between the phase-locked SG-DBR laser and the reference laser with (red) and without (black) data modulation. The ESA background noise (blue), and the 100-MHz RF signal phase noise (green) are also plotted.

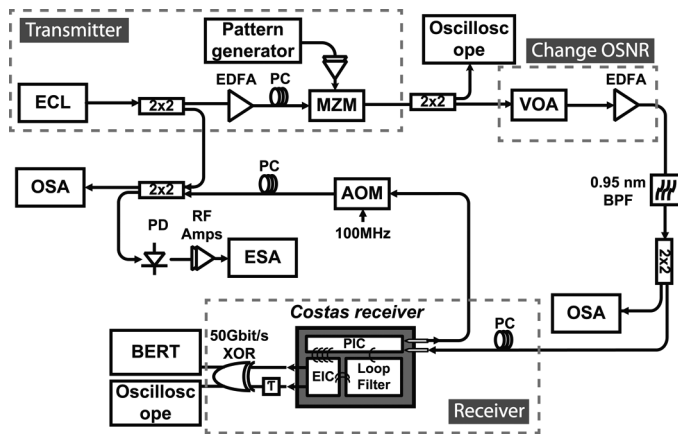


Fig. 16. Test setup for the BER measurement. The three dashed boxes indicate the transmitter, the receiver and the section that is used to vary the OSNR. The rest parts of the test setup are for monitoring purpose.

without the decoding circuit, and a 70 GHz sampled oscilloscope with a remote sampling head is used. Since the application of limiting amplifiers in EIC, BER cannot be estimated from the eye diagrams.

The test setup is shown in Fig. 16. The transmitter part is the same as the previous experiments, and $2^{31} - 1$ PRBS pattern is used. A variable optical attenuator (VOA) and an EDFA are

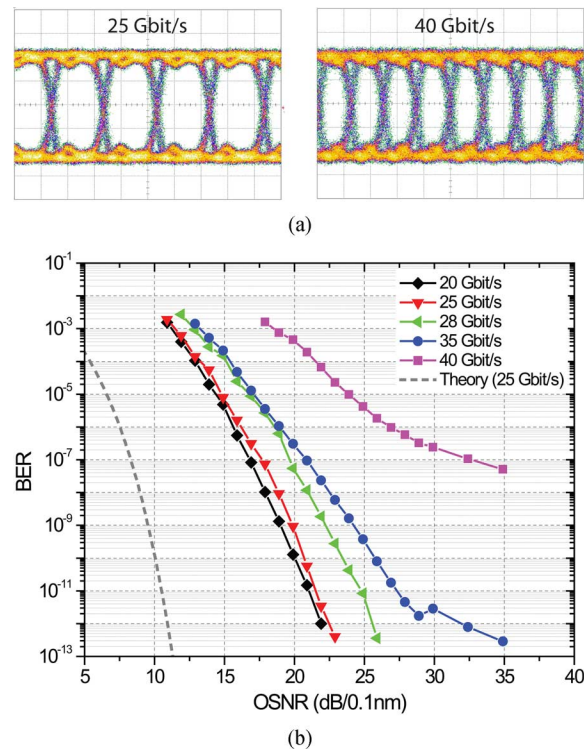


Fig. 17. (a) The eye diagrams of received data at 25 Gbit/s and 40 Gbit/s. (b) The bit error rate measurement results of the coherent receiver. The BER vs OSNR curves were measured at the data rate of 20, 25, 28, 35, 40 Gbit/s. The theoretical curve is also plotted at 25 Gbit/s data rate for an ideal receiver.

used to change the optical signal-to-noise ratio (OSNR). An optical filter with an FWHM bandwidth of 0.95 nm is used to filter out the amplified spontaneous emission (ASE) noise from the EDFA. The incoming signal is coupled to the receiver through a lensed fiber, and demodulated signal is detected by a 50 Gbit/s BERT through the decoding circuit. The BER is measured by the BERT. The RF cable is kept as short as possible to avoid excessive loss from the receiver to the measurement equipment. The measured eye diagrams at 25 and 40 Gbit/s are shown in Fig. 17(a), from which we can see the eyes are fairly open even at 40 Gbit/s. The BER measurement are carried out at the bit rates of 20, 25, 28, 35, and 40 Gbit/s. By varying the VOA, the OSNR from the EDFA output changes, and therefore the BERs are measured at different OSNR. The results are shown in Fig. 17(b). The theoretical BER for an ideal receiver is also calculated at 25 Gbit/s data rate. Comparing the measured BER and the theoretical BER, there is a 6–10 dB OSNR penalty. There are several potential factors that may introduce this difference. First, the residual LO laser phase noise may have influence on the receiver power penalty. Since the free running LO has a linewidth of 10 MHz, even with a 1 GHz OPLL loop bandwidth, the residual phase noise can be more than 10 degrees, which will cause a higher BER for the receiver performance, especially when OSNR is high. Second, since the device is not packaged, mechanical vibration can possibly cause worse BER. More specifically, the vibration of the fiber coupling can introduce optical amplitude noise on the photodetector, and the amplitude noise will pass through OPLL and change the LO laser phase and introduce phase error in consequence. The phase error variance of the OPLL directly influences the BER.

As shown in Fig. 17(b), error free ($\text{BER} < 10^{-12}$) is achieved at the data rate up to 35 Gbit/s. At 40 Gbit/s, it is believed that the phase shifter, which is used to introduce a 1 bit delay in the differential decoding circuit, reaches its bandwidth. However, the differential decoding circuit can be potentially integrated in the EIC, and therefore it will not limit the receiver performance.

V. CONCLUSIONS

In this paper, an optical Costas receiver is demonstrated, and real-time 40 Gbit/s coherent communication is achieved without any DSP. We achieve error free up to 35 Gbit/s BPSK signal. By recovering the phase of the carrier, the LO laser ‘clones’ the linewidth of the transmitting laser. The OPLL closed-loop bandwidth is 1.1 GHz. With 2.6°C temperature change, the OPLL still stays locked, which indicates more than 30 GHz hold-in range (> 15 GHz for single sideband). The power consumption is < 3 Watt without taking thermoelectric cooler power consumption into account.

REFERENCES

- [1] R. Essiambre, G. Kramer, P. Winzer, G. Foschini, and B. Goebel, “Capacity limits of optical fiber networks,” *J. Lightw. Technol.*, vol. 28, no. 4, pp. 662–701, 2010.
- [2] T. Omiya, K. Toyoda, M. Yoshida, and M. Nakazawa, “400 Gbit/s Frequency-Division-Multiplexed and Polarization-Multiplexed 256 QAM-OFDM transmission over 400 km with a spectral efficiency of 14 bit/s/Hz,” in *Proc. Opt. Fiber Commun. Conf.*, 2012, Paper OM2A.7.
- [3] D. Welch *et al.*, “The realization of large-scale photonic integrated circuits and the associated impact on fiber-optic communication systems,” *J. Lightw. Technol.*, vol. 24, no. 12, pp. 4674–4683, 2006.
- [4] K. Kikuchi, “Coherent optical communications: Historical perspectives and future directions,” in *High Spectral Density Optical Communication Technologies*, M. Nakazawa, K. Kikuchi, and T. Miyazaki, Eds. Berlin Heidelberg, Germany: Springer, 2010, vol. 6, Optical and Fiber Communications Reports, pp. 11–49.
- [5] L. Kazovsky, G. Kalogerakis, and W. Shaw, “Homodyne phase-shift-keying systems: Past challenges and future opportunities,” *J. Lightw. Technol.*, vol. 24, no. 12, pp. 4876–4884, 2006.
- [6] M. Fice, A. Chiuchiarelli, E. Ciaramella, and A. Seeds, “Homodyne coherent optical receiver using an optical injection phase-lock loop,” *J. Lightw. Technol.*, vol. 29, no. 8, pp. 1152–1164, 2011.
- [7] L. Kazovsky, “Decision-driven phase-locked loop for optical homodyne receivers: Performance analysis and laser linewidth requirements,” *J. Lightw. Technol.*, vol. 3, no. 6, pp. 1238–1247, 1985.
- [8] T. Hodgkinson, “Costas loop analysis for coherent optical receivers,” *Electron. Lett.*, vol. 22, no. 7, pp. 394–396, 1986.
- [9] S. Norimatsu and K. Iwashita, “PLL propagation delay-time influence on linewidth requirements of optical PSK homodyne detection,” *J. Lightw. Technol.*, vol. 9, no. 10, pp. 1367–1375, 1991.
- [10] T. Sakamoto, A. Chiba, A. Kanno, I. Morohashi, and T. Kawanishi, “Real-time homodyne reception of 40-Gb/s BPSK signal by digital optical phase-locked loop,” in *Proc. ECOC*, 2010, pp. 1–3.
- [11] H. Park, M. Lu, E. Bloch, T. Reed, Z. Griffith, L. Johansson, L. Coldren, and M. Rodwell, “40 Gbit/s coherent optical receiver using a Costas loop,” *Opt. Exp.*, vol. 20, no. 26, pp. B197–B203, Dec. 2012.
- [12] E. Ip and J. Kahn, “Carrier synchronization for 3-and 4-bit-per-symbol optical transmission,” *J. Lightw. Technol.*, vol. 23, no. 12, pp. 4110–4124, 2005.
- [13] T. Koch, U. Koren, R. Gnall, F. Choa, F. Hernandez-Gil, C. Burrus, M. Young, M. Oron, and B. Miller, “GaInAs/GaInAsP multiple-quantum-well integrated heterodyne receiver,” *Electron. Lett.*, vol. 25, no. 24, pp. 1621–1623, 1989.
- [14] L. Kazovsky, “Balanced phase-locked loops for optical homodyne receivers: Performance analysis, design considerations, and laser linewidth requirements,” *J. Lightw. Technol.*, vol. 4, no. 2, pp. 182–195, 1986.
- [15] S. Norimatsu, K. Iwashita, and K. Sato, “PSK optical homodyne detection using external cavity laser diodes in Costas loop,” *IEEE Photon. Technol. Lett.*, vol. 2, no. 5, pp. 374–376, 1990.
- [16] M. Grant, W. Michie, and M. Fletcher, “The performance of optical phase-locked loops in the presence of nonnegligible loop propagation delay,” *J. Lightw. Technol.*, vol. 5, no. 4, pp. 592–597, Apr. 1987.
- [17] U. Gliese, T. Nielsen, M. Bruun, E. L. Christensen, K. Stubkjaer, S. Lindgren, and B. Broberg, “A wideband heterodyne optical phase-locked loop for generation of 3–18 GHz microwave carriers,” *IEEE Photon. Technol. Lett.*, vol. 4, no. 8, pp. 936–938, Aug. 1992.
- [18] H. Park, M. Lu, E. Bloch, T. Reed, Z. Griffith, L. Johansson, L. Coldren, and M. Rodwell, “40 Gbit/s coherent optical receiver using a Costas loop,” in *Proc. ECOC*, 2012, Paper Th.3.A.2.
- [19] S. Ristic, A. Bhardwaj, M. Rodwell, L. Coldren, and L. Johansson, “An optical phase-locked loop photonic integrated circuit,” *J. Lightw. Technol.*, vol. 28, no. 4, pp. 526–538, 2010.
- [20] M. Lu, H. Park, E. Bloch, A. Sivananthan, A. Bhardwaj, Z. Griffith, L. Johansson, M. Rodwell, and L. Coldren, “Highly integrated optical heterodyne phase-locked loop with phase/frequency detection,” *Opt. Exp.*, vol. 20, no. 9, pp. 9736–9741, 2012.
- [21] R. Steed *et al.*, “Monolithically integrated heterodyne optical phase-lock loop with RF XOR phase detector,” *Opt. Exp.*, vol. 19, no. 21, pp. 20 048–20 053, 2011.
- [22] M. Lu, H. Park, E. Bloch, A. Sivananthan, J. Parker, Z. Griffith, L. Johansson, M. Rodwell, and L. Coldren, “A photonic integrated circuit for a 40 Gbaud/s homodyne receiver using an optical Costas loop,” in *Proc. IEEE Photon. Conf.*, Sep. 2012, Paper P.D. 4.
- [23] M. Lu, H.-C. Park, A. Sivananthan, J. Parker, E. Bloch, L. Johansson, M. Rodwell, and L. Coldren, “Monolithic integration of a high-speed widely tunable optical coherent receiver,” *IEEE Photon. Technol. Lett.*, vol. 25, no. 11, pp. 1077–1080, 2013.
- [24] E. Bloch, H. Park, M. Lu, T. Reed, Z. Griffith, L. Johansson, L. Coldren, D. Ritter, and M. Rodwell, “A 1–20 GHz InP HBT phase-lock-loop IC for optical wavelength synthesis,” in *Proc. MTT*, 2012, pp. 1–3.
- [25] E. Bloch, H. Park, M. Lu, T. Reed, Z. Griffith, L. A. Johansson, L. A. Coldren, D. Ritter, and M. J. Rodwell, “A 1–20 GHz all-digital InP HBT optical wavelength synthesis IC,” *IEEE Trans. Microw. Theory Tech.*, vol. PP, no. 99, pp. 1–11, 2012.
- [26] D. Messerschmitt, “Frequency detectors for PLL acquisition in timing and carrier recovery,” *IEEE Trans. Commun.*, vol. 27, no. 9, pp. 1288–1295, 1979.
- [27] F. M. Gardner, *Phaselock Techniques*. New York, NY, USA: Wiley-Interscience, 2005.
- [28] L. A. Coldren, L. A. Johansson, M. Lu, H. c. Park, J. Parker, A. Sivananthan, and M. Rodwell, “Single-chip integrated transmitters and receivers,” *Opt. Exp.*, vol. 20, no. 26, pp. B377–B385, Dec. 2012.
- [29] P. Corcoran, O. Girard, and J. I. F. De Faria, “On the thermal contribution to the FM response of DFB lasers: Theory and experiment,” *IEEE J. Quantum Electron.*, vol. 30, no. 11, pp. 2485–2490, 1994.

Author biographies not included at authors’ request due to space constraints.

Integrated Circuits for Wavelength Division De-multiplexing in the Electrical Domain

Hyun-chul Park⁽¹⁾, Molly Piels⁽¹⁾, Eli Bloch⁽²⁾, Mingzhi Lu⁽¹⁾, Abirami Sivananthan⁽¹⁾, Zach Griffith⁽³⁾,
Leif Johansson⁽¹⁾, John Bowers⁽¹⁾, Larry Coldren⁽¹⁾, and Mark Rodwell⁽¹⁾

⁽¹⁾ ECE Department, University of California at Santa Barbara, Santa Barbara, CA 93106-9560, USA,
hcpark@ece.ucsb.edu

⁽²⁾ Department of Electrical Engineering, Technion – Israel Institute of Technology, Haifa 32000, Israel,

⁽³⁾ Teledyne Scientific & Imaging Company, 1049 Camino Dos Rios, Thousand Oaks, CA 91360, USA.

Abstract We propose a new concept for a single-chip multi-channel WDM receiver which can scale toward Tbps operation. The receiver, consisting of a single photonic IC and a single electrical IC, multiplies data detection capacity by the number of electrical subcarrier channels. In a first demonstration, two BPSK-modulated wavelength channels have been successfully demodulated.

Introduction

Tbps WDM super-channels are expected to lead to improved spectral efficiency and higher overall system capacity^{1,2}. Current systems typically consist of several precisely spaced, but uncorrelated optical carriers^{1,3}. Demodulation requires an optical de-multiplexer and an array of coherent receivers, each tuned to a discrete optical carrier. As DAC and ADC speed and resolution improve, the number of optical carriers can be reduced and higher order modulation formats may be used, albeit at the cost of reduced optical reach¹.

In this work, we propose a coherent receiver architecture which is scalable to Tbps single optical carrier rates while maintaining optical reach. Fig. 1 shows a schematic of the proposed receiver in which a single coherent receiver

converts several modulated optical carriers to RF subcarriers, and an array of image reject mixers de-multiplexes the subcarriers to recover the data. The total capacity is ultimately limited by the bandwidth of the photo-detectors (PDs) and the de-mux IC, and by the modulation spectral efficiency. The architecture can scale beyond 1 Tbps capacity using 200 GHz bandwidth detectors and ICs together with dual polarization 16-QAM^{4,5}.

Coherent single chip multi-channel receivers

The WDM receiver has a simple circuit configuration, can provide high spectral efficiency, and accommodates a range of channel spacing and data modulation formats. Fig. 1 shows a receiver that de-multiplexes six WDM channels simultaneously using a single photonic IC (PIC) and a single electrical IC

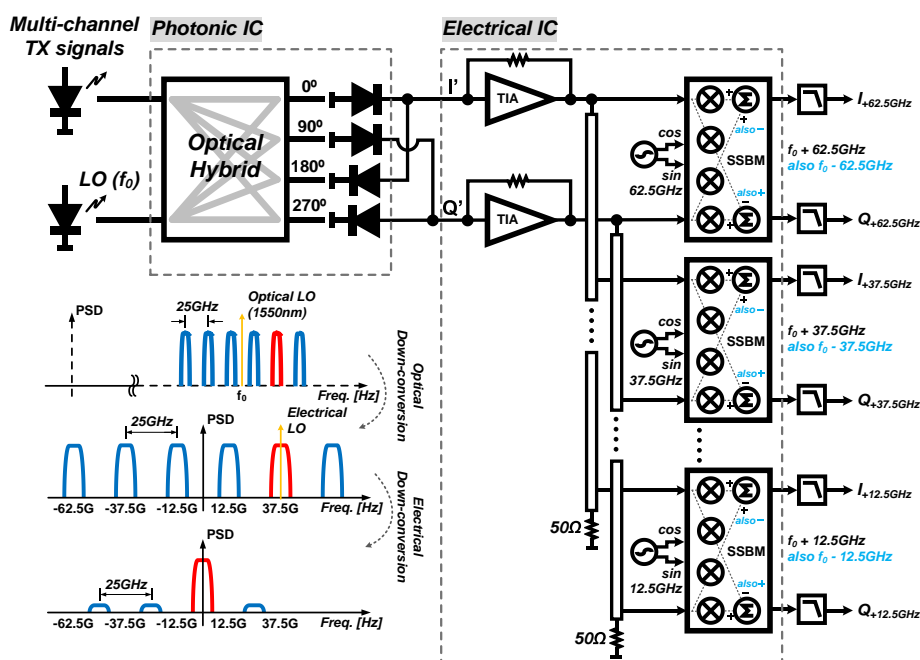


Fig. 1: A schematic for a coherent single-chip multi-channel WDM receiver and its de-multiplexing flows for six-modulated channels

Integrated Circuits for Wavelength Division De-multiplexing in the Electrical Domain

Hyun-chul Park⁽¹⁾, Molly Piels⁽¹⁾, Eli Bloch⁽²⁾, Mingzhi Lu⁽¹⁾, Abirami Sivananthan⁽¹⁾, Zach Griffith⁽³⁾,
Leif Johansson⁽¹⁾, John Bowers⁽¹⁾, Larry Coldren⁽¹⁾, and Mark Rodwell⁽¹⁾

⁽¹⁾ ECE Department, University of California at Santa Barbara, Santa Barbara, CA 93106-9560, USA,
hcpark@ece.ucsb.edu

⁽²⁾ Department of Electrical Engineering, Technion – Israel Institute of Technology, Haifa 32000, Israel,

⁽³⁾ Teledyne Scientific & Imaging Company, 1049 Camino Dos Rios, Thousand Oaks, CA 91360, USA.

Abstract We propose a new concept for a single-chip multi-channel WDM receiver which can scale toward Tbps operation. The receiver, consisting of a single photonic IC and a single electrical IC, multiplies data detection capacity by the number of electrical subcarrier channels. In a first demonstration, two BPSK-modulated wavelength channels have been successfully demodulated.

Introduction

Tbps WDM super-channels are expected to lead to improved spectral efficiency and higher overall system capacity^{1,2}. Current systems typically consist of several precisely spaced, but uncorrelated optical carriers^{1,3}. Demodulation requires an optical de-multiplexer and an array of coherent receivers, each tuned to a discrete optical carrier. As DAC and ADC speed and resolution improve, the number of optical carriers can be reduced and higher order modulation formats may be used, albeit at the cost of reduced optical reach¹.

In this work, we propose a coherent receiver architecture which is scalable to Tbps single optical carrier rates while maintaining optical reach. Fig. 1 shows a schematic of the proposed receiver in which a single coherent receiver

converts several modulated optical carriers to RF subcarriers, and an array of image reject mixers de-multiplexes the subcarriers to recover the data. The total capacity is ultimately limited by the bandwidth of the photo-detectors (PDs) and the de-mux IC, and by the modulation spectral efficiency. The architecture can scale beyond 1 Tbps capacity using 200 GHz bandwidth detectors and ICs together with dual polarization 16-QAM^{4,5}.

Coherent single chip multi-channel receivers

The WDM receiver has a simple circuit configuration, can provide high spectral efficiency, and accommodates a range of channel spacing and data modulation formats. Fig. 1 shows a receiver that de-multiplexes six WDM channels simultaneously using a single photonic IC (PIC) and a single electrical IC

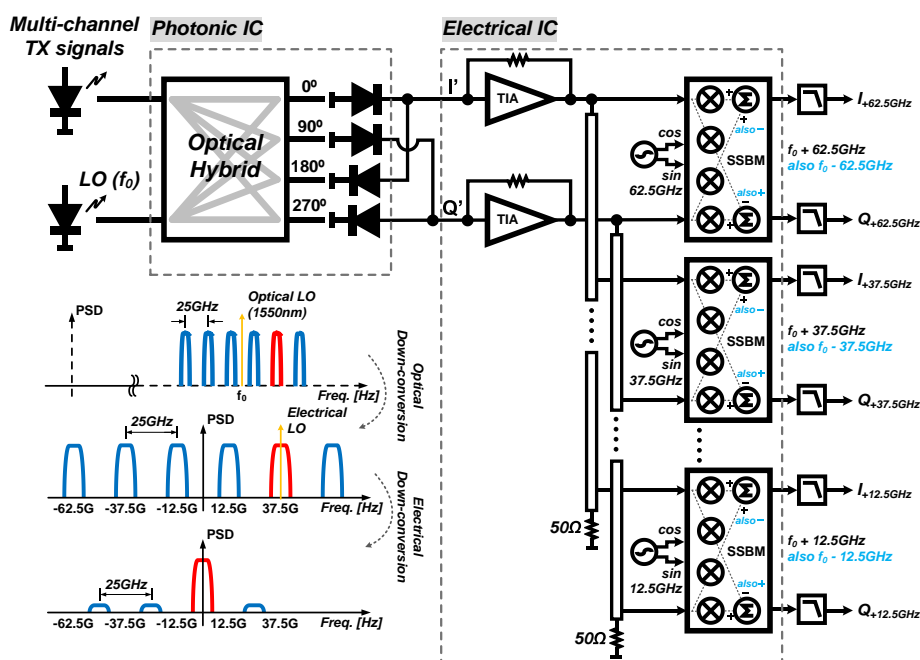


Fig. 1: A schematic for a coherent single-chip multi-channel WDM receiver and its de-multiplexing flows for six-modulated channels

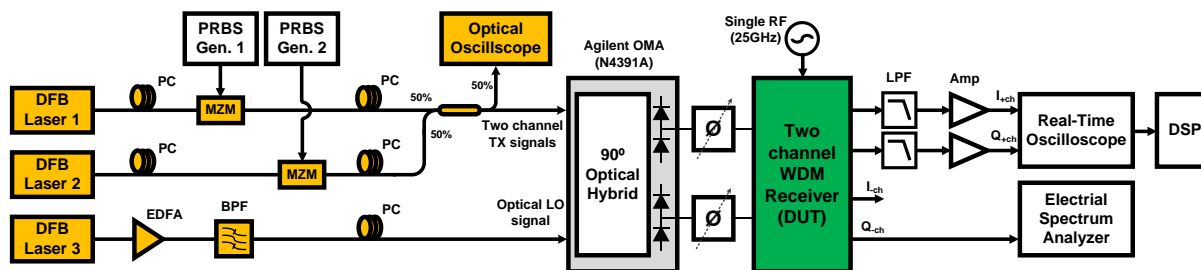


Fig. 4: Test setup for the two-channel WDM receiver

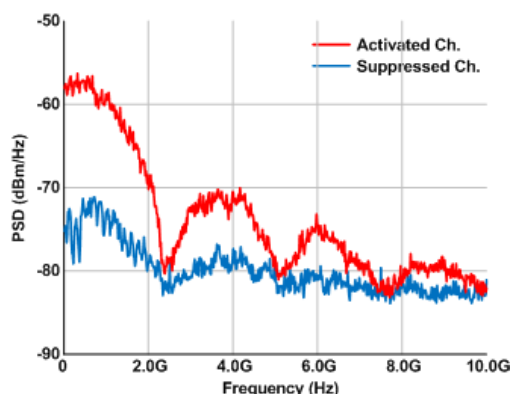


Fig. 5: Measured spectral outputs (red: activated ch. spectrum and blue: suppressed ch. spectrum) (RBW: 2MHz, VBW: 100kHz)

The standard PIC parts are replaced by an Agilent optical modulation analyzer (OMA) N4391A in this test. The OMA includes a free-space 90 degree optical hybrid and balanced PDs which are expected to have > 33GHz bandwidth. In the OMA, optical to electrical path length has been carefully matched below < 50ps using additional RF cables and phase shifters, and the connection between the OMA and the WDM receiver was maintained at 50 Ω by using k-band RF cables and four-finger RF probes. The WDM receiver outputs for one channel are low-pass filtered, amplified, monitored, and finally saved by the real-time oscilloscope, and frequency and phase errors are compensated by offline DSP. Meanwhile, the other channel is connected to a spectrum analyzer to determine whether the down-converted signal intensity is activated or suppressed as shown in Fig. 5. The spectral results show 15dB (~5x voltage) image suppression ratio due to imperfect amplitude and phase balance on I' and Q' between the OMA to the WDM receiver. Fig. 6 shows eye diagrams after the offline DSP. Fig. 6 (a) is the activated +channel eye output and (b) is the suppressed -channel eye output from a single modulated carrier. As expected, only Fig. 6 (a) shows open eye diagram compared with (b). Regarding two modulated carriers, both \pm channels on Fig. 6 (c), (d) show open eye diagram outputs, proving that the dual channel

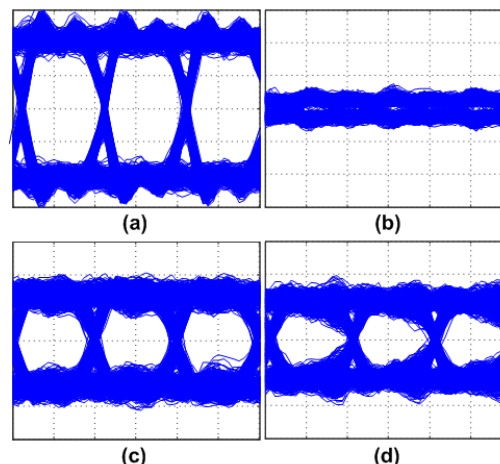


Fig. 6: Output eye diagrams after DSP. (a)

Activated +ch. from a single modulated carrier, (b) suppressed -ch. from the same modulated carrier, (c) and (d) +ch. and -ch. when two modulated carriers are transmitted

WDM receiver can receive both channels simultaneously. The 50%/50% directional coupler was added to the transmitter after the single-sided transmission tests and as a result, the received power in Fig.6 (c), (d) is half the received power in Fig.6 (a), (b). This degraded the signal to noise performance as expected.

Conclusions

A novel WDM receiver concept which is capable of 1Tbps single-chip optical fiber communication has been proposed. An initial demonstration of a two-channel WDM receiver has shown good performance, indicating the promise of this approach. A six-channel receiver is now being tested.

Acknowledgements

This work was supported by PICO project by the DARPA. The author would like to thank Teledyne Science Company for EIC Fabrication.

References

- [1] A. Deore, in finera IEEE meetings superchannels
- [2] X. Liu, et al., ECOC'12, PD, Th3C5, (2012)
- [3] J. Renaudier, et al., OFC'12, OW4C2, (2012)
- [4] E. Rouvalis, et al., OE **20**, 9172-9177 (2012)
- [5] M. Urteaga, et al., IPRM'08, 1-5 (2008)

I. Photonic Integrated Circuits

D. Coherent Beam Steering PICs

Hybrid silicon free-space source with integrated beam steering

J. K. Doylend, M. J. R. Heck, J. T. Bovington, J. D. Peters, M. L. Davenport, L. A. Coldren, and J. E. Bowers

ECE Dept., Univ. of California, Santa Barbara (United States)

ABSTRACT

Free-space beam steering using optical phase arrays are desirable as a means of implementing Light Detection and Ranging (LIDAR) and free-space communication links without the need for moving parts, thus alleviating vulnerabilities due to vibrations and inertial forces. Implementing such an approach in silicon photonic integrated circuits is particularly desirable in order to take advantage of established CMOS processing techniques while reducing both device size and packaging complexity.

In this work we demonstrate a free-space diode laser together with beam steering implemented on-chip in a silicon photonic circuit. A waveguide phased array, surface gratings, a hybrid III-V/silicon laser and an array of hybrid III/V silicon amplifiers were fabricated on-chip in order to achieve a fully integrated steerable free-space optical source with no external optical inputs, thus eliminating the need for fiber coupling altogether. The chip was fabricated using a modified version of the hybrid silicon process developed at UCSB, with modifications in order to incorporate diodes within the waveguide layer as well as within the III-V gain layer. Beam steering across a 12° field of view with $\pm 0.3^\circ$ accuracy and $1.8^\circ \times 0.6^\circ$ beam width was achieved, with background peaks suppressed 7 dB relative to the main lobe within the field of view for arbitrarily chosen beam directions.

Keywords: silicon photonics, LIDAR, free-space communication, optical phased array, laser, hybrid silicon, integrated optics, beam steering, photonic integrated circuit

1. INTRODUCTION

The ability to steer and shape a beam in free space is of interest for a wide range of applications. One application of especial note is light detection and ranging (LIDAR), which provides images at higher resolution than is possible with radar together with the capability to penetrate forest canopy and other obscurants such that hidden landmarks, vehicles, and personnel may be located and identified without sacrificing resolution by resorting to long-wavelength microwave radar [1]. Another application of particular interest is point-to-point free-space communication links, in which beam steering may be used either to select specific recipients for targeted burst transmissions or to maintain a link between non-stationary entities such that low bit-error-rate transmission is maintained despite location shift/sway (e.g. links between buildings) or even significant positional change (e.g. inter-satellite communication). In either case, beam steering using adaptive optics generally requires the use of mechanically moving parts which are therefore subject to degradation in performance from inertial forces and vibrations as well as being susceptible to mechanical wear.

1.1 Optical phased arrays and photonic integrated circuits

Optical phased arrays can be used to steer and shape a beam in free space without mechanical motion [2], and have been demonstrated as such both for LIDAR [3] and for free-space communication links [4], however this approach has largely been implemented thus far using bulk optical components which must be assembled, aligned, and co-packaged. An integrated optical approach in which all optical components are contained within a photonic integrated circuit offers several key advantages over bulk optical assemblies:

- (1) Size. Since individual components are not coupled via either optical fiber or lens assemblies and do not require individual mechanical mounts, space can be devoted solely to a single mount for a chip which contains all required optical components within it, thus saving both volume and weight.

- (2) Optical alignment: since the optical components are fabricated together, optical alignment is accomplished by routing planar waveguides between components on-chip using standard lithography with nanometer-scale tolerances and without the need for independent alignment of micro-optical elements or optical fibers, thus both saving cost and improving system performance.
- (3) Tolerance of vibration and mechanical shock. With optical alignment determined by on-chip fabrication rather than lenses and optical fiber, vibration and mechanical shock poses less of a risk to optical alignment since there are no mechanically-affixed components which can be shifted or shaken loose within the beam path.
- (4) Packaging cost. By eliminating the need to separately assemble and align individual optical components as well as the need for robust mechanical sub-assembly fixtures to hold optical components in place relative to each other, overall packaging cost can be reduced. Additionally, since the photonic integrated circuit can be encapsulated as a single chip, robust functionality in adverse conditions involving particulates and moisture can be achieved without resorting to hermetic packaging.

1.2 Silicon photonics for optical phased arrays

Optical phased arrays can be realized in photonic integrated circuits (PICs) using silicon photonics, thus taking advantage of the fabrication processes and facilities already in widespread use within the electronics industry. Such PICs have been demonstrated using passive silicon waveguides/splitters and gratings together with resistive heaters for thermo-optic control [5][6][7] on silicon-on-insulator (SOI), but this approach necessitates an off-chip source laser which is coupled to the chip via either optical fiber or micro-optics and which must be co-packaged with the chip after being optically aligned, thus diminishing the advantages of using a PIC in the first place (although still vastly preferable, from a packaging standpoint, to aligning/co-packaging the much larger number of components that were thus successfully integrated on-chip). Furthermore, since optical coupling from fiber to SOI involves a large index mismatch, reflections and losses at the interface are inevitable. Optical propagation and scattering losses within the PIC are also inevitable, and the optical phased array itself cannot emit all power into the main beam lobe with 100% efficiency.

It is therefore preferable to have a means of amplifying on-chip light rather than relying on huge input power coupled from a fiber at a single input. Such a capability also offers the additional advantage of providing a means to compensate for phase-dependent losses which must necessarily be introduced on-chip as a result of fast phase-modulation techniques such as carrier-injection and carrier-depletion should beam sweeping at speeds in excess of that achievable thermo-optically be required. Particularly well-suited to this task is the hybrid silicon platform, in which III-V material is die or wafer-bonded to already-patterned SOI waveguides such that optical modes guided within the silicon layer can be electrically pumped due to their evanescent overlap with quantum wells in the III-V material. This approach enables the integration of gain elements for on-chip amplifiers [8] and lasers [9] without the need for separate optical alignment of these components since they are patterned lithographically in the III-V after bonding to the silicon waveguides. This report describes the design, fabrication, and demonstrated beam-sweeping capability of such a device.

2. CONCEPT

In a standard phased array for two-dimensional beam steering, emitter elements or antennae are arranged in a two-dimensional array and phase adjusted to shape/steer the beam. Free-space emission from waveguides in a planar photonic circuit can be achieved using surface gratings, however, and these have the advantage of functioning as 1D phased arrays in their own right since each grating tooth scatters power from the guided mode with a phase delay determined by the effective index of the mode propagating within the waveguide. As such, the emission from a waveguide surface grating is a line in the far field whose emission angle is dictated by the grating pitch (i.e. period between grating teeth), waveguide effective index, and wavelength according to Eq. (1)

$$\sin \theta = \frac{\Lambda n_{eff} - \lambda}{\Lambda}. \quad (1)$$

By tuning wavelength, therefore, the beam in the far field can be steered in one axis and will automatically be collimated in that axis (subject to the finite length of the emission). An array of such gratings enables two-dimensional beam steering since wavelength determines the beam direction in one axis (henceforth referred to as θ) and relative phase across the grating array determines the beam shape/direction in the other axis (henceforth referred to as ψ). In overall concept the PIC-based optical phased array can be realized using a tunable laser coupled to a beam splitter to separate the beam into N channels, a phase modulator for each channel, and finally a grating emitter for each channel. In practice

it is preferable to amplify the beam after the tunable laser and then separately amplify each channel so as to provide both gain and phase adjustment for each emitter. The initial amplifier after the tunable laser (henceforth referred to as the “preamplifier”) not only increases the power launched into the splitter but also provides an easy means of (a) blanking the beam when output to the far field is not desired, and (b) tailoring the far field output power to compensate for variable on-chip losses (this will be discussed in more detail in the Results section). A schematic of the overall concept is shown in Figure 1.

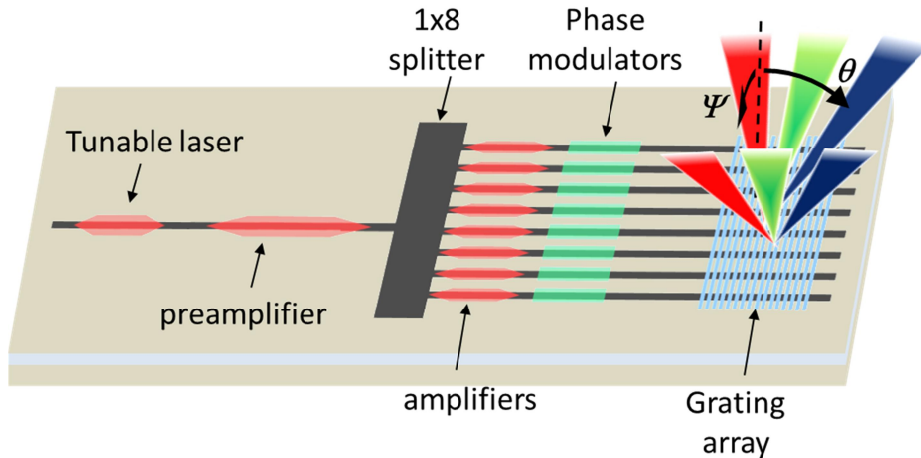


Figure 1. Optical phased array photonic integrated circuit concept. A tunable source laser is followed by a semiconductor optical amplifier (SOA) preamplifier, after which the beam is split into multiple channels (in this case 8). Each channel is separately amplified and phase tuned before being routed to an array of surface gratings. Emission angle of the beam from the surface gratings is determined by wavelength (here symbolized by color) in the θ (longitudinal) axis and by relative phase in the ψ axis.

Because wavelength is used to control steering in one axis and because the shape of the beam in that axis is determined by the grating lithography rather than by active control, an array of N elements requires $2N+1$ controls to steer the beam (N phase controls, N gain controls, and one wavelength control) rather than N^2 as would be required for a standard 2D array architecture, and is therefore inherently more scalable.

3. DESIGN

The design of the system begins with the design of individual components, and for this one must work backward from the beam requirements to arrive at the system capability. In this work the full-width half-maximum (FWHM) beam width goal was $<2^\circ$ with a steering range goal of $>12^\circ$. Since lens optics can in principle be used to expand or contract both the beam and the steering range in a given axis, the true goal was for a minimum of 6×6 (i.e. total steering range divided by beam width) evenly spaced resolvable spots in the far field with a background suppression ratio (i.e. the ratio of the main lobe peak intensity to background peak intensity within the field of view) of 10 dB.

3.1 Channel spacing

The spacing d between channel waveguides determines the angular separation between the main lobe and the side lobes in the far field. With a required separation of 12° to meet the steering range requirement (i.e. one must be able to steer the main lobe by $\pm 6^\circ$ in ψ without causing a side lobe to enter the field of view), the separation between waveguides must not exceed $6.5 \mu\text{m}$ (calculated for 1550 nm wavelength). Note that for this calculation it is not sufficient to maintain a peak-to-peak separation between main lobe and side lobe of 12° ; rather the base of the side lobe exceeding the background suppression must be separated from the main lobe by $>12^\circ$. For the system we chose a channel separation of $5.5 \mu\text{m}$ such that significant background power within the side lobes must fall 14.8° from the main lobe and can be easily aperture without clipping the main lobe at the edges of the field of view.

3.2 Array width and channel count

The lateral width of the overall array (i.e. the product $(N-1)d$, where N is the number of channel waveguides and d is the separation between them) determines the far field beam width in the ψ axis. For far field beam width $<2^\circ$, the array must have a lateral extent $>35 \mu\text{m}$; for d set to $5.5 \mu\text{m}$, $N = 8$. Plots of the calculated side lobe separation vs. waveguide separation and beam width vs. array width are shown in Figure 2.

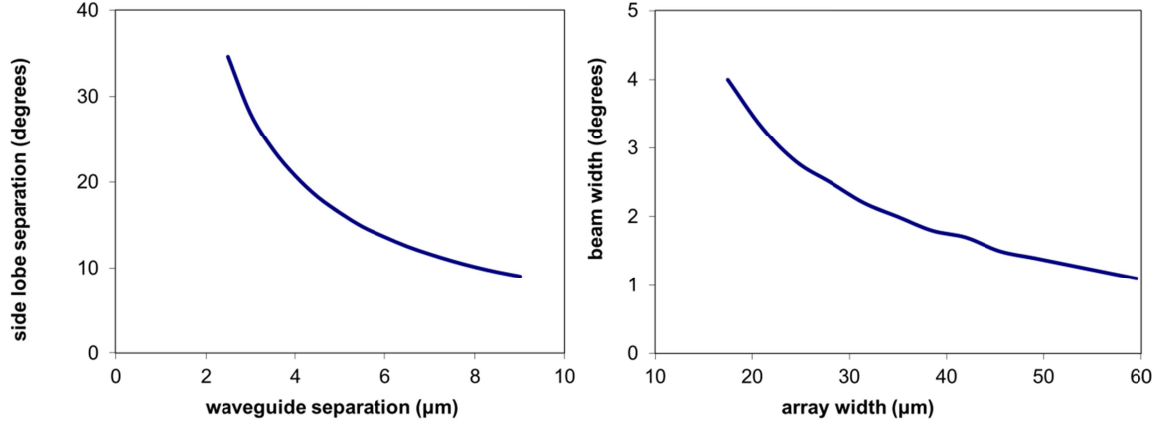


Figure 2. Calculated far field separation between main lobe and base of side lobe (>-10 dB relative to main lobe peak) vs. waveguide separation (left), and calculated far field beam width vs. array width (right).

The longitudinal beam width is determined by the grating strength; for this work the grating emitter used was identical to that reported and characterized in [6], and was thus known in advance to have a beam width of 0.6° .

3.3 Phase modulator design

The phase modulator was designed so as to tune phase thermo-optically by applying forward bias to a $p-i-n$ diode straddling the waveguide. By maintaining large separation between the p and n regions, carrier density within the optical mode was rendered negligible, thus avoiding phase-dependent loss due to free-carrier absorption. The silicon slab between phase modulators was etched to the buried oxide so as to mitigate thermal crosstalk between channels. It should be noted, however, that the measured device exhibited significant output power fluctuations for variations in phase tuning; this was attributed to poor thermal isolation between the phase modulators and the gain elements and will be described in more detail in the Results section. As such, although free-carrier absorption was negligible, the output power was still phase dependent such that the advantage of thermo-optic tuning was largely negated. Subsequent designs therefore employ electro-optic tuning and will be described in a forthcoming report.

Diode dopant profile after ion implantation and annealing was modeled using the Silvaco ATHENA software package, and the current-voltage characteristics and associated carrier densities within the waveguide were modeled using the Silvaco ATLAS software package. Carrier lifetimes within the waveguide for this calculation were assumed to be 0.9 ns in accordance with the data reported by Dimitropoulos et al. [10]. Thermal tuning was predicted to be $57 \text{ mW}/\pi$ using the relation given in Eq. (2):

$$P_\pi = \frac{\lambda \sigma w}{2t \frac{dn}{dT}}, \quad (2)$$

where λ is wavelength, $\sigma = 1.35 \times 10^{-2} \text{ W cm}^{-1} \text{ K}^{-1}$ is the thermal conductivity of the buried oxide [11], w is the effective width of the area over which the heat is dissipated (approximated by the width of the intrinsic region within the diode, or $10 \mu\text{m}$), $t = 1 \mu\text{m}$ is the thickness of the buried oxide, and $dn/dT = 1.86 \times 10^{-4} \text{ K}^{-1}$ [12] is the thermo-optic coefficient of silicon.

The phase modulator cross-section and a plot of expected carrier density vs. bias are shown in Figure 3 for a phase modulator length of 2 mm .

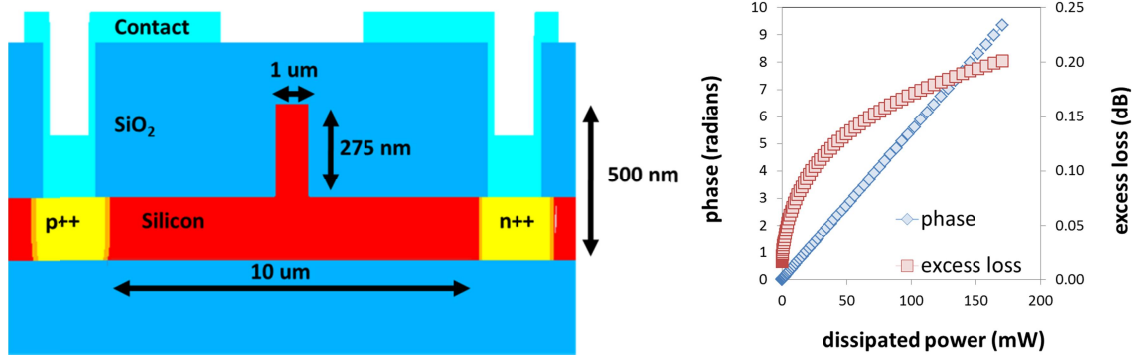


Figure 3. Cross-section of the phase modulator profile (left), and predicted thermo-optic tuning and free-carrier induced excess loss vs. thermal power (right).

3.4 Amplifiers and laser

The gain elements within both the SOA's and the tunable laser were based on the design reported by Kurczveil et al. [13] with the exception of rib waveguide width, which was chosen to be 2.5 μm within the SOA's in order to increase mode volume and hence maximum output power. Length of these elements was chosen to be 2.3 mm (also with the intention of increasing output power), while the preamplifier's length and rib width were chosen to be 1 mm and 2 μm respectively for higher gain/mm. The tunable laser was composed of two bus waveguides each with a gain section, coupled together with ring resonators having circumferences of 400 μm and 420 μm respectively such that their respective transmission spectra would overlap at only one wavelength within the available gain bandwidth. Thermo-optic tuning of the ring spectra by means of resistive heaters overlying them allowed the common transmission peak to be shifted so as to tune the laser. This tunable laser will be described in greater detail in a forthcoming publication.

3.5 Integrated device

The CAD layout of the overall 8-channel device is shown in Figure 4.

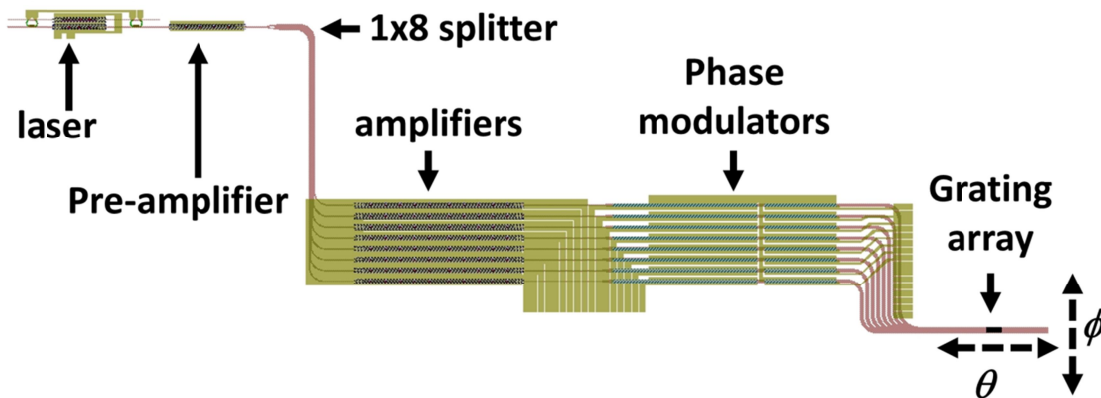


Figure 4. CAD layout of the overall device showing the tunable laser, pre-amplifier, waveguide splitter, channel amplifiers, phase modulators, and grating array.

4. FABRICATION

Silicon-on-insulator (SOI) with 500 nm lightly p-doped ($3 \times 10^{15} \text{ cm}^{-3}$) top silicon and 1 μm buried oxide was used as the starting material. Rib waveguides were patterned and etched to a depth of 275 nm in the SOI. Boron and phosphorus dopants were introduced via ion implantation and a 10 minute 1050°C anneal to form the phase modulators diodes. The grating array for free-space emission was patterned using e-beam lithography and etched to a depth of 50 nm. III-V quantum well laser material was then wafer-bonded to the top silicon surface, after which the bonded chip was lithographically patterned and etched to form diodes within the III-V material to serve as electrically pumped gain

elements. Metal contacts were formed via e-beam evaporation and liftoff. Buffer layers composed of SU8 and PECVD SiO₂ were used over the waveguides to maintain sufficient separation between the overlying metal traces and the waveguides to avoid excess optical losses.

5. RESULTS

5.1 Phase modulators

Phase tuner current-voltage characteristics were used to estimate the effective carrier lifetime, which was determined to be 1.9 ns rather than the expected value of 0.9 ns. Calculations of the associated carrier densities suggested free-carrier absorption of 0.75 dB and free-carrier induced phase shift of -0.8 radians for 100 mW of dissipated i^2R power, degrading the thermo-optic tuning efficiency accordingly. Tuning efficiency was measured on a test structure Mach-Zehnder interferometer and found to be $97 \text{ mW}/\pi$. The measured result together with a fit using the carrier lifetimes derived from the current-voltage characteristic and the measured thermo-optic efficiency is shown in Figure 5.

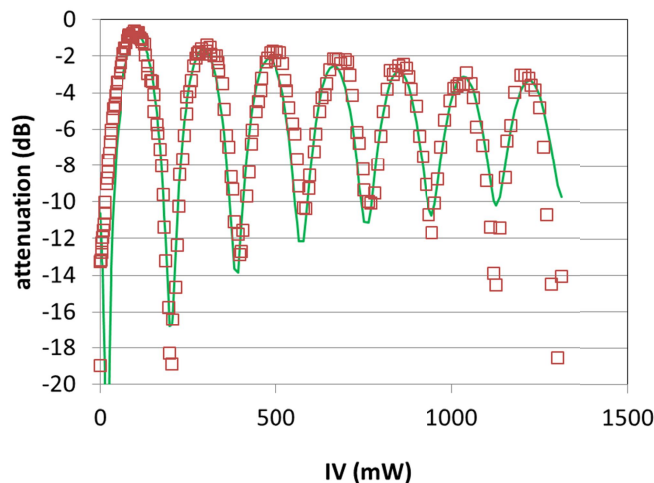


Figure 5. Measured thermo-optically tuned Mach-Zehnder interferometer transfer function to determine the phase tuning efficiency. The fitted curve was calculated using the measured phase-tuning efficiency together with calculated attenuation from free-carrier absorption deduced from the effective carrier lifetime.

5.2 On-chip laser

The on-chip laser within the 8-channel system was not tunable owing to faulty tuner probe pads, however a similar laser on the same chip was measured and found to have 5.5 mW output power, $< 7 \text{ MHz}$ linewidth, 46 dB sidemode suppression, and 40 nm tuning range (1561 nm to 1601 nm).

5.3 Photonic integrated circuit

The overall device was characterized by recording the beam profile in the far field using an IR camera and imaging lens system and using a feedback algorithm to adjust the phase on each channel with an 8-channel laser driver, similar to the method described in [6]. Power emitted from each channel was first equalized by turning on one channel at a time and observing the intensity of the far field line thus produced on the IR camera. One channel (channel 5) was observed to be faulty and was turned off for the duration of the measurement – this limited the maximum possible background suppression to 8.3 dB within the field of view; 7 dB background suppression was consistently achieved/measured with a beam width of 1.8° in ψ and 0.6° in θ . Due to significant heating of the top silicon layer, the gain from the SOAs was found to be highly dependent on the phase modulator settings. Accordingly the phase modulators and SOAs were cycled at 125 Hz, 20% duty cycle to mitigate on-chip heating. In order to avoid contamination of the observed far field pattern during SOA and phase modulator ramp-up, the preamplifier was used to blank the beam for the first 800 μs of the on-cycle before being turned on for the remaining 800 μs . With the chip mounted on a heat sink held at 18° C , the beam was profiled and steered across the far field at 1° increments from -6° to $+6^\circ$ at a single wavelength. It is noteworthy that with the observed tuning range (40 nm) for the on-chip laser and measured wavelength steering of $0.14^\circ/\text{nm}$ [6], tuning of 5.6° in the longitudinal direction is possible. A plot of measured and predicted beam cross-sections for each

axis is shown in Figure 6, and plots of the beam steered to directions in the far field across a 12° range are shown in Figure 7.

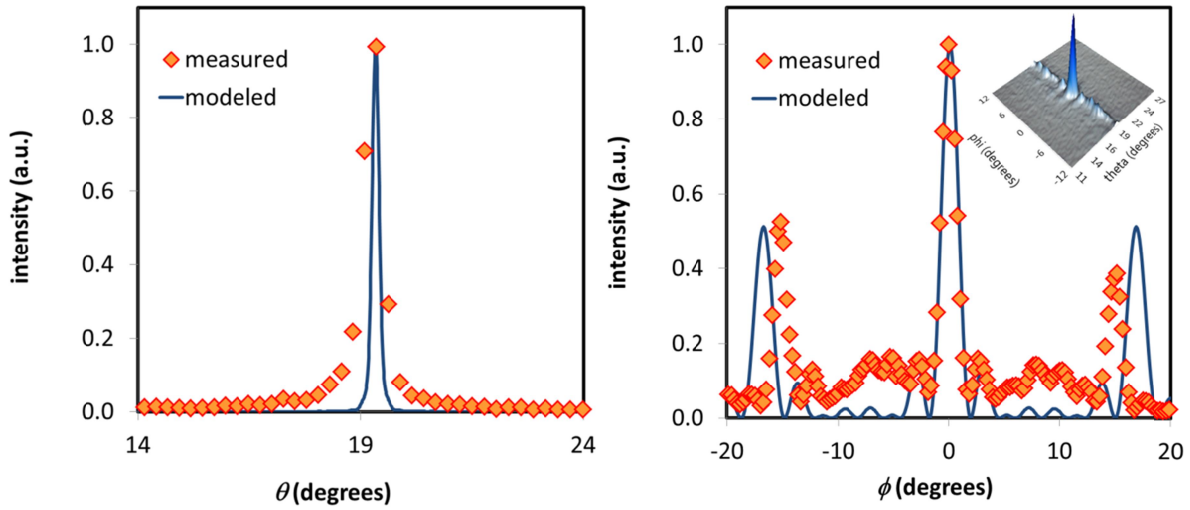


Figure 6. Measured and predicted beam cross-sections in the longitudinal (wavelength-tuned) axis (left) and lateral (phase-tuned) axis (right). The inset shows the 2D profile of the beam measured on an IR camera.

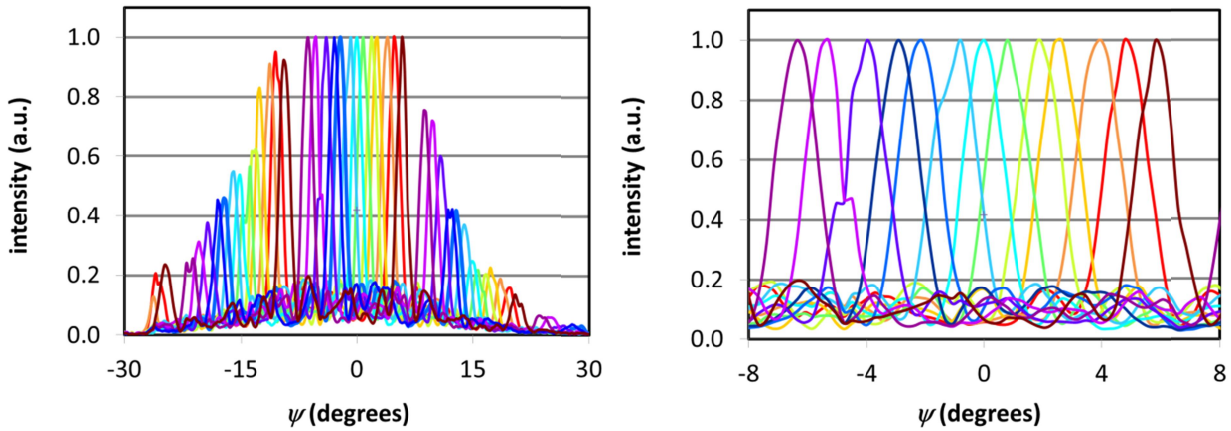


Figure 7. Measured beam profiles in the far field for the beam steered from -6° to +6° showing both the main and side lobes (left) and the aperture field of view (right).

As mentioned above, the beam power was not uniform or even predictable for disparate phase settings / steering angles in the far field owing to the effect of phase tuner heating on the gain elements within the circuit. However it was found that adjusting the preamplifier current preserved the beam shape (i.e. beam width and background suppression) while simultaneously enabling the beam power variations to be completely compensated such that the far field profile could be rendered flat as a function of steering angle. The variation in beam power with and without pre-amplifier adjustment is shown in Figure 8 together with the measured beam profiles for the required range of preamplifier settings.

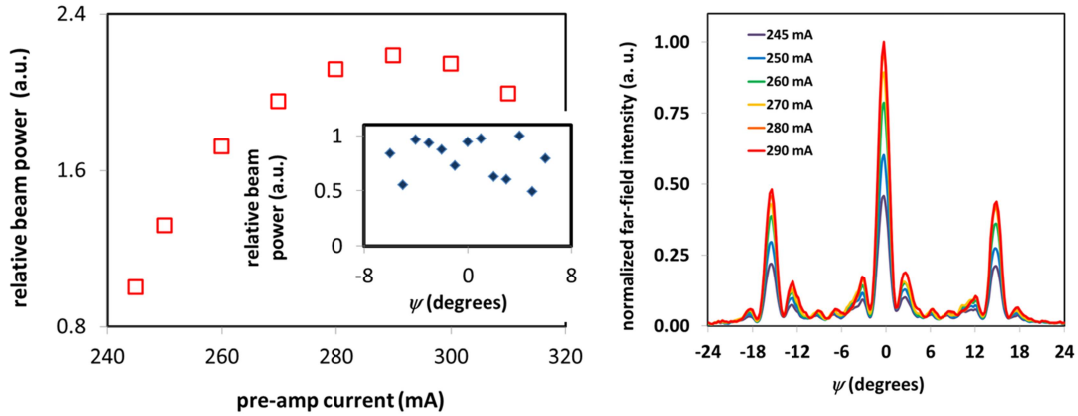


Figure 8. Relative beam power vs. preamplifier current (left) together with relative beam power without pre-amplifier current adjustment (inset left), and beam profiles vs. pre-amplifier current (right).

The beam power was measured by steering the beam to a detector positioned in the far field and found to be $4.1 \mu\text{W}$. Far field linewidth and sidemode suppression were measured by steering the beam to a fiber collimator connected to an APEX 2051A optical spectrum analyzer. Linewidth of the far field output was 36 MHz and sidemode suppression was 30 dB, both somewhat degraded from the characteristics of the standalone laser. This is not surprising given the many sources of feedback into the laser which are present in the integrated device. However the degradation was small enough as to make no significant different to the beam relative to the target metrics of background suppression and beam width in the far field.

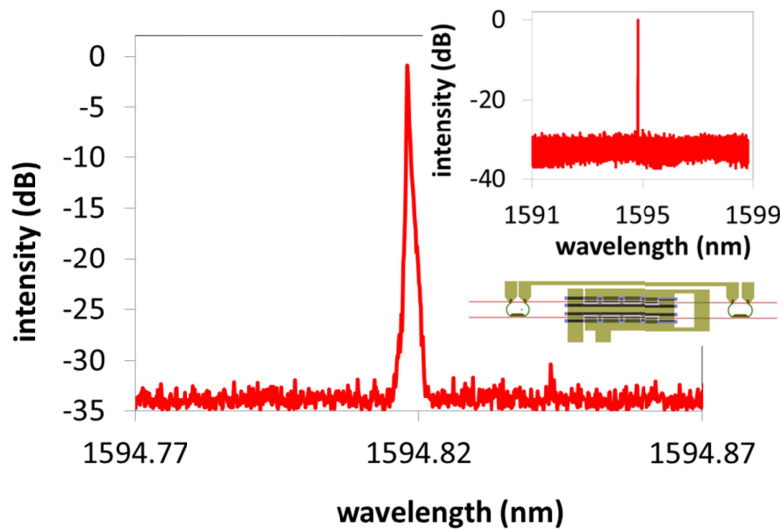


Figure 9. Far field laser spectrum measured on an optical spectrum analyzer. The insets show a broader spectrum to illustrate the suppression of longitudinal modes (upper inset) and a CAD layout of the tunable on-chip laser (lower inset).

6. CONCLUSION

A photonic integrated circuit fabricated according to the hybrid silicon platform has been used to demonstrate a free-space steerable laser using an optical phased array integrated with a tunable laser. The device exhibited 12° phase-controlled steering with $1.8^\circ \times 0.6^\circ$ beam width, and the on-chip laser was shown to be tunable over a range consistent with 5.6° steering in θ for a combined beam steering capability of 7×9 resolvable spots in the far field with 7 dB background suppression.

The authors would like to thank Pietro Binetti, Weihua Guo, Chad Althouse, Scott Rodgers, Josh Conway, and Predrag Milojkovic for useful discussions.

REFERENCES

- [1] Marino, R. M., and Davis, W. R., "Jigsaw: a foliage-penetrating 3D imaging laser radar system," *Lincoln Lab. Journal* 15, 23–36 (2005).
- [2] McManamon, P. F., Bos, P. J., Escuti, M. K., Heikenfeld, J., Serati, S., Huikai, X., and Watson, E. A., "A Review of Phased Array Steering for Narrow-Band Electrooptical Systems," *Proc. IEEE* 97, 1078-1096 (2009).
- [3] Schweinsberg, A., Shi, Z., Vornehm, J., and Boyd, R., "A slow-light laser radar system with two-dimensional scanning," *Opt. Lett.* 37, 329-331 (2012).
- [4] Henderson, C. J., Leyva, D. G., and Wilkinson, T. D., "Free Space Adaptive Optical Interconnect at 1.25 Gb/s, With Beam Steering Using a Ferroelectric Liquid-Crystal SLM," *J. Lightwave Technol.* 24, 1989-1997 (2006).
- [5] Van Acoleyen, K., Rogier, H., and Baets, R., "Two-dimensional optical phased array antenna on silicon-on-insulator," *Opt. Express* 18, 13655-13660 (2010).
- [6] Doylend, J. K., Heck, M. J. R., Bovington, J. T., Peters, J. D., Coldren, L. A., and Bowers, J. E., "Two-dimensional free-space beam steering with an optical phased array on silicon-on-insulator," *Opt. Express* 19, 21595-21604 (2011).
- [7] Sun, J., Timurdogan, E., Yaacobi, A., Hosseini, E. S., & Watts, M. R., "Large-scale nanophotonic phased array," *Nature*, 493, 195-199, (2013).
- [8] Park, H., Kuo, Y.-H., Fang, A. W., Jones, R., Cohen, O., Paniccia, M. J., and Bowers, J. E., "A Hybrid AlGaInAs-Silicon Evanescent Amplifier," *IEEE Photon. Technol. Lett.* 19, 230-232 (2007).
- [9] Fang, A. W., Sysak, M. N., Koch, B. R., Jones, R., Lively, E., Kuo, Y., Liang, D., Raday, O., and Bowers, J. E., "Single-Wavelength Silicon Evanescent Lasers," *IEEE J. Sel. Top. Quantum. Electron.* 15, 535-544 (2009).
- [10] Dimitropoulos, D., Jhaveri, R., Claps, R., Woo, J. C. S., and Jalali, B., "Lifetime of photogenerated carriers in silicon-on-insulator rib waveguides," *Appl. Phys. Lett.* 86, 071115-1 – 071115-3 (2005).
- [11] Lide, D. R., [CRC Handbook of Chemistry and Physics], "Thermal Conductivity of Glasses", CRC Press, Boca Raton, 12-205 – 12-208 (2005).
- [12] McCaulley, J. A., Donnelly, V. M., Vernon, M., Taha, I., "Temperature dependence of the near-infrared refractive index of silicon, gallium arsenide, and indium phosphide," *Phys. Rev. B* 49, 7408-7417 (1994).
- [13] Kurczveil, G., Heck, M. J., Peters, J. D., Garcia, J. M., Spencer, D., Bowers, J. E., "An Integrated Hybrid Silicon Multiwavelength AWG Laser," *IEEE J. Sel. Top. Quantum Electron.* 17, 1521-1527 (2011).

InP Photonic Integrated Circuit with On-chip Tunable Laser Source for 2D Optical Beam Steering

Weihua Guo, Pietro R. A. Binetti, Chad Althouse, Leif A. Johansson, and Larry A. Coldren

Department of Electrical and Computer Engineering, University of California Santa Barbara, CA93106, USA

Email: guow@ece.ucsb.edu

Abstract: 2D optical beam steering through an InP photonic integrated circuit with on-chip tunable laser source has been demonstrated for the first time.

OCIS codes: (250.5300) Photonic integrated circuits; (280.3640) Lidar

1. Introduction

Electronically controlled optical beam steering is potentially useful for applications such as free-space optical communication, light detection and ranging (LIDAR), 3D imaging, etc. Several methods have been demonstrated for this purpose such as the phased array for 1D optical beam steering [1], 1D phased array combined with emission gratings for 2D optical beam steering [2]. In [3] we demonstrated an InP photonic integrated circuit (PIC) for 2D optical beam steering using the approach of 1D phased array plus 2nd-order emission grating. Instead of using a single triangle contact to control the phase of the phased array, we use separate contact to control the phase of each channel in the phased array. This increases the number of controls, but does give us more tolerance for fabrication. Also the phase needed is much less because a module of 2π can be used. We have demonstrated 2D optical beam steering with the longitudinal direction controlled by the input wavelength and the lateral direction controlled by the phased array [3]. The tunable laser source used for the beam steering is either an external cavity widely tunable laser or an off-chip sample-grating DBR laser (SG-DBR) [5]. Fiber coupling is used to input to the PIC. It would be ideal to integrate the tunable laser source onto the beam sweeping PIC so that a single PIC can achieve the full function of electronically controlled 2D optical beam steering. In this work we demonstrated the first attempt of such integration: a widely tunable SG-DBR laser is integrated onto the beam sweeping chip.

2. PIC layout, fabrication and measurement

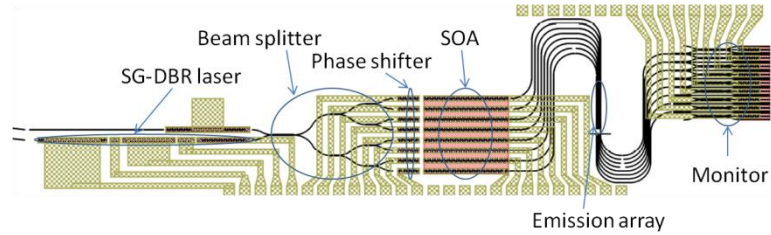


Fig. 1 Layout of the PIC

Fig. 1 shows the layout of the PIC. From left to right, the PIC contains the SG-DBR widely tunable laser, the 1×8 beam splitter consisting of cascaded 1×2 MMIs, 8 phase shifters, 8 semiconductor optical amplifiers (SOA), the emission array consisting of 8 waveguides with buried 2nd-order gratings, and the array of monitors. The waveguide spacing in the emission array is uniformly $5.5 \mu\text{m}$. 90° bends are added to make all the channels have the same length as shown in Fig. 1. The detailed structure of the monitors can be found in [4]. These monitors can be used to characterize the phase shifters on-site through monitoring the interference between adjacent channels [4]. To realize the active and passive integration required by the PIC, we use the quantum well intermixing (QWI) technology [3]. The gratings for both the SG-DBR laser and the emission array are patterned by E-beam lithography and etched by a two-step etching process to realize two different etch depths: the laser grating is 70 nm etched into the waveguide core but the emission grating is only 20 nm etched. These gratings are then buried by P-doped InP cladding layers through a blanket regrowth. Deep ridge waveguides (about $5 \mu\text{m}$) are used for both the active and passive waveguides for the simplicity of fabrication. The waveguides for the emission array are passive as well. The top of the waveguide is anti-reflection coated by a $\lambda/4$ -thick SiN_x layer. There is also an aperture opened in the backside contact metal aligned with the emission array. The emission grating scatters the light from the waveguide equally upward and downward. The downward emission is captured by a far-field imaging system which has the ability to record an angle range of $34.8^\circ \times 26.7^\circ$ of the far-field with a resolution of 0.1° . The 8 phase shifters are controlled separately by 8 current outputs from a DAC card. The 8 SOAs are biased together by a single voltage source. A

variable resistor network connected in series with these SOAs is used to compensate for their series resistance variation so that a single source can still realize uniform current injections into these SOAs. The back mirror, front mirror, gain section and the pre-amplifier SOA of the SG-DBR laser are biased through different current sources. The phase section is left unbiased. So in the tuning demonstrated below only super mode selection is shown. A quasi-continuous tuning can be realized if the back mirror, front mirror and the phase section biases are adjusted in coordination [5]. In the following measurement 100 mA is injected into each SOA of the 8-SOA array. The gain section of the laser is biased at 100 mA as well. The pre-amplifier of the laser is biased at 40 mA. We do notice some unwanted feedback into the laser from the emission gratings due to imperfect control of the duty cycle of the gratings. If we bias the pre-amplifier very hard the laser working would be influenced. Here we select a moderate current of 40 mA to try to minimize the effect. This however reduces the output power of the laser.

3. Results

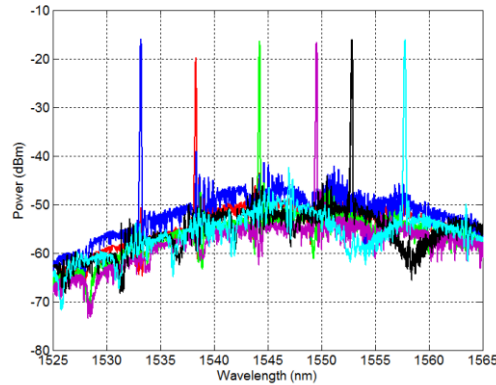


Fig. 2 Super modes of the on-chip SG-DBR laser

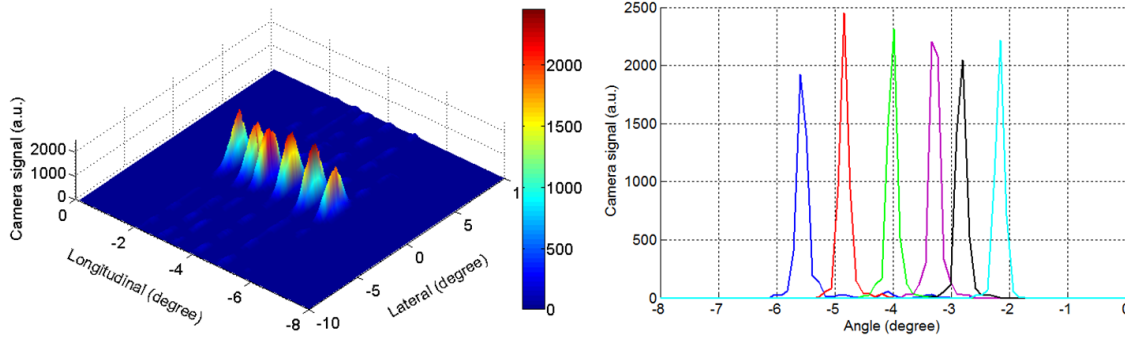


Fig. 3 (a) 3D plot of the far-field pattern for different wavelengths superposed together; (b) far-field across the peak in the longitudinal direction

First the tunable laser is characterized by measuring its super modes. The laser spectrum output through the back mirror coupled by a lensed fiber is shown in Fig. 2. 6 super modes can be seen which corresponds to an expected total tuning range >30 nm [5]. Then for each super mode the far-field pattern is optimized for the lateral angle of 0° by setting the phase shifter currents through the particle swarm optimization algorithm [3]. Each current is varied from 1 to 20 mA. The far-field patterns for different wavelengths are superposed in Fig. 3 (a). The field across the peak in the longitudinal direction is shown in Fig. 3 (b). Very narrow (FWHM about 0.2°) and clean peaks are observed. The peak is narrow due to a long ($500 \mu\text{m}$) and relatively weakly coupled grating being used. A beam steering efficiency of $0.14^\circ/\text{nm}$ has been observed which corresponds well to our expectation. Then the wavelength is fixed at 1538 nm and the beam is steered to different lateral angles through controlling those phase shifters. The far-field patterns for different angles are superposed in Fig. 4 (a). The field across the peak in the lateral direction is shown in Fig. 4 (b). Because 8 waveguides in the array only span about $40 \mu\text{m}$, the far-field in the lateral direction is broad (FWHM about 2°) so the fields overlap with each other as seen from Fig. 4 (b). The waveguide spacing of $5.5 \mu\text{m}$ determines the 1st-order diffraction peak to be 16° away from the 0th-order peak, which can be clearly seen from Fig. 4 (b). A side-lobe suppression >10 dB around the 0th-order diffraction peak is also realized. Finally we combine

the wavelength change with the phase shifter controls to realize a 2D beam steering. The results are shown in Fig. 5. A beam steering angle range longitudinally from -5.6° to -2.1° and laterally from -5° to 5° has been realized.

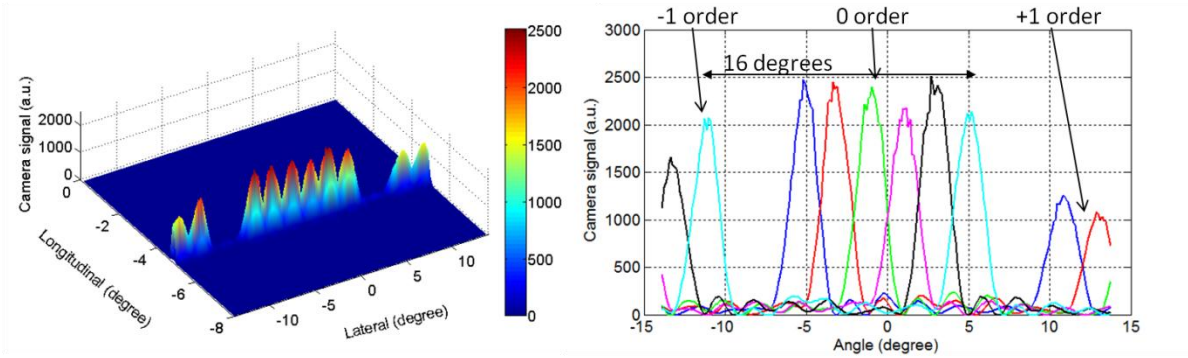


Fig. 4 (a) 3D plot of the far-field pattern for different lateral angles superposed together for the wavelength of 1538 nm; (b) far-field across the peak in the lateral direction

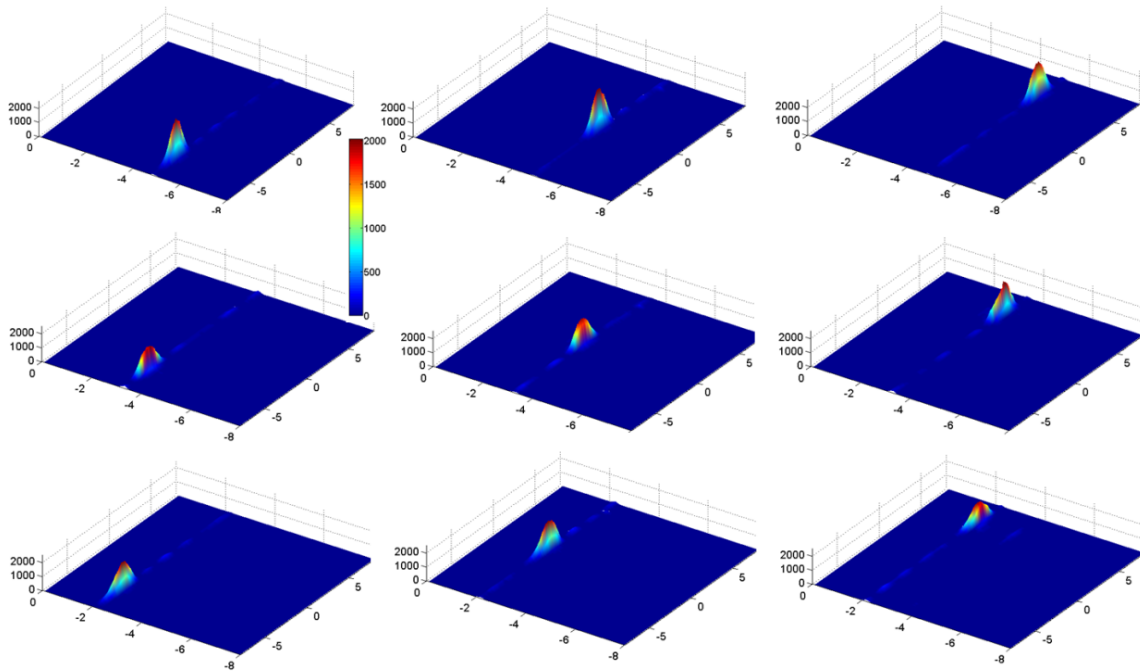


Fig. 5 2D optical beam steering: wavelength controlling the longitudinal direction (vertical in the plot) and phase shifters controlling the lateral direction (horizontal in the plot)

4. Summary

In summary 2D optical beam steering from an InP PIC with integrated on-chip tunable laser source has been demonstrated. Beam steering angle range of 3.5° in the longitudinal direction and 10° in the lateral direction has been realized.

5. Reference

- [1] P. F. McManamon, T. A. Dorschner, D. L. Corkum, L. J. Friedman, D. S. Hobbs, M. Holz, S. Liberman, H. Q. Nguyen, D. P. Resler, R. C. Sharp, and E. A. Watson, "Optical phased array technology," *Proc. IEEE* **84**, 268-298 (1996).
- [2] K. V. Acoleyen, W. Bogaerts, J. Jagerska, N. L. Thomas, R. Houdre, and R. Baets, "Off-chip beam steering with a one-dimensional optical phased array on silicon-on-insulator," *Opt. Lett.* **34**, 1477-1479 (2009).
- [3] W. H. Guo, P. R. Binetti, C. Althouse, A. Bhardwaj, J. K. Doylend, H. P. M. M. Ambrosius, L. A. Johansson, and L. A. Coldren, "InP photonic integrated circuit for 2D optical beam steering," Post-deadline paper, IEEE Photonics 2011 (IPC11), 2011.
- [4] W. H. Guo, P. R. Binetti, C. Althouse, H. P. M. M. Ambrosius, L. A. Johansson, and L. A. Coldren, "InP photonic integrated circuit with on-chip monitors for optical beam steering," MA6, ISLC2012, San Diego, CA, USA (2012).
- [5] L. A. Coldren, "Monolithic tunable diode lasers," *IEEE J. Sel. Topics Quantum Electron.* **6**, 988-999 (2000).

Two-Dimensional Optical Beam Steering With InP-Based Photonic Integrated Circuits

Wei-hua Guo, Pietro R. A. Binetti, Chad Althouse, Milan L. Mašanović, *Member, IEEE*, Huub P. M. M. Ambrosius, Leif A. Johansson, *Member, IEEE*, and Larry A. Coldren, *Fellow, IEEE*

(Invited Paper)

Abstract—Two-dimensional optical beam steering using an InP photonic integrated circuit has been demonstrated. Lateral beam steering controlled by a 1-D phased array has been made easier through on-chip interferometer monitors. Longitudinal beam steering controlled by the input wavelength has demonstrated an efficiency of $0.14^\circ/\text{nm}$. Very fast beam steering ($>10^7$ °/s) in both dimensions has been demonstrated as well. As the latest development, a widely tunable sampled-grating distributed Bragg reflector laser has been monolithically integrated and 2-D beam steering has been demonstrated with this on-chip tunable laser source.

Index Terms—Light detection and ranging (LIDAR), optical beam steering, optical phased array (OPA), photonic integrated circuits (PICs).

I. INTRODUCTION

ELECTRONICALLY controlled optical beam steering is potentially useful for a number of applications such as light detection and ranging (LIDAR), free space secure laser communication, printing, etc. Various methods have been demonstrated to achieve this goal. One typical method is the optical phased array (OPA), which is used for 1-D optical beam steering [1]. Different material systems have been used to realize OPAs such as liquid crystal [2] and GaAs [3].

To achieve 2-D optical beam steering, the most natural implementation might be to mimic the active electronically scanned array which consists of a 2-D array of transmitters and receivers. It is used for 2-D RADAR scanning [4]. A 2-D array of optical emitters such as a 2-D vertical-cavity-surface-emitting-laser (VCSEL) array can be used as the transmitter in this approach. Making lasers in the array coherent to each other is essential

for optical beam steering. This has been demonstrated by the way of injection locking [5] or adjacent laser coupling [6]. Also needed by this approach is a 2-D array of phase shifters. Each phase shifter in the array should ideally be able to generate 2π phase change. This, however, is very challenging.

A two-dimensional microelectromechanical system (MEMS) array has also been used for 2-D optical beam steering [7], however achieving high-speed and large-angle beam steering simultaneously is a big challenge for this scheme.

Recently, there has been a demonstration of using wavelength tuning to steer the optical beam in one dimension through waveguide dispersion [8]. This is essentially similar to using surface-emitting gratings, in which the emitting angle depends on the input wavelength. By combining 1-D OPA with surface-emitting gratings, 2-D optical beam steering has been realized [9]. The benefit of this scheme is that the beam steering in one dimension is only controlled by one variable, i.e., the wavelength, so the entire control is much simpler. The OPA has been demonstrated to be controlled by using a single triangular contact as well [9].

Recently, the authors demonstrated 2-D optical beam steering with an InP photonic integrated circuit (PIC) using the scheme of 1-D OPA plus wavelength tuning with surface-emitting gratings [10]. However, instead of using one triangular pad, individual pads for each single channel in the OPA were used. Analogous efforts by our coworkers on the silicon-on-insulator platform have also been carried out and similar results have been demonstrated [11]. This approach does increase the number of controls needed, but allows large tolerances for device fabrication because the phase errors due to imperfect fabrications of the channel waveguides can be compensated by the individually controlled phase shifters.

Also, the overall phase needed to be generated is much less compared to the single triangular pad because modulo of 2π for phase can be used. In other words, it is not needed to generate more than 2π phase change for a single channel, which is not the case for the triangular pad. Considering that in InP, a phase change induced by current injections is always associated with some amount of loss, less phase change also means less loss.

We chose the InP platform for the integration because of several reasons: first, InP is a very mature platform for large-scale photonic integration [12], and various active-passive devices, such as widely tunable lasers, have been implemented in it; therefore potentially all components necessary for 2-D beam steering can be integrated on a single PIC; second, in InP, semiconductor optical amplifiers (SOAs) can be integrated to boost

Manuscript received November 1, 2012; revised December 31, 2012; accepted December 31, 2012. This work was supported by the DARPA SWEEPER Program.

W. H. Guo, P. R. A. Binetti, M. L. Mašanović, L. A. Johansson, and L. A. Coldren are with the Department of Electrical and Computer Engineering, University of California Santa Barbara, CA 93106 USA (e-mail: guow@ece.ucsb.edu; pbinetti@ece.ucsb.edu; mashan@ece.ucsb.edu; leif@ece.ucsb.edu; coldren@ece.ucsb.edu).

C. Althouse was with the Department of Electrical and Computer Engineering, University of California Santa Barbara, CA 93106 USA. He is now with Innovative Micro Technology, Goleta, CA 93117 USA (e-mail: althouse@umail.ucsb.edu).

H. P. M. M. Ambrosius is with the Department of Electrical Engineering, Eindhoven University of Technology, 5600 MB Eindhoven, The Netherlands (e-mail: H.P.M.M.Ambrosius@tue.nl).

Color versions of one or more of the figures in this paper are available online at <http://ieeexplore.ieee.org>.

Digital Object Identifier 10.1109/JSTQE.2013.2238218

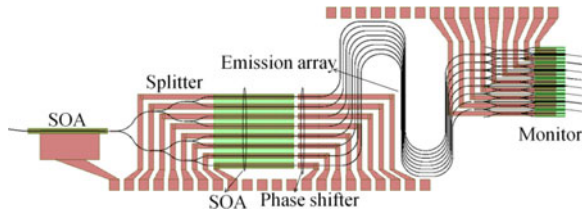


Fig. 1. Layout of the PIC.

the optical power, so that potentially the PIC can generate high optical power which is essential for LIDAR applications; third, the phase shifters in InP with current injections can have up to a gigahertz bandwidth, the tuning speed of the widely tunable laser, such as the sampled-grating distributed Bragg reflector (SGDBR) laser [13], can reach a few nanoseconds [14], so potentially an InP PIC can achieve very fast optical beam steering.

The rest of this paper is organized as follows: the PIC layout and processing are introduced in Sections II and III, respectively; Section IV introduces the PIC test in detail including the following subsections: test setup, contact to the PIC and bias control, beam steering controlled by phase shifters, beam steering controlled by wavelength tuning, 2-D beam steering, and fast beam steering; Section V introduces the latest development where a widely tunable SGDBR laser is monolithically integrated; the summary is given in Section VI.

II. PIC LAYOUT

The PIC layout is shown in Fig. 1. From left to right, the PIC contains an SOA preamplifier, a 1×8 splitter consisting of cascaded 1×2 multimode interferometers (MMIs) which splits the input into eight equal channels, an array of eight SOAs, an array of eight phase shifters, bends, emission array, and the monitor array. All the SOAs are $800 \mu\text{m}$ long and $2.7 \mu\text{m}$ wide. All the phase shifters are $200 \mu\text{m}$ long and $2.7 \mu\text{m}$ wide. The emission array consists of eight uniformly spaced waveguides. Buried second-order gratings are used for the surface emission. The gratings are $500 \mu\text{m}$ long and the waveguide spacing is $5.5 \mu\text{m}$ which is chosen to ensure that the final beamwidth (full-width at half-maximum—FWHM) will be within 2° . The waveguide gap in the emission array is thus $2.8 \mu\text{m}$ which makes the crosstalk between waveguides negligible when deeply etched ridge waveguides are used. As seen from Fig. 1, the bends used in each channel are the same: the same radius of $200 \mu\text{m}$ and the same total bending angle of 1.5π . These bends are added to make each channel have the same total length. They are needed because the SOA array has a spacing of $100 \mu\text{m}$ which is much larger than the spacing in the emission array.

The detailed structure of the monitor array is shown in Fig. 2(a) and (b). Each channel is split into three equal parts through a 1×3 MMI. The central part outputs directly for possible far-field analysis. The two neighboring parts from two adjacent channels are combined by a 2×1 MMI with the output entering into a photodiode which is $5 \mu\text{m}$ wide and $200 \mu\text{m}$ long. Two more waveguides are added at the output interface of the 2×1 MMI sandwiching the central output as seen from Fig. 2(b). When the two inputs of the 2×1 MMI have a π

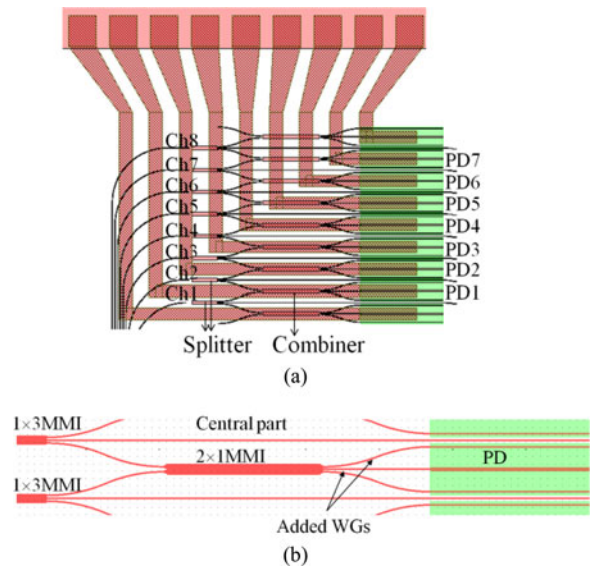


Fig. 2. Blow-up of (a) the monitor array and (b) a single channel of the monitor array.

phase difference, they will interfere destructively at the output interface of the MMI. Two spots will be formed at the entrance of the two added waveguides and will be guided away so that they do not enter into the central output waveguide. The interference extinction ratio is thus increased. From Fig. 2(a) and (b), it can be seen that two adjacent channels form interferometer structures with the interference monitored by the on-chip photodiodes. These monitors can help to characterize the phase shifters in each channel on-site. This point will be explained in detail in Section IV.

In this first experiment, the input signal was fiber coupled from an off-chip SGDBR widely tunable laser into the PIC. As our latest development, an SGDBR has been monolithically integrated which has demonstrated similar results [15] (see Section V). The SGDBR laser contains the back mirror section, phase section, gain section, front mirror section, and the output SOA section. In our practical measurement, the gain section and the front SOA section are biased with fixed currents. Different current sources are used to control the bias to the front and back mirror sections separately so as to tune the laser. The phase section is left floated. In the following tuning experiment, we mainly show the supermode selection of the laser. But it is known that by controlling the current injected into the mirrors and the phase section in a coordinated way, the laser can be tuned to any wavelength covered by its quasi-continuous tuning range [13].

III. PIC FABRICATION

To realize the passive-active integration required by the PIC, the quantum-well intermixing (QWI) technology is employed [16]. A base epi-structure as shown in Fig. 3(a) has been used. The waveguide core includes the upper and lower optical confinement layers which are 105-nm -thick InGaAsP material with a bandgap of $1.3 \mu\text{m}$ ($1.3Q$), and quantum wells (QWs) (ten wells, 6.5 nm thick with 0.9% compressive strain; 11 barriers, 8.0 nm thick with 0.2% tensile strain; the QWs have a

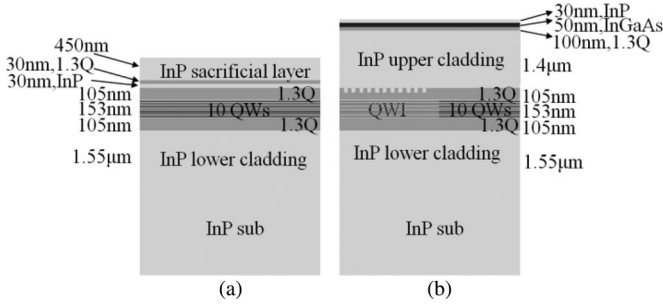


Fig. 3. (a) Base epi-structure. (b) Wafer structure after regrowth.

photoluminance peak at $1.54 \mu\text{m}$). The top 450-nm-thick InP is sacrificial and is used for phosphorus ion implantation. The implantation will form a shallow surface layer with defects on the wafer. Rapid thermal annealing afterward is used to drive vacancies created by the point defects down through the QWs which cause atoms to interdiffuse between the wells and barriers and cause the bandgap of the QWs to increase so as to become transparent to the emission of the QWs without intermixing.

After the QWI step, the sacrificial InP layer and the 1.3Q etching stop layer are removed through selective wet etching. Then, second-order gratings for emission are patterned through E-beam lithography. The gratings are etched 20 nm into the 1.3Q upper optical confinement layer through the reactive ion etching with a gas combination of $\text{CH}_4/\text{H}_2/\text{Ar}$. After the grating step, one time blanket regrowth is used to finish the whole wafer structure. The regrowth structure is shown in Fig. 3(b). It can also be seen that the grating is formed in the passive waveguide region.

After the whole wafer structure has been finished, waveguides are patterned using an I-line stepper. Two layers of hard masks are used: 70-nm Chrome and 600-nm SiO_2 . The etching of InP is carried out by inductively coupled plasma through a gas combination of $\text{Cl}_2/\text{H}_2/\text{Ar}$. Optimized etching condition ensures a very smooth and vertical sidewalls of the waveguides [17]. For processing simplicity, deep ridge waveguides (about $5 \mu\text{m}$) are used for both passive and active waveguides. This is not ideal for active waveguides because of surface recombination and weakened thermal dissipation. It would be ideal to use surface ridge waveguides for those active waveguides. Then, surface-deep ridge transitions with low loss and low reflection will have to be used, which however will make the processing much more complex [12].

After the waveguides are formed, 350-nm SiN_x is deposited for electrical isolation; then, P-vias are opened and Pt/Ti/Pt/Au P-contact metal is deposited through the liftoff process. The SiN_x on top of the waveguides in the emission array is removed as well, but there is no metal deposited on top. The InP protection layer on the waveguide top is wet etched right before the metal deposition, which is beneficial to reduce the contact resistance. Considering that in the structure metal wires cross waveguides at many places as seen from the layout in Fig. 1, photosensitive benzocyclobutene (BCB) is spin on top of the wafer to planarize. The vias for those metal contacts are opened simply through exposure and development of the BCB. The BCB on top of the waveguides in the emission array has been removed as well.

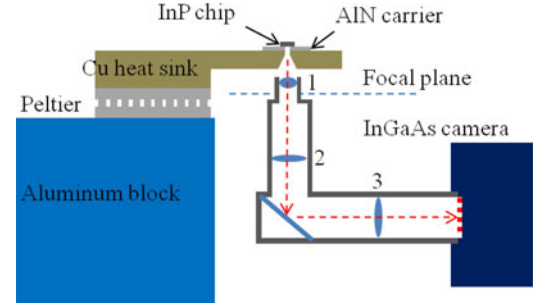


Fig. 4. Schematic of the measurement setup.

After curing BCB, 200-nm SiN_x is deposited on top of the wafer. This SiN_x layer has twofold functions: one is to help the later deposited pad metal to stick and the other is to act as an antireflection coating layer for the emission array. The final step for the top-side processing is depositing the Ti/Au thick metal stack for pads and the wires leading to the pads. After thinning the wafer down to approximately $100 \mu\text{m}$, the N-contact metal is deposited on the backside of the wafer.

The grating emits vertically both upward and downward. Theoretical calculation [18] and practical measurement using a larger area ($5 \text{ mm} \times 5 \text{ mm}$) Germanium detector show that the powers radiated upward and downward are approximately equal to each other. In the following measurement, only the downward emission is imaged, as will be shown in Section IV. So an aperture has to be opened through the backside metal and has to be aligned with the emitting gratings. This is achieved through a liftoff process and an infrared contact aligner. After the whole process, the PIC is cleaved and mounted onto an AlN carrier facing up. Because the emission is downward, there is a hole opened in the AlN carrier as well. This hole is aligned to the emission window in the backside metal of the PIC during the soldering process with a flip-chip bonding machine. The PIC on carrier is now ready for test. The final finished PIC is approximately 6 mm long and 2 mm wide.

The passive waveguide loss and the active waveguide gain are tested through some test structures fabricated with the PIC at the same time. A loss level of approximately 2.0 dB/mm is observed. The active waveguide can have a maximum gain reaching 35 dB/mm at the current density of 9 kA/cm^2 . The maximum power that can be generated by a single SOA is approximately 20 mW under the dc driving condition. The 200- μm -long phase shifter is able to generate 2π phase change with a current injection less than 20 mA. The additional loss associated with 2π phase change is approximately 1.5 dB.

IV. PIC TEST

A. Test Setup

A schematic of the measurement setup is shown in Fig. 4. Three lenses installed in lens tubes are used for the far-field imaging. The first lens with the smallest focal length (10 mm) and the highest numerical aperture (0.55) is used to capture the emission from the PIC as much as possible. The closer the lens to the PIC, the larger the angle range it can capture. The far-field pattern of the emission is generated on the lower focal

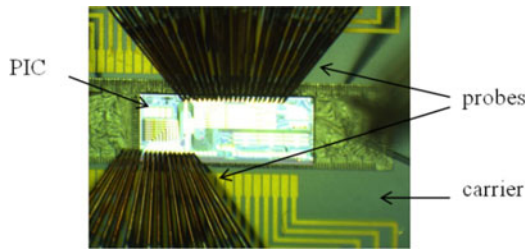


Fig. 5. Microscope image of the PIC on the setup contacted by multiprobes.

plane of the first lens. Another two lenses are used to project the far-field pattern onto the image plane of the InGaAs camera with a low level of magnification. The effective focal lengths of the second and third lenses are 75 and 100 mm, respectively. The camera has a 2-D array of pixels with $25\text{-}\mu\text{m}$ pitch in both dimensions and the array size is 320×256 . This determines that our imaging system has the ability to resolve the far field with the angle range of $34.8^\circ \times 27.7^\circ$ and the angle resolution is 0.1° in both dimensions.

B. Contact to the PIC and Bias Control

As seen from Fig. 4, the PIC is soldered onto an AlN carrier first and then the carrier is placed onto a copper heat sink. The emission is downward, so there is a tapered hole in the part hanging off the heat sink which is aligned with the hole in the carrier. The temperature is controlled through a Peltier and a thermistor which is embedded in the heat sink close to the carrier. In our measurement, the temperature is controlled at 16°C .

To make contacts to the PIC, two multiprobes are used to probe the pads on the PIC directly. A microscope image in Fig. 5 shows the probes contacting the pads. The first thing normally done is to measure the I - V curves of all the diodes on the PIC to check if they work. The single PIC has nine SOAs, eight phase shifters, and nine photodiodes. It is not difficult to find a PIC with all the diodes working after processing. The typical series resistance is around $5\ \Omega$. Normally, the preamplifier SOA is biased through a current source and the eight-SOA array is biased through another voltage source. To account for the variation of the SOA series resistance, each SOA is connected with a variable resistor (variable range from 0 to $50\ \Omega$) and a fixed $10\text{-}\Omega$ resistor.

A schematic of the connections is shown in Fig. 6. First the variable resistor is maximized and the voltage output from the voltage source is fixed at 4 V. Then, the variable resistor is adjusted and the voltage drop upon the $10\text{-}\Omega$ fixed resistor is monitored to find out the current. When the voltage drop is 1 V, the adjustment is stopped. This means that the current injected into the corresponding SOA is 100 mA. The adjustment to each channel is made in sequence. Because the shared connections between channels have resistance as well, when one channel is adjusted, the other channels are slightly influenced. This process is repeated several times until all of the channels have a current of approximately 100 mA. The eight phase shifters are biased independently through the current outputs of a 16-bit DAC card.

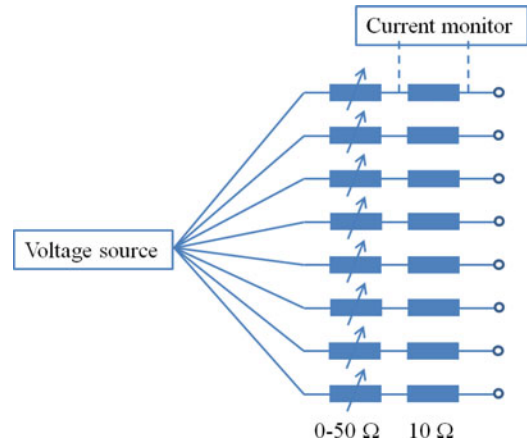


Fig. 6. Variable resistance network connected to the SOA array.

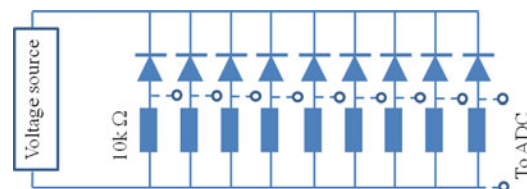


Fig. 7. Connections to the monitor photodiode array.

The current output range from the DAC card is from 0.1 to 20.2 mA. The nine monitor photodiodes are reverse biased by a single voltage source at $-2\ \text{V}$ through a connection sketched in Fig. 7. The connected series resistance is $10\ \text{k}\Omega$. The voltage drops through the resistances is monitored by an ADC card.

C. Beam Steering Controlled by Phase Shifters

As introduced previously, the scheme of 1-D OPA plus wavelength tuning of surface-emitting gratings is employed to realize 2-D optical beam steering. The OPA controls the beam steering in the direction perpendicular to the waveguide in the emission array. This direction is designated as the lateral direction in the following. The wavelength tuning controls the beam steering along the waveguide in the emission array. This direction is designated as the longitudinal direction. In the following, lateral beam steering is demonstrated first through controlling the array of phase shifters.

The input signal from the off-chip SGDBR laser has a fixed wavelength at 1539 nm in this case. Our control strategy is to characterize the phase shifters on-site first using the on-chip monitors [19], and then use these characteristics to predict the currents needed for lateral beam sweeping. To do so, first the current injected into the channel 1 phase shifter is fixed at 1 mA and then, the current injected into the channel 2 phase shifter is scanned from 1 to 20 mA. The signal response from the photodiode 1, which monitors the interference between channels 1 and 2, is recorded. The channels and photodiodes are numbered as shown in Fig. 2(a). Then, the current injected into the channel 2 phase shifter is fixed at 1 mA and the current injected into the channel 3 phase shifter is scanned from 1 to 20 mA, and the response from the photodiode 2 is recorded. The above process

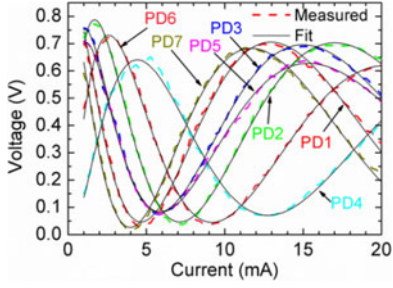


Fig. 8. Measured interference curves through the on-chip monitors and the fitting to a theoretical model.

is repeated until the current injected into the channel 8 phase shifter has been scanned.

All the results are shown in Fig. 8 as dashed lines. These curves clearly show that all the phase shifters are working and 1–20 mA is enough to generate more than 2π phase change. Then, the measured curves are fit to a theoretical model to find out the generated phase by each phase shifter. The model is shown in the following equation:

$$V_{m-1}(I) = C_0 [1 + \exp(-2\alpha) + 2 \exp(-\alpha) \cos(\Delta\phi)] + C_1$$

$$\Delta\phi_m(I) = \Delta\psi + C_2\sqrt{I} + C_3I, \quad \alpha = C_4(\Delta\phi - \Delta\psi) \quad (1)$$

where V_{m-1} is the voltage signal generated by the monitor photodiode ($m-1$), m is from 2 to 8, I is the current injected into the phase shifter m , C_i , i is from 0 to 4, are fitting parameters, α is the loss caused by injected current, $\Delta\psi$ is the initial phase difference when no current is injected, and $\Delta\phi_m$ is the total phase difference between the m -channel and the $(m-1)$ -channel. The theoretical model is derived based on the following considerations [20]: the index change induced by current injection is proportional to carrier density in InP-based phase shifters; the relationship between carrier density and current can normally be expressed as $I \propto BN^2 + CN^3$, where N is carrier density, BN^2 accounts for spontaneous emission, and CN^3 account for Auger recombination; spontaneous emission is the dominant term if the carrier density is relatively low, which is why normally phase change is proportional to $I^{1/2}$; in (1), the term C_3I is added to account for the Auger recombination; the loss coefficient α is proportional to phase change where the proportionality coefficient is related to the linewidth enhancement factor; the derivation of the interference signal V is straightforward by considering a Mach–Zehnder interferometer. The fitted curves are shown in Fig. 8 as solid lines.

Very good fitting effect has been obtained. From the fitting, the differential phase $\Delta\phi_m$ versus current for the channel- m phase shifter has been obtained. The reference of this differential phase is the $(m-1)$ -channel with its phase shifter current set at 1 mA, i.e., $\Delta\phi_2(I)$ is relative to channel 1, $\Delta\phi_3(I)$ is relative to channel 2, and so on. To more conveniently use the obtained phase-current relationship of each phase shifter, it would be ideal to change the phase reference of all channels to a unified reference. The simplest way to unify the phase reference is to make all channels refer to channel 1 with its phase shifter current set at 1 mA. This yields the phase-current relationship

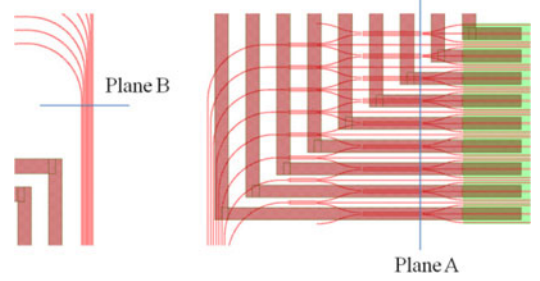


Fig. 9. Blown-up of the layout showing the interference positions.

for channel 2 phase shifter to be $\phi_2(I) = \Delta\phi_2(I)$, and for channel 3 $\phi_3(I) = \Delta\phi_2(I = 1 \text{ mA}) + \Delta\phi_3(I)$, and so on. In general, there is

$$\phi_m(I) = \Delta\phi_m(I) + \sum_2^{m-1} \Delta\phi_n(I = 1 \text{ mA}), \quad m = 2 \dots 8. \quad (2)$$

Typical results of the phase-current relationships are similar to what is shown in Fig. 10. Once the phase-current relationship for each phase shifter is known, it is easy to steer the beam, because steering the beam means adding a phase slope to the phased array according to the formula:

$$\phi'_m = \frac{2\pi}{\lambda} d \sin(\theta)(m-1), \quad m = 2 \dots 8 \quad (3)$$

where ϕ'_m is the phase that the channel- m phase shifter has to generate, d is the waveguide spacing in the emission array, λ is the wavelength, and θ is the angle the beam steers to.

From the phase-current relationship, the current needed to set for each phase shifter can be obtained through interpolation. If the phase that needs to set is beyond the range covered by the obtained phase-current relationship, a modulus of 2π can be used. The first thing attempted was to steer the beam to zero angle in the lateral direction. This means that for each channel, the phase has to be set to zero. When the settings described previously were made, the far-field pattern of the beam is actually not that good. There are two major reasons behind this. One is that the reference position for the differential phase $\Delta\phi_m$ is at the output interface of the 2×1 MMI (Plane A in Fig. 9) instead of the ideal position which is at the entrance of the grating (plane B in Fig. 9).

There are long waveguides between the entrance of the gratings and the output interface of the combiner MMI. These waveguides will cause additional differential phases. In other words, if the differential phase is zero at plane A, it is not at plane B. The second reason is that when the phases at 1 mA phase shifter current are added together [see (2)] in order to unify the phase reference, there is phase error accumulation. For example, if there is some error generated for channel 2 with its phase shifter current at 1 mA, this error will be transferred to channel 3 and channel 4, and so on. In other words, when we say channel 8 has zero phase, it has bigger uncertainties than channel 2. To solve these problems, the seven phase shifter currents I_m , $m = 2 \dots 8$, are adjusted to optimize the far-field pattern at the lateral zero angle using the particle swarm

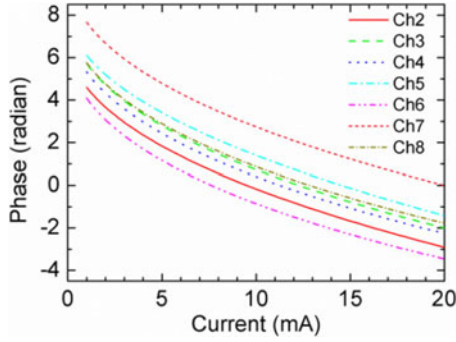


Fig. 10. Phase current curves for phase shifters obtained from the on-chip monitors.

optimization (PSO) algorithm [21]. The channel 1 phase shifter current is fixed at 1 mA. For the optimization, the side-lobe suppression is maximized around the peak at the lateral zero angle within the angle range $[-10^\circ, 10^\circ]$. Once a good beam is obtained—high side lobe suppression and good beam shape—now all the channels have zero phases at the current sets I_m . Thus, the previously found phase-current relationships for all phase shifters are corrected to make sure that all curves have the value of zero at the specific current sets I_m . This can be easily done using the following formula:

$$\phi_m''(I) = \phi_m(I) - \phi_m(I_m), \quad m = 2 \dots 8. \quad (4)$$

The new phase current curves are the basis of our following beam steering in the lateral direction. Fig. 10 shows these curves.

Fig. 11(a) shows the 3-D plot of the optimized far field at the lateral zero angle. A very elliptical beam can be seen. The FWHM of the beam in the longitudinal direction is about 0.2° , and in the lateral direction, it is about 1.7° . This is determined by the array itself. The emission array has eight channels at the moment. With a $5.5 \mu\text{m}$ spacing, the array spans a lateral size about $40 \mu\text{m}$. Assuming the emission is uniform among all channels, the far-field pattern will be a sinc function with the FWHM of 1.8° , which is in good agreement with the experimental value.

In the longitudinal direction, the grating is $500 \mu\text{m}$ long. When the grating is etched 20 nm into the 1.3Q upper optical confinement layer, the scattering loss due to grating calculated using the scattering matrix method [22] is only about 0.8 cm^{-1} , much smaller than the intrinsic loss of the waveguide. The grating turns out to be too shallow in terms of scattering power out of the waveguide. So the field (amplitude) inside the waveguide is exponentially decaying at a rate about 1 dB/mm caused by the intrinsic waveguide loss. This determines the far field to be a Lorentzian line shape with the FWHM about 0.16° , which is in agreement with the result we obtained experimentally.

Fig. 12 shows that the beam is steered to different lateral angles using the technique explained earlier. That is, Fig. 10 is used to adjust the phase-shifter currents with no additional reoptimization. It can be seen that good beam shape and good side-lobe suppression around the zeroth diffraction peak have been kept when the beam is steered. The $5.5 \mu\text{m}$ waveguide spacing determines that the $\pm 1\text{st}$ -order diffraction peaks are

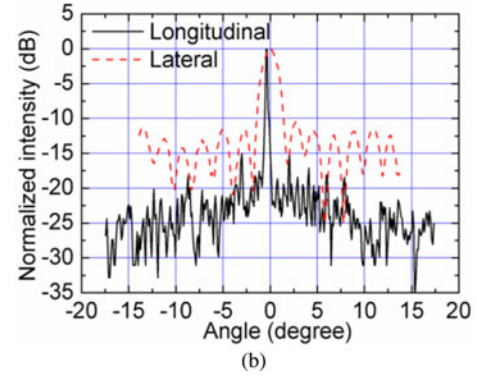
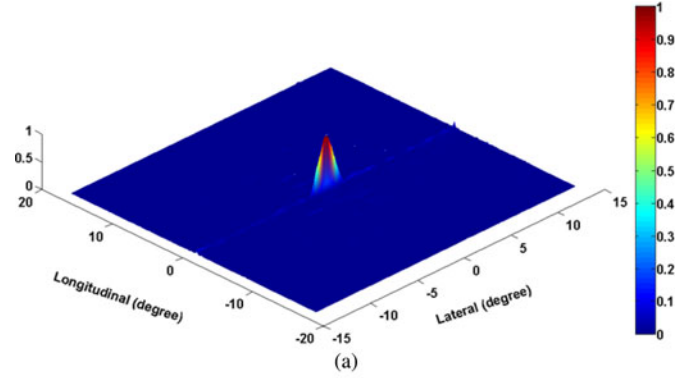


Fig. 11. (a) Three-dimensional plot of the optimized far field at the lateral angle zero. (b) Far field across the peak in the longitudinal and the lateral direction.

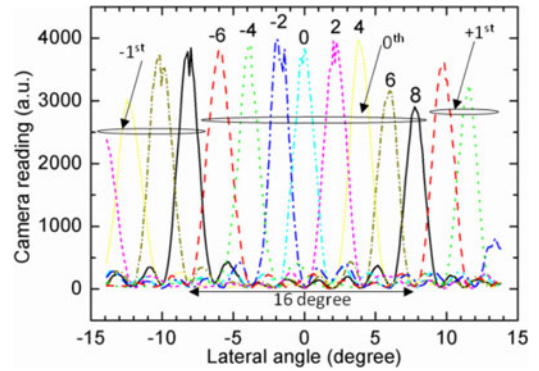


Fig. 12. Far field in the lateral direction for different angles.

about 16° away from the zeroth-order diffraction peak, which can be clearly seen from Fig. 12.

It is known that as long as each phase shifter can generate 2π phase change, the beam can be steered to any angle, not limited to the angles shown in Fig. 12. But a problem is that uniform waveguide spacing, as employed in our emission array, causes periodicity in the far field; i.e., when the zeroth-order diffraction peak is steered out of the range from -8° to 8° , determined by the spacing, the first-order diffraction peaks will enter into this range. This can be seen from Fig. 13 when the beam is further steered to 10° and -10° . The zeroth-order diffraction peaks now overlap with the $\pm 1\text{st}$ -order peaks of -6° and 6° .

In our future work, a nonuniformly spaced array will be used, and this will eliminate all high-order diffraction beams and leave

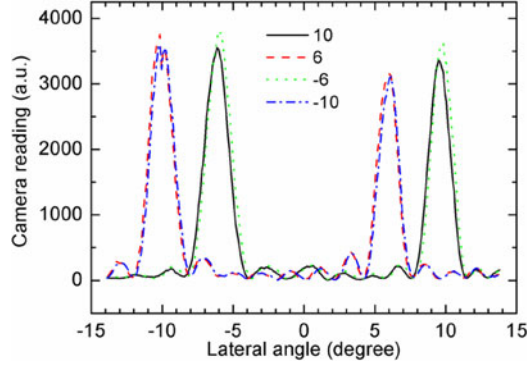


Fig. 13. Far field in the lateral direction for the lateral angles of -10° , -6° , 6° , and 10° .

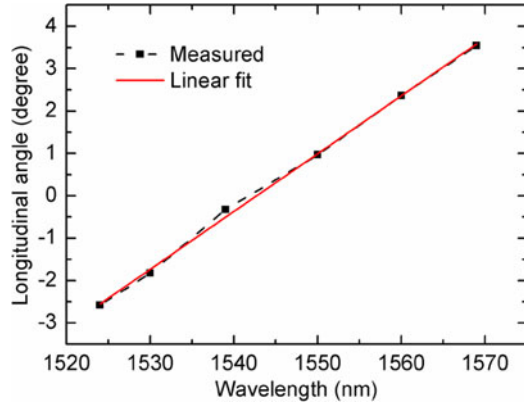


Fig. 14. Beam position in the longitudinal direction versus wavelength.

only the zeroth-order diffraction beam, so this problem will not exist anymore.

D. Beam Steering Controlled by Wavelength Tuning

Longitudinal beam steering is demonstrated by changing the input wavelength. The emission angle relies on the input wavelength through the following relation:

$$\sin(\theta) = \frac{\lambda}{\Lambda} - n_{\text{eff}} \quad (5)$$

where Λ is the pitch of the grating and n_{eff} is the effective index of the waveguide. For small emission angles, it can be approximated as

$$\theta = \frac{\lambda}{\Lambda} - n_{\text{eff}}. \quad (6)$$

The efficiency of the beam steering in terms of $d\theta/d\lambda$ is

$$\frac{d\theta}{d\lambda} = \frac{n_g}{\lambda} \frac{180}{\pi} \quad (7)$$

where n_g is the group index; $d\theta$ has the units of degrees. Our waveguide has a group index around 3.75, so the efficiency is expected to be $0.14^\circ/\text{nm}$.

Fig. 14 shows the experimentally obtained beam position in the longitudinal direction versus wavelength. The slope is $0.14^\circ/\text{nm}$ in agreement with the theoretical prediction. When the input wavelength is varied to steer the beam longitudinally,

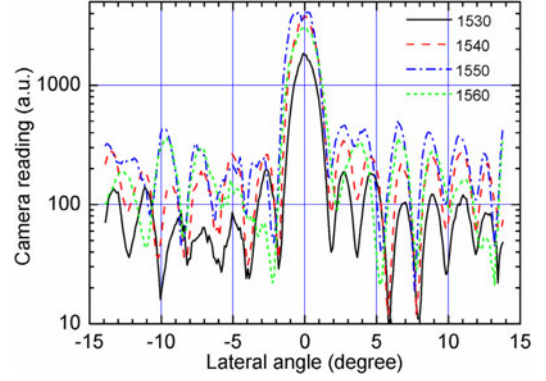


Fig. 15. Far field in the lateral direction for different wavelengths; the beam steers to the lateral angle of zero degree.

it would be good that there is no need to reset the phase shifter current in order to keep the beam in a good shape. This is, however, difficult because very long deep ridge waveguides especially long bends in the channel have been used, and there are also SOAs in the channel. In the layout, all channels are designed to be exactly the same. “Exactly” means that first the positions of all the SOAs relative to the splitters are the same so that the input power to the SOAs is ideally to be the same; second, the same bends are used in each channel, so their effects are ideally to cancel with each other. In Fig. 15, the far field in the lateral direction is shown for different wavelengths and for the same lateral angle, 0° .

When wavelength changes, the beam power also changes. This is caused by the limited gain-bandwidth of the SOAs. For 1550-nm wavelength, the camera is a little saturated so that the peak looks cutoff in the figure. However, it can be seen that the beam continues to have a relatively good shape, good side-lobe suppression, and beamwidth. Of course, careful fabrication is still needed to reduce variations among channels even with a very cautious design.

For some of our devices, some far-field variations are still seen when changing wavelength without resetting the phase shifter currents. Even for the devices with relatively good far-field patterns, improvement is still desired. Reasons for these variations include bend losses, which can add about 3 dB due to their length of approximately 1.5 mm. The layout is also pretty complex as seen from Fig. 1, and this will become a hurdle if scaling up to a larger array with significantly more channels. Thus, equal channel length designs may not worth the additional loss and layout complexities required, given that the promised simplicity in operation may not provide the needed performance. Simpler, short, low waveguide loss designs may be better, especially for larger arrays, although these would require large phase-shifter current changes for each wavelength. The control circuits may not be much more complex than required for small changes, however.

E. Two-Dimensional Optical Beam Steering

To carry out 2-D optical beam steering, the phase shifter control and the input wavelength control need to be combined.

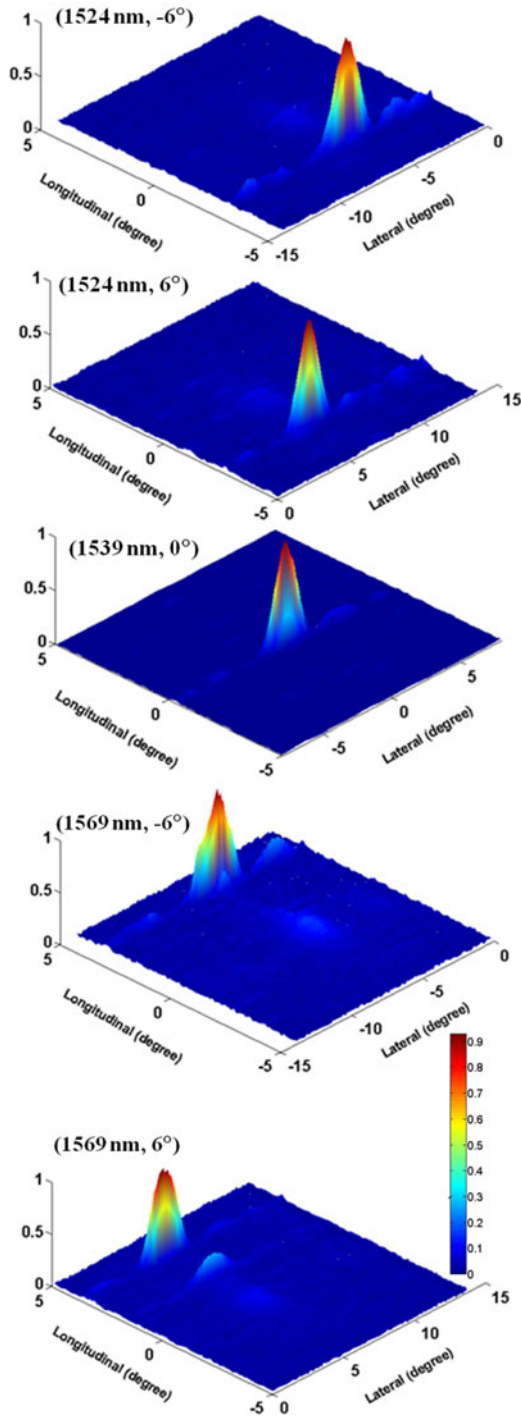


Fig. 16. Three-dimensional plot of the far-field patterns for some critical angles in the 2D plane.

The process is relatively simple: first optimize the far field for the wavelength of 1539 nm pointing at the lateral angle of zero degrees using the PSO algorithm; then spread the controls across different lateral angles using those phase-current relationships of phase shifters (see Fig. 10); and then spread the controls across the 2-D plane by changing wavelength (see Fig. 14). Initially, no further far-field optimizations are done for any angles. Fig. 16 shows a 3-D plot of the far-field patterns for some critical angles

of the 2-D plane. Although relatively good, improvements can be done by using the PSO algorithm around the current setting that is already available from the plots. When the input wavelength is away from the gain peak, for some lateral angles (specific phase shifter current settings), the influence from the reflections of the gratings (1569 nm, 6° in Fig. 16) is seen. In the future, we will take measures to reduce the grating reflections such as laterally angling the interface of the grating tooth relative to the waveguide, angling the emission in the longitudinal direction by pushing the Bragg reflection wavelength far out of the gain window, etc.

In the following, some comments on how to further improve the beam steering angle range, i.e., the total field of view (TFOV) are made. What has been shown here is 12° in the lateral direction and 6° in the longitudinal direction. For a larger angle in the longitudinal direction, a larger wavelength tuning range can be used, or lenses can be employed to magnify the angle [23]. The former method is very challenging. Considering the available tuning range of the monolithic integrated tunable laser and the SOA effective gain bandwidth, a tuning range about 80 nm can most likely be achieved [24]. This will yield a TFOV of about 11°. To get an even larger TFOV, lens magnification has to be used. When using lenses to magnify the TFOV, the beamwidth is also increased by the same amount, which means that to satisfy the requirement on the final beamwidth, the original beamwidth has to be reduced by the same amount. This can be achieved by using longer and shallower gratings.

For the lateral direction, there is no limitation to the steering angle if a 2π phase change can be achieved for each phase shifter. However, there is another limitation which is the side-lobe suppression. Because the waveguide spacing has to be relatively large (for low loss and independent phase control), high side-lobe suppression is difficult to be achieved in a large angle range, but it is possible to be realized in a rather small angle range. For example, it is difficult to realize 20 dB side-lobe suppression in a 45° angle range, but it is not that hard for a 10° angle range by simply using nonuniformly spaced arrays. Any emission beyond this relatively smaller angle range is blocked. Then, lenses are used to magnify the steering angle range. In this way, one can achieve large steering angle and high side-lobe suppression simultaneously. So to achieve good side-lobe suppression within a large angle range, the best way is probably still to use lens magnification. In other words, lenses are employed to magnify the TFOV in both directions. For the same reason to make the beamwidth still within the same metric, a larger array (more channels) has to be used. This, however, involves a much bigger effort than increasing the grating length, because more channels means much larger integration and many more controls. Fortunately, only one dimension (lateral) requires individual phase controls.

F. Fast Optical Beam Steering

One big advantage of electronically controlled beam steering is that the beam can potentially be steered to different directions very fast. In our situation, the steering speed is limited by the phase shifter bandwidth and the tuning speed of the tunable

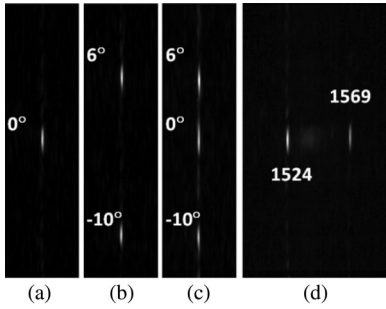


Fig. 17. Camera images of the far-field spot for two lateral angles without (a), (b) and with (c) fast beam steering. (d) Far-field spot when wavelength is fast switching.

laser. The current-injection phase shifters used in our PIC are 200 μm long, so even considering the carrier lifetime, the bandwidth can approach the gigahertz range. The SGDBR tunable laser can potentially have a few nanoseconds tuning speed [14]. So our PIC can potentially have a very fast beam steering speed. In the following, some preliminary tests for fast beam steering based on our PIC are demonstrated. We are primarily limited by the electrical connections to PIC, which only allows megahertz modulation. However, custom drive circuits in fabrication should soon enable the predicted ~ 100 MHz speed. If phase shifters employing the electrooptical effect and traveling wave electrodes were used, lateral steering bandwidths in the tens of gigahertz would be possible [25].

Here, fast beam steering in the lateral direction is reported. Seven function generators (FGs) are employed to control seven phase shifters. These FGs are synchronized by using one of them as the master: its clock output is used to synchronize all the other FGs. Series termination resistors of 50 Ω are connected to the phase shifters. Square waves of 1 MHz with 50% duty cycle are employed. The dc offset and amplitude of the square wave from each FG is optimized using the previous dc results for good far-field spots. The FGs are used as voltage sources and the dc offset is changed to scan the I - V curve of the phase shifters. The current is found by monitoring the voltage drop on the 50- Ω series resistance. Then, the optimal voltages can be decided from the required currents (datasets already established from previous experiments). Two lateral angles are selected: one is 0° and the other one is -10° . The wavelength is fixed at 1539 nm. Good beams are demonstrated at both excursions of the square wave, demonstrating more than sufficient PIC response bandwidth.

Fig. 17(a) and (b) shows the camera images of the far-field spots for the two states. When the modulation is on, the beam is switched between the two directions at 1 MHz speed which is much faster than the frame rate of the camera, so two states on the camera are observed simultaneously. To check if the beam is really switching between the two states, a photodetector is placed on top of the PIC to try to capture the upward emission. The signal of the detector is maximized when the beam is pointing at 0° . When the modulation is on, the detector signal is monitored by an oscilloscope.

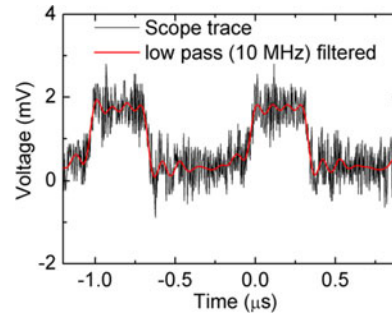


Fig. 18. Oscilloscope trace from the detector placed above the PIC.

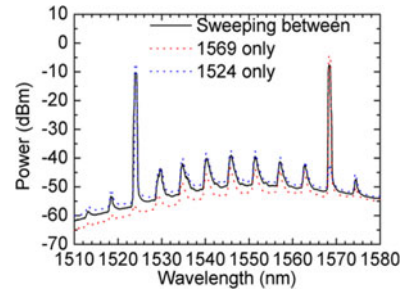


Fig. 19. Laser output spectra for two wavelengths and for fast switching between them.

The result is shown in Fig. 18. A very weak signal has been captured, so it is very noisy on the real-time oscilloscope. However, a clear indication of 1 MHz sweeping speed can be seen. So, fast steering between two angles in the lateral direction through controlling the phase shifters has been demonstrated. The speed is $10^\circ/0.5 \mu\text{s} = 2 \times 10^7$ $^\circ/\text{s}$. We believe that by using proper electrical connections and by using faster current drivers, the PIC should be able to achieve much higher steering speeds as mentioned earlier.

In the longitudinal dimension, fast beam steering is achieved by quickly changing the output wavelength of the tunable laser. To do this, the back mirror current of the SGDBR laser is fixed. The front mirror in series connection with a 50- Ω resistance is driven by an FG also by a square wave with 50% duty cycle at 1 MHz. The dc offset and amplitude of the square wave are optimized to select two output wavelengths. The laser output spectra at these two specific states are shown in Fig. 19.

When the laser output is quickly switching between these two states at 1 MHz, the spectrum analyzer captures the two output wavelengths at the same time. The same happens to the camera which captures the two far-field spots corresponding to the two wavelengths simultaneously, as shown in Fig. 17(d). To check if the wavelength is really quickly switching, the output of the laser is tapped and then passes through a narrow-band optical filter tuned to align with the 1529-nm wavelength. The output after the filter is monitored by a TIA integrated photodiode. The response from the detector is recorded by the same oscilloscope with the trace shown in Fig. 20. Clearly a switching speed of 1 MHz has been demonstrated. Considering the two states are 6° apart (see Fig. 14) in the longitudinal direction, 1.2×10^7 $^\circ/\text{s}$ steering speed has thus been achieved. There is still margin to improve.

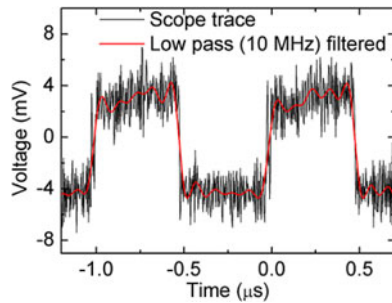


Fig. 20. Oscilloscope trace from the photodiode that monitors the wavelength switching.

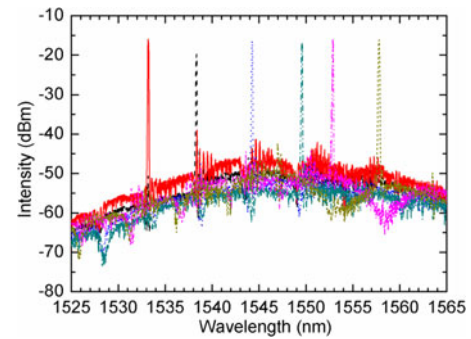


Fig. 22. Spectra of the on-chip SGDBR laser output from the back mirror.

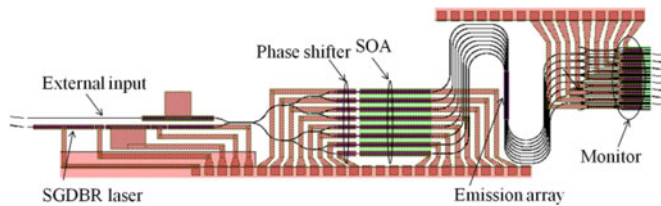


Fig. 21. Layout of the PIC with on-chip SGDBR laser.

The SGDBR laser has demonstrated a few nanoseconds tuning speed over a wide wavelength range [14].

V. SGDBR LASER INTEGRATED ON-CHIP

More recently, we have integrated the widely tunable SGDBR laser with the PIC shown in Fig. 1. The new layout is shown in Fig. 21.

Compared with the previous PIC layout shown in Fig. 1, the first splitter has been changed from a 1×2 MMI to a 2×2 MMI. This allows us to add one input as the on-chip SGDBR widely tunable laser. From the left to right, the laser includes the back mirror section, phase section, gain section, front mirror section, and the SOA section. Processing the new PIC is similar except that two steps of etching are used to form the sampled gratings used for the SGDBR laser and the surface-emitting gratings. The sampled gratings are etched 80 nm into the upper optical confinement layer, so much deeper than the surface-emitting gratings (20 nm). Another change for the new PIC is that phase shifters are placed in front of channel SOAs. This is to employ the SOA saturations to reduce the variations of the power entering into the emission array when phases are adjusted by injecting currents into the phase shifters.

What has been done first is to characterize the on-chip SGDBR laser. Fig. 22 shows the spectra of the on-chip SGDBR laser output from the back mirror. Here, only supermodes of the laser are shown. They are selected by tuning the front and back mirror sections but leaving the phase section unbiased. A total tuning range close to 30 nm is expected from this on-chip tunable laser.

Then, the beam is steered in the longitudinal direction by tuning the on-chip tunable laser. Fig. 23(a) shows the 3-D plot of the far-field spots for different wavelengths superimposed together. The beam steers to zero degree in the lateral direction. Fig. 23(b) shows the far-field distribution across the peak in the

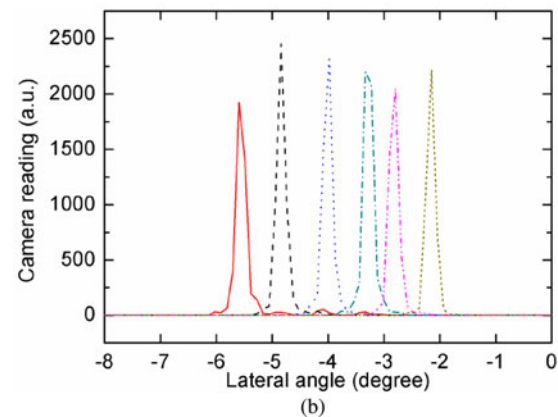
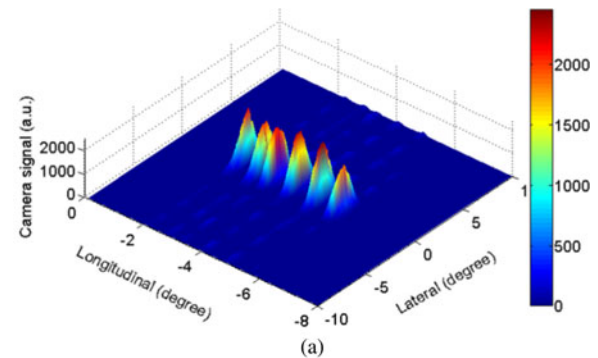


Fig. 23. (a) Three-dimensional plot of the far-field pattern for different wavelengths superposed together. (b) Far field across the peak in the longitudinal direction.

longitudinal direction. Very narrow (FWHM about 0.2° similar to previous results) and clean peaks are seen.

Then, the wavelength of the SGDBR laser is fixed at 1538 nm and the beam is steered in the lateral direction by using the array of phase shifters. Fig. 24(a) shows the 3-D plot of the far field patterns for lateral angles from -5° to 5° with a step of 2° superimposed together and (b) shows the far-field distribution across the peak in the lateral direction. The far-field in the lateral direction is broad so they overlap with each other when superimposed together. The FWHM of the beam in the lateral direction is about 2° , so similar to previous results as well.

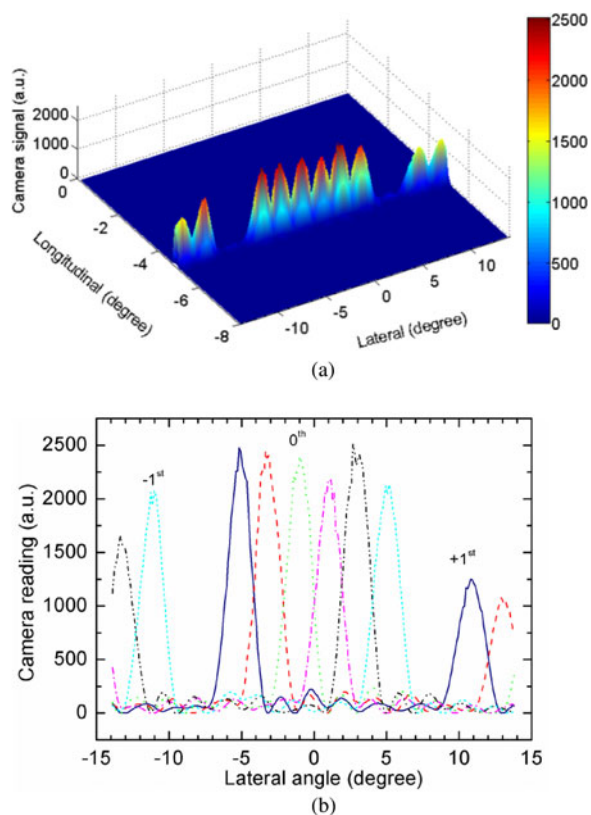


Fig. 24. (a) Three-dimensional plot of the far-field patterns. (b) Far-field distribution in the lateral direction for lateral angles from -5° to 5° with a step of 2° superimposed together.

VI. CONCLUSION

In summary, 2-D optical beam steering with an InP PIC using a 1-D OPA and wavelength tuning with surface-emitting gratings has been demonstrated. The on-chip monitors have made the 1-D OPA calibration and control easier. In general, because of fewer control elements, controlling this PIC for 2-D optical beam steering is going to be much easier than the method that uses a 2-D array of elements, such as VCSEL array or MEMS array. The tunable SGDBR laser has been successfully integrated and 2-D beam steering has been demonstrated with this on-chip tunable laser source as well. Looking forward to obtaining even larger beam steering angles and higher side-lobe suppressions, the best way is to use lens magnification as discussed in this paper. However, to make the beamwidth still within the metric a larger circuit: more channels and longer gratings must be used. More channels are also helpful to increase the output power as long as the thermal issue is well managed. So the PIC demonstrated in the paper has the ability to scale up and is promising toward practical applications.

REFERENCES

[1] P. F. McManamon, T. A. Dorschner, D. L. Corkum, L. J. Friedman, D. S. Hobbs, M. Holz, S. Liberman, H. Q. Nguyen, D. P. Resler, R. C. Sharp, and E. A. Watson, "Optical phased array technology," *Proc. IEEE*, vol. 84, no. 2, pp. 268–298, Feb. 1996.

[2] D. P. Resler, D. S. Hobbs, R. C. Sharp, L. J. Friedman, and T. A. Dorschner, "High-efficiency liquid-crystal optical phased-array beam steering," *Opt. Lett.*, vol. 21, no. 9, pp. 689–691, May 1996.

[3] F. Vasey, F. K. Reinhart, R. Houdre, and J. M. Stauffer, "Spatial optical beam steering with an AlGaAs integrated phased array," *Appl. Opt.*, vol. 32, no. 18, pp. 3220–3232, Jun. 1993.

[4] [Online]. Available at http://en.wikipedia.org/wiki/Active_electronically_scanned_array

[5] G. Hergenhan, B. Lucke, and U. Brauch, "Coherent coupling of vertical-cavity surface-emitting laser arrays and efficient beam combining by diffractive optical elements: concept and experimental verification," *Appl. Opt.*, vol. 42, no. 9, pp. 1667–1680, Mar. 2003.

[6] D. F. Siriani and K. D. Choquette, "Electronically controlled two-dimensional steering of in-phase coherently coupled vertical-cavity laser arrays," *IEEE Photon. Technol. Lett.*, vol. 23, no. 3, pp. 167–169, Feb. 2011.

[7] A. Tuantranont, V. M. Bright, J. Zhang, W. Zhang, J. A. Neff, and Y. C. Lee, "Optical beam steering using MEMS-controllable microlens array," *Sens. Actuators A*, vol. 91, no. 3, pp. 363–372, Jul. 2001.

[8] F. Xiao, W. W. Hu, and A. S. Xu, "Optical phased-array beam steering controlled by wavelength," *Appl. Opt.*, vol. 44, no. 26, pp. 5429–5433, Sep. 2005.

[9] K. V. Acoleyen, W. Bogaerts, J. Jagerska, N. L. Thomas, R. Houdre, and R. Baets, "Off-chip beam steering with a one-dimensional optical phased array on silicon-on-insulator," *Opt. Lett.*, vol. 34, no. 9, pp. 1477–1479, May 2009.

[10] W. H. Guo, P. R. A. Binetti, C. Althouse, A. Bhardwaj, J. K. Doyle, H. P. M. M. Ambrosius, L. A. Johansson, and L. A. Coldren, "InP photonic integrated circuit for 2D optical beam steering," presented at the Proc. IEEE Photon., Arlington, VA, 2011, Post-deadline Paper.

[11] J. K. Doyle, M. J. R. Heck, J. T. Bovington, J. D. Peters, L. A. Coldren, and J. E. Bowers, "Two-dimensional free-space beam steering with an optical phased array on silicon-on-insulator," *Opt. Exp.*, vol. 19, no. 22, pp. 21595–21604, Oct. 2011.

[12] S. C. Nicholes, M. L. Masanovic, B. Jevremovic, E. Lively, L. A. Coldren, and D. J. Blumenthal, "An 8×8 InP monolithic tunable optical router (MOTOR) packet forwarding chip," *J. Lightw. Technol.*, vol. 28, no. 4, pp. 641–650, Feb. 2010.

[13] L. A. Coldren, "Monolithic tunable diode lasers," *IEEE J. Sel. Topics Quantum Electron.*, vol. 6, no. 6, pp. 988–999, Nov. 2000.

[14] J. E. Simsarian, M. C. Larson, H. E. Garrett, H. Xu, and T. A. Strand, "Less than 5-ns wavelength switching with an SG-DBR laser," *IEEE Photon. Technol. Lett.*, vol. 18, no. 4, pp. 565–567, Feb. 2006.

[15] W. H. Guo, P. R. A. Binetti, C. Althouse, L. A. Johansson, and L. A. Coldren, "InP photonic integrated circuit with on-chip tunable laser source for 2D optical beam steering," presented at the Opt. Fiber Commun. Conf., Anaheim, CA, 2013, Paper OTh31.7.

[16] E. J. Skogen, J. S. Barton, S. P. Denbaars, and L. A. Coldren, "A quantum-well-intermixing process for wavelength-agile photonic integrated circuits," *IEEE J. Sel. Topics Quantum Electron.*, vol. 8, no. 4, pp. 863–869, Jul. 2002.

[17] J. S. Parker, E. J. Norberg, R. S. Guzzon, S. C. Nicholes, and L. A. Coldren, "High verticality InP/InGaAsP etching in Cl₂/H₂/Ar inductively coupled plasma for photonic integrated circuits," *J. Vac. Sci. Technol. B*, vol. 29, no. 1, pp. 011016–011020, Jan. 2011.

[18] S. Park, S. H. Song, C. H. Oh, and P. S. Kim, "Ray-optical determination of the coupling coefficient of grating waveguide by use of the rigorous coupled-wave theory," *J. Lightw. Technol.*, vol. 19, no. 1, pp. 120–125, Jan. 2001.

[19] W. H. Guo, P. R. A. Binetti, C. Althouse, H. P. M. M. Ambrosius, L. A. Johansson, and L. A. Coldren, "InP photonic integrated circuit with on-chip monitors for optical beam steering," presented at the Int. Semicond. Laser Conf., San Diego, CA, Oct. 2012, Paper MA6.

[20] L. A. Coldren, S. W. Corzine, and M. L. Mashanovitch, *Diode Lasers and Photonic Integrated Circuits*, 2nd ed. New York: Wiley, Mar. 2012.

[21] J. Robinson and Y. Rahmat-Samii, "Particle swarm optimization in electromagnetics," *IEEE Trans. Antennas Propag.*, vol. 52, no. 2, pp. 397–407, Feb. 2004.

[22] Q. Y. Lu, W. H. Guo, R. Phelan, D. Byrne, J. F. Donegan, P. Lambkin, and B. Corbett, "Analysis of slot characteristics in slotted single-mode semiconductor lasers using the 2-D scattering matrix method," *IEEE Photon. Technol. Lett.*, vol. 18, no. 24, pp. 2605–2607, Dec. 2006.

[23] W. H. Guo, P. R. A. Binetti, C. Althouse, H. P. M. M. Ambrosius, L. A. Johansson, and L. A. Coldren, "Improved performance of optical beam steering through an InP photonic integrated circuit," presented at the Conf. Lasers Electro-Opt., San Jose, CA, May 2012, Paper CW1 K.2.

- [24] B. Mason, J. Barton, G. A. Fish, L. A. Coldren, and S. P. DenBaars, "Design of sampled grating DBR lasers with integrated semiconductor optical amplifiers," *IEEE Photon. Technol. Lett.*, vol. 12, no. 7, pp. 762–764, Jul. 2000.
- [25] R. Fabian, W. Pease, D. A. B. Miller, and T. H. Lee, "High-speed optical beam-steering based on phase-arrayed waveguides," *J. Vac. Sci. Technol. B: Microelectron. Nanometer Struct.*, vol. 26, no. 6, pp. 2124–2126, Nov. 2008.



Weihua Guo received the B.Sc. degree in physics from Nanjing University, Nanjing, China, in 1998, and the Ph.D. degree from the Institute of Semiconductors, Chinese Academy of Sciences, Beijing, China, in 2004. His Ph.D. research was focused on simulation and fabrication of optical microcavities and semiconductor optical amplifiers.

From September 2004 to October 2010, he was a Postdoctoral Researcher at the Department of Physics, Trinity College Dublin, Dublin, Ireland, where he did research on various topics such as optical performance monitoring techniques and tunable integrated sources for coherent wavelength division multiplexing systems.

In November 2010, he joined the Department of Electrical and Computer Engineering, University of California Santa Barbara, Santa Barbara, as an Assistant Project Scientist. His current research interests include using InP photonic integrated circuits to realize novel functions.



Pietro R. A. Binetti received the Ph.D. degree in electrical engineering from the COBRA Research Institute, Eindhoven University of Technology, Eindhoven, The Netherlands, in 2009.

He is currently a Postdoctoral Researcher at the University of California Santa Barbara, Santa Barbara. His research interests include design, fabrication, and characterization of photonic integrated circuits for analog and digital applications.



Chad Althouse received the B.S. degree from Penn State University, University Park, in 2007, and the M.S. degree from the University of California Santa Barbara (UCSB), Santa Barbara, in 2012, both in materials. As a Ph.D. student in material science at UCSB, he designed, fabricated, and tested photonic integrated circuits including integrated optical isolators and injection-locked tunable lasers for high-speed communication.

He is currently a Process Engineer at Innovative Micro Technology, Goleta, CA, USA, where he is

working to develop microelectromechanical systems technology. He has worked on various other government-funded research projects throughout his studies at Penn State University and UCSB.



Milan L. Mašanović (S'98–M'04) received the Dipl.Eng. degree from the School of Electrical Engineering, University of Belgrade, Belgrade, Yugoslavia, in 1998, and the M.S. and Ph.D. degrees from the University of California Santa Barbara, Santa Barbara, in 2000 and 2004, respectively, all in electrical engineering.

He is currently a Research Scientist at the University of California Santa Barbara. He is also a founder of Freedom Photonics, a photonic integration company in Santa Barbara, CA. He is the author or

coauthor of more than 70 research papers. His current research interests include InP photonic integration related to applications in packet-switched optical networks.

Dr. Mašanović was the recipient of the 2003 Best Student Paper Award at the Indium Phosphide and Related Materials Conference and the 2004 IEEE Lasers and Electro-Optics Society Graduate Student Fellowship Award.



Huub P. M. M. Ambrosius received the Ph.D. degree in chemistry from the Catholic University of Nijmegen (now Radboud University), Nijmegen, The Netherlands, in 1981.

He then joined Philips Research Labs in Eindhoven, The Netherlands, working on III/V technology for lasers and photodetectors. From September 1987 to September 1988, he worked as ex-pat at the Philips Research Lab in Limeille-Brevannes (France) working on the first planetary MOVPE reactor. After the acquisition of the Philips Optoelectronic

Centre by Uniphase (later JDS Uniphase) in 1998 he was Engineering Manager in the Waferfab until JDS Uniphase closed down the facility in Eindhoven in 2004. In 2005, he cofounded Cedova BV in Eindhoven, and in 2009, he joined the Optoelectronic Devices Group at the Eindhoven University of Technology, Eindhoven, responsible for the cleanroom activities and the technology. Recently, he became Managing Director of NanoLab@TU/e, the cleanroom facility of the Eindhoven University of Technology.



Leif A. Johansson (M'04) received the Ph.D. degree in engineering from University College London, London, U.K., in 2002.

He is currently a Research Scientist with the University of California Santa Barbara, Santa Barbara. His current research interests include design and characterization of integrated photonic devices for analog and digital applications and analog photonic systems and subsystems.



Larry A. Coldren (S'67–M'72–SM'77–F'82) received the Ph.D. degree in electrical engineering from Stanford University, Stanford, CA, in 1972.

He is currently the Fred Kavli Professor of Optoelectronics and Sensors at the University of California Santa Barbara (UCSB), Santa Barbara. After 13 years in the research area at Bell Laboratories, he joined UCSB in 1984, where he is currently with the Department of Materials and the Department of Electrical and Computer Engineering. In 1990, he cofounded Optical Concepts, later acquired as Gore Photonics,

to develop novel vertical-cavity surface-emitting laser (VCSEL) technology. In 1998, he cofounded Agility Communications, later acquired by JDSU, to develop widely tunable integrated transmitters. At Bell Labs, he initially worked on waveguided surface-acoustic-wave signal processing devices and coupled-resonator filters. He later developed tunable coupled-cavity lasers using novel reactive-ion etching technology that he created for the then new InP-based materials. At UCSB, he continued work on multiple-section tunable lasers, in 1988, inventing the widely tunable multielement mirror concept, which is now used in some JDSU products. Near this same time period, he also made seminal contributions to efficient VCSEL designs that continue to be implemented in practical devices to this day. More recently, his group has developed high-performance InP-based photonic integrated circuits as well as high-speed VCSELs, and they continue to advance the underlying materials growth and fabrication technologies. He has authored or coauthored more than a thousand journal and conference papers, seven book chapters, and one textbook and has been issued 64 patents. He has presented dozens of invited and plenary talks at major conferences.

Dr. Coldren is a Fellow of the Optical Society of America, the Institution of Electrical Engineers, and a member of the National Academy of Engineering. He was a recipient of the 2004 John Tyndall and 2009 Aron Kressel Awards.

Large-scale InP Photonic Integrated Circuit Packaged with Ball Grid Array for 2D Optical Beam Steering

Weihua Guo¹, Pietro R. A. Binetti², Milan L. Masanovic¹, Senior Member, IEEE, Leif A. Johansson¹, Member, IEEE, and Larry A. Coldren¹, Fellow, IEEE

¹Department of Electrical and Computer Engineering, University of California, Santa Barbara, CA 93106, USA

²JDSU-R&D Communications and Commercial Optical Products, 430 North McCarthy Boulevard, Milpitas, CA 95035, USA
Email: guow@ece.ucsb.edu

Abstract: Large-scale InP photonic integrated circuit containing 1×32 optical phased array packaged with ball grid array has demonstrated two-dimensional (2D) optical beam steering.

OCIS codes: (250.5300) Photonic integrated circuits; (280.3640) Lidar;

1. Introduction

Electronically controlled two-dimensional (2D) optical beam steering is potentially useful for light detection and ranging (LIDAR), secure laser communication, printing, etc. Recently we have demonstrated an InP photonic integrated circuit (PIC) consisting of an optical phased array (OPA) with embedded surface-emitting gratings for this purpose [1]. The OPA consisting of 8 waveguides was controlled to steer the beam in the lateral dimension perpendicular to the waveguide in the array while wavelength tuning was used to steer the beam in the longitudinal dimension along the waveguide in the array [1]. In this work the waveguide number in the OPA has been upgraded to 32 so that the PIC is larger and contains many more diodes. To make contacts to all the diodes and control them, a packaging scheme based on ball grid array has been developed. Finally the packaged PIC has successfully demonstrated 2D optical beam steering.

2. Layout of the PIC and packaging strategy

Fig. 1 (a) shows the layout of the PIC. The left side contains two ports: one is for the output of the on-chip sample-grating DBR (SGDBR) widely tunable laser; the other one is for the external input. The beam splitter is a simple star coupler which has two inputs and 32 outputs: the input beam from either the on-chip SGDBR laser or the external input is split into 32 channels. Each channel has its own phase shifter followed by a high power semiconductor optical amplifier (SOA). After amplification the light enters into the grating region for out-of-plane emission. The emission is downward through the substrate. On top of the grating there is gold reflector which makes the emission uni-directional. After grating is the on-chip monitor array [1]. The PIC contains 104 diodes in total. To test the PIC a way of packaging is needed: the PIC is first flip-chip bonded onto an optical carrier; then the optical carrier is soldered onto a print circuit board (PCB) called intermediate board; finally the intermediate board plugs into a big PCB board which connects to DAC cards and high power current sources. In order to solder the optical carrier onto the intermediate board, first solder spheres with 300 μm diameter were fixed onto pads of the intermediate board using a stencil; then the optical carrier with matching pads was placed onto these solder spheres with the alignment carried out by a flip-chip bonding machine; finally the solder spheres were melted. Fig. 1(b) shows an image of the optical carrier soldered onto the intermediate board. This is similar to the ball grid array packaging technique used broadly in electronics, with the modification that the solder spheres were placed on the PCB board. A micro-channel cooler was soldered onto the backside of the carrier to cool the optical chip when high current was pumped into the SOA array. The final packaged system is shown in Fig. 1 (c).

3. Measurement

Two DAC cards were used to control the 32 phase shifters. The input signal to the PIC was fiber coupled from an external tunable laser. The 32-SOA array was biased together by a high power current source with each SOA having the current about 300 mA. The emission from the gratings was monitored by a far-field imaging system consisting of three lenses and an infrared camera [1]. First the input wavelength was fixed at 1550 nm and the current injected into each phase shifter of the 32-phase shifter array was adjusted to steer the beam to a specific angle in the lateral direction. The side-lobe suppression within the angle range from -10° to 10° around the selected angle was optimized through the particle swarm optimization algorithm [1]. A typical result of the beam pointed at the lateral 0° angle is shown in Fig. 2, where Fig. 2(a) shows the 3D plot and (b) shows the beam profile across the peak in the

longitudinal and lateral directions. The full width half maximum (FWHM) of the beam is 0.3 degree in the longitudinal direction and 1.2 degrees in the lateral direction. The side lobe suppression is about 15 dB. Then the phase shifter currents were adjusted to steer the beam laterally to -5° , 0° , and 5° , respectively. The beam profiles in the lateral direction are shown in Fig. 3 (a). Because non-uniformly spaced array is used, higher order diffraction peaks disappear. This is very different from the case when uniformly spaced array being used [1]. Then the input wavelength was changed from 1540 to 1570 nm, and the phase shifter currents were adjusted accordingly to keep the beam pointing at the lateral 0° angle. Fig. 3 (b) shows the beam profiles in the longitudinal direction for the wavelength of 1540, 1550, 1560, and 1570 nm, respectively. The intensity changes due to the dependence of gain on wavelength.

4. Summary

In summary large scale InP PIC with 1×32 OPA and 104 diodes has been packaged and has demonstrated 2D optical beam steering by a combination of wavelength tuning and OPA control.

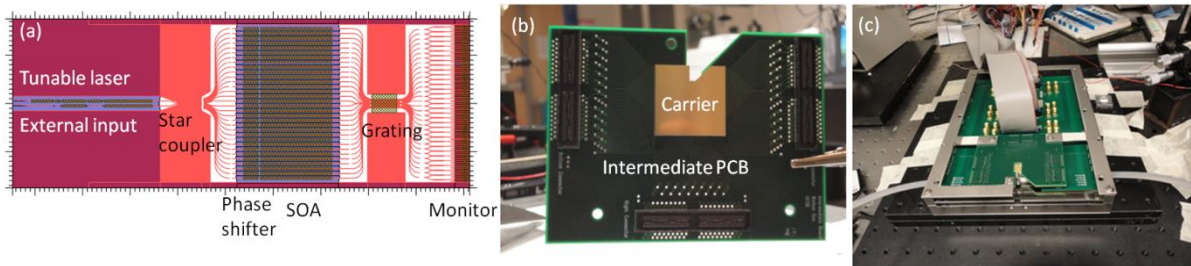


Fig. 1 (a) Layout of the PIC; (b) Carrier with PIC soldered onto the intermediate PCB board; (c) Packaged system

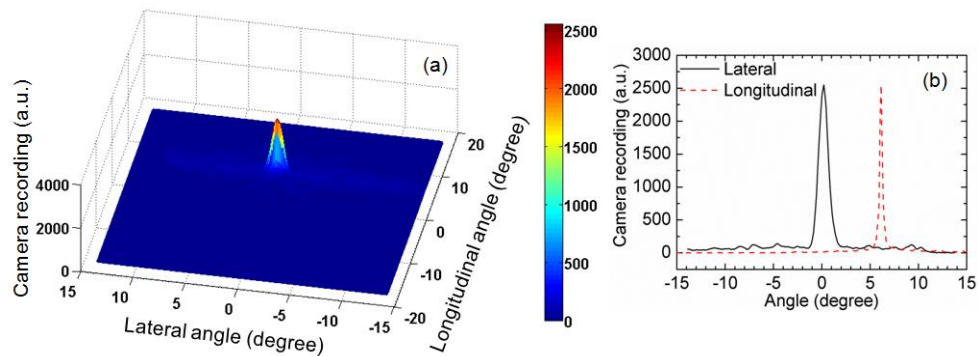


Fig. 2 (a) 3-dimensional plot of the beam spot; (b) Beam profile across the peak in the longitudinal and lateral directions.

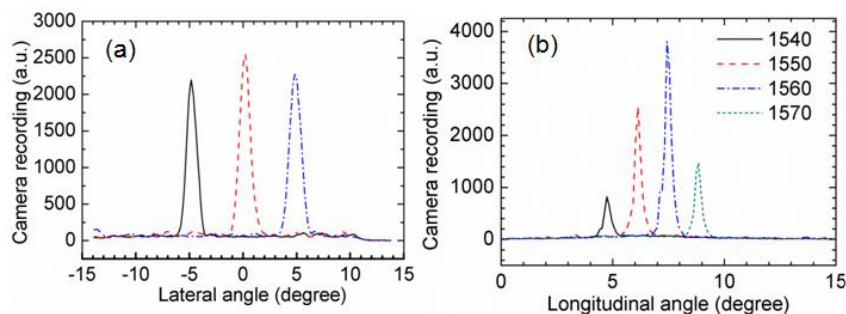


Fig. 3 (a) Beam profiles for different lateral angles and the same wavelength of 1550 nm; (b) Beam profiles for different wavelengths and for the same lateral angle of 0° .

5. Reference

[1] W. H. Guo, P. R. A. Binetti, C. Althouse, M. L. Masanovic, H. P. M. M. Ambrosius, L. A. Johansson, and L. A. Coldren, "Two-dimensional optical beam steering with InP-based photonic integrated circuits," Special issue on semiconductor lasers, J. Sel. Topics Quantum Electron., 2013.

II. Vertical-Cavity Surface-Emitting Lasers (VCSELs)

Chapter 7

Design and Performance of High-Speed VCSELs

Yu-Chia Chang and Larry A. Coldren

Abstract Over the past several years, high-speed vertical-cavity surface-emitting lasers (VCSELs) have been the subject of intensive worldwide research due to their applications in optical interconnects and optical data networks. The performance of VCSELs, especially with respect to their high-speed characteristics, has made significant progress. In this chapter, we first present the basic theory for current-modulated VCSELs using rate equations and small-signal analysis. Factors that affect the modulation bandwidth, including the intrinsic laser responses and extrinsic parasitics, are identified. Once these limitations are known, we discuss various designs that have been implemented in VCSELs to specifically address them, followed by a review of the current high-speed VCSEL performance based on these designs at several different wavelengths, including 850 nm, 980 nm, 1.1 μm , and 1.3–1.6 μm . Finally, we consider new modulation schemes based on loss modulation in coupled-cavity VCSELs, which has the potential to reach even higher speeds.

7.1 Introduction

The rapid explosion of information has created ever increasing demands for data bandwidth. Optical fiber communication now dominates long-haul and metropolitan telecommunication networks, and it has made many in-roads into data-communication networks in campus and high-performance computing environments. However, traditional electrical signaling is still used for many tele- and data-communication links at the edge of these networks where data rates are still modest. But, even here

Y.-C. Chang (✉) · L. A. Coldren
Department of Electrical and Computer Engineering,
University of California, Santa Barbara, CA, USA
e-mail: yuchia@engineering.ucsb.edu

L. A. Coldren
e-mail: coldren@ece.ucsb.edu

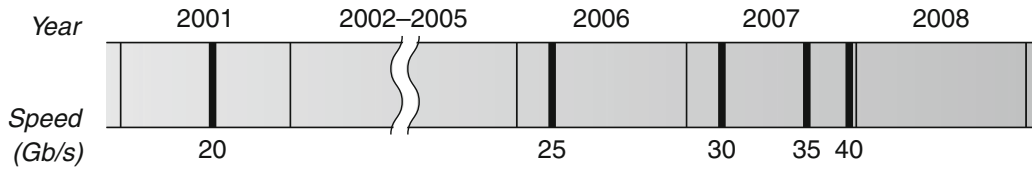


Fig. 7.1 Timeline of the first reported 20, 25, 30, 35, and 40 Gb/s direct current modulation of VCSELs

optical techniques are beginning to look more attractive as the optical component cost becomes more competitive and the bandwidth demands increase. Also as space and power dissipation become important, some fundamental limitations come into play [1]. Optics is progressively replacing many electrical links, from networks to eventually even chip-to-chip and on-chip interconnects within computers. Low-cost, power-efficient, high-speed optical sources are one of the main keys to enable this transition.

Vertical-cavity surface-emitting lasers (VCSELs) are inherently suitable for optical data transmission for various reasons. Their small volume fundamentally implies that low power consumption and high-speed operation can be realized simultaneously. Due to surface emission, VCSELs can produce a more circular output beam with less divergence, can easily be fabricated in arrays, and can support on-wafer testing. All these lead to a significant reduction of the testing and packaging costs.

Over the past several years, worldwide research efforts to improve the performance of VCSELs for optical data links have reached fruition, especially with respect to their high-speed aspects. Figure 7.1 summarizes the timeline of the first reported data rates of 20, 25, 30, 35, and 40 Gb/s for directly modulated VCSELs. In 2001, 20-Gb/s operation was reported by Kuchta et al. using oxide-confined 850-nm VCSELs [2]. Not until 2006, 25-Gb/s operation was achieved by Suzuki et al. in NEC using 1.1- μm -wavelength VCSELs [3]. One year later, data rate was further pushed to 30 Gb/s by the same group using buried tunnel junction (BTJ) VCSELs [4]. Just after six months, a data rate of 35 Gb/s was reported by Chang et al. using oxide-confined 980-nm VCSELs [5]. Three months later, the 40-Gb/s milestone was finally hit by Anan et al., again by NEC, using BTJ VCSELs [6]. So, in the year 2007, the direct modulation speed of VCSELs was pushed from 25 to 40 Gb/s, a tremendous progress.

Of at least equal importance, many system-level optical links based on VCSELs have been demonstrated in this period. For example, an aggregate data rate of 500 Gb/s has been reported using 48 channels of 10.42-Gb/s data transmitted over a parallel 12-fiber ribbon with four wavelengths per fiber [7]. These links have demonstrated that power consumption is equally important to speed, so a significant emphasis on reducing overall power-consumption/data-rate ratio is also a goal for both optical interconnects and optical data links. The total link power consumption, including driver and receiver electronics, for 500 Gb/s is 3.3 W, corresponding to a power-consumption/data-rate ratio of 6.6 mW/(Gb/s). For waveguide-based

chip-to-chip optical links, an aggregate data rate of 160 Gb/s has been reported with 4×4 VCSEL and photodiode arrays, each operated at 10 Gb/s [8]. The total link power consumption is 2.5 W, corresponding to 15.6 mW/(Gb/s). More results will be presented in Chaps. 15 and 16 of this book.

Long-wavelength VCSELs (LW-VCSELs) have made significant progress as well. Novel structures and new materials have been pursued to overcome the material challenges faced by LW-VCSELs. Based on different technologies, several groups and companies have demonstrated data transmission at 10 Gb/s over single-mode fibers (SMF) [9–13]. At this writing such components are beginning to be sampled commercially by some companies. Although intense efforts on 1300–1550 nm VCSELs are expected to continue, it is unlikely that such devices will reach the modulation bandwidths ultimately available in the shorter 850–1100 nm range due to both material and cavity volume constraints that will be discussed in the next section.

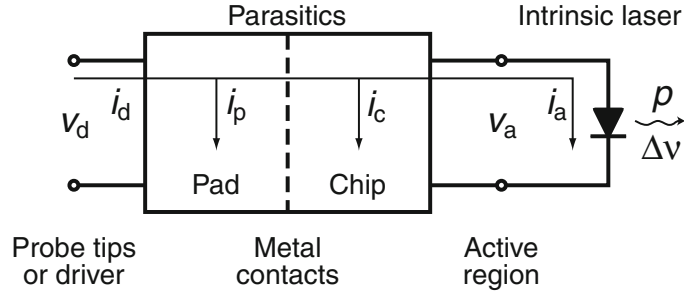
This chapter is organized as follows. Section 7.2 presents the theoretical background for current-modulated VCSELs. The device designs are covered in Sect. 7.3, and Sect. 7.4 reviews some of the high-speed VCSEL results. Section 7.5 discusses loss-modulated VCSELs, and Sect. 7.6 concludes this chapter.

7.2 Theoretical Background

Before jumping to the design of high-speed VCSELs, it is important to understand how the bandwidth of VCSELs is determined. Once various factors that can limit the bandwidth are known, the VCSEL structure can be specifically optimized to address these restrictions. In this section, the necessarily theoretical background for directly current modulating VCSELs is provided.

Just like other diode lasers, the bandwidth of VCSELs is determined by the intrinsic laser response as well as the extrinsic parasitic response. To facilitate our discussion, the cascaded two-port model for representing a diode laser, shown in Fig. 7.2, is used to separate the intrinsic laser and the parasitics [14]. The intrinsic laser is the active region where it is desirable to concentrate the current and optical modes to maximize the carrier and photon densities, which are coupled via stimulated recombination. The parasitics, defined between the intrinsic laser and the driving circuit, are split into the pad parasitics and chip parasitics at the metal contacts. The input variables in the model are the drive voltage v_d and drive current i_d . The currents entering the pad and chip parasitics are i_p and i_c , respectively. The voltage and current seen by the intrinsic laser are v_a and i_a , respectively. The output variables are the output power p and frequency shift $\Delta\nu$. For short-distance optical data links, dispersion is usually not a concern and $\Delta\nu$ will not be considered.

Fig. 7.2 Cascaded two-port model for VCSEL



7.2.1 Intrinsic Laser Response

Rate Equation Analysis

We start with the phenomenological rate equations, which describe the supply and loss of the carriers and photons within the active region [15]:

$$\frac{dN}{dt} = \frac{\eta_i I}{qV} - \frac{N}{\tau} - v_g g N_p \quad (7.1a)$$

$$\frac{dN_p}{dt} = \Gamma v_g g N_p + \Gamma R'_{sp} - \frac{N_p}{\tau_p} \quad (7.1b)$$

where N is the carrier density, N_p is the photon density, η_i is the injection efficiency, I is the terminal current, q is the electronic charge, V is the volume of the active region, τ is the carrier lifetime, v_g is the group velocity, g is the gain, Γ is the confinement factor, R'_{sp} is the spontaneous recombination rate into the mode of interest, and τ_p is the photon lifetime.

The gain g can be well approximated by a four-parameter logarithmic formula [15]

$$g(N, N_p) = \frac{g_0}{1 + \varepsilon N_p} \ln \left(\frac{N + N_s}{N_{tr} + N_s} \right) \quad (7.2)$$

where g_0 is the gain coefficient, ε is the gain compression factor, N_{tr} is the transparency carrier density, and N_s is a shift to make g equal the unpumped absorption at $N=0$.

Once we have the rate equations ready, small-signal frequency analysis can be applied. Assume there is a small sinusoidal modulating current with an amplitude of I_1 superimposed on the steady-state bias current I_0 , we have

$$I(t) = I_0 + I_1 e^{j\omega t} \quad (7.3a)$$

$$N(t) = N_0 + N_1 e^{j\omega t} \quad (7.3b)$$

$$N_p(t) = N_{p0} + N_{p1} e^{j\omega t} \quad (7.3c)$$

where N_0 and N_{p0} are the steady-state carrier and photon densities, N_1 and N_{p1} are the corresponding small-signal modulation amplitudes, and ω is the angular frequency. Substituting (7.3) into (7.1), neglecting the products of the small-signal terms, but retaining other first-order deviations, we obtain the modulation transfer function

$$H_{\text{int}}(\omega) \equiv \frac{p(\omega)}{i_a} = A_i \frac{\omega_r^2}{(\omega_r^2 - \omega^2 + j\omega\gamma)} \quad (7.4)$$

where A_i is the DC slope efficiency, $\omega_r = 2\pi f_r$ is the relaxation resonance frequency, and γ is the damping factor. This transfer function is in the form of a second-order low-pass filter with a damped resonance peak.

The relaxation resonance frequency is the natural oscillation frequency between the carriers and photons in the laser cavity and can be approximately expressed as

$$\omega_r = \left[\frac{v_g a N_{p0}}{\tau_p} \right]^{1/2} = \left[\frac{v_g a}{q V_p} \eta_i (I_0 - I_{\text{th}}) \right]^{1/2} \quad (7.5)$$

where $a = \partial g / \partial N|_{\text{th}}$ is the differential gain at threshold, V_p is the mode volume, and I_{th} is the threshold current. As clearly shown in (7.4), the relaxation resonance frequency basically determines how fast an intrinsic diode laser can be modulated when the damping is not severe. Therefore, it is important to increase the relaxation resonance frequency for higher bandwidth. Examining (7.5) tells that higher differential gain a , larger photon density N_{p0} , and smaller photon lifetime τ_p can improve the relaxation resonance frequency. (But, one must be careful not to think that adding internal loss is good, because it always reduces N_{p0} more than τ_p .)

The only parameter, to the first-order approximation, in (7.5) that depends on the operating conditions is the photon density, which can be increased with higher current. A figure of merit commonly used to evaluate how efficient an intrinsic laser can be modulated is the D -factor [16]

$$D \equiv \frac{f_r}{(I - I_{\text{th}})^{1/2}} = \frac{1}{2\pi} \left[\frac{v_g a}{q V_p} \eta_i \right]^{1/2}.$$

To evaluate the device's overall high-speed performance, the related factor, modulation current efficiency factor (MCEF), is more commonly used [17]

$$\text{MCEF} \equiv \frac{f_{3\text{dB}}}{(I - I_{\text{th}})^{1/2}}$$

where $f_{3\text{dB}}$ is the 3-dB frequency, which is approximately equal to $1.55f_r$ when the parasitics and damping are relatively small.

The damping represents the rate of energy loss in the laser cavity, which effectively reduces the strength of the resonance peak. The damping factor γ is given as

$$\gamma = v_g a N_{p0} \left[1 + \frac{\Gamma a_p}{a} \right] + \frac{1}{\tau_{\Delta N}} + \frac{\Gamma R'_{\text{sp}}}{N_{p0}} \quad (7.6)$$

where $\tau_{\Delta N}$ is the differential carrier lifetime, and

$$a_p = -\left. \frac{\partial g}{\partial N_p} \right|_{N_{p0}} = \frac{\varepsilon g}{1 + \varepsilon N_{p0}}. \quad (7.7)$$

At normal high-speed operating conditions, spontaneous-emission-related damping can be neglected, and γ increases with N_{p0} , which is proportional to f_r^2 . The proportionality is the K -factor given as

$$K = 4\pi^2 \tau_p \left[1 + \frac{\Gamma a_p}{a} \right]. \quad (7.8)$$

Practically, K -factor is empirically determined by fitting γ versus f_r^2 . As the photon density keeps increasing to a point, the modulation response becomes overdamped and the bandwidth decreases. The maximum theoretically damping-limited f_{3dB} is given as

$$f_{3dB} |_{\max} = \sqrt{2} \frac{2\pi}{K} \quad (\gamma/\omega_r = \sqrt{2}). \quad (7.9)$$

Since K -factor increases with gain compression factor ε through a_p , reducing gain nonlinearity is also important to achieve high bandwidth.

Beyond the Rate Equations

The proceeding rate equation analysis is appealing due to its simplicity but still providing intuitive insights. However, many effects were not included, and we summarize some of them here.

First discovered in 1991, carrier transport in the separate-confinement heterostructure (SCH) region actually plays an important role in the dynamics of quantum-well (QW) lasers [18]. To reduce the carrier transport effects, it is necessary to minimize the time for carriers to reach and fall into QWs and maximize the time for carriers to escape back from QWs to SCH region. This can be treated with a modified set of rate equations that incorporates a second carrier reservoir [15], but we shall not go into that complexity here.

We also have implicitly assumed that the carrier and photon densities are uniform across the active region in (7.1a) and (7.1b). In reality, the photon density varies spatially as the square of the optical mode field due to the waveguiding of the cavity, which causes the stimulated emission rate to vary accordingly. This spatial non-uniformity of the stimulated emission rate results in an overdamping of the relaxation resonance frequency, which reduces the bandwidth [19]. In addition, carriers are depleted faster where the optical intensity is higher, a phenomenon referred to *spatial hole burning*, and the carrier gradient drives diffusion [20]. It has been shown that the lateral carrier diffusion does not significantly reduce the bandwidth but increases the damping [21].

In (7.2), the nonlinearity of gain was included through the gain compression factor ε . This saturation of gain at high photon density is attributed to the *spectral*

hole burning and carrier heating effects [22]. It is important to minimize the gain nonlinearity so that damping can be reduced.

Many parameters in the rate equations are actually temperature dependent. Excessively high junction temperature degrades the differential gain, reduces the injection efficiency, increases the threshold current, affects the transverse modes, and red-shifts the cavity mode and gain peak. All these lead to a reduction of the bandwidth. Therefore, thermal management is a main issue for high-speed VCSELs.

Many of the limitations on modulation bandwidth are more acute in the longer wavelength VCSELs, especially the thermal effects due to the relative importance of Auger recombination. Thermal management is even more important, but quaternary materials tend to have very poor thermal conductivities, so additional ‘engineering fixes’ are required. Gain materials at longer wavelengths also usually have lower inherent differential gain, and the cavity volume tends to be larger because of lower inherent index contrast for lattice-matched alloys, which either directly results in a longer mirror, or requires an intracavity contact.

7.2.2 Extrinsic Parasitic Response

When dealing with high-frequency devices, parasitics are always a concern. Parasitics divert the modulated current i_d from entering the intrinsic laser due to i_p and i_c . In most cases, it is desirable to minimize the parasitics so that the intrinsic bandwidth can be achieved.

The parasitics vary depending on the device structure. Here a typical oxide-confined VCSEL, whose cross-sectional schematic and parasitic elements are shown in Fig. 7.3, is used as an example. The pad capacitance C_p represents the capacitance between the signal and ground from the probe tips/driver to the metal contacts. The value of C_p varies from tens to hundreds of femto-farads, depending on the pad layout and the materials between the pads. The pad resistance R_p accounts for the pad loss. Since it is usually relatively small, in the ohm range, compared with the impedance of C_p at the frequency of interest, it is sometimes omitted in the small-signal model.

The mirror resistance R_{mirr} includes the resistances from both DBRs. It includes the net differential impedances of the mirror heterobarriers at the bias point. R_{sheet} represents the sheet resistance in the n -contact layer, and R_{cont} is the contact resistance for both contacts. All these resistances, usually dominated by R_{mirr} , can be grouped together into $R_m = R_{\text{mirr}} + R_{\text{sheet}} + R_{\text{cont}}$ in the small-signal model. The mesa capacitance C_{mesa} is the oxide capacitance in series with the capacitance associated with the intrinsic region below the aperture. C_{mesa} depends on the diameters of the mesa and aperture and the thicknesses of the oxide and intrinsic semiconductor layer.

The capacitance C_j represents the diode junction capacitance in the apertured area where current flows. Under normal forward bias condition, C_j is usually dominated by the diffusion capacitance, which models the modulation of the minority carriers stored in the intrinsic SCH [23]. It has been shown that the diffusion capacitance not only depends on the carrier lifetime but also depends on the design of the SCH [24].

Fig. 7.3 Cross-sectional schematic of an oxide-confined VCSEL superimposed with its parasitics

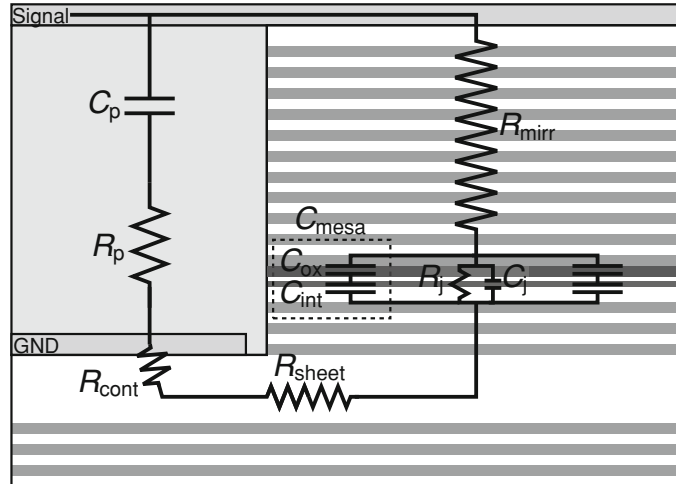
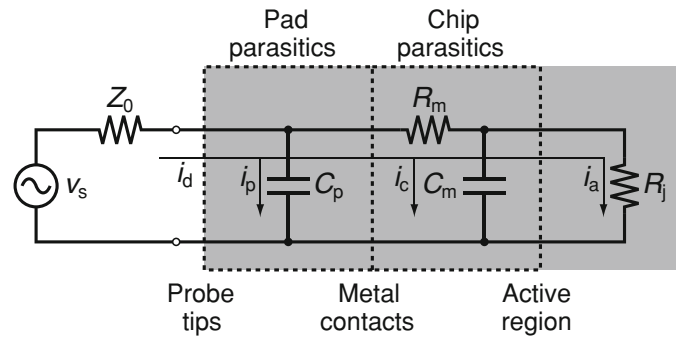


Fig. 7.4 Small-signal model with the driving source. The grayed area represents the VCSEL



For simplicity, C_{mesa} and C_j are grouped together into $C_m = C_{\text{mesa}} + C_j$. Lastly, the intrinsic laser is represented by the junction resistance R_j .

Figure 7.4 plots the small-signal model of VCSEL and the RF driving source. The VCSEL is represented by four elements, including C_p , R_m , C_m , and R_j . The RF driving source consists of a voltage source v_s and a characteristic impedance of Z_0 . Here we have assumed that the device is driven by 50- Ω -terminated instruments, and Z_0 is included to account for the RF power reflection due to impedance mismatch.

The effects of the parasitics can be described by a transfer function, $H_{\text{ext}}(\omega)$ [25]:

$$H_{\text{ext}}(\omega) \equiv \frac{\text{current flowing into the intrinsic diode}}{\text{voltage from the voltage source}} = \frac{i_a(\omega)}{v_s}.$$

The frequency at which $|H_{\text{ext}}(\omega)|^2 / |H_{\text{ext}}(0)|^2 = 1/2$ is defined as the parasitic 3-dB frequency ω_{rc} . This transfer function can be approximated by a single-pole low-pass filter function:

$$H_{\text{ext}}(\omega) = \frac{A_e}{1 + j\omega/\omega_0} \quad (7.10)$$

where A_e is a proportional constant and ω_0 is the parasitic roll-off frequency, which may be different from ω_{rc} .

The overall electrical modulation frequency response $H(\omega)$ is given as:

$$H(\omega) \equiv \left| \frac{p(\omega)}{v_s} \right|^2 = \left| \frac{i_a(\omega)}{v_s} \cdot \frac{p(\omega)}{i_a(\omega)} \right|^2 = |H_{\text{ext}}(\omega) \cdot H_{\text{int}}(\omega)|^2 \quad (7.11)$$

$$\propto \left(\frac{1}{1 + (\omega/\omega_0)^2} \frac{\omega_r^4}{(\omega_r^2 - \omega^2)^2 + \gamma^2 \omega^2} \right).$$

This gives the commonly used three-pole equation, which is squared when considering electrical-to-electrical links, for fitting the frequency response to extract ω_r , γ , and ω_0 .

7.3 Design of High-Speed VCSELs

In Sect. 7.2, we have discussed various factors that can affect the bandwidth of VCSELs based on small-signal analysis. Now we will review different designs to specifically address these limitations for better high-speed performance.

7.3.1 Active Region

The choice of active region is mainly determined by the wavelength and the substrate. However, some designs are better than the others in terms of high-speed performance. Most of them are related to the improvement in differential gain. Differential gain depends on the sensitivity of the quasi-Fermi levels (and thus gain) to small changes in carrier density [15]. To have higher differential gain, the density of states (DOS) needs to be more peaked near the band edges, and the quasi-Fermi levels, where the slopes of the Fermi functions are at their maximum, need to be aligned to the band edges.

In order to improve differential gain, a number of refinements to the active region have been explored. Originally, quantum dots (QDs) were proposed as a superior gain region because of their inherent delta-function-like DOS, which should have a huge differential gain [26], but all experimental QDs have a very broad DOS due to variable dot size and the associated inhomogeneous broadening. Adding strain in the QWs reduces the anisotropy between the DOS of electron and hole as well as pushes the hole quasi-Fermi level towards the valence band edge, which improves differential gain [15, 27]. In addition, strain advantageously reduces the transparency carrier density [15]. However, gain nonlinearity and damping increase with strain due to the increased valence-band curvature [22]. *P*-doping the active region increases the carrier-carrier scattering rate and thus decreases the intraband relaxation times, which reduces the gain nonlinearity induced by spectral hole burning [27]. *P*-doping also moves the quasi-Fermi levels down to a more symmetrical position and can increase

the differential gain [15]. However, the experimentally observed improvement in differential gain due to p -doping is more pronounced in unstrained systems than in strained systems [28]. In short, strained QWs perform better than unstrained QWs due to higher differential gain, and p -doped strained QWs perform better than undoped strained QWs due to reduced gain nonlinearity.

Within the strain limit, increasing the number of QWs is generally preferable for high-speed operation due to the differential gain enhancement [29]. However, the gain enhancement factor from the standing-wave effect, unique for VCSELs, decreases with increased number of QWs and must be considered [15]. Deeper wells are also favorable for high-speed and high-temperature operation because carriers have less chance to escape from the QWs, which reduces the carrier transport effects and carrier leakage.

7.3.2 Lateral Mode Confinement and Single Modeness

Since the relaxation resonance frequency increases with the square root of the photon density, it is desirable to increase the photon density for high-speed operation. This can be done by (1) increasing the current above threshold that contributes to the number of photon, i.e., $\eta_i(I - I_{th})$, (2) reducing the mode volume, and (3) maintaining single-mode operation to insure that the photon density must increase as the current increases. For given device dimensions and bias current, single-mode devices have higher photon density because photons do not spread among the mutually orthogonal modes. Maintaining single-mode operation is also necessary for some applications which use SMF or require better beam quality. However, some past applications have desired multimode VCSELs to match multimode fibers or waveguides. Unfortunately, these are not well suited for high data rate applications. Here we will mention some approaches to achieve single-mode operation, and more details can be found in Chap. 5 of this book.

For gain-guided VCSELs without any deliberate index guiding, the lateral mode confinement is mainly provided through thermal lensing effects, which can be unstable under dynamic operation due to time-dependent temperature variation [30]. Although gain-guided VCSELs have demonstrated 14.5 GHz modulation bandwidth [31], index guiding is more common nowadays for high-speed VCSELs, both to insure single mode operation, as well as reduce the mode volume.

The most common approach to implement lateral index guiding, at least for GaAs-based VCSELs, is to use a dielectric aperture. The discovery of wet thermal oxidation of high aluminum content semiconductors provides an easy way to form thermally stable aluminum oxide inside a VCSEL cavity. Oxide-confined VCSELs have shown superior performance in many aspects due to reduced internal losses, and simultaneously providing good electrical and optical confinement. Various aperture designs have been incorporated in high-speed VCSELs, including standard quarter-wavelength-thick blunt aperture [32], double apertures [33, 34], thin aperture (~ 30 nm) [35], and tapered oxide aperture [36, 37].

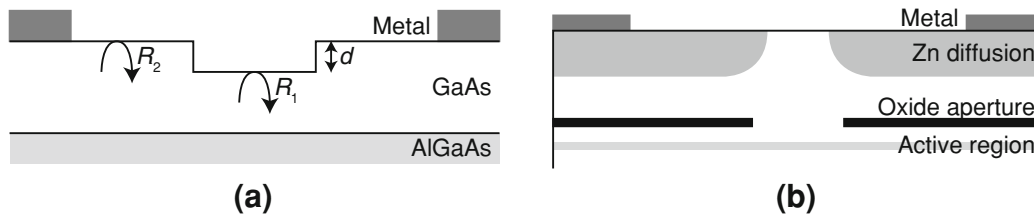


Fig. 7.5 Two approaches to achieve single-mode VCSELs. **a** Illustration of the inverted surface relief structure on the top surface of a VCSEL. Reflectivity R_2 is lower due to an extra thickness of d , and the center is etched down to restore the high reflectivity R_1 for the fundamental mode. **b** Illustration of Zn diffusion from the top surface to create a higher-order mode absorber

There are several advantages of using a tapered oxide aperture. First, it can achieve lower optical scattering losses if designed properly [38, 39]. This is because a tapered oxide aperture, if placed at the standing-wave node, can produce a nearly ideal parabolic lens that eliminates the optical scattering loss. Second, the nonlinear damping effects can be reduced for higher bandwidth by confining the current smaller than the optical mode [19, 40]. Third, the parasitic capacitance from the oxide can be lower due to the increased oxide thickness at high radii where the area is large. Fourth, the eigenmodes are Hermite–Gaussian modes, which diffract less and have no sidelobes, so that external coupling and focusing can be done more ideally. On the other hand, a tapered oxide aperture also reduces the losses that differentiate the fundamental and higher-order modes, and the devices tend to be multi-mode unless some mode-dependent loss is added. Fortunately, the higher-order modes have significantly larger diameters, so this can also be done more easily than in other cases.

Approaches have been proposed to achieve single-mode operation for larger-diameter devices, which can also be implemented for tapered-oxide-apertured devices. Many of them involve creating some mode-dependent losses, usually in the perimeter of the top mirror, to favor the more centered fundamental mode. For example, a surface relief structure, as illustrated in Fig. 7.5a, increases the mirror loss [41], or Zn diffusion, shown in Fig. 7.5b, increases the internal loss for the higher-order modes [42]. High-speed, single-mode VCSELs have been demonstrated with these two approaches [13, 43].

Aperturing using an etched tunnel junction and then performing a regrowth over it to form a BTJ, which is common for InP-based LW-VCSELs, can also provide mode confinement as well as current confinement. This is due to the larger optical cavity length, where the unetched tunnel junction material remains in the center of the cavity. Single-mode operation can be achieved with BTJ for diameters up to 7 and 9 μm at 1.3- and 1.55- μm wavelengths, respectively [44].

7.3.3 Chip Parasitics

Parasitics are one of the main limiting factors for high-speed VCSELs. As can be seen in Table 7.1, most devices have relatively close $f_{3\text{dB}}$ and f_{rc} , indicating they are

Table 7.1 Parasitic elements for different high-speed VCSELs from the literature

Authors Reference	Lear [45]	AL-Omari [32]	Chang [46]	Lin [47]	Suzaki [3]	Yashik [4]
λ (μm)	0.85	0.85	0.98	0.98	1.1	1.1
Size (μm^2)	4×4	$3.5^2\pi$	$1.5^2\pi$	$3^2\pi$	$3.5^2\pi$	$2.5^2\pi$
I_0 (mA)	N/A	4.5	4.5	6.0	7.0	4.0
C_p (fF)	41.7	62	29	22	56	33
R_p (Ω)	15.9	17	0	0	0	0
R_m (Ω)	28.3	45	103	34.1	63.3	38
C_m (fF)	44.3	151	87.9	152	133	130
R_j (Ω)	288.7	64.4	146.5	92.0	71.6	134
f_{rc} (GHz)	36.4	21.8	22.8	22.5	23.6	21.0
f_{3dB} (GHz)	21.5	17	>20	17	20	24 ^a

^a Obtained from 5- μm -diameter devices

partially parasitic-limited. In the following, we will discuss approaches to reduce the parasitics.

Chip Parasitic Resistance

Due to the alternating layers in the DBR mirrors, VCSELs inherently have much higher series resistance, ranging from tens to hundreds of ohms, compared with edge emitters. This excess resistance can limit the modulation bandwidth due to RC limitations and heating. Various bandgap-engineering schemes at the DBR interfaces, mostly for the p -mirror, have been proposed to simultaneously achieve low resistance and loss [48, 49]. Since n -type materials are less lossy and resistive, p -down configuration has also been pursued for top-emitting VCSELs [32, 50].

To eliminate the resistances and losses from the doped semiconductor DBR mirrors, one or both intracavity contacts with (partially) undoped semiconductor mirror/abrupt interfaces, mostly for oxide-confined VCSELs [35, 36], or dielectric DBR mirror, mostly for BTJ VCSELs with a regrown n -spacer for lower loss [6, 51], have been used. For dielectric DBR, several periods usually provide sufficient reflectivity due to large index contrast, which helps to compress the optical modes in the longitudinal direction. However, the uniformity of current injection, lateral sheet resistance, and optical loss from the highly-doped contact layers near the active region can be issues for intracavity contacts and must be considered in the device design [39].

Chip Parasitic Capacitance

Another source of the parasitics is the shunt mesa capacitance surrounding the active region. Figure 7.6 illustrates the sources of the mesa capacitance for oxide-confined and BTJ VCSELs. For oxide-confined VCSELs, the shunt mesa capacitance is the oxide capacitance C_{ox} in series with the capacitance from the intrinsic active region below the oxide aperture C_{int} . For BTJ VCSELs, the oxide capacitance is replaced by the depletion capacitance C_{dep} from the reverse-biased p - n junction.

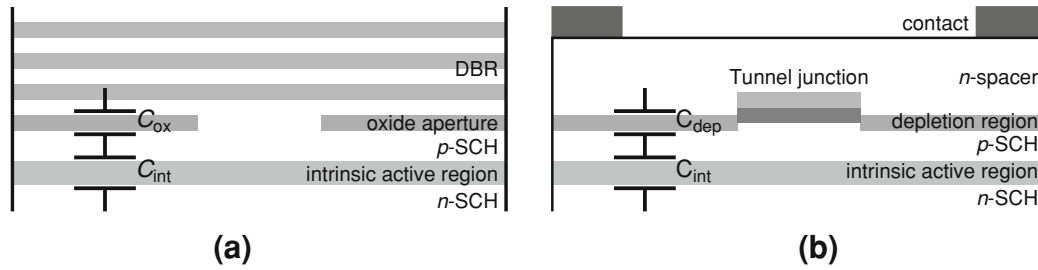


Fig. 7.6 Schematics illustrating parasitic mesa capacitance for **a** oxide-confined VCSEL and **b** BTJ VCSEL

Since all these layers are relatively thin, the mesa capacitance can be quite large. Combined with high series resistance, parasitics can greatly reduce the achievable bandwidth. To reduce the mesa capacitance, it is necessary to create additional (thick) nonconducting layers inside the mesa above or below these high-capacitance current blocking junctions, and this is commonly done using implantation [6, 37, 50]. For oxide-confined VCSELs with semiconductor mirrors, the nonconducting layers can also be formed by oxidizing additional one (double aperture) [34] or several higher aluminum layers (deep oxidation layers) [36]. This can be performed simultaneously with the oxide aperture to eliminate one fabrication step. Since the dielectric constant for the aluminum oxide is much smaller than that of the semiconductor, the total thickness of the nonconducting layers can be smaller. This reduces the funneled distance, usually at the lowest-doped layers, that current has to conduct, which is beneficial for resistance.

For edge emitters, which typically work at relatively high currents, the junction resistance is practically negligible. Therefore, the diffusion capacitance, which is in parallel with the junction resistance, can be neglected. However, this is not the case for VCSELs due to their small currents. The junction resistance and diffusion capacitance have to be considered. A graded SCH layer can potentially reduce the diffusion capacitance [23] and has been employed in high-speed VCSELs [33].

7.3.4 Pad Parasitics

Since the pad parasitics are in parallel with the current path of the intrinsic laser, it is important for these to have a high impedance, i.e., smaller pad capacitance and higher pad shunt resistance, to prevent current flowing through them.

Reasonable size pads are necessary to drive VCSELs, especially for bonding. However, the associated pad parasitics can greatly reduce the modulation bandwidth if precautions are not taken. For example, the pad capacitance for a $100 \times 100 \mu\text{m}^2$ pad on a 200-nm-thick nitride is $\sim 3.3 \text{ pF}$, which is very large (see Table 7.1). To overcome this limitation, some thick low-dielectric-constant resin can be used underneath the signal pad. The two most common choices are polyimide [32, 50] and

benzocyclobutene (BCB) [34, 36], although silicon dioxide has also been used [37]. Just as a comparison, the same $100 \times 100 \mu\text{m}^2$ pad on a $5\text{-}\mu\text{m}$ -thick BCB gives a pad capacitance of ~ 47 fF, a 70 times reduction.

VCSELs grown on semi-insulating substrates can also have lower pad parasitics through co-planar transmission lines with lower microwave loss due to the removal of the resistive substrate. Similarly, removing the part of the contact layer that is underneath the signal pad also reduces the pad capacitance by enabling a higher impedance co-planar interconnecting line [5].

7.3.5 Thermal Management

Thermal management is always an important issue for high-speed devices. For VCSELs, most of the heat generated in the diode junction and DBRs is dissipated through the substrate. To more efficiently remove the heat, we can either integrate the devices on a substrate with higher thermal conductivity [52], e.g., copper which has ~ 9 times of the thermal conductivity of GaAs, or provide additional heat sinking from the top surface and sidewalls using gold [53] or copper plating [54]. Compared with gold, copper is inexpensive and has high thermal conductivity, which makes it really attractive.

Figure 7.7 shows SEMs and schematic cross-section of copper-plated VCSELs [54]. The $4\text{-}\mu\text{m}$ -overlapped devices show considerably better thermal properties compared with the non-overlapped devices. This is because heat first flows laterally to the sidewalls and can eventually dissipate in the substrate through the copper, bypassing the more thermally-resistive bottom DBR. However, this relies on good thermal contact between the overlapped copper and substrate and would result a high parasitic capacitance if a thin dielectric is used. This trade-off can be addressed using flip-chip bonding so that heat can be dissipated through the bonded interface instead of the substrate, which relieves the restriction of the thickness of the dielectric layer [45].

In addition to improve heat dissipation, reducing the amount of heat generated is another way to prevent thermal degradation. Ideally, the relaxation resonance frequency should increase as the square root of the current density $J_0 = I_0/\text{Area}$. For a given current density, the temperature rise should be *lower* for smaller devices because power dissipation is roughly proportional to the area and thermal impedance is inversely proportional to the diameter [15]. However, smaller devices typically suffer from higher losses. If the size-dependent losses can be minimized, scaling the devices down should yield better performance. Size-dependent losses have been reduced by incorporating tapered apertures and this has allowed much smaller devices to be created with high bandwidths [55]. Perhaps more importantly, these smaller devices have lower currents for a given bandwidth, and a data-rate/power dissipation of 35 Gbps/10 mW has been reported [5].

Once the operating temperature is determined by the ambient temperature, heat generation and dissipation, the devices have to be optimized at that temperature.

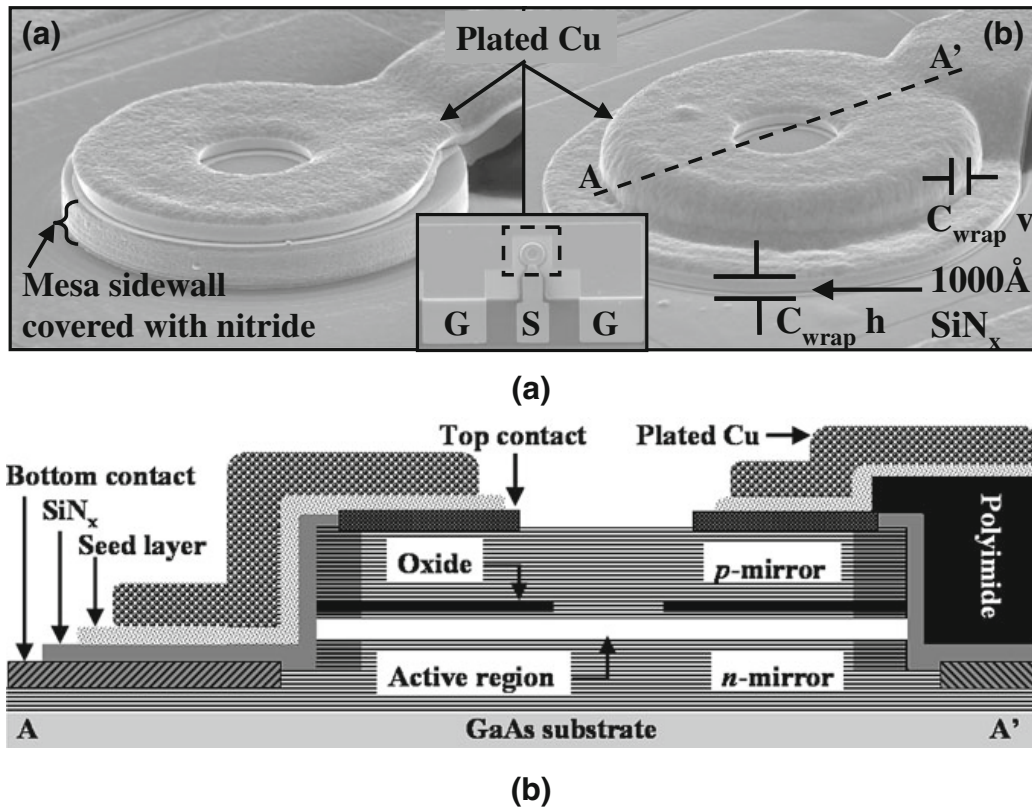


Fig. 7.7 **a** SEMs of copper-plated VCSELs. *Left*: heat sink from the top surface. *Right*: heat sink from both the top surface and sidewalls with 4- μm overlap with the substrate. **b** Cross-sectional schematic of the device [54] (© 2006 IEEE)

As the temperature increases, both the cavity mode and gain peak red-shift, but at different rates. Take 980-nm VCSELs with InGaAs QWs as an example, cavity-mode and gain peak shift at approximate 0.07 and 0.3 nm/°C, respectively [39]. By deliberately detuning the cavity-gain offset at room temperature, better high-temperature performance has been realized [56].

7.4 Performance of High-Speed VCSELs

This section reviews some of the high-speed VCSEL results at several different wavelengths. High-speed VCSELs operated at the datacom wavelengths, ranging from 0.83 to 1.1 μm , are exclusively GaAs-based and mainly for optical interconnects and short-distance optical links. Typical wavelengths include 850 nm, 980 nm, and 1.1 μm . LW-VCSELs operated at 1.3 and 1.55 μm are attractive as alternative light sources for optical links transmitting longer distances over SMF due to the low loss and dispersion of fibers at these wavelengths; both GaAs- and InP-based devices exist at the longer wavelengths.

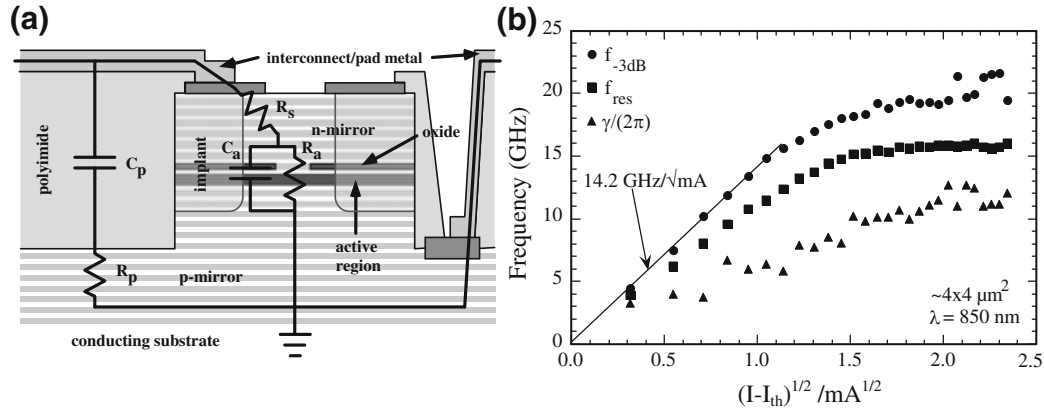


Fig. 7.8 **a** Device structure and **b** $f_{3\text{dB}}$, f_r , and $\gamma/(2\pi)$ vs. $(I - I_{\text{th}})^{1/2}$ for the 850-nm VCSELs with a bandwidth of 21.5 GHz [45] (© 1997 OSA)

7.4.1 850-nm VCSELs

VCSELs operating at 850-nm wavelength are probably the most mature VCSEL technology to date, because 850 nm has several fiber-based standards for short-haul datacom. Products using 850-nm VCSELs for 10 Gigabit Ethernet have been commercially available on the market for some time.

There are several active region choices for 850-nm emission including GaAs/AlGaAs [37], InGaAs/AlGaAs [34], InAlGaAs/AlGaAs [57], and InGaAsP/InGaP [58]. We will focus on the GaAs/AlGaAs and InGaAs/AlGaAs designs, which are more common nowadays.

GaAs/AlGaAs 850-nm VCSELs

The unstrained GaAs/AlGaAs multiple quantum wells (MQW) is the most common active region choice for 850-nm VCSELs, and many high-speed records were achieved with it. For example, the first VCSEL to demonstrate a bandwidth in excess of 20 GHz was achieved with this active region in 1997, and this is still the highest reported bandwidth for 850-nm VCSELs [50]. Figure 7.8 shows a cross-sectional schematic and $f_{3\text{dB}}$, f_r , and $\gamma/(2\pi)$ vs. $(I - I_{\text{th}})^{1/2}$ for the $4 \times 4 \mu\text{m}^2$ devices that achieved a 21.5-GHz bandwidth.

One of the reasons that these devices achieved a high bandwidth was their low-parasitic structure (see the first column of Table 7.1). The pad capacitance is only 42 fF using 5- μm -thick polyimide underneath the pad. The pad resistance is due to the dielectric loss of the polyimide. The series resistance is reduced to 28.3 Ω using n -up configuration. Despite the junction resistance is 289 Ω , high-dose proton implantation brings C_m down to 44.3 fF so that current still flows through the intrinsic laser. Since $f_{rc} = 36.4$ GHz, the bandwidth is not parasitic-limited. Because the relaxation resonance frequency and 3-dB frequency both saturate at about the same current, the bandwidth is limited by the intrinsic laser response. The damping-limited

bandwidth, extracted from K -factor, is 58 GHz. Therefore, the devices are limited by thermal effects.

The highest data rate reported for 850-nm VCSELs with GaAs QWs is 30 Gb/s at a bias current of 8 mA using 6- μ m-diameter devices [37]. The maximum bandwidth is 19 GHz at that bias.

InGaAs/AlGaAs 850-nm VCSELs

One of the issues with unstrained GaAs/AlGaAs QWs is that it has lower differential gain compared with strained QWs. It has been shown that adding some indium, typically 10% or less, in the wells can double the achievable gain and differential gain [59]. In addition, the presence of indium has been shown to suppress the propagation of dark-line defects, which prevents sudden failure of the devices [60]. Data rates of 32 Gb/s [61] and 39 Gb/s [62] have been demonstrated using 850-nm VCSELs with InGaAs QWs.

The 9- μ m devices which achieved 32-Gb/s operation at 25°C have a threshold current of 0.6 mA, fairly low for this size, and a slope efficiency of 0.8 W/A, which corresponds to a differential quantum efficiency (DQE) of \sim 55%. The parasitics are reduced using BCB, an undoped substrate, double oxide apertures, and bandgap-engineered DBRs. The series resistance is approximately 90 Ω . They also reported 25-Gb/s operation up to 85°C.

The devices that achieved a 39-Gb/s data rate have a diameter of \sim 6 μ m, confined by an oxide aperture. BCB is used for reducing the pad parasitics, and a relatively large lower mesa for the bottom DBR is used for better heat dissipation, lower resistance, and easier manufacturing. The bias current for large-signal modulation is 9 mA, corresponding to a fairly low current density of \sim 10 kA/cm². Eye diagram at 40 Gb/s is also shown. The signal-to-noise ratio reduces from above 6.3 to 3.6, preventing error-free operation at 40 Gb/s.

7.4.2 980-nm VCSELs

Another common wavelength for high-speed VCSELs is 980 nm, which typically employs strained InGaAs/GaAs QWs. This aluminum-free active region offers high differential gain, low transparent carrier density, and superior reliability. Due to the transparency of GaAs substrates at 980 nm, bottom-emitting structure is commonly used.

InGaAs/GaAs 980-nm VCSELs

The highest MCEF for any QW-based VCSELs to date is 16.8 GHz/mA^{1/2} using InGaAs/GaAs VCSELs at 970 nm [33]. One of the keys to achieve such high MCEF is the small mode volume. The dimensions of the devices are 3 \times 3 μ m², confined with double oxide apertures. Pad capacitance is estimated to be 40 fF for a 75 \times 120 μ m² bond pad. The threshold current is 0.37 mA and the DQE is 45%. The bandwidth

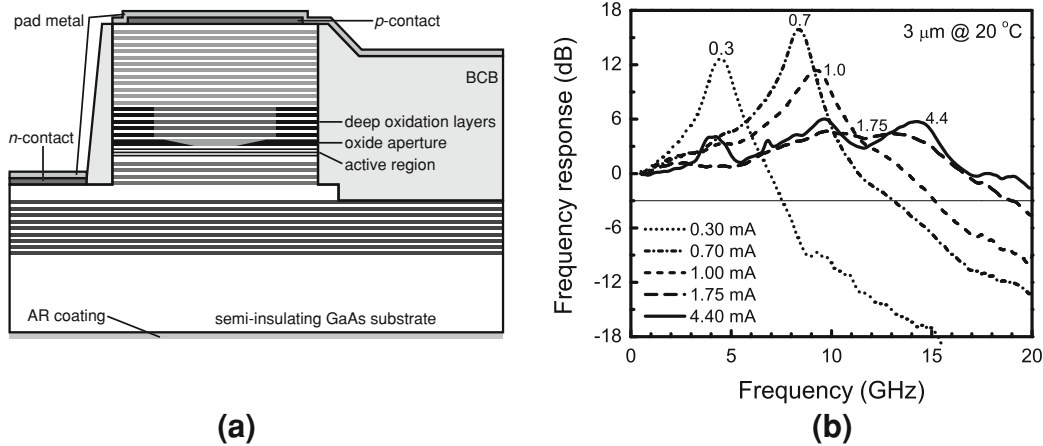


Fig. 7.9 **a** Structure and **b** frequency responses for 3- μm -diameter devices achieving 35-Gb/s operation

reaches 11.2 GHz at a bias current of only 1 mA, and the maximum bandwidth is 16.3 GHz at 4.5 mA.

The highest data rate reported for 980-nm VCSELs is 35 Gb/s using the structure shown in Fig. 7.9a [5]. Instead of the conventional quarter-wavelength-thick blunt oxide aperture, a half-wavelength-thick tapered oxide aperture is used. The taper length is carefully chosen to provide sufficient mode confinement while still maintaining low optical scattering losses [55]. This enables the smaller 3- μm devices, which typically suffer from high optical losses, to be used. The low pad capacitance of 29 fF is realized by using BCB, selectively etching off the n -GaAs contact layer underneath the signal pad, and shrinking the pad dimensions. Deep oxidation layers as well as the thick oxide aperture effectively reduce C_m down to ~ 88 fF. The devices have a threshold current of only 0.14 mA and a slope efficiency of 0.67 W/A (DQE = 0.54). The series resistance is approximately 250 Ω .

Figure 7.9b plots the frequency responses of the devices at 20°C. Due to the small size, a bandwidth of 15 GHz is achieved at a bias current of only 1 mA, corresponding to a power dissipation of 1.3 mW. The temperature rise is estimated to be 4.3°C. It is evident that small devices are more efficient and can achieve the bandwidth with lower currents and temperature rise, even with a somewhat higher series resistance than desired in this case. A bandwidth exceeding 20 GHz is also demonstrated for currents larger than 2 mA. The bandwidth is limited by multimoding above 2 mA; simulations illustrate that the maximum bandwidth would be ~ 25 GHz if single-mode operation were maintained. The MCEF at low biases is 16.7 GHz/mA^{1/2}. 35-Gb/s operation was achieved with a bias current of only 4.4 mA. This corresponds to a very high data-rate/power-dissipation ratio of 3.5 (Gb/s)/mW.

InAs QD 980-nm VCSELs

Another active region choice for 980-nm VCSELs is submonolayer deposited quantum dots, which provides higher differential gain and better temperature

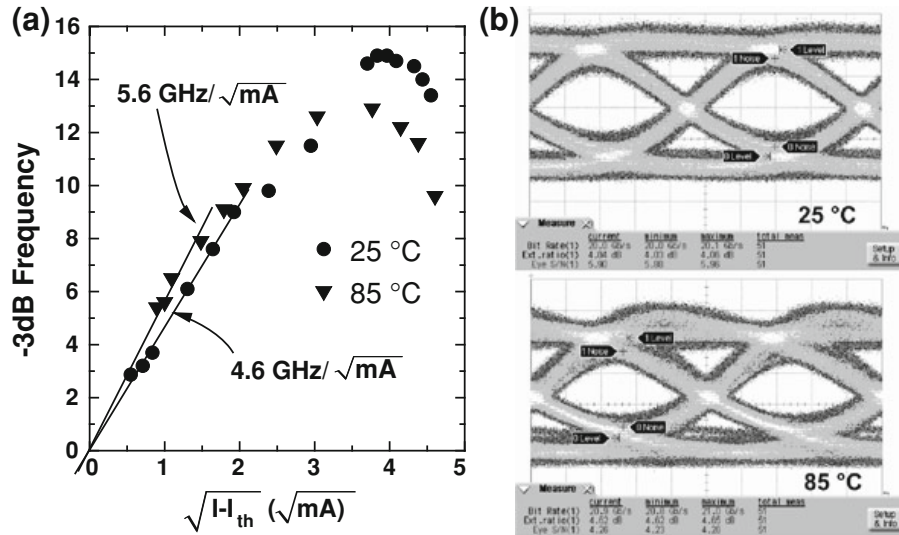


Fig. 7.10 a $f_{3\text{dB}}$ vs. $(I - I_{\text{th}})^{1/2}$ and b 20-Gb/s eye diagrams for 6- μm QD VCSELs at 25°C and 85°C [63] (© 2006 SPIE)

insensitivity [63]. Their 1- μm single-mode devices show the highest MCEF of 19 GHz/ $\text{mA}^{1/2}$ for any VCSELs to date. For their 6- μm multimode devices, the threshold currents at 25°C and 85°C are 0.29 and 0.16 mA, respectively, due to better cavity–gain alignment at elevated temperatures.

Figure 7.10 shows $f_{3\text{dB}}$ vs. $(I - I_{\text{th}})^{1/2}$ and eye diagrams for 6- μm devices at 25°C and 85°C. The MCEF drops from 5.6 to 4.6 GHz/ $\text{mA}^{1/2}$ for the temperature increased from 25°C to 85°C. The maximum bandwidth at 25°C and 85°C are 15 and 13 GHz, respectively. These bandwidths still can support 20-Gb/s operation as shown in the eye diagrams. The eye is slightly degraded at 85°C. Recently, they demonstrated 20-Gb/s operation up to 120°C using 2- μm single-mode devices [64].

7.4.3 1.1- μm VCSELs

High-speed VCSELs operating in the 1.1- μm -wavelength range have resulted from engineering the MQW InGaAs/GaAs active region to have the maximum allowable strain as well as p -type modulation doping [65]. The active region consists of three thin highly-strained In_{0.3}Ga_{0.7}As/GaAs (5/10 nm) QWs. The GaAs barriers are modulation doped p -type at $2 \times 10^{18} \text{ cm}^{-3}$ to reduce gain nonlinearity. Two types of device structures have been reported: oxide-confined VCSELs and BTJ VCSELs.

Figure 7.11a shows their oxide-confined VCSEL structure. The 6.9- μm -diameter devices have a threshold current of 0.4 mA and a series resistance of 135 Ω . Because the mesa is relatively large at 33 μm in diameter, proton implantation is used to reduce the mesa capacitance. The pad capacitance is lowered using polyimide. The

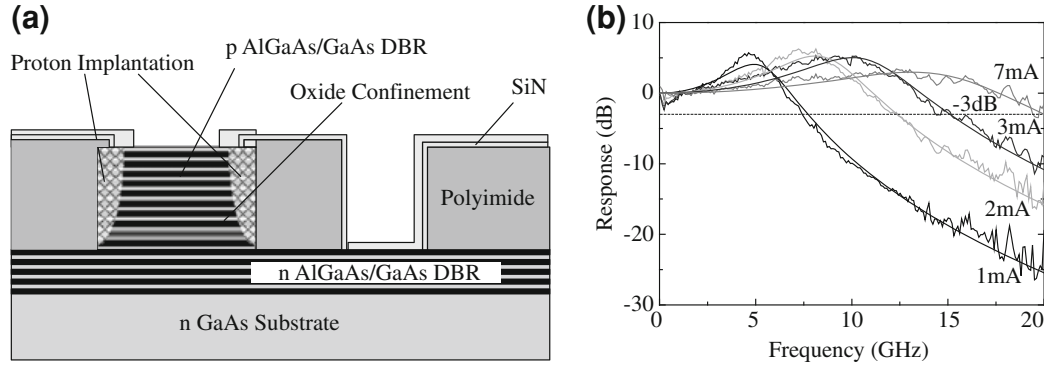


Fig. 7.11 **a** Cross-sectional schematic and **b** frequency responses of oxide-confined 6.9- μm -diameter 1.1- μm VCSELs [66] (© 2007 IEEE)

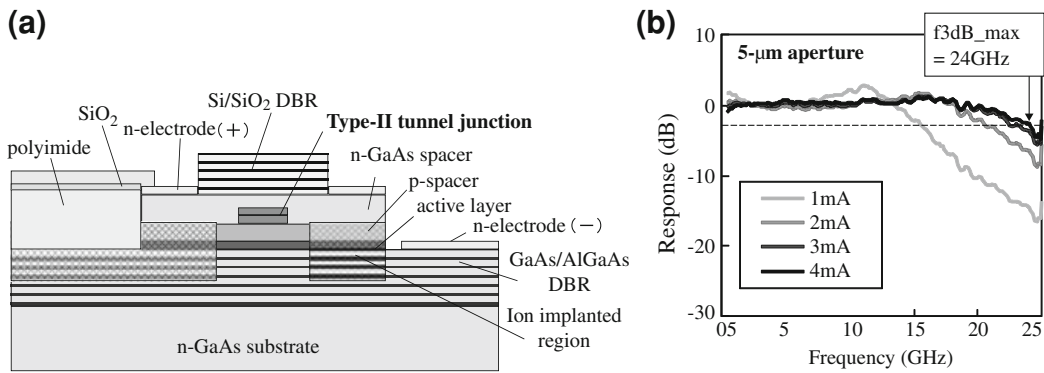


Fig. 7.12 **a** Structure and **b** frequency responses for 1.1- μm , BTJ VCSELs [67] (© 2008 OSA)

devices achieve a maximum bandwidth of 20 GHz at a bias of 7 mA, as shown in Fig. 7.11. Transmission at 30 Gb/s back-to-back and over 100-m multi-mode fiber have been done, and the power penalty is ~ 2 dB.

The main limiting factor in their oxide-confined devices is self-heating effect, which causes the relaxation resonance frequency to saturate at high biases. To address this limitation, a low-resistance type-II BTJ is used so that the more resistive p -layer can be replaced with a less resistive n -spacer. The devices use top-emitting, double-intracavity structure shown in Fig. 7.12a.

The electrical and optical confinement is achieved by selectively etching the tunnel junction and regrowing the n -GaAs spacer layer. Oxygen ions are implanted around the tunnel junction to reduce the mesa capacitance. The pad capacitance is similarly reduced using polyimide. Dielectric Si/SiO₂ DBR is used for the top mirror.

Figure 7.12b plots the frequency responses for 5- μm -diameter devices. The maximum 3-dB frequency is 24 GHz at a bias current of 4 mA, which is the highest bandwidth reported for directly current-modulated VCSELs to date. A data rate of 40 Gb/s, which is also the highest data rate for VCSELs to date, is achieved using 6- μm devices at a bias current of 5 mA.

All these results were achieved at room temperature. To improve the high-temperature performance, they have also developed a new active region with strain-compensated $\text{In}_{0.3}\text{Ga}_{0.7}\text{As}/\text{GaAs}_{0.8}\text{P}_{0.2}$ QWs [68]. By increasing the conduction-band offset, electrons are better confined at the elevated temperature. A data rate of 25 Gb/s is achieved using oxide-confined structure.

7.4.4 Long-Wavelength VCSELs

Several technologies exist for LW-VCSELs, and they will be covered in more detail in Chaps. 11 and 12 of this book. The main application of high-speed LW-VCSELs is to use for optical networks, which currently require transmission up to 10 Gb/s over SMF. Here we summarize some current high-speed results for LW-VCSELs.

GaAs-Based Long-Wavelength VCSELs

GaAs-based LW-VCSELs are attractive due to the well-established technologies of short-wavelength VCSELs such as oxide apertures and bandgap-engineered, high-index-contrast DBRs. The main challenge is the choice of the gain media that can be pseudomorphically grown on GaAs substrates to reach longer emission wavelengths. Currently, GaAs-based LW-VCSELs are mainly operated below 1.3- μm wavelength, and there are three active region candidates [69]: highly strained InGaAs QWs, GaInNAs QWs, and InAs QDs.

The structure of GaAs-based LW-VCSELs is usually pretty similar to short-wavelength VCSELs except with a different gain media. Transmission at 10 Gb/s over 9-km SMF from 25°C to 85°C has been reported using highly strained InGaAs QWs emitting at 1.28 μm [13]. The indium content of the QWs is increased to 42% to push the gain peak to 1220 nm, and the cavity mode is detuned at 1275 nm, giving a large gain-cavity offset for better high-temperature stability [70]. An inverted surface relief is patterned on the top mirror for single-mode operation. However, the threshold current seems fairly high and reduces at higher temperature due to better cavity–gain alignment. The bandwidth is mostly limited by parasitics.

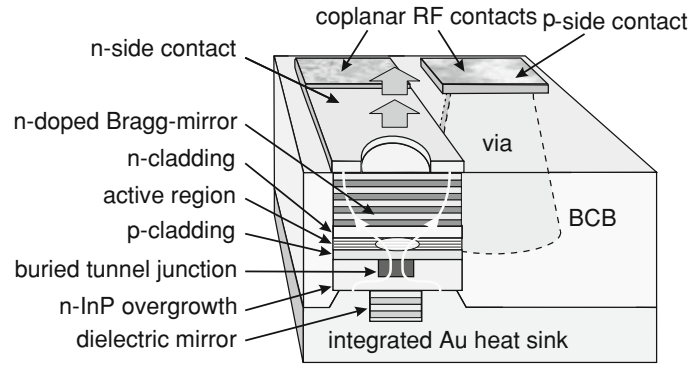
LW-VCSELs based on a GaInNAs active region emitting at 1.28 μm have also demonstrated 10-Gb/s transmission over 20-km SMF [11]. These devices show good reliability and have been placed into production [11, 71].

InP-Based Long-Wavelength VCSELs

For InP-based LW-VCSELs, the mature high-reliability InAlGaAs or InGaAsP active region can be used. The main issues are (a) the lack of DBR materials which provide high reflectivity and thermal conductivity, (b) the more extreme sensitivity to elevated temperatures, and (c) the realization of lateral mode confinement.

The first of these issues was addressed with an all-epitaxial approach using lattice-matched AlGaAsSb DBRs, which offer relatively high reflectivity, and an air-gap aperture formed by selectively etching tunnel junction. These have been explored

Fig. 7.13 Structure of InP-based BTJ LW-VCSEL [73] (© 2008 IEEE)



and demonstrated reasonable DC characteristics as well as 3.125-Gb/s operation up to 60°C [72]. The poor electrical and thermal conductivity of the quaternary DBRs was addressed by using *n*-type intracavity InP contact layers, but these also added to the cavity length, which increased the cavity volume, and thus, reduced the frequency response.

Another approach is to use BTJ, pioneered by Amann et al. at Walter Schottky Institute. Some of the best high-speed performance for LW-VCSELs to date are demonstrated based on this platform. Figure 7.13 shows the structure of their devices. The lateral current and mode confinement is provided by the BTJ, which also enables the regrown InP spacing layer to be *n*-type for lower loss and resistance. The back mirror consists of several periods of CaF₂/ZnS dielectric DBR and a gold termination layer, which also works as a heat sink. The device is passivated with BCB for high-speed operation.

Based on this structure, bandwidth exceeding 10 GHz has been demonstrated for both 1.3- and 1.55- μm wavelengths at room temperature [12, 51] and is limited by parasitics and thermal effects. Transmission at 10 Gb/s for 22 km and 12.5 Gb/s for 3 km have also been reported at 1.3- and 1.55- μm wavelengths, respectively.

Corning also reported LW-VCSELs with 10-Gb/s transmission for both 1.3- and 1.55- μm wavelengths up to 85°C [10]. Their devices, shown in Fig. 7.14, are based on similar BTJ technology with a dielectric top mirror. However, they use double-intracavity contacts with top emission, which greatly simplifies the device structure and can be mass manufactured more easily.

Wafer-Fused Long-Wavelength VCSELs

Both InP-based active region and GaAs-based DBRs are preferable for LW-VCSELs. Therefore, wafer fusion, pioneered by Bowers et al. at University of California, Santa Barbara, has been used to combine these two material systems. Transmission at 10 Gb/s over 10-km standard SMF has been reported [44]. The structure consists of undoped top and bottom AlGaAs/GaAs DBRs, wafer fused with InAlGaAs/InP cavity grown on an InP substrate. A tunnel junction is used for lateral confinement.

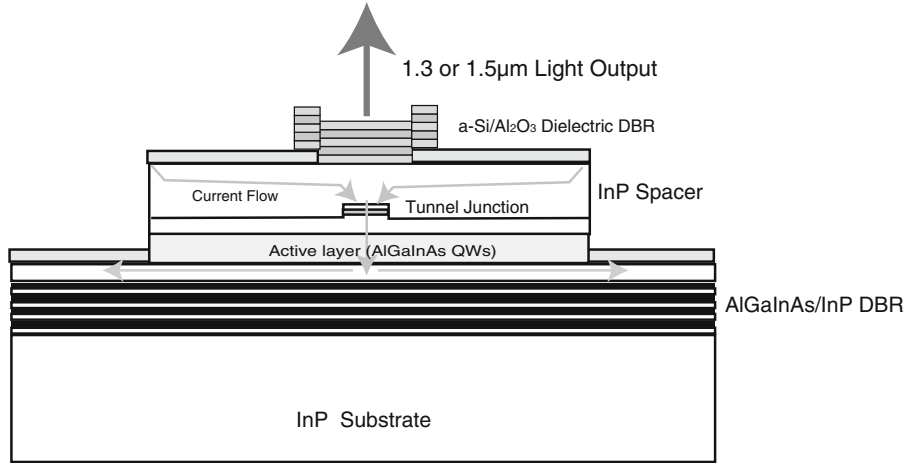


Fig. 7.14 Cross-sectional schematic of BTJ LW-VCSELs with double-intracavity contacts [74] (© 2005 IEEE)

7.5 Loss-Modulated High-Speed VCSELs

Due to inherent damping limitations, it would be very challenging for directly current-modulated VCSELs to reach bandwidth beyond 40 GHz, even after the parasitic and thermal limitations have been removed. The highest modulation bandwidth to date is still limited below 25 GHz [6]. Alternative approaches have to be pursued to extend the bandwidth, e.g., optical injection locking and loss modulation. Optically injection locked VCSELs have demonstrated an impressive modulation bandwidth of 66 GHz based on a cascaded configuration [75]. However, a separated master laser is required. Therefore, we only consider coupled-cavity loss-modulated VCSELs here.

7.5.1 Principle of Operation

All the devices that have been discussed so far are based on current modulation, which is an indirect way to modulate the photon density. Alternatively, the photon density can be modulated by varying the cavity loss, which has been theoretically predicted to have higher modulation bandwidth [76].

In the rate equations discussed in Sect. 7.2, the losses are included through the photon lifetime $\tau_p^{-1} = v_g(\alpha_i + \alpha_m)$, where α_i and α_m are the internal loss and mirror loss, respectively. Here, we apply the small-signal analysis for loss modulation, similar to (7.3a), by assuming

$$\frac{1}{\tau_p} = v_g(\alpha_0 + \alpha_1 e^{j\omega t}) = \frac{1}{\tau_{p0}}(1 + m e^{j\omega t}) \quad (7.12)$$

where α_0 is the steady-state total loss, α_1 is the small-signal loss modulation amplitude, $\tau_{p0} = (v_g \alpha_0)^{-1}$ is the steady-state photon lifetime, and $m = \alpha_1 / \alpha_0$ is the loss

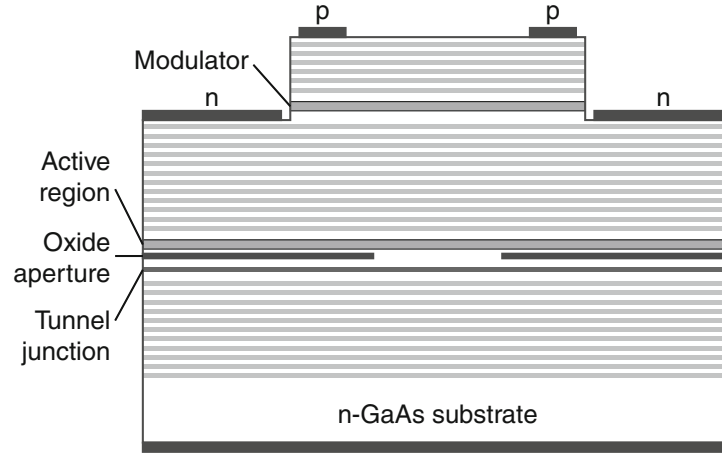


Fig. 7.15 Cross-sectional schematic of EAM-VCSEL [78]

modulation depth. Following the same procedure as we did for current modulation, the transfer function for loss-modulated intrinsic laser can be written as [77]

$$H_L(\omega) = \frac{m}{\tau_{p0}} \frac{\omega_r^2 \tau_p + j\omega}{(\omega_r^2 - \omega^2 + j\omega\gamma)}. \quad (7.13)$$

The main difference between loss modulation and current modulation is the decay rate after the resonance: $1/\omega$ (20 dB/decade) for loss modulation and $1/\omega^2$ (40 dB/decade) for current modulation. In addition, the resonance peak is also stronger for loss modulation, which can be an issue for data transmission.

Two mechanisms have been used to achieve loss modulation in coupled-cavity VCSELs. One is to modulate the internal loss α_i using an electroabsorption modulator, and the other is to modulate the mirror loss α_m using an electrooptical modulator.

7.5.2 VCSELs with an Electroabsorption Modulator

Figure 7.15 shows the cross-sectional schematic of VCSEL with an intracavity electroabsorption modulator (EAM-VCSEL). It is basically a p - n - p configuration with a tunnel junction below the active region to reverse the polarity of the bottom contact. Reverse-biased MQW, placed at the standing-wave peak for maximal efficiency, is used as the modulator. A 17-GHz modulation bandwidth with a distinct 20 dB resonance peak has been reported [78]. The roll-off slope is ~ 45 dB/decade with parasitics ($f_0 \sim 8$ GHz), showing a slower decay rate compared with current-modulated devices.

Recently, the same group demonstrated optically decoupled loss modulation in a duo-cavity VCSELs by carefully detuning the resonances of the cavities [79]. The photon density in the active region remains unchanged under loss modulation, similar

to the case of using an external modulator with a continuous-wave laser. Relatively flat frequency responses up to 20 GHz have been shown.

7.5.3 VCSELs with an Electrooptical Modulator

Another possible way of achieving loss modulation is to integrate an electrooptical modulator in the VCSEL structure (EOM-VCSEL). The refractive index of the electrooptical modulator (MQW) can be tuned by an applied voltage. If properly designed, the cavity mode of the modulator cavity can be tuned in and out of the resonance of the VCSEL cavity, which effectively modulates the mirror reflectivity, i.e., the mirror loss α_m . Small-signal modulation bandwidth up to 35 GHz, limited by the photodiode, has been reported with EOM-VCSELs [80].

7.6 Conclusion

The chapter provides an overview of the current status for high-speed VCSELs. We discussed the basic theory for current modulation of VCSELs, various high-speed designs, and device performance. Novel structures and new material systems have been pursued to overcome many of the bandwidth limitations to achieve higher performance. For short-wavelength VCSELs, bandwidth up to 24 GHz and a data rate of 40 Gb/s have been successfully demonstrated. For LW-VCSELs, single-mode, 10-Gb/s transmission over a wide temperature range has also been reported by several groups. We also considered loss-modulated VCSELs which are still under development and have the potential to reach even higher bandwidth. As these technologies become more mature and the supporting components such as high-speed photodetectors are ready, VCSELs will be used as low-cost, power-efficient, high-speed light sources for most optical data communications.

Acknowledgments The authors would like to thank the support of DARPA via the C2OI project and IBM and Corning via the UC-MICRO program.

References

1. D.A.B. Miller, Physical reasons for optical interconnection. *Int. J. Optoelectronics* **11**, 155 (1997)
2. D.M. Kuchta, P. Pepeljugoski, Y. Kwark, VCSEL modulation at 20Gb/s over 200m of multimode fiber using a 3.3v SiGe laser driver IC, in *Technical Digest LEOS Summer Topical Meeting*, Copper Mountain, CO (2001), p. 49

3. N. Suzuki, H. Hatakeyama, K. Fukatsu, T. Anan, K. Yashiki, M. Tsuji, 25-Gbps operation of 1.1- μm -range InGaAs VCSELs for high-speed optical interconnections, in *Proceedings of Optical Fiber Communication Conference, OFC 2006*, Anaheim, CA (2006)
4. K. Yashiki, N. Suzuki, K. Fukatsu, T. Anan, H. Hatakeyama, M. Tsuji, 1.1- μm -range tunnel junction VCSELs with 27-GHz relaxation oscillation frequency, in *Proceedings of Optical Fiber Communication Conference, OFC 2007*, Anaheim, CA (2007)
5. Y.-C. Chang, C.S Wang, L.A Coldren, High-efficiency, high-speed VCSELs with 35 Gbit/s error-free operation. *Electron. Lett.* **43**(19), 1022 (2007)
6. T. Anan, N. Suzuki, K. Yashiki, K. Fukatsu, H. Hatakeyama, T. Akagawa, K. Tokutome, M. Tsuji, High-speed InGaAs VCSELs for optical interconnects. in *Proceedings of International Symposium on VCSELs and Integrated Photonics*, paper E3, Tokyo, Japan (2007)
7. B.E. Lemoff, M.E. Ali, G. Panotopoulos, E. de Groot, G.M. Flower, G.H. Rankin, A.J. Schmit, K.D. Djordjev, M.R.T. Tan, A. Tandon, W. Gong, R.P. Tella, B. Law, D.W. Dolfi, Parallel-WDM for multi-Tb/s optical interconnects, in *Proceedings of IEEE Lasers and Electro-Optical Society Annual Meeting, LEOS 2005*, Sydney (2005), p. 359
8. C.L. Schow, F.E. Doany, O. Liboiron-Ladouceur, C. Baks, D.M. Kuchta, L. Schares, R. John, J.A. Kash, 160-Gb/s, 16-channel full-duplex, single-chip CMOS optical transceiver, in *Proceedings of Optical Fiber Communication Conference, OFC 2007*, Anaheim, CA (2007)
9. J. Cheng, C.-L. Shieh, X. Huang, G. Liu, M. Murty, C.C. Lin, D.X. Xu, Efficient CW lasing and high-speed modulation of 1.3- μm AlGaInAs VCSELs with good high temperature lasing performance. *IEEE Photon. Technol. Lett.* **17**(1), 7 (2005)
10. N. Nishiyama, C. Caneau, J.D. Downie, M. Sauer, C.-E. Zah, 10-Gbps 1.3 and 1.55- μm InP-based VCSELs: 85°C 10-km error-free transmission and room temperature 40-km transmission at 1.55- μm with EDC, in *Proceedings of Optical Fiber Communication Conference, OFC 2006*, Anaheim, CA (2006)
11. J. Jewell, L. Graham, M. Crom, K. Maranowski, J. Smith, T. Fanning, 1310 nm VCSELs in 1–10 Gb/s commercial applications, in *Vertical-Cavity Surface-Emitting Lasers X*, ed. by C. Lei, K.D. Choquette, Proceedings of SPIE, vol. 6132 (2007), p. 613204-1
12. W. Hofmann, N.H. Zhu, M. Ortsiefer, G. Böhm, Y. Liu, M.-C. Amann, High speed (> 11GHz) modulation of BCB-passivated 1.55 μm InGaAlAs-InP VCSELs. *Electron. Lett.* **42**(17), 976 (2006)
13. E. Söderberg, J.S. Gustavsson, P. Modh, A. Larsson, Z. Zhang, J. Berggren, M. Hammar, High-temperature dynamics, high-speed modulation, and transmission experiments using 1.3- μm InGaAs single-mode VCSELs. *J. Lightwave Technol.* **25**(9), 2791 (2007)
14. R.S. Tucker, High-speed modulation of semiconductor lasers. *J. Lightwave Technol.* **3**(6), 1180 (1985)
15. L.A. Coldren, S.W. Corzine, *Diode Lasers and Photonic Integrated Circuits* (Wiley, New York, 1995)
16. D. Tauber, G. Wang, R.S. Geels, J.E. Bowers, L.A. Coldren, Large and small signal dynamics of vertical cavity surface emitting lasers. *Appl. Phys. Lett.* **62**(4), 325 (1993)
17. T.R. Chen, B. Zhao, L. Eng, Y.H. Zhuang, J. O'Brien, A. Yariv, Very high modulation efficiency of ultralow threshold current single quantum well InGaAs lasers. *Electron. Lett.* **29**(17), 1525 (1993)
18. R. Nagarajan, T. Fukushima, S.W. Corzine, J.E. Bowers, Effects of carrier transport on high-speed quantum well lasers. *Appl. Phys. Lett.* **59**(15), 1835 (1991)
19. Y. Liu, W.-C. Ng, B. Klein, K. Hess, Effects of the spatial nonuniformity of optical transverse modes on the modulation response of vertical-cavity surface-emitting lasers. *IEEE J. Quantum Electron.* **39**(1), 99 (2003)
20. J.W. Scott, R.S. Geels, S.W. Corzine, L.A. Coldren, Modeling temperature effects and spatial hole burning to optimize vertical-cavity surface-emitting laser performance. *IEEE J. Quantum Electron.* **29**(5), 1295 (1993)

21. S.F. Yu, W.N. Wong, P. Shum, E.H. Li, Theoretical analysis of modulation response and second-order harmonic distortion in vertical-cavity surface-emitting lasers. *IEEE J. Quantum Electron.* **32**(12), 2139 (1996)
22. M. Willatzen, T. Takahashi, Y. Arakawa, Nonlinear gain effects due to carrier heating and spectral hole burning in strained-quantum-well lasers. *IEEE Photon. Technol. Lett.* **4**(7), 682 (1992)
23. Y. Liu, W.-C. Ng, F. Oyafuso, B. Klein, K. Hess, Simulating the modulation response of VCSELs: the effects of diffusion capacitance and spatial hole-burning. *IEE Proc. Optoelectron.* **149**(4), 182 (2002)
24. J. Strologas, K. Hess, Diffusion capacitance and laser diodes. *IEEE Trans. Electron Devices* **51**(3), 506 (2004)
25. K.Y. Lau, A. Yariv, Ultra-high speed semiconductor lasers. *IEEE J. Quantum Electron.* **21**(2), 121 (1985)
26. Y. Arakawa, A. Yariv, Quantum well lasers—gain, spectra, dynamics. *IEEE J. Quantum Electron.* **22**(9), 1887 (1986)
27. J.D. Ralston, S. Weisser, I. Esquivias, E.C. Larkins, J. Rosenzweig, P.J. Tasker, J. Fleissner, Control of differential gain, nonlinear gain, and damping factor for high-speed application of GaAs-based MQW lasers. *IEEE J. Quantum Electron.* **29**(6), 1648 (1993)
28. A. Schönfelder, S. Weisser, I. Esquivias, J.D. Ralston, J. Rosenzweig, Theoretical investigation of gain enhancements in strained $\text{In}_{0.35}\text{Ga}_{0.65}\text{As}/\text{GaAs}$ MQW lasers via p-doping. *IEEE Photon. Technol. Lett.* **6**(4), 475 (1994)
29. B. Zhao, T.R. Chen, A. Yariv, The extra differential gain enhancement in multiple-quantum-well lasers. *IEEE Photon. Technol. Lett.* **4**(2), 124 (1992)
30. K.L. Lear, R.P. Schneider Jr., K.D. Choquette, S.P. Kilcoyne, Index guiding dependent effects in implant and oxide confined vertical-cavity lasers. *IEEE Photon. Technol. Lett.* **8**(6), 740 (1996)
31. Y. Satuby, M. Orenstein, Limits of the modulation response of a single-mode proton implanted VCSEL. *IEEE Photon. Technol. Lett.* **10**(6), 760 (1998)
32. A.N. AL-Omari, K.L. Lear, Polyimide-planarized vertical-cavity surface-emitting lasers with 17.0-GHz bandwidth. *IEEE Photon. Technol. Lett.* **16**(4), 969 (2004)
33. K.L. Lear, A. Mar, K.D. Choquette, S.P. Kilcoyne, R.P. Schneider Jr., K.M. Geib, High-frequency modulation of oxide-confined vertical cavity surface emitting lasers. *Electron. Lett.* **32**(5), 457 (1996)
34. P. Westbergh, J.S. Gustavsson, Å. Haglund, H. Sunnerud, A. Larsson, Large aperture 850 nm VCSELs operating at bit rates up to 25 Gbit/s. *Electron. Lett.* **4**(15), 907 (2008)
35. B.J. Thibeault, K. Bertilsson, E.R. Hegblom, E. Strzelecka, P.D. Floyd, R. Naone, L.A. Coldren, High-speed characteristics of low-optical loss oxide-apertured vertical-cavity lasers. *IEEE Photon. Technol. Lett.* **9**(1), 11 (1997)
36. Y.-C. Chang, C.S. Wang, L.A. Johansson, L.A. Coldren, High-efficiency, high-speed VCSELs with deep oxidation layers. *Electron. Lett.* **42**(22), 1281 (2006)
37. R.H. Johnson, D.M. Kuchta, 30 Gb/s directly modulated 850 nm datacom VCSELs, in *Conference on Lasers and Electro-Optics*, CLEO 2008, San Jose, CA (2008)
38. E.R. Hegblom, D.I. Babic, B.J. Thibeault, L.A. Coldren, Scattering losses from dielectric apertures in vertical-cavity lasers. *IEEE J. Select. Topics Quantum Electron.* **3**(2), 379 (1997)
39. L.A. Coldren, E.R. Hegblom, Fundamental issues in VCSEL design. Chap. 2 in *Vertical-Cavity Surface-Emitting Lasers*, ed. by C. Wilmsen, H. Temkin, L.A. Coldren (Cambridge University Press, Cambridge, 1999), pp. 32–67
40. Y.H. Chang, H.C. Kuo, F.-I. Lai, K.F. Tzeng, H.C. Yu, C.P. Sung, H.P. Yang, S.C. Wang, High speed (>13 GHz) modulation of 850 nm vertical cavity surface emitting lasers (VCSELs) with tapered oxide confined layer. *IEE Proc. Optoelectron.* **152**(3), 170 (2005)
41. Å. Haglund, J.S. Gustavsson, P. Modh, A. Larsson, Dynamic mode stability analysis of surface relief VCSELs under strong RF modulation. *IEEE Photon. Technol. Lett.* **17**(8), 1602 (2005)

42. C.C. Chen, S.J. Liaw, Y.J. Yang, Stable single-mode operation of an 850-nm VCSEL with a higher order mode absorber formed by shallow Zn diffusion. *IEEE Photon. Technol. Lett.* **13**(4), 266 (2001)
43. J.-W. Shi, C.-C. Chen, Y.-S. Wu, S.-H. Guol, C. Kuo, Y.-J. Yang, High-power and high-speed Zn-diffusion single fundamental-mode vertical-cavity surface-emitting lasers at 850-nm wavelength. *IEEE Photon. Technol. Lett.* **20**(13), 1121 (2008)
44. A. Syrbu, A. Mereuta, V. Iakovlev, A. Caliman, P. Royo, E. Kapon, 10 Gbps VCSELs with high single mode output in 1310nm and 1550 nm wavelength bands, in *Proceedings of Optical Fiber Communication Conference, OFC 2008*, San Diego, CA (2008)
45. K.L. Lear, A.N. Al-Omari, Progress and issues for high-speed vertical cavity surface emitting lasers, in *Vertical-Cavity Surface-Emitting Lasers XI*, ed. by K.D. Choquette, J.K. Guenter, Proceedings of SPIE, vol. 6484 (2007), p. 64840J-1
46. Y.-C. Chang, L.A. Coldren, Efficient, high-data-rate, tapered oxide-aperture vertical-cavity surface-emitting lasers. *IEEE J. Select. Topics Quantum Electron.* **15**(3), 704 (2009)
47. C.-K. Lin, A. Tandon, K. Djordjev, S.W. Corzine, M.R.T. Tan, High-speed 985 nm bottom-emitting VCSEL arrays for chip-to-chip parallel optical interconnects. *IEEE J. Select. Topics Quantum Electron.* **13**(5), 1332 (2007)
48. M.G. Peters, B.J. Thibeault, D.B. Young, J.W. Scott, F.H. Peters, A.C. Gossard, L.A. Coldren, Band-gap engineered digital alloy interfaces for lower resistance vertical-cavity surface-emitting lasers. *Appl. Phys. Lett.* **63**(25), 3411 (1993)
49. K.L. Lear, R.P. Schneider Jr., Uniparabolic mirror grading for vertical cavity surface emitting lasers. *Appl. Phys. Lett.* **68**(5), 605 (1996)
50. K.L. Lear, V.M. Hietala, H.Q. Hou, J. Banas, B.E. Hammons, J. Zolper, S.P. Kilcoyne, Small and large signal modulation of 850 nm oxide-confined vertical-cavity surface-emitting lasers, in *Conference on Lasers and Electro-Optics, CLEO'97*, Baltimore, MD (1997)
51. M. Ortsiefer, W. Hofmann, E. Rönneberg, A. Boletti, A. Gatto, P. Boffi, J. Roskopf, R. Shau, C. Neumeyr, G. Böhm, M. Martinelli, M.-C. Amann, High speed 1.3 μ m VCSELs for 12.5 Gbit/s optical interconnects. *Electron. Lett.* **44**(16), 974 (2008)
52. D.L. Mathine, H. Nejad, D.R. Allee, R. Droopad, G.N. Maracas, Reduction of the thermal impedance of vertical-cavity surface-emitting lasers after integration with copper substrates. *Appl. Phys. Lett.* **69**(4), 463 (1996)
53. T. Wipiejewski, D.B. Young, M.G. Peters, B.J. Thibeault, L.A. Coldren, Improved performance of vertical-cavity surface-emitting laser diodes with Au-plated heat spreading layer. *Electron. Lett.* **31**(4), 279 (1995)
54. A.N. Al-Omari, G.P. Carey, S. Hallstein, J.P. Watson, G. Dang, K.L. Lear, Low thermal resistance high-speed top-emitting 980-nm VCSELs. *IEEE Photon. Technol. Lett.* **18**(11), 1225 (2006)
55. Y.-C. Chang, L.A. Coldren, Optimization of VCSEL structure for high-speed operation, in *Proceedings of IEEE International Semiconductor Laser Conference, ISLC 2008*, Sorrento, Italy (2008), p. 159
56. D.B. Young, J.W. Scott, F.H. Peters, M.G. Peters, M.L. Majewski, B.J. Thibeault, S.W. Corzine, L.A. Coldren, Enhanced performance of offset-gain high-barrier vertical-cavity surface-emitting lasers. *IEEE J. Quantum Electron.* **29**(6), 2013 (1993)
57. J. Ko, E.R. Hegblom, Y. Akulova, B.J. Thibeault, L.A. Coldren, Low-threshold 840-nm laterally oxidized vertical-cavity lasers using AlInGaAs-AlGaAs strained active layers. *IEEE Photon. Technol. Lett.* **9**(7), 863 (1997)
58. H.C. Kuo, Y.S. Chang, F.Y. Lai, T.H. Hsueh, L.H. Lai, S.C. Wang, High-speed modulation of 850 nm InGaAsP/InGaP strain-compensated VCSELs. *Electron. Lett.* **39**(14), 1051 (2003)
59. T. Aggerstam, R.M.V. Würtemberg, C. Runnström, E. Choumas, Large aperture 850 nm oxide-confined VCSELs for 10 Gb/s data communication, in *Vertical-Cavity Surface-Emitting Lasers VI*, ed. by C. Lei, S.P. Kilcoyne, Proceedings of SPIE, vol. 4649 (2002), p. 19

60. S.L. Yellen, A.H. Shepard, R.J. Dalby, J.A. Baumann, H.B. Serreze, T.S. Guido, R. Soltz, K.J. Bystrom, C.M. Harding, R.G. Waters, Reliability of GaAs-based semiconductor diode lasers: 0.6–1.1 μm . *IEEE J. Quantum Electron.* **29**(6), 2058 (1993)
61. P. Westbergh, J.S. Gustavsson, Å. Haglund, A. Larsson, H. Hopfer, G. Fiol, D. Bimberg, A. Joel, 32 Gbit/s multimode fibre transmission using a high speed, low current density 850 nm VCSEL. *Electron. Lett.* **45**(7), 366 (2009)
62. S.A. Blokhin, J.A. Lott, A. Mutig, G. Fiol, N.N. Ledentsov, M.V. Maximov, A.M. Nadtochiy, V.A. Shchukin, D. Bimberg, 40 Gbit/s oxide-confined 850 nm VCSELs. *Electron. Lett.* **45**(10), 501 (2009)
63. F. Hopfer, A. Mutig, G. Fiol, M. Kuntz, S.S. Mikhlin, I.L. Krestnikov, D.A. Livshits, A.R. Kovsh, C. Bornholdt, V. Shchukin, N.N. Ledentsov, V. Gaysler, N.D. Zakharov, P. Werner, D. Bimberg, 20 Gb/s direct modulation of 980 nm VCSELs based on submonolayer deposition of quantum dots, in *Workshop on Optical Components for Broadband Communication*, ed. by P.-Y. Fonjallaz, T.P. Pearsall, Proceedings of SPIE, vol. 6350 (2006), p. 635003-1
64. A. Mutig, G. Fiol, P. Moser, F. Hopfer, M. Kuntz, V. Shchukin, N. Ledentsov, D. Bimberg, S. Mikhlin, I. Krestnikov, D. Livshits, A. Kovsh, 120 °C 20 Gbit/s operation of 980 nm single mode VCSEL, in *Proceedings of IEEE International Semiconductor Laser Conference, ISLC 2008*, Sorrento, Italy (2008), p. 9
65. N. Suzuki, H. Hatakeyama, K. Tokutome, M. Yamada, T. Anan, M. Tsuji, 1.1 μm range InGaAs VCSELs for high-speed optical interconnections, in *Proceedings of IEEE Lasers and Electro-Optical Society Annual Meeting, LEOS 2005*, Sydney (2005), p. 394
66. K. Fukatsu, K. Shiba, Y. Suzuki, N. Suzuki, H. Hatakeyama, T. Anan, K. Yashiki, M. Tsuji, 30-Gbps transmission over 100 m-MMFs (GI32) using 1.1 μm -range VCSELs and receivers, in *Proceedings of International Conference on Indium Phosphide and Related Materials*, Matsue, Japan (2007), p. 434
67. T. Anan, N. Suzuki, K. Yashiki, K. Fukatsu, H. Hatakeyama, T. Akagawa, K. Tokutome, M. Tsuji, High-speed 1.1- μm -range InGaAs VCSELs, in *Proceedings of Optical Fiber Communication Conference, OFC 2008*, San Diego, CA (2008)
68. H. Hatakeyama, T. Anan, T. Akagawa, K. Fukatsu, N. Suzuki, K. Tokutome, M. Tsuji, Highly reliable high speed 1.1 μm -InGaAs/GaAsP-VCSELs, in *Vertical-Cavity Surface-Emitting Lasers XIII*, ed. by K.D. Choquette, C. Lei, Proceedings of SPIE, vol. 7229 (2009), p. 722902-1
69. P. Gilet, E. Pugeoise, L. Grenouillet, P. Grosse, N. Olivier, S. Poncet, A. Chelnokov, J.M. Gérard, R. Stevens, R. Hamelin, M. Hammar, J. Berggren, P. Sundgren, 1.3 μm VCSELs: InGaAs/GaAs, GaInNAs/GaAs multiple quantum wells and InAs/GaAs quantum dots—three candidates as active material, in *Vertical-Cavity Surface-Emitting Lasers XI*, ed. by K.D. Choquette, J.K. Guenter, Proceedings of SPIE, vol. 6484 (2007), p. 64840F-1
70. S. Mogg, N. Chitica, U. Christiansson, R. Schatz, P. Sundgren, C. Asplund, M. Hammar, Temperature sensitivity of the threshold current of long-wavelength InGaAs-GaAs VCSELs with large gain-cavity detuning. *IEEE J. Quantum Electron.* **40**(5), 453 (2004)
71. J. Jewell, L. Graham, M. Crom, K. Maranowski, J. Smith, T. Fanning, M. Schnoes, Commercial GaInNAs VCSELs grown by MBE. *Phys. Status Solidi C* **5**(9), 2951 (2008)
72. D. Feezell, L.A. Johansson, D.A. Buell, L.A. Coldren, Efficient modulation of InP-based 1.3- μm VCSELs with AsSb-based DBRs. *IEEE Photon. Technol. Lett.* **17**(11), 2253 (2005)
73. W. Hofmann, M. Ortsiefer, E. Rönneberg, C. Neumeyr, G. Böhm, M.-C. Amann, 1.3 μm InGaAlAs/InP VCSEL for 10G Ethernet, in *Proceedings of IEEE International Semiconductor Laser Conference, ISLC 2008*, paper MB3, Sorrento, Italy (2008)
74. N. Nishiyama, C. Caneau, B. Hall, G. Guryanov, M.H. Hu, X.S. Liu, M.-J. Li, R. Bhat, C.E. Zah, Long-wavelength vertical-cavity surface-emitting lasers on InP with lattice matched AlGaInAs-InP DBR grown by MOCVD. *IEEE J. Select. Topics Quantum Electron.* **11**(5), 990 (2005)
75. X. Zhao, D. Parekh, E.K. Lau, H.-K. Sung, M.C. Wu, W. Hofmann, M.C. Amann, C.J. Chang-Hasnain, Novel cascaded injection-locked 1.55- μm VCSELs with 66 GHz modulation bandwidth. *Opt. Express* **15**(22), 14810 (2007)

76. E.A. Avrutin, V.B. Gorfinkel, S. Luryi, K.A. Shore, Control of surface-emitting laser diodes by modulating the distributed Bragg mirror reflectivity: small-signal analysis. *Appl. Phys. Lett.* **63**(18), 2460 (1993)
77. J. van Eisdén, M. Yakimov, V. Tokranov, M. Varanasi, O. Romyantsev, E.M. Mohammed, I.A. Young, S.R. Oktyabrsky, High frequency resonance-free loss modulation in a duo-cavity VCSEL, in *Vertical-Cavity Surface-Emitting Lasers XII*, ed. by C. Lei, J.K. Guenter, Proceedings of SPIE, vol. 6908 (2008), p. 69080M-1
78. J. van Eisdén, M. Yakimov, V. Tokranov, M. Varanasi, E.M. Mohammed, I.A. Young, S. Oktyabrsky, Modulation properties of VCSEL with intracavity modulator, in *Vertical-Cavity Surface-Emitting Lasers XI*, ed. by K.D. Choquette, J.K. Guenter, Proceedings of SPIE, vol. 6484 (2007), p. 64840A-1
79. J. van Eisdén, M. Yakimov, V. Tokranov, M. Varanasi, E.M. Mohammed, I.A. Young, S.R. Oktyabrsky, Optically decoupled loss modulation in a duo-cavity VCSEL. *IEEE Photon. Technol. Lett.* **20**(1), 42 (2008)
80. A. Paraskevopoulos, H.J. Hensel, W.D. Molzow, H. Klein, N. Grote, N.N. Ledentsov, V.A. Shchukin, C. Möller, A.R. Kovsh, D.A. Livshits, I.L. Krestnikov, S.S. Mikhlin, P. Matthijsse, G. Kuyt, Ultra-high-bandwidth (>35 GHz) electrooptically-modulated VCSEL, in *Proceedings of Optical Fiber Communication Conference, OFC 2006* Anaheim, CA (2006)

Ultra-compact, high-yield intra-cavity contacts for GaAs/AlGaAs-based vertical-cavity surface-emitting lasers

Chin-Han Lin,^{a)} Brian J. Thibeault, Yan Zheng, Mark J. W. Rodwell, and Larry A. Coldren
Department of Electrical and Computer Engineering, University of California, Santa Barbara, California 93106

Alok Mehta and Anis Husain
Ziva Corporation, San Diego, California 92121

(Received 20 August 2012; accepted 12 November 2012; published 11 December 2012)

A novel method of fabricating compact intra-cavity contacts with high yield for GaAs/AlGaAs-based vertical-cavity surface-emitting lasers is presented. By carefully tailoring the composition of high-aluminum content layer, a highly selective Al₂O₃ etch-stop layer can be formed simultaneously with the oxide aperture during wet thermal oxidation. With this technique, contact metals can be uniformly deposited on deeply embedded contact layers over large substrate areas. Utilizing this embedded etch-stop design, dual intra-cavity contacted three-terminal vertical-cavity surface-emitting lasers were fabricated, demonstrating submilliampere threshold currents, over 54% differential quantum efficiencies and over 9 mW output powers. © 2013 American Vacuum Society. [<http://dx.doi.org/10.1116/1.4769856>]

I. INTRODUCTION

Over the past few years, vertical-cavity surface-emitting lasers (VCSELs) have become the most commercially successful GaAs/AlGaAs-based semiconductor lasers due to their versatility in the communication and sensing areas.¹ The main driving force is the emerging need for high-speed, highly efficient laser sources to power the optical links in data centers and high performance computing (HPC) systems. Compared to edge-emitting semiconductor lasers, VCSELs have the advantages of small footprint, high-speed modulation with low power consumption, capability of two-dimensional array fabrication, and a circular beam shape for efficient fiber coupling. Researchers also showed that by replacing the legacy AlGaAs/GaAs quantum wells (QWs) with strained InGaAs/GaAs quantum wells as the active region, it is possible to achieve higher data rate and lower power dissipation (less than a pJ/bit).^{2,3}

In addition to diode VCSELs, multi-terminal VCSELs have also drawn some recent interest due to their new functionalities and applications, such as direct gain modulation for potentially higher speed,⁴ polarization switching,⁵ and direct loss modulation.⁶ The third terminal is often inserted in the form of extra intra-cavity contact layer, adding complexity to the epitaxial growth and the device fabrication.

The strength of the GaAs/AlGaAs material system for VCSELs is the wide bandgap range available on a lattice-matched platform, so stacks of distributed Bragg reflectors (DBRs) mirrors can be grown epitaxially. Typical mirror thickness requires etching depths of several microns to reach the deeply embedded intra-cavity contact layers, limiting the adoption of intra-cavity contacts on the mass production level, since a laser monitor has to be used to stop the dry etch at the desired layer.

However, even with the assist of a laser monitor, it is still very challenging to obtain high device yield on a large wafer due to the fact that nearly all the dry-etching techniques, including reactive ion etch (RIE) and inductively coupled plasma etch (ICP), create a depth gradient where edge parts get etched more than the center part of the wafer. In order to accommodate this etch gradient the thickness of the intra-cavity contact layer can be increased as long as it is exactly an odd multiple of the designed wavelength in that material (1/4-λ, 3/4-λ, 5/4-λ, 7/4-λ, etc., in GaAs) to maintain the phase matching conditions of DBR mirrors. However, this leads to two significant negative impacts on the device performance:

- (i) Higher threshold current and lower differential quantum efficiency (DQE). The thicker contact layers needed for process control, the more dopants have to be placed in the high electric field regions within the cavity, resulting in higher free carrier absorption loss that increases the internal loss α_i , which leads to higher threshold gain g_{th} providing the same confinement factor Γ and mirror loss α_m [Eq. (1)]. To compensate for this effect, higher threshold current I_{th} is required for the increased threshold gain g_{th} [Eqs. (2) and (3)]. Here, A represents the active area, and g_o and J_{tr} are the gain parameters.

$$\Gamma g_{th} = \alpha_i + \alpha_m, \quad (1)$$

$$I_{th} = A \cdot J_{th}, \quad (2)$$

$$g_{th} = g_o \ln \frac{J_{th}}{J_{tr}}, \quad (3)$$

$$\eta_d = \eta_i \frac{\alpha_m}{\alpha_i + \alpha_m}. \quad (4)$$

The differential quantum efficiency η_d , given the same injection efficiency η_i , will also be reduced since internal

^{a)}Electronic mail: chinhan@ece.ucsb.edu

loss α_i is increased [Eq. (4)]. These two effects result in a lower output power at a given biasing current, which is a common disadvantage for multi-terminal VCSELs.

- (ii) Lower differential gain and lower direct modulation speed. Higher threshold current means lower differential gain a [Eq. (5)]. Longer effective cavity length means larger mode volume V_P . Both of these effects reduce the small signal modulation bandwidth f_{3dB} [Eq. (6)].

$$a \propto \left. \frac{\partial g}{\partial J} \right|_{J_{th}} = \frac{g_0}{J_{th}}, \quad (5)$$

$$f_{3dB} \propto \sqrt{a/V_P}. \quad (6)$$

It is possible to stop the etch on AlGaAs by adding a small amount of SF₆ to chloride-based etch chemistry,⁷ but the gas has to be turned on just before the target layer. Since a deep etch (3–4 μm) would produce a large nonuniformity (80 nm for 2%), this technique would not work over large areas even with the assist of a laser monitor.

In this paper, a novel method will be proposed to make thin intra-cavity contact layers through the incorporation of an etch-stopping mechanism, which is essential to enhance the performance of multi-terminal VCSELs and make them feasible for mass production.

II. OBSERVATION OF ETCHING UNIFORMITY

A. RIE loading effect

To quantify the dry-etch nonuniformity in a RIE system, a 2 in. semi-insulating GaAs wafer was diced into quarters and then patterned with SPR220-7 photoresist.

The etch tool was a home-built RIE system with pure Cl₂ as the only reactant. The wafers were mounted by MUNG II, a type of silicon based thermal vacuum grease, to a silicon backing wafer which was water cooled to regulate the temperature. Before turning on the reactant gas, the etch chamber was pumped down to 1×10^{-7} Torr background pressure range, to minimize background O₂ and H₂O concentrations. The intake of Cl₂ was regulated by a mass flow controller (MFC) to maintain a constant flow rate of 7.2 sccm, with the chamber pressure kept at 1.6 mTorr. Etching proceeded for 10 min with 40 W of RIE power.

The first sample was etched alone. The second sample was surrounded by dummy pieces of GaAs wafers when loading into the etch chamber. Following the etch, both samples were then soaked in 1165 stripper to remove the photoresist. Step heights were measured using a DekTek 6 profilometer across the whole wafer to determine etch rate and uniformity. The results are shown in Fig. 1. For the 2 in. quarter GaAs that was etched alone, an average etch rate of 195 nm/min was observed at the center of the wafer, while the edge was etched around 20% faster than the center. For the other quarter that was accompanied by dummy GaAs wafers, an average etch rate of 104 nm/min was observed at the center of the wafer, while the edge was etched around 10% faster

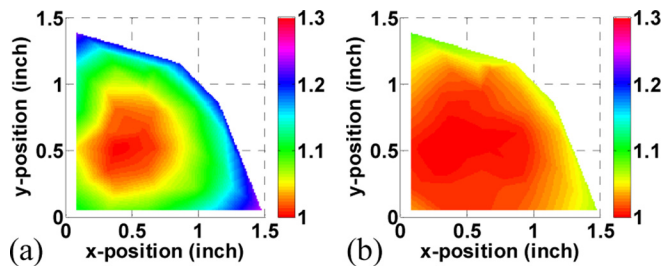


FIG. 1. (Color online) RIE etch uniformity map of (a) stand-alone 3 in. GaAs quarter wafer, normalized to 195 nm/min etch rate; (b) 3 in. GaAs quarter wafer surrounded by dummy GaAs pieces, normalized to 104 nm/min etch rate.

than the center. By surrounding the target wafer with dummy pieces of the same material, the etching uniformity can be significantly improved, with the trade-off of lower etch rate.

However, even the uniformity variation can be lowered to 10%, an intra-cavity GaAs contact layer will still need to be 500 nm thick for a common 5 μm deep etch, which is about 1.75λ thick for a 980 nm VCSEL or 2λ thick for a 850 nm VCSEL. To further reduce the required thickness of intra-cavity contact layers while maintaining good yield, an etch-stopping process is necessary.

B. Oxidized AlGaAs as the etch-stop layer

The formation of robust, high-quality native oxide on silicon embarked the tremendous commercial success of Si integrated circuit technology. On the other hand, a similarly robust oxide for compound semiconductors was not found until 1990,⁸ when researchers discovered that the selective lateral wet thermal oxidation of high aluminum content semiconductors could form a mechanically stable aluminum oxide, Al₂O₃. Over the years, this process has been employed in the fabrication of various electronics and photonic devices, among which VCSELs have benefited the most and achieved performance leaps.⁹

This aluminum oxide provides not only an insulating layer to funnel the current into the active region, thus greatly enhance the injection efficiency, but also provides a low-to-high-to-low index contrast at the aperture, confining the optical mode in a similarly way as an optical lens does. In other words, both electrical and optical confinements can be achieved with the same structure. Moreover, this Al₂O₃ layer is impervious to Cl₂-based dry-tech, making it a good candidate for the etch-stop layer.

In Sec. III, we will propose a three-terminal VCSEL designed and fabricated with an embedded Al₂O₃ layer, which enables a compact cavity design and improved DC characteristics.

III. EXPERIMENTAL SETUP

A. Device design

To demonstrate the etch-stopping process, a bottom-emission, dual intra-cavity contacted 3-terminal VCSEL design was chosen. The schematic is shown in Fig. 2. The lower p -contact layer is a $7/4\lambda$ thick p -type GaAs with δ -

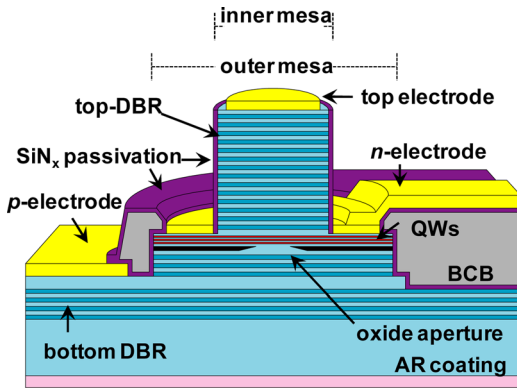


FIG. 2. (Color online) Schematic of a compact cavity three-terminal VCSEL.

doping at the optical nodes to enhance conductivity while minimizing optical loss. The upper n -contact layer is a 160 nm thick GaAs active layer that includes three $\text{In}_{0.18}\text{Ga}_{0.82}\text{As}$ quantum wells with δ -doped silicon in the four adjacent GaAs barriers, so the actual n -contact layer is about $1/4-\lambda$ thick. The n -type δ -doping provides free carriers in the quantum wells and forms two-dimensional electron gas (2DEG), so the carriers can be injected laterally into the active region with lower resistance.¹⁰ An embedded etch-stop layer will be formed directly on top of the n -contact layer to facilitate the dry-etch and be removed later with a selective wet-etch.

A two-step etch is needed for the double mesa structure. The outer mesa is formed with the first RIE etch, which stops at the p -contact layer. After the outer mesa etch, a wet thermal oxidation step creates the oxide aperture as well as the etch-stop layer. Afterward, the inner mesa mask is defined on top of the mesas, and then bottom p -contact layer is coated with thick photoresist. Hence, only the doughnut-shaped region between the inner and outer mesa circumferences will be etched by the second RIE etch, which will stop at the embedded Al_2O_3 etch-stop layer.

During the wet thermal oxidation step, different compositions of AlGaAs in the mesa structure will be oxidized at different rates. These oxides can be categorized into four groups, as shown in Fig. 3: top-DBR oxidation (with a length of l_1), etch-stop layer (with a length of l_2), oxide aperture (with a length of l_3), deep oxidation layer (with a length of l_4). It is very critical to tailor the layer compositions according to the device geometries, such as the inner mesa radius r_1 , the outer mesa radius r_2 , and the aperture radius r_3 . The importance and design rules of each of the four oxides are discussed below.

(a) The high aluminum content layers in the top-DBR will oxidize partially into ring oxides, which mask the second RIE etch and create an unwanted “coliseum wall” around the outer mesa circumference. The higher aluminum content in the top-DBRs, the deeper the sidewall oxidation and the thicker the coliseum wall will be, which is harder to be removed. On the other hand, higher aluminum content provides higher index contrast for each period of the GaAs/AlGaAs DBRs, facili-

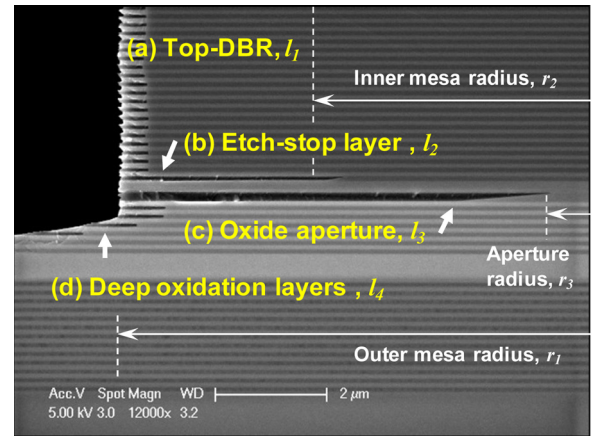


FIG. 3. (Color online) SEM cross-sectional image of various oxide layers incorporated in the VCSEL structure; (a) sidewall-oxidation of the GaAs/Al_{0.9}Ga_{0.1}As top DBR pairs; (b) etch-stop layer modified from the first GaAs/Al_{0.9}Ga_{0.1}As DBR; (c) tapered oxide aperture layer; (d) deep oxidation layers.

tating the optical confinement in the longitudinal direction. As a result, there is a design trade-off between fabrication ease and confinement strength.

(b) The etch-stop oxide has to extend long enough to provide enough coverage as the etch-stop [Eq. (7)], but shorter than the oxide aperture in order not to create extra optical loss to the cavity [Eq. (8)]

$$l_2 > r_1 - r_2, \quad (7)$$

$$l_2 < l_3. \quad (8)$$

This etch-stop layer can be created by inserting a layer of AlAs to the first period of the top-DBR, so the oxidation rate is faster than the rest of the top-DBR.

(c) The oxide aperture has to be the longest, since it is the oxide layer that actually provides optical and electrical confinement. A taper oxide design was chosen as it confines the optical mode very effectively without introducing extra cavity-loss.¹¹

(d) The deep oxidation layers reduce the parasitic capacitance between the two intra-cavity contact layers. Its design is less critical than the other three oxides’.

To achieve the desired device geometry, calibration samples were grown and processed, with these four groups of oxides verified with scanning electron microscopy (SEM). The optimized designs through iterations were summarized in Table I.

B. Material growth

Once the layer design was decided, the complete VCSEL structure was grown on 3 in. semi-insulating GaAs (100) substrate on a Veeco GenIII MBE system equipped with a custom-designed CBr₄ digital doping system¹² for p -type dopant control. The overall epitaxial thickness is around 9 μm .

C. Device fabrication

For precise control of the outer mesa dimension, a three-level mask was used to define the patterns, including

TABLE I. Oxide design.

Category	Layer design	Thickness (Å)	Oxidation length l (μm) vs time t (min)	Oxide shape
Top DBR	GaAs	546		
	Linear grading	160		
	Al _{0.9} Ga _{0.1} As	654		
	Linear grading	160	$l_1 = 0.0567t - 0.1866$ ($R^2 = 0.9798$)	Blunt
Etch-stop layer	GaAs	505		
	Parabolic grading	200		
	AlAs	96		
	Al _{0.93} Ga _{0.07} As	524		
Tapered oxide aperture	Parabolic grading	200	$l_2 = 0.0085t^2 + 0.2541t - 0.2283$ ($R^2 = 0.9999$)	Tapered (taper length around 0.3 μm)
	p -AlAs	100	$l_3 = 0.0158t^2 + 0.5358t - 1.0612$ ($R^2 = 0.9999$)	Tapered (taper length around 1.4 μm)
	p -Al _{0.93} Ga _{0.07} As	1367		
Deep oxidation layer	p -GaAs	563		
	p -parabolic grading	280		
	p -Al _{0.93} Ga _{0.07} As	458		
	p -parabolic grading	280	$l_4 = 0.0926t - 0.2388$ ($R^2 = 0.9996$)	Blunt

Note: Parabolic curve fitting worked better for the etch-stop layer and the tapered oxide aperture.

2500 nm silicon nitride (SiN_x) deposited on the GaAs/AlGaAs base structure with plasma-enhanced chemical vapor deposition (PECVD), followed by 100 nm Cr and 900 nm SPR955CM-0.9 photoresist (PR) defined by stepper lithography. The Cr was etched in a Panasonic ICP etcher at 15C substrate temperature using a low power Cl₂/O₂ based recipe with a PR-to-Cr selectivity of 1:1. The PR was removed and the SiN_x mask was defined in the Panasonic ICP etcher with a CF₄/O₂-based recipe with SiN_x-to-Cr selectivity of 30:1. After solvent cleaning, the sample was etched in a parallel plate RIE etcher with pure Cl₂ down to the lower p -type intra-cavity contact, with the assist of a laser monitor.

After the outer mesa was formed [Fig. 4(a)], the sample was cleaned with solvent and pure ammonia hydroxide to remove the natural oxides on the sidewall and then directly transferred into a tube furnace for wet thermal oxidation. The oxidation conditions for a target oxide aperture length of 8 μm were 410 °C for 12'30" [Fig. 4(b)].

After the oxidation, the inner mesa pattern was defined by SPR220-7 photoresist. The Panasonic ICP etcher was used to etch these patterns on the remaining SiN_x hard mask. The CF₄/O₂ recipe for SiN_x etch had a superior SiN_x-to-GaAs selectivity of 90:1, so the amount of GaAs machined away by the SiN_x dry-etch was negligible. The SPR220-7 masking the SiN_x layer was then stripped away, and a new layer of SPR220-7 was coated and then partially developed window to expose the semiconductor between the inner mesa and the outer mesa circumferences [Fig. 4(c)]. This PR layer was used to protect the bottom area from being attacked by the second RIE etch. A small wafer cut from the original VCSEL epitaxial wafer was mounted next to the actual wafer for laser-monitoring. The second RIE with pure Cl₂ was performed to etch down to the etch-stop oxide, with extra overetch time to ensure good etching uniformity. The selectivity between AlGaAs and Al₂O₃ was measured to be greater than 50:1 in such kind of etching chemistry. After

the inner mesa etch, the PR was removed with 1165 stripper, leaving behind the unwanted coliseum wall structures resulting from the top-DBR oxidation [Fig. 4(d)]. The AZ-400 K developer, a combination of potassium hydroxide and surfactants, was used to remove the coliseum walls as well as the etch-stop oxide layers, revealing the thin intra-cavity contact layer [Fig. 4(e)]. At this point, both intra-cavity contact layers were exposed with no observable surface damage.

Afterward, a bilayer photoresist was used to lift-off the 200/200/5000 Å of Ti/Pt/Au Ohmic contact on p -layer. The p -GaAs layer was then partially removed with patterned wet-etch to reduce to pad capacitance [Fig. 4(f)]. 2000 Å of PECVD silicon nitride was used to cover the whole device, followed by lithography and dry-etch to open vias to the ring n -contact layer and the top of the inner mesa [Fig. 4(g)]. This process is commonly used by heterojunction bipolar transistor (HBT) researchers to create semi-self-aligned dielectric spacers,¹³ allowing contact metal to be put direct next to the mesa ankle. A 800/300/3000 Å of AuGe/Ni/Au ring Ohmic contact and a 800/300/3000 Å of AuGe/Ni/Au top contact were then deposited, followed by a rapid thermal annealing step for contacts at 410 °C for 2 min in forming gas [Fig. 4(h)].

After annealing, a layer of Cyclotene 4022-25 photosensitive benzocyclobutene (BCB) was spun on, lithographically defined, and then cured in an oven. 2000 Å of PECVD SiN_x was deposited to form an adhesive layer, then both vias to the n -contact metal and p -contact metal were opened by dry-etch [Fig. 4(i)], followed by the final Ti/Au pad metallization step. The backside of the GaAs wafer was then polished and anti-reflection (AR) coated [Fig. 4(j)] to allow emission through the substrate.

IV. RESULTS AND DISCUSSION

The fabrication results were checked with a SEM to verify the details, with some of the intermediate results shown

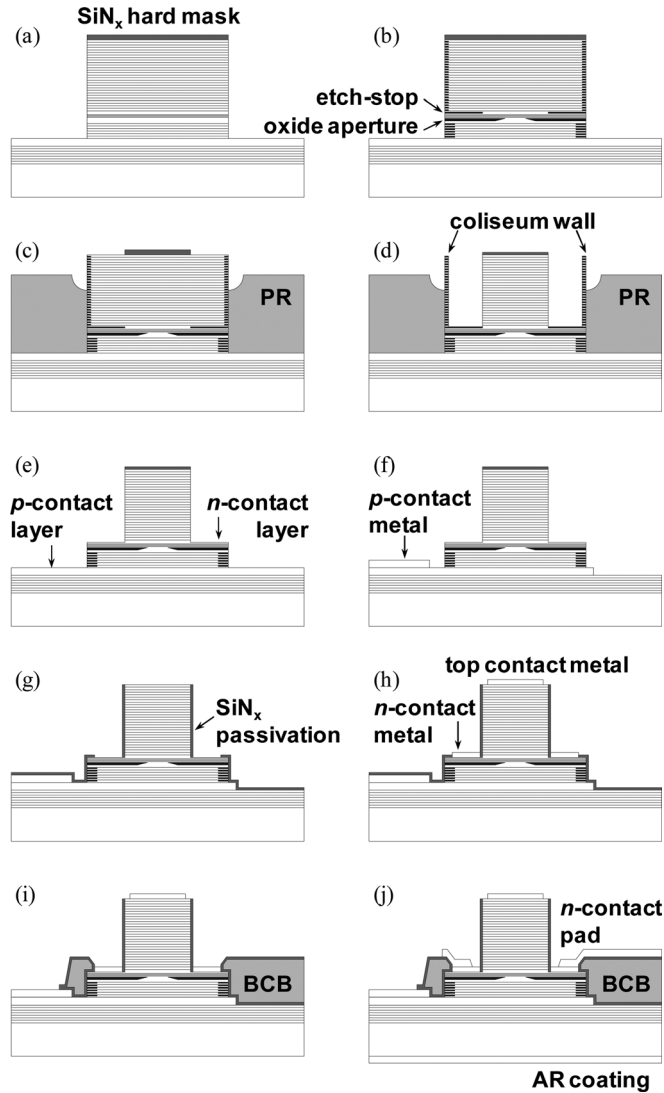


FIG. 4. Process flow for ultracompact dual intra-cavity contacted VCSEL; (a) outer mesa etch; (b) oxidation; (c) inner mesa hard-mask etch and photoresist protective layer definition; (d) inner mesa etch, leaving behind the coliseum wall of GaAs/AlGaAs stacks; (e) coliseum wall and etch-stop layer removal; (f) *p*-contact metal deposition and *p*-contact layer partial removal. (g) SiN_x passivation, and via etch (h) *n*-contact metal deposition, top-contact metal deposition, contact annealing, (i) BCB planarization and curing, (j) *n*-contact pad deposition, back-side polishing, and AR coating.

in Fig. 5. After the inner mesa etch, the residual coliseum wall structure [Fig. 5(a)] is removed with AZ-400 K developer dip, exposing the smooth intra-cavity *n*-contact layer [Fig. 5(b)]. The top-DBR and the intra-cavity *n*-contact layer are isolated with a vertical SiN_x sidewall [Fig. 5(c)].

The fabricated devices were characterized with continuous-wave (CW) operation at 20 °C, with a forward bias provided between the *n*-electrode and the *p*-electrode. Figure 6 shows the voltage and output power versus current (L - I - V) curves for devices with 3, 4, 5, 6, 7 μm of aperture diameters. The lasing wavelength is around 990 nm. All devices have a submilliampere threshold current and a differential quantum efficiency above 54%, corresponding to a slope efficiency of 0.68 (W/A). The threshold voltage is around 1.53 V, only 290 mV higher than the photon energy.

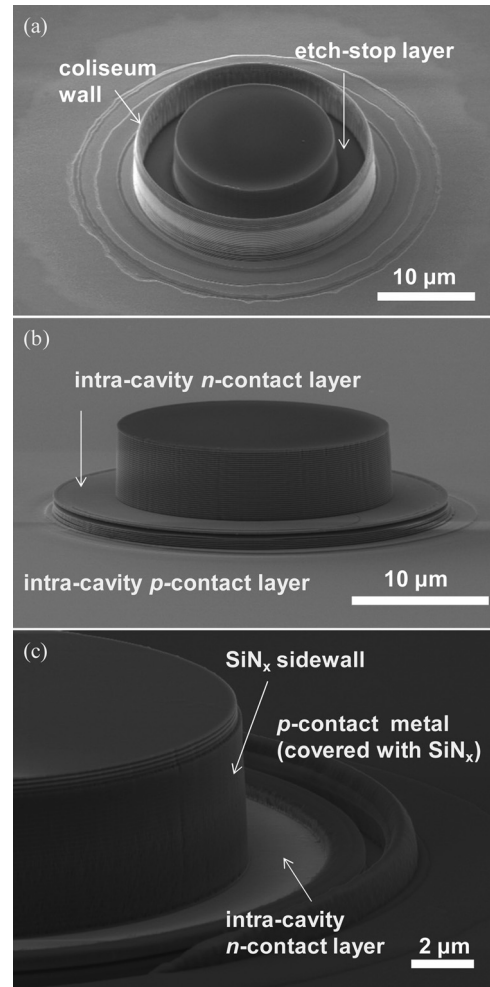


FIG. 5. SEM images of some intermediate steps of the process flow: (a) after inner mesa etch and the removal of thick protective photoresist. (b) After the coliseum wall removal with AZ-400 K developer, revealing both intra-cavity contact layers. (c) After blanket SiN_x passivation and via opening, showing the semi-self-aligned spacer and the open contact layers.

Only the 3 μm device supports single-mode operation up to 1.5 mA of bias current. With a dual intra-cavity contact configuration, the current tends to flow near the rim of the aperture, favoring higher-order modes in a large device. The

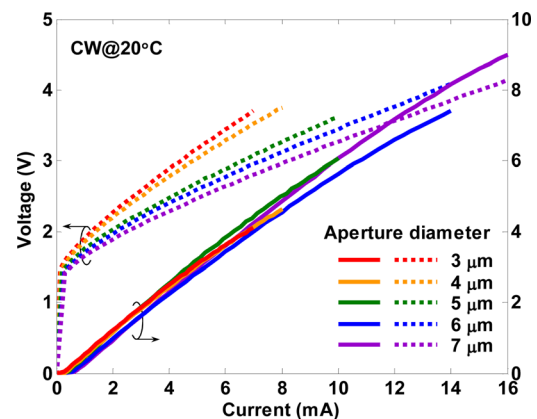


FIG. 6. (Color online) Voltage and output power vs current (L - I - V) curves for devices with different aperture diameters.

TABLE II. Device parameter and performance results.

Device aperture (μm)	3	7
Inner mesa diameter, r_2 (μm)	17	21
Outer mesa diameter, r_1 (μm)	24	28
Slope efficiency (mW/mA)	0.68	0.69
DQE	0.54	0.55
Threshold current, I_{th} (μA)	223	648
Threshold voltage, V_{th} (V)	1.53	1.54
Series resistance (Ω)	298	156
Maximum output power (mW)	4.11	9.00
Peak wall-plug efficiency	0.28	0.26

Note: DC measurements done at 20 °C.

series resistance decreases monotonically as the aperture diameter increases, from 298 Ω on a 3 μm device to 156 Ω on a 7 μm device. All devices have a peak wall-plug efficiency higher than 25%. The highest output power of 9 mW is achieved with a 7 μm device.

The direct current (DC) results of the smallest 3 μm device and the largest 7 μm device are listed in Table II.

V. CONCLUSIONS

We have demonstrated a novel method of making compact intra-cavity contacts. By changing the aluminum content above the contact layer, an embedded Al_2O_3 etch-stop layer can be formed along with the oxide aperture, without additional cost for device fabrication. After dry-tech, this Al_2O_3 etch-stop layer as well as the residual structures can be easily removed using AZ-400 K developer, without introducing extra damage to the mesa structure. Blanket PECVD SiN_x deposition and ICP etch creates a self-aligned sidewall, which allows the contact metal to be deposited directly next to the mesa ankle to reduce lateral resistance. This method

can also be applied to fabricate all the other GaAs-based electronic and photonic devices, including HBTs, high electron mobility transistors, DBR lasers, and distributed feedback lasers.

ACKNOWLEDGMENTS

The authors wish to thank Donald Freeborn and Tony Bosch for fine tuning the RIE chamber and oxidation furnace. This work was supported by DARPA through a STTR with Ziva Corporation and by NSF through a GOALI program. A portion of this work was done in the UCSB nanofabrication facility, part of the NSF funded NNIN network.

¹A. Larsson, *IEEE J. Sel. Top. Quantum Electron.* **17**, 1552 (2012).

²S. Imai *et al.*, *IEEE J. Sel. Top. Quantum Electron.* **17**, 1614 (2012).

³L. A. Coldren, Y.-C. Chang, Y. Zheng, and C.-H. Lin, *IEEE Topical Meeting Series of the Photonics Society*, Playa del Carmen, Riviera Maya, Mexico, 19–21 July 2010, Invited Paper No. TuD2.1.

⁴C.-H. Lin, Y. Zheng, M. J. W. Rodwell, and L. A. Coldren, *22nd IEEE International Semiconductor Laser Conference*, Kyoto, Japan, 26–30 September 2010, Paper No. PD2.

⁵Y. Zheng, C.-H. Lin, and L. A. Coldren, *IEEE Photonics Technol. Lett.* **23**, 305 (2011).

⁶C. Chen, P. O. Leisher, C. Long, D. M. Grasso, and K. D. Choquette, *IET Optoelectron.* **3**, 93 (2009).

⁷S. Salimian, C. B. Cooper, R. Norton, and J. Bacon, *Appl. Phys. Lett.* **51**, 1083 (1987).

⁸J. M. Dallesasse, N. Holonyak, A. R. Sugg, T. A. Richard, and N. El-Zein, *Appl. Phys. Lett.* **57**, 2844 (1990).

⁹D. L. Huffaker, D. G. Deppe, K. Kumar, and T. J. Rogers, *Appl. Phys. Lett.* **65**, 97 (1994).

¹⁰C.-H. Lin, Y. Zheng, M. Gross, M. J. W. Rodwell, L. A. Coldren, Device Research Conference, Santa Barbara, CA, 20–22 June 2011, Paper No. VII. A-3.

¹¹E. R. Hegblom, D. I. Babic, B. J. Thibeault, and L. A. Coldren, *IEEE J. Sel. Top. Quantum Electron.* **3**, 379 (1997).

¹²Y.-C. Chang, Y. Zheng, J. H. English, A. W. Jackson, and L. A. Coldren, *J. Vac. Sci. Technol. B* **28**, C3F10 (2010).

¹³M. J. W. Rodwell, M. Le, and B. Brar, *Proc. IEEE* **96**, 271 (2008).

High Speed Polarization Modulation of Oxide Confined Asymmetric VCSELs in Multimode Regime

Ajit V. Barve^a, Yan Zheng^a, Leif Johansson^a, Alok Mehta^c, Anis Husain^c, and Larry Coldren^{a,b,*}

^aDepartment of Electrical and Computer Engineering, University of California Santa Barbara, CA 93106, USA

^bDepartment of Materials, University of California Santa Barbara, CA 93106, USA

^cZiva Corporation, San Diego, CA 92121, USA

Abstract: Polarization resolved optical spectral analysis of multimode, oxide-confined asymmetric VCSELs is presented. High-extinction-ratio polarization switching has been observed even in the multimode regime of these VCSELs. Furthermore, high-frequency polarization modulation of over a GHz with gated RF electrical modulation has been achieved.

Due to the symmetric nature of vertical-cavity surface-emitting lasers (VCSELs), the output polarization is hard to control. In a symmetric VCSEL, each transverse mode is typically associated with two non-degenerate linearly polarized modes. These linear polarization modes are usually bistable and exhibit thermally driven polarization switching at certain bias currents. Mode competition between different transverse polarization modes gives rise to complex mode selection dynamics in the multimode regime. In a symmetric VCSEL, although very high extinction ratio for the polarization switching is possible in the single-mode regime, the polarization extinction-ratio is typically very low (<2) in the multimode regime, due to simultaneous lasing in several different modes with different polarization characteristics. In this paper, we present the polarization resolved optical spectrum for asymmetric oxide confined VCSELs in multimode regime. We also demonstrate the electrically driven, RF frequency induced ultrafast polarization modulation in multimode regime of the VCSEL, for the first time, and achieve high speed modulation of over 1GHz. This is more than two orders of magnitude faster than previously achieved electrically controlled polarization modulation frequency for multimode VCSELs.

Highly-strained VCSEL material with a InGaAs/GaAs quantum-well active region, operating at 1060nm was chosen for this study. The VCSEL under test has an elliptical mesa with major radius of $28\mu\text{m}$ and minor radius of $16\mu\text{m}$. The axes of ellipse are oriented along crystallographic $\langle 110 \rangle$ and $\langle 1-10 \rangle$ axes. A tapered-oxide aperture, with oxidation length of $7\mu\text{m}$ was used to confine the carriers and provide index guiding. The eccentricity of the oxide aperture is much larger than that of the mesa. The substrate of the bottom-emitting VCSEL was antireflection coated to minimize optical feedback. We have previously demonstrated [1,2] that ultrafast polarization modulation of a VCSEL is possible by applying gated electrical RF signals to the VCSEL in the single-mode regime.

Figure 1 shows the polarization resolved LI curve for constant stage temperature of 20°C for DC conditions and with a 3GHz RF signal of 5dBm nominal power overlaying on top of the DC bias current. Here, the major axis of the VCSEL is along Y-direction. Some interesting features of this LI curve are: (a) even in this highly asymmetric device, both the polarization outputs are still present; (b) very high polarization extinction ratios are observed even in the multimode regime; and (c) both X and Y modes emit similar power in the multimode regime, below 2mA, for the measurements with 3GHz RF signal, which is similar to that observed before in the single mode regime [1-2].

To get insights into the mode structure of this VCSEL, polarization resolved optical spectral measurements were carried out. Figure 2 shows two dimensional contour plots obtained by plotting optical spectral measurements for different bias currents on a same plot for (a) X polarization and (b) Y polarization. Individual optical spectra are also shown at two different bias currents, in Figure 2(c) and (d), to get an idea about the exact nature of the curves and powers in each mode. It can be seen from Figure 2(a) and (b) that the fundamental mode (TEM₀₀) switches between X and Y polarization components, while the first excited state has only a dominant Y component, due to the asymmetric nature of the VCSEL. This leads to high extinction ratio switching even in multimode regime.

Polarization resolved time domain measurements, similar to those described in Barve et al [1] were performed to estimate the speed of the polarization modulation. The VCSEL was subjected to periodic bursts of RF currents. The VCSEL output was passed through a polarizer, then focused onto a multimode optical fiber, detected and amplified. A low pass filter was used after the amplifier to block the carrier RF signal. Fig. 3 shows the time-domain response for X and Y polarized outputs at modulation frequency of 1.05GHz (DC component of the signal was blocked). The frequency of the RF source was kept constant at 2.5 GHz, and the modulation power was 5dBm. It is clear that the polarization mode changes from dominant X mode to dominant Y mode as we go from 'on' to 'off' state of the RF burst. This was measured at 2mA of DC bias applied to the VCSEL, which corresponds to the multimode regime, as seen from Fig. 2. This is, by far, the fastest reported polarization modulation using electrical injection in multimode regime.

In conclusion, we present insights into high extinction ratio polarization switching in highly asymmetric VCSELs. We also demonstrate ultrafast polarization modulation in multimode regime, which is attractive for increasing the output power of the VCSEL while maintaining high speed polarization modulation.

Disclaimer: The views expressed are those of the authors and do not reflect the official policy or position of the Department of Defense or the U.S. Government. Approved for Public Release, Distribution Unlimited

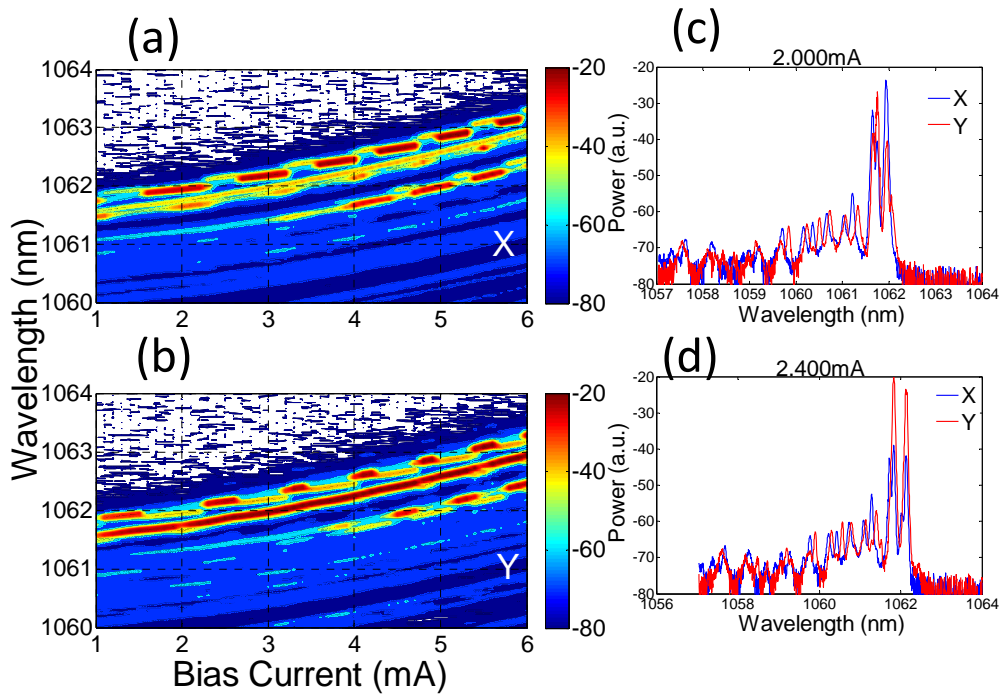
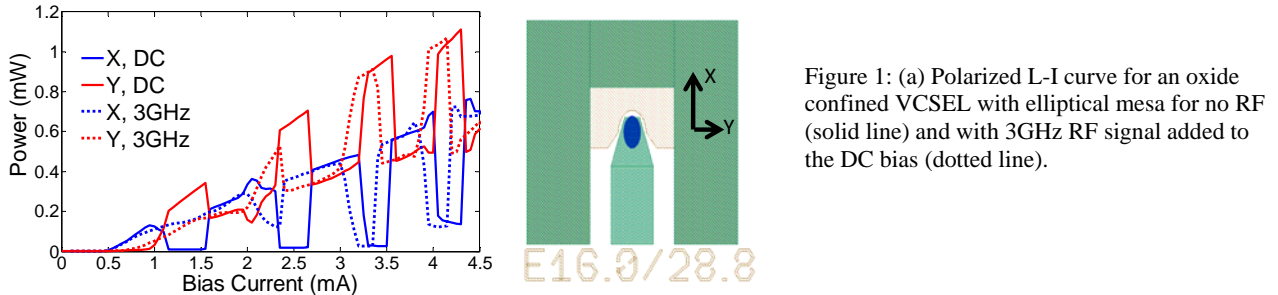


Figure 2: Contour plots of optical spectra as a function of bias for an elliptical device with major axis along Y direction for (a) X polarization, (b) Y Polarization and (c) Optical spectrum at 2.0mA, (d) 2.4mA

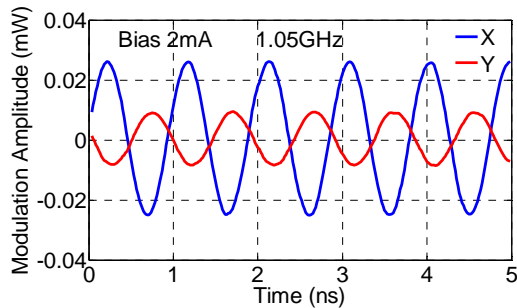


Fig. 3. Polarization modulation response for VCSEL in X and Y polarizations for modulation frequency of 1.05 GHz at 2 mA bias. RF frequency is 2.5GHz and modulation power is 5dBm

References:

- [1] Barve et al, Appl. Phys. Lett. **101**(25), pp 251104, 2012
- [2] Barve et al, IEEE Photonics Conference, TuF 3, 2012.

Fast, electrically controlled polarization modulation of multimode vertical-cavity surface-emitting lasers by RF frequency modulation

Ajit V. Barve,¹ Yan Zheng,¹ Leif A. Johansson,¹ Alok Mehta,² Anis Husain,² and Larry A. Coldren^{1,*}

¹Department of Electrical and Computer Engineering, University of California, Santa Barbara, California 93117, USA

²Ziva Corporation, San Diego, California 92121, USA

*coldren@ece.ucsb.edu

Abstract: We report on a study of polarization properties of asymmetric, multimode vertical-cavity surface-emitting lasers (VCSEL) subjected to electrical RF modulation. When subjected to RF modulation, complex frequency-dependent polarization properties, especially near the polarization switching point are revealed. We propose a scheme of rapidly switching the two RF frequencies modulating the VCSEL, in order to achieve fast polarization modulation in these VCSEL. Polarization modulation up to 300 MHz by modulating the RF frequency and up to 1.5 GHz with RF power modulation has been demonstrated; the fastest reported electrically controlled polarization modulation for multimode VCSELs.

©2013 Optical Society of America

OCIS codes: (140.0140) Lasers and laser optics; (250.0250) Optoelectronics.

References and links

1. G. Verschaffelt, K. Panajotov, J. Albert, B. Nagler, M. Peeters, J. Danckaert, I. Veretennicoff, and H. Thienpont, "Polarisation Switching in Vertical-cavity surface-emitting lasers: from experimental observations to applications," *Opto-Electron. Rev.* **9**(3), 257 (2001).
2. K. D. Choquette, R. P. Schneider, K. L. Lear, and R. E. Leibenguth, "Gain-dependent polarization properties of vertical-cavity lasers," *IEEE J. Sel. Top. Quantum Electron.* **1**(2), 661 (1995).
3. L. M. Augustin, E. Smalbrugge, K. D. Choquette, F. Karouta, R. C. Srijbos, G. Verschaffelt, E. J. Geluk, T. G. van de Roer, and H. Thienpont, "Controlled polarization switching in VCSELs by means of asymmetric current injection," *IEEE Photon. Technol. Lett.* **16**(3), 708–710 (2004).
4. Y. Zheng, C.-H. Lin, and L. A. Coldren, "Control of polarization phase offset in low threshold polarization switching VCSELs," *IEEE Photon. Technol. Lett.* **23**(5), 305–307 (2011).
5. Y. Sato, K. Furuta, T. Katayama, and H. Kawaguchi, "Polarization switching in vertical-cavity surface-emitting lasers by asymmetrical current injection," *IEEE Photon. Technol. Lett.* **20**(17), 1446–1448 (2008).
6. M. P. Tan, A. M. Kasten, T. Strand, and K. D. Choquette, "Low power polarization modulation of vertical cavity surface emitting lasers," in *Proceedings of Conference on Lasers and Electro-Optics (CLEO) 1-6 May 2011*.
7. K. Panajotov, B. Nagler, G. Verschaffelt, A. Georgievski, H. Thienpont, J. Danckaert, and I. Veretennicoff, "Impact of in-plane anisotropic strain on the polarization behavior of vertical-cavity surface-emitting lasers," *Appl. Phys. Lett.* **77**(11), 1590 (2000).
8. M. San Miguel, Q. Feng, and J. Moloney, "Light-polarization dynamics in surface-emitting semiconductor lasers," *Phys. Rev. A* **52**(2), 1728–1739 (1995).
9. J. Martin-Regalado, F. Prati, M. San Miguel, and N. B. Abraham, "Polarization properties of vertical-cavity surface-emitting lasers," *IEEE J. Quantum Electron.* **33**(5), 765–783 (1997).
10. A. Valle, I. Gatara, K. Panajotov, and M. Sciamanna, "Transverse mode switching and locking in vertical-cavity surface-emitting lasers subject to orthogonal optical injection," *IEEE J. Quantum Electron.* **43**(4), 322–333 (2007).
11. M. Virte, K. Panajotov, H. Thienpont, and M. Sciamanna, "Deterministic polarization chaos from a laser diode," *Nat. Photonics* **7**(1), 60–65 (2012).
12. M. Sciamanna, A. Valle, P. Mégret, M. Blondel, and K. Panajotov, "Nonlinear polarization dynamics in directly modulated vertical-cavity surface-emitting lasers," *Phys. Rev. E* **68**(1), 016207 (2003).
13. A. Valle, M. Sciamanna, and K. Panajotov, "Irregular pulsating polarization dynamics in gain-switched vertical-cavity surface-emitting lasers," *IEEE J. Quantum Electron.* **44**(2), 136–143 (2008).

14. R. Al-Seyab, K. Schires, N. A. Khan, A. Hurtado, I. D. Henning, and M. J. Adams, "Dynamics of polarized optical injection in 1550-nm VCSELs: theory and experiments," *IEEE J. Sel. Top. Quantum Electron.* **17**(5), 1242–1249 (2011).
15. K. D. Choquette, K. L. Lear, R. E. Leibenguth, and M. T. Asom, "Polarization modulation of cruciform vertical-cavity laser diodes," *Appl. Phys. Lett.* **64**(21), 2767 (1994).
16. K. Panajotov, B. Ruykin, J. Danckaert, M. Peeters, H. Thienpont, and I. Veretennicoff, "Polarization switching in VCSEL's due to thermal lensing," *IEEE Photon. Technol. Lett.* **10**(1), 6–8 (1998).
17. G. Verschaffelt, J. Albert, B. Nagler, M. Peeters, J. Danckaert, S. Barbay, G. Giacomelli, and F. Marin, "Frequency response of polarization switching in vertical-cavity surface-emitting lasers," *IEEE J. Quantum Electron.* **39**(10), 1177–1186 (2003).
18. D. L. Boiko, G. M. Stephan, and P. Besnard, "Fast polarization switching with memory effect in a vertical cavity surface emitting laser subject to modulated optical injection," *J. Appl. Phys.* **86**(8), 4096 (1999).
19. T. Mori, Y. Yamayoshi, and H. Kawaguchi, "Low-switching-energy and high-repetition-frequency all-optical flip-flop operations of a polarization bistable vertical-cavity surface-emitting laser," *Appl. Phys. Lett.* **88**(10), 101102 (2006).
20. S. Jiang, Z. Pan, M. Dagenais, R. A. Morgan, and K. Kojima, "High-frequency polarization self-modulation in vertical-cavity surface-emitting lasers," *Appl. Phys. Lett.* **63**, 3545–3547 (1993).
21. M. Sciamanna, T. Erneux, F. Rogister, O. Deparis, P. Me'gret, and M. Blondel, "Bifurcation bridges between external-cavity modes lead to polarization self-modulation in vertical-cavity surface-emitting lasers," *Phys. Rev. A* **65**(4), 041801 (2002).
22. A. V. Barve, Y. Zheng, L. Johansson, A. Mehta, A. Husain, and L. Coldren, "Ultrafast polarization modulation in vertical cavity surface emitting lasers with frequency dependent current injection," *Appl. Phys. Lett.* **101**(25), 251104 (2012).
23. A. V. Barve, Y. Zheng, L. A. Johansson, A. Mehta, A. Husain, and L. A. Coldren, "Fast polarization modulation in vertical cavity lasers with electrical RF injection," *Proc. 23rd IEEE Semiconductor Laser Conference*, paper no. PD1.4, San Diego, CA (2012).
24. Y. Zheng, C.-H. Lin, A. V. Barve, and L. A. Coldren, "P-type δ -doping of highly-strained VCSELs for 25Gbps operation," *IEEE Photon. Conf. IPC2012*, 131–132 (2012).
25. A. Valle, L. Pesquera, and K. A. Shore, "Polarization selection and sensitivity of external cavity vertical-cavity surface-emitting laser diodes," *IEEE Photon. Technol. Lett.* **10**(5), 639–641 (1998).

1. Introduction

Polarization properties of VCSELs are extremely interesting and yet, poorly understood. It is well known [1] that VCSELs generally exhibit abrupt polarization switching as a function of bias current, from higher to lower frequency mode (type-I switching) or vice-versa (type-II switching), depending on the detuning between the polarization modes and their relative position with respect to the gain spectrum [2]. It has also been found that the VCSEL polarization can be affected by the temperature [2], magnitude and directionality of current injection [3–6], stress [7] and with polarized optical injection. Theoretical modeling based on 'Spin-Flip Model' [8,9] has been successfully used to predict certain static [10, 11] and dynamic [12–14] polarization properties of VCSELs. However, the exact nature the complex dynamics accompanied by the polarization switching, especially in multimode VCSELs in presence of current modulation at GHz frequency scale are largely unknown. In this paper we report on experimental observations of extremely rich polarization resolved frequency response of current modulated asymmetric multimode VCSELs, showing that, even though at low frequencies VCSEL exhibits only one type of polarization, it still exhibits polarization mode competition at higher frequencies. Furthermore, we can use this frequency dependence to modulate the polarization output of the VCSEL, at GHz rate, by simply varying the RF frequency or power. High resolution optical spectral measurements reveal the details on the polarization mode-competition for multi-transverse mode, asymmetric VCSEL.

Although the polarization modulation up to 50 MHz has been previously demonstrated [15,16], the thermal nature of this effects limits high speed operation [17]. High-speed polarization modulation has been demonstrated with optical injection [18,19], but it requires complex optical injection locking and polarization controllable master laser source, thus, is not scalable. Polarization self-modulation at much higher frequencies has also been reported [20,21]. We have previously demonstrated high-speed polarization modulation by modulating the electrical RF power applied to a single mode VCSEL [22,23]. In this paper, we report on a new scheme for polarization modulation by rapidly switching the frequency of RF signal

incident on the VCSEL. This scheme leads to polarization modulation with higher modulation depths. Furthermore, since the polarization modulation is achieved by varying only the frequency of electrical signal, the results prove that the polarization modulation is purely due to electrical frequency variation, and not caused by thermal effects. We also note that faster polarization modulation, up to 1.5 GHz has also been obtained, even in multimode regime, by modulating the RF power. This ultrafast polarization modulation does not require any special fabrication steps, or a complex experimental setup, as it can be performed on simple two terminal VCSELs.

2. Design and fabrication

VCSELs used for these measurements consisted of highly-strained InGaAs/GaAs quantum-well (QW) active region, operating at 1060 nm. Details of this design can be found in Zheng et al [24]. The material was processed into elliptical mesa VCSELs with varying sizes. The electrical and optical confinement was provided with a tapered oxide aperture, with a total oxidation length of 7 μm . The devices have a simple two contact geometry with a bottom-emitting configuration. The backside of the substrate was coated with an antireflection (AR) coating of magnesium oxide (MgO) after fabrication, to avoid the optical feedback during measurements.

3. Experimental results

After fabrication, polarization resolved light-current (L-I) characteristics were measured using a Si-based broad-area DC detector and a wire-grid polarizer. A constant stage temperature of 20°C was maintained in all the measurements. Y direction is the direction which is along the major axis of ellipse, which is orthogonal to X. X and Y are found to be aligned to $\langle 110 \rangle$ and $\langle \bar{1}\bar{1}0 \rangle$ crystalline directions. L-I characteristic measured from one of the elliptical VCSELs is shown in Fig. 1(a). In this VCSEL, major axis is 22 μm and minor axis is 16 μm . It should be noted that the ellipticity of the actual oxide aperture is different than the outer mesa geometry. It is clear that this highly asymmetric VCSEL still supports both X and Y linearly polarized modes. Interesting thing to note here is that although the VCSEL operates in multimode regime above current of 2.8 mA, it still exhibits very high extinction ratio thermal polarization switching. This behavior, observed in several asymmetric VCSELs, is in contrast with the traditional circular mesa devices. Polarization resolved optical spectral measurements have been plotted as a function of bias current in Figs. 1(b) and 1(c). These measurements reveal that the high contrast switching even at higher bias currents in multimode regime is due to the two polarization modes corresponding to the fundamental transverse mode, switch back and forth as a function of bias current. Due to the asymmetric nature of the VCSEL, the threshold for first higher-order transverse mode in one direction is much lower than the orthogonal mode. As a result, only the fundamental mode emits in one of the two orthogonal polarizations, even in the multimode regime, resulting in high contrast polarization switching. The multiple polarization switching in the fundamental mode is believed to be a result of imperfect AR coating, resulting in weak optical feedback [25].

When the VCSELs are subjected to electrical RF modulation with 2 dBm nominal power, at RF frequencies ranging from 0.1 GHz to 20 GHz, a complex nature of polarization dynamics is revealed. Figures 2 (a) and 2(b) shows the contour plots of modulation response (S_{21}) measured from this VCSEL at different bias currents for X polarization, Y polarization, respectively. The ratio of powers in X and Y mode is shown in Fig. 2(c), in which red corresponds to X mode and blue corresponds to Y mode. It is apparent that even though at DC, the VCSEL exhibits one of the two polarizations, there is a rich, complimentary, frequency dependence of powers in each linear polarization mode, especially near the polarization switching point. It is to be noted that this dependence has similar functional form for both, type I (from high frequency mode to low frequency mode) and type II polarization switch (from low frequency mode to high frequency mode). Figure 2(d) shows the individual

response at bias current of 4.4 mA, corresponding to the multimode regime, showing that the polarization contrast ratio in excess of 30 dB can be obtained by this technique. These measurements are extremely repeatable, proving that the frequencies of polarization switch are not determined by spontaneous emission noise. Similar behavior of rapidly switching polarization direction was also observed in single mode regime. In both the regimes, there is strong frequency dependence to the modulation amplitude, with sharp peaks in one type of polarization corresponding to dips in other polarization. Due to relatively small modulation depth and high bias current operation, period doubling nonlinear dynamics were not observed.

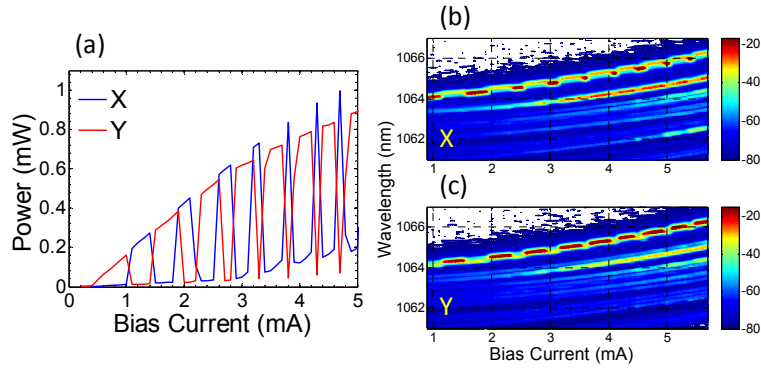


Fig. 1. (a) Measured L-I characteristics of an elliptical, oxide confined VCSEL showing high polarization contrast ratio even in multimode regime (b)-(c) high resolution optical spectral measurements as a function of current, for X and Y polarization.

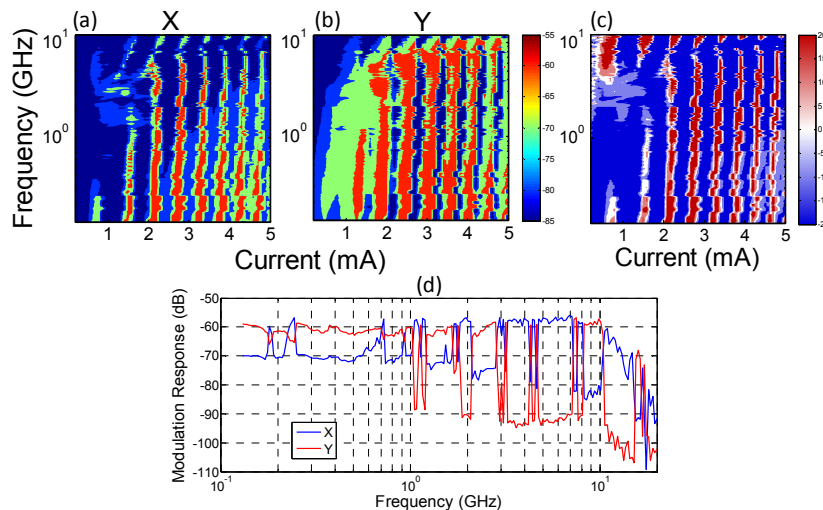


Fig. 2. Contour plots of modulation responses at different bias currents, for (a) X-polarization, (b) Y-polarization and (c) Difference between X and Y, showing the mode stability plot for the VCSEL. (d) Modulation response 4.4mA, showing abrupt switching between X and Y modes as a function of frequency.

Using this strong frequency dependence, it is possible to modulate the polarization state of the VCSEL. For this, it is necessary to switch the frequency of the current modulation of the VCSEL at a rapid rate. This was achieved with a setup schematically shown in Fig. 3. Two RF source of equal amplitude are passed through double-balanced mixers, with direct and inverted signal from a square-wave generator, respectively. At the output of each mixer, the corresponding RF signal is switched on and off, exactly out-of-phase with each other. The output was then combined in a resistive splitter, which produces a RF signal of constant

amplitude and with frequency varying at the same rate as the square wave frequency (f_m), as shown in the inset of Fig. 3. Path lengths of the two arms were matched in order to get a minimum overlap between the two RF signal bursts. This RF signal was then amplified to the same power levels used in the previous measurement (2 dBm nominal power) and applied to the VCSEL along with a fixed DC bias using a bias-tee network. The output of the VCSEL was collimated onto a multimode fiber, after passing through a wire-grid polarizer, and then detected by a high speed detector. The output of the detector was amplified and then passed through a low-pass filter, which blocks the RF carrier frequencies (f_1 and f_2), while transmitting f_m for an envelope detection. This measurement setup ensures that all the parameters except the frequency of RF signal are unchanged, and the observed polarization modulation can only be explained by the RF frequency induced polarization modulation effect described earlier.

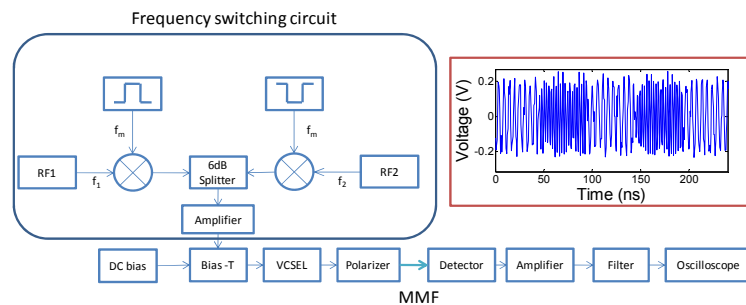


Fig. 3. Schematics of the experimental setup used for rapidly switching between f_1 and f_2 for modulating the VCSEL. The inset shows the output of the amplifier before the bias-T network.

Figures 4 (a)-(c) shows the modulation response for the VCSEL in multimode regime, at three different f_m . For this measurement, f_1 and f_2 was set to 5.4 GHz and 2.25 GHz, respectively. It is clear that, up to 300 MHz modulation frequency, the two polarizations are 180° out-of-phase with each other, indicating that the frequency sweep is changing the power in each linear polarization mode, as expected. At higher frequencies, the two polarization modes do not change exactly 180° from each other. Here, it should be noted that f_m of 300 MHz means that each polarization mode is being modulated at 300 MHz frequency; the actual polarization change is occurring at twice the frequency. This polarization modulation frequency is much higher than the typical polarization switching frequencies due to thermal polarization switching or mode hopping. It should also be noted that the DC component of the electrical signal has been blocked by the amplifier. Corresponding DC measurements reveal that polarization contrast ratio of above 15:1 can be obtained by this technique.

It is possible to further increase the polarization modulation speed by modulating the RF power instead of RF frequency, as previously shown [22,23] for single mode VCSELs. For this, only one RF source is needed, the output of which is combined with a square wave, similar to that shown in Fig. 3. In this case, the polarization modulation takes place due to the RF power dependence of polarization for the VCSEL subjected to a constant RF frequency (not shown here). Figure 5 shows the polarization modulation response obtained with this technique, in multimode regime of the VCSEL, at the modulation frequency of 1.5 GHz. A sinusoidal pattern was obtained due to the low pass filter used to block the carrier RF. VCSEL was biased at 4.4 mA, and RF frequency of 4.95 GHz was used for this experiment. It is to be noted that in this case, the polarization modulation is faster than the frequency-sweep experiment described earlier, because only the faster frequency is used as the carrier frequency. This polarization modulation frequency is, by far, the fastest reported for polarization modulation in electrically-controlled multimode VCSELs.

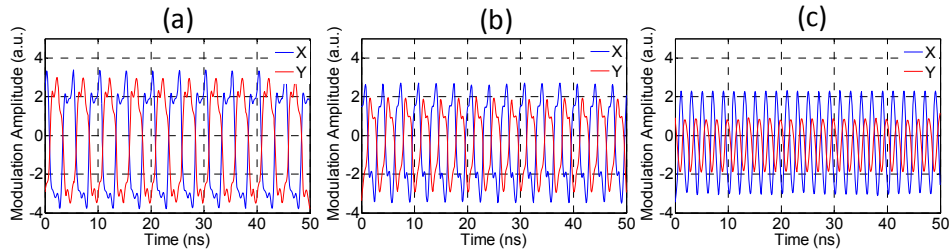


Fig. 4. Polarization modulation of the VCSEL, subjected to varying RF signal with frequency modulated at (a) 200 MHz (b) 300 MHz and (c) 500 MHz.

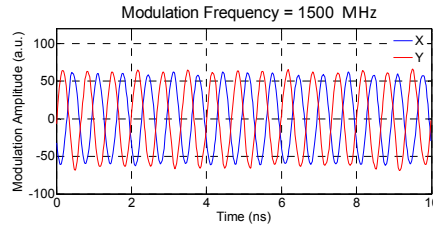


Fig. 5. Polarization modulation response for the VCSEL subjected to a fixed RF frequency and the RF power modulated at 1.5 GHz.

4. Conclusions

In conclusion, we report on the observations of rich and complex frequency response of a VCSEL subjected to RF current modulation. It has been observed that near the polarization switching point, VCSEL can be controllably switched between the two linear polarization modes as a function of the frequency of current modulation. We demonstrate that, using this effect, it is possible to modulate the polarization of the VCSEL at high speeds, either by modulating the frequency of RF signal, or the power of RF signal applied to the VCSEL. Polarization modulation of 300 MHz and 1.5 GHz has been demonstrated with these two techniques, respectively, in the multimode regime of the VCSEL.

Acknowledgment

This work was supported by DARPA, via STTR with Ziva Corp. Disclaimer: The views expressed are those of the authors and do not reflect the official policy or position of the Department of Defense or the U.S. Government. Distribution Statement “A” (Approved for Public Release, Distribution Unlimited).